

# Interplay between non-collinear magnetism and nanoscale structural properties in epitaxial Fe-based ultrathin films

Dissertation  
zur Erlangung des Doktorgrades  
an der Fakultät für Mathematik, Informatik und  
Naturwissenschaften  
Fachbereich Physik  
der Universität Hamburg

vorgelegt von  
Aurore Finco

Hamburg  
2018

Gutachter/innen der Dissertation:	Prof. Dr. Roland Wiesendanger Dr. Robert Frömter
Zusammensetzung der Prüfungskommission:	Prof. Dr. Roland Wiesendanger Dr. Robert Frömter Prof. Dr. Michael Rübhausen Prof. Dr. Michael Potthoff Prof. Dr. Ralf Röhlsberger
Vorsitzende/r der Prüfungskommission:	Prof. Dr. Michael Rübhausen
Datum der Disputation:	09.07.2018
Vorsitzender Fach-Promotionsausschusses PHYSIK:	Prof. Dr. Wolfgang Hansen
Leiter des Fachbereichs PHYSIK:	Prof. Dr. Michael Potthoff
Dekan der Fakultät MIN:	Prof. Dr. Heinrich Graener

# Abstract

In view of creating devices taking advantage of the properties of non-collinear magnetic states in ultrathin films, the ability to stabilize and reliably control them is essential. In particular, topological spin configurations like skyrmions exhibit special transport properties and an enhanced stability compared to trivial states. In this thesis, non-collinear magnetism is studied in epitaxial ultrathin films. In the case of a perfect pseudomorphic growth, an ultrathin film with a thickness of a few atomic layers is an ideal system to study the fundamental features of complex magnetic structures and compare experimental and theoretical results. However, in many situations, the atomic structure of the films is more complicated, because of strain relief for example, and some additional structural patterns are present. The systems become less simple, but a broad range of new phenomena appears. The investigation of the interplay between these nanoscale structural patterns and the non-collinear magnetic states could give some information about the more complex mechanisms which take place in sputtered films and for instance lead to pinning. Pinning reduces the mobility of skyrmions and is currently an obstacle to the development of energy-efficient skyrmion-based devices.

This thesis is a spin-polarized scanning tunneling microscopy study of the magnetic states in Fe-based ultrathin films on Ir(111) which exhibit a structural pattern. The spin spirals and the skyrmions in a Fe triple atomic layer grown on Ir(111) are analyzed in detail. The Fe film is uniaxially relaxed through the formation of dislocation lines which have a large influence on the characteristics of the spirals and the skyrmions. Furthermore, the thermal stability of this system is investigated. A large increase of the period of the spirals with temperature is observed and interpreted using a phenomenological model based on differences in the magnetic properties of each atomic layer. The ability to write and delete the magnetic skyrmions using electric fields is also demonstrated. Besides strain relief effects, patterns can be generated in ultrathin films by the incorporation of H atoms. Several different H superstructures appear in the Fe monolayer and double layer on Ir(111) and modify their magnetic states. A skyrmionic phase can thus be stabilized in the Fe double layer whereas the symmetry of the superstructure dictates modifications of the symmetry of the nanoskyrmion lattice in the Fe monolayer. In the ferromagnetic system Ni/Fe/Ir(111), a triangular dislocation pattern induced by the strain relief is responsible for an unusual behavior of the domain walls. They are strongly pinned on the lines defined by the structural pattern and thus follow long paths rather than minimizing their length.



# Zusammenfassung

Die Fähigkeit, nicht-kollineare magnetische Zustände in ultradünnen Schichten zu stabilisieren und verlässlich zu steuern, ist notwendig, um Bauelemente, die ihre Eigenschaften ausnutzen, zu entwickeln. Topologische Spinstrukturen wie Skyrmionen zeigen besondere Transporteigenschaften und eine höhere Stabilität im Vergleich zu trivialen Zuständen. In dieser Dissertation wird nicht-kollinear Magnetismus in epitaktischen ultradünnen Schichten studiert. Wenn das Wachstum perfekt pseudomorph ist, ist eine ultradünne Schicht mit einer Dicke von ein paar Atomen ein ideales System, um die Besonderheiten von komplexen magnetischen Strukturen zu studieren, und um experimentelle und theoretische Ergebnisse zu vergleichen. Dennoch ist oft die atomare Struktur der Schichten komplizierter, zum Beispiel wegen des Abbaus von Verspannungen, und zusätzliche strukturelle Muster sind vorhanden. Das System verliert an Einfachheit, aber ein breites Spektrum neuer Phänomene erscheint. Die Untersuchung der Wechselwirkung zwischen diesen nanoskaligen strukturellen Mustern und den nicht-kollinearen magnetischen Zuständen könnte Informationen über die komplexen Mechanismen, die in gesputterten Schichten stattfinden und Pinning erzeugen können, geben. Pinning verringert die Mobilität der Skyrmionen und ist derzeit ein Hindernis für die Entwicklung von energiesparenden Bauelementen, die Skyrmionen benutzen.

In dieser Dissertation wird spin-polarisierte Rastertunnelmikroskopie verwendet, um die magnetischen Zustände in Fe-basierten ultradünnen Schichten auf Ir(111), welche ein strukturelles Muster zeigen, zu untersuchen. Die Spinspiralen und die Skyrmionen in einer dreifachen atomaren Fe-Schicht auf Ir(111) werden detailliert analysiert. Die Fe-Lage ist entlang einer Achse relaxiert durch die Bildung von Versetzungslinien, die einen deutlichen Einfluss auf die Eigenschaften der Spinspiralen und Skyrmionen haben. Außerdem wird die thermische Stabilität dieses Systems erforscht. Eine starke Zunahme der Periode der Spiralen mit der Temperatur wird beobachtet, und mit einem phänomenologischen Modell erklärt, welches beinhaltet, dass die drei atomaren Fe-Schichten verschiedene magnetische Eigenschaften haben. Zusätzlich wird die Möglichkeit demonstriert, die Skyrmionen mit einem elektrischen Feld zu schreiben und zu löschen. Strukturelle Muster können nicht nur durch Abbau von Spannungen erzeugt werden, sondern auch durch den Einbau von H-Atomen in der Fe-Schicht. Mehrere verschiedene H-Überstrukturen erscheinen in der Fe-Monolage und der Fe-Doppellage auf Ir(111) und verändern ihre magnetischen Zustände. So wird eine Skyrmionenphase in der Fe-Doppellage stabilisiert, während die Symmetrie der Überstruktur Änderungen der Symmetrie des Nanoskyrmionengitters in der Monolage hervorruft. In dem ferromagnetischen System Ni/Fe/Ir(111) ist ein dreieckiges Muster, das aus dem Abbau von Verspannungen resultiert, verantwortlich für das ungewöhnliche Verhalten der Domänenwände. Sie sind stark an den Linien des Musters gepinnt und folgen Versetzungslinien anstatt ihre Länge zu minimieren.



# Table of contents

<b>Abbreviations and notations</b>	<b>9</b>
<b>I Introduction</b>	<b>11</b>
<b>II Context</b>	<b>13</b>
II.1 Non-collinear magnetism in ultrathin films . . . . .	14
II.1.1 Magnetic interactions and energies . . . . .	14
II.1.2 Non-collinear structures . . . . .	18
II.2 Measuring non-collinear states down to the atomic scale: SP-STM . . . . .	26
II.2.1 Scanning tunneling microscopy . . . . .	26
II.2.2 Spin-polarized scanning tunneling microscopy . . . . .	30
II.3 Structure of epitaxial films at the nanoscale . . . . .	37
II.3.1 Stacking of epitaxial ultrathin films . . . . .	37
II.3.2 Creation of superstructures . . . . .	38
II.3.3 Strain relief by the formation of dislocations . . . . .	38
II.3.4 Surface reconstructions . . . . .	40
II.4 The Fe monolayer on Ir(111) . . . . .	41
II.4.1 Growth of the Fe monolayer . . . . .	41
II.4.2 The incommensurate square nanoskyrmion lattice in the fcc Fe monolayer . . . . .	42
II.4.3 The hexagonal nanoskyrmion lattice in the hcp Fe monolayer . . . . .	43
<b>III Non-collinear magnetism in uniaxially relaxed Fe ultrathin films</b>	<b>47</b>
III.1 Overview of the Fe/Ir(111) system . . . . .	48
III.1.1 Growth of the Fe film . . . . .	48
III.1.2 Non-collinear magnetic state . . . . .	49
III.2 The cycloidal spin spirals in the Fe double layer on Ir(111) . . . . .	51
III.2.1 Film morphology . . . . .	51
III.2.2 Details about the spin spirals . . . . .	53
III.3 Determination of the tip magnetic sensitivity using spin spirals . . . . .	57
III.3.1 Spiral model . . . . .	57
III.3.2 Data fitting . . . . .	58
<b>IV Detailed investigation of the effects of strain, temperature and electric field on the triple layer Fe on Ir(111)</b>	<b>61</b>
IV.1 Strain relief effects . . . . .	62
IV.1.1 Known effects of strain on non-collinear magnetism . . . . .	62
IV.1.2 Two types of dislocation lines inducing changes in the shape of the spirals . . . . .	63
IV.1.3 Correlation between the dislocation line spacing and the spin spiral period . . . . .	68
IV.1.4 Simple 1D micromagnetic analysis . . . . .	69

IV.1.5	Investigation of the transition magnetic field in the different areas . . . . .	71
IV.2	Strong temperature-induced increase of the spin spiral period . . . . .	78
IV.2.1	Calibration of the STM . . . . .	78
IV.2.2	Stable spin spirals up to room temperature . . . . .	81
IV.2.3	A classical model with layer dependent couplings . . . . .	85
IV.3	Electric field switching of magnetic skyrmions . . . . .	89
IV.3.1	Spin structure of the skyrmions . . . . .	89
IV.3.2	Reliable writing and deleting of the skyrmions . . . . .	92
IV.3.3	Demonstration of the role of an electric field in the switching mechanism . . . . .	95
<b>V</b>	<b>Tuning of non-collinear magnetism in Fe ultrathin films on Ir(111) by hydrogenation</b>	<b>101</b>
V.1	Effect of hydrogenation on the triple layer spin spirals . . . . .	103
V.1.1	Incorporation of the H atoms at the dislocation lines . . . . .	103
V.1.2	Increase of the spin spiral period . . . . .	103
V.2	Emergence of a skyrmionic phase in the hydrogenated Fe double layer	107
V.2.1	Morphology of the hydrogenated film . . . . .	107
V.2.2	Magnetism in the two hydrogenated phases . . . . .	109
V.2.3	Ab initio calculations . . . . .	111
V.3	Modification of the nanoskyrmion lattice in the Fe monolayer by hydrogenation . . . . .	114
V.3.1	Formation of two superstructures . . . . .	114
V.3.2	The hexagonal nanoskyrmion lattice in the $p(2\times 2)$ superstructure . . . . .	120
V.3.3	Another two-dimensional magnetic lattice in the square superstructure . . . . .	131
V.3.4	Summary . . . . .	137
<b>VI</b>	<b>Effect of metallic cover layers on the Fe monolayer on Ir(111)</b>	<b>139</b>
VI.1	Strong domain wall pinning in Ni/Fe/Ir(111) . . . . .	140
VI.1.1	Previous work: ferromagnetic nanoislands . . . . .	140
VI.1.2	Growth of extended Ni/Fe films . . . . .	142
VI.1.3	Pinning of the domain walls to the bridge lines . . . . .	146
VI.1.4	Summary . . . . .	155
VI.2	Comparison between the various systems based on the Fe/Ir interface .	156
<b>VII</b>	<b>Summary</b>	<b>159</b>
	<b>Bibliography</b>	<b>172</b>
	<b>List of publications</b>	<b>173</b>
	<b>Acknowledgements</b>	<b>175</b>

## Abbreviations

bcc	body centered cubic
DFT	density functional theory
DMI	Dzyaloshinskii-Moriya interaction
fcc	face centered cubic
hcp	hexagonal close packed
LDOS	local density of states
NCMR	non-collinear magnetoresistance
STM	scanning tunneling microscope/microscopy
SP-STM	spin-polarized scanning tunneling microscopy
TAMR	tunnel anisotropic magnetoresistance
TMR	tunnel magnetoresistance
UHV	ultra high vacuum

## Notations

$e$	elementary charge
$h$	Planck constant
$\hbar$	reduced Planck constant
$\mu_0$	vacuum permeability
$m_e$	mass of an electron
$E_F$	Fermi energy
$\delta(x)$	Dirac delta function



# I. Introduction

Non-collinear magnetic states in ultrathin films have recently attracted great interest because of the development of the field of spintronics.<sup>1</sup> Spintronic devices do not only take advantage of the electronic charge of the electrons but also of their spin degree of freedom. Starting from this principle, ideas of various devices for data storage and computation were developed. For example, the concept of racetrack memory<sup>2</sup> was extended to be used with skyrmions<sup>3</sup> rather than domain walls. A skyrmion is a localized non-collinear magnetic configuration in which the magnetic moments wrap the whole unit sphere. Because of this topological property<sup>4</sup>, they should be particularly stable and they exhibit special transport properties, which make them very interesting for applications.

Recently, they could be stabilized at room temperature and progress has been made towards their reliable movement<sup>5</sup> but a major issue remains unsolved. The movement of the skyrmions is hindered by their pinning at defects and grain boundaries in polycrystalline sputtered magnetic films.

However, skyrmions can also be observed in epitaxial systems, where the film structure is better ordered. In this case, they have a well-defined circular shape<sup>6</sup> and can be manipulated using the tip of a scanning tunneling microscope (STM). Pinning of the skyrmions at defects also occurs in these systems<sup>7</sup> but is better defined and understood.

In this thesis, the effect of structural patterns in epitaxial ultrathin films on their magnetic state is investigated using spin-polarized STM (SP-STM). This technique allows to resolve both the structure of the films at the atomic scale and their magnetic state. The systems studied are Fe-based epitaxial films grown on Ir(111) which exhibit some structural modulations induced either by strain relief or the incorporation of H atoms. These structures are usually ordered (even though not perfectly) and are defined well enough to be understood. The study of their interplay with complex non-collinear magnetic states allows to gain some knowledge about mechanisms which modify the magnetic properties of the films. The magnetic configuration could then be tuned by taking advantage of these structural patterns.

<sup>1</sup> S. Wolf et al. *Science* 294, 1488–1495 (2001) [1]

<sup>2</sup> S. Parkin et al. *Science* 320, 190–194 (2008) [2]

<sup>3</sup> A. Fert et al. *Nature Nanotechnology* 8, 152–156 (2013) [3]

<sup>4</sup> N. Nagaosa et al. *Nature Nanotechnology* 8, 899–911 (2013) [4]

<sup>5</sup> S. Woo et al. *Nature Materials* 15, 501–506 (2016) [5]

<sup>6</sup> N. Romming et al. *Science* 341, 636–639 (2013) [6]

<sup>7</sup> C. Hanneken et al. *New Journal of Physics* 18, 055009 (2016) [7]

Chapter II gives some background information about the sample systems and the SP-STM technique used to perform and analyze the measurements.

Chapter III is an introduction to the structure and the magnetic state of Fe ultrathin films on Ir(111), which are uniaxially relaxed when their coverage exceeds one monolayer.

Chapter IV is a detailed study of the spin spirals and the skyrmions in the Fe triple layer on Ir(111), focussing on the effects of non-uniform strain relief, temperature, and electric fields.

Chapter V shows how the magnetism of the Fe films on Ir(111) is modified by the incorporation of H atoms.

Chapter VI deals with the NiFe bilayer on Ir(111). This system is ferromagnetic and exhibits a structural triangular pattern created by strain relief which has a strong influence on the domain walls.

## II. Context

This chapter gathers the relevant background knowledge needed to perform and analyze the experiments detailed in the rest of this thesis. The first section (II.1) of this initial chapter describes the various magnetic interactions involved in the stabilization of non-collinear magnetic states and provides details about the three magnetic structures studied in this work: magnetic domain walls, spin spirals and skyrmions. The second part (II.2) explains the working principle of spin-polarized STM, which is the experimental technique used throughout this work. Some details about the growth of magnetic ultrathin films and the formation of structural patterns at the nanoscale are given in section II.3. Section II.4 summarizes the results about the complex magnetic state of the Fe monolayer on Ir(111), as a basis for the study of further Fe-based films on Ir(111) presented in the next chapters.

## II.1 Non-collinear magnetism in ultrathin films

Magnetic ordering is stabilized in ultrathin films by various, mostly short-ranged, interactions between the magnetic moments. They either favor a collinear state (ferromagnetic or antiferromagnetic ordering) or a non-collinear arrangement. Section II.1.1 gives an overview of the relevant contributions for the study of Fe ultrathin films on Ir(111). The competition between them gives rise to the formation of different structures like domain walls, spin spirals and magnetic skyrmions, which are presented in section II.1.2. These magnetic states have attracted interest in the last years because they could be used in new devices. New magnetic memories called *racetrack memories* rely on the movement of either domain walls<sup>1</sup> or skyrmions<sup>2</sup>. Other possible applications of skyrmions are logic gates<sup>3</sup> or neuromorphic computing<sup>4</sup>.

<sup>1</sup> S. Parkin et al. *Science* 320, 190–194 (2008) [2]

<sup>2</sup> A. Fert et al. *Nature Nanotechnology* 8, 152–156 (2013) [3]

<sup>3</sup> X. Zhang et al. *Scientific Reports* 5, 9400 (2015) [8]

<sup>4</sup> D. Prychynenko et al. *Physical Review Applied* 9, 014034 (2018) [9]

### II.1.1 Magnetic interactions and energies

#### II.1.1.1 Magnetic anisotropy

Because of the crystalline structure of the materials and the shape of the samples, there are usually some preferred directions for the orientation of the magnetic moments. In the case of a thin film, in a first order approximation, this effect can be described as an effective magnetic anisotropic term, which gathers three different contributions:<sup>5</sup>

$$\mathcal{E}_{\text{an}} = -K_{\text{eff}} m_z^2 = -\left(K_{\text{vol}} + \frac{K_{\text{surf}}}{t} + K_{\text{shape}}\right) m_z^2 \quad (\text{II.1})$$

where  $\vec{m}$  is the normalized magnetization,  $t$  the thickness of the film,  $K_{\text{vol}}$  is the magnetocrystalline volume anisotropy,  $K_{\text{surf}}$  is the surface anisotropy and  $K_{\text{shape}}$  the shape anisotropy originating from the demagnetizing field. If  $K_{\text{eff}}$  is negative, the system has an *easy plane* anisotropy and the magnetic moments preferably align in the  $(xy)$  plane whereas if  $K_{\text{eff}}$  is positive, there is an effective *easy axis* anisotropy and the magnetic moments rather align along the  $z$  axis.

<sup>5</sup> S. Blundell. Oxford University Press, 2001 [10]

<sup>6</sup> P. Bruno. Forschungszentrum Jülich: IFF-Ferienkurs, 1993, 24.1–24.28 [11]

**Magnetocrystalline volume anisotropy** The magnetocrystalline volume anisotropy arises mostly from spin-orbit coupling<sup>6</sup> and depends strongly on the symmetry of the crystal structure. Its value is intrinsic to the material considered but can be modified by lattice strain. Since this is a volume term, it is usually rather small in ultrathin films.

**Surface anisotropy** The atoms located at the surface of the film have a different environment than the ones located in the bulk, they have fewer neighbors and the symmetry is different at the interface. Consequently, there is an additional contribution to the magnetic anisotropy<sup>7</sup> which becomes dominant if the film is very thin. When this term favors an out-of-plane magnetization, it competes with the shape anisotropy (see below) which favors an in-plane magnetization in the film. If the film is thin enough, which is the case for the system studied in this thesis, the surface anisotropy can dominate and the film can become perpendicularly magnetized. Films with perpendicular magnetic anisotropy (PMA) have various technological applications.<sup>8</sup>

**Shape anisotropy** The shape anisotropy is created by the dipolar interaction between the magnetic moments. The dipolar energy term can be expressed as:

$$\mathcal{E}_{\text{dip}} = \frac{\mu_0}{4\pi} \sum_{i \neq j} \frac{1}{r_{ij}^3} \left[ \vec{\mu}_i \cdot \vec{\mu}_j - \frac{3}{r_{ij}^2} (\vec{\mu}_i \cdot \vec{r}_{ij})(\vec{\mu}_j \cdot \vec{r}_{ij}) \right] \quad (\text{II.2})$$

for magnetic dipoles  $\vec{\mu}_i$  ( $i$  is the atom index), where  $\vec{\mu}_i$  and  $\vec{\mu}_j$  are separated by the distance  $\vec{r}_{ij}$ . Since this is a long-range interaction, the boundaries have an influence on the whole sample. The corresponding dipolar field exerted on each moment thus depends on the shape of the sample. This contribution can be included in an additional anisotropy term, the shape anisotropy. For a thin film, the shape anisotropy always favors an in-plane alignment of the moments and its expression is simply:

$$K_{\text{shape}} = \frac{\mu_0}{2} M_s^2 \quad (\text{II.3})$$

where  $M_s$  is the saturation magnetization.

The effective anisotropy can be measured, for example, using magnetization curves or by ferromagnetic resonance (FMR).<sup>9</sup>

### II.1.1.2 Exchange interactions

The exchange interaction between two electrons arises from the Coulomb interaction and the Pauli exclusion principle. The wave function of a system with two electrons must be antisymmetric under the exchange of the electrons, thus if the spatial part of the wave function is symmetric, the spin part must be antisymmetric (singlet) and if it is antisymmetric, the spin part must be symmetric (triplet). Via the Pauli principle, the spin has an influence on the spatial part of the wave function, although for a simple electrostatic Coulomb interaction, the Hamiltonian does not depend on the spin. Consequently, it is possible to rewrite it as an effective Hamiltonian of the form:<sup>10</sup>

$$\mathcal{H} = -J \vec{S}_1 \cdot \vec{S}_2 \quad (\text{II.4})$$

<sup>7</sup> L. Néel. *Journal de Physique et le Radium* 15, 225–239 (1954) [12]

<sup>8</sup> B. Tudu et al. *Vacuum* 146, 329–341 (2017) [13]

<sup>9</sup> S. Ikeda et al. *Nature Materials* 9, 721–724 (2010) [14]

<sup>10</sup> S. Blundell. Oxford University Press, 2001 [10]

<sup>11</sup> M. Ruderman  
et al. *Physical  
Review* 96, 99–102  
(1954) [15]

<sup>12</sup> T. Kasuya.  
*Progress of  
Theoretical Physics*  
16, 45–57 (1956)  
[16]

<sup>13</sup> K. Yosida.  
*Physical Review*  
106, 893–898  
(1957) [17]

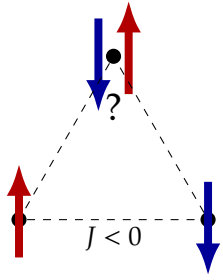


Figure II.1:  
Geometrical  
frustration of an  
antiferromagnetic  
exchange coupling.

<sup>14</sup> S. Klingler  
et al. *Journal of  
Physics D: Applied  
Physics* 48, 015001  
(2015) [18]

<sup>15</sup> I.  
Dzyaloshinskii.  
*Journal of Physics  
and Chemistry of  
Solids* 4, 241–255  
(1958) [19]

<sup>16</sup> T. Moriya.  
*Physical Review*  
120, 91 (1960) [20]

where  $J$  is the exchange constant describing the strength of the coupling and  $\vec{S}_1$  and  $\vec{S}_2$  the pair of interacting spins. This model can be extended to a system with a large number of electrons and classical magnetic moments, which corresponds then to the following bilinear energy term (classical Heisenberg model):

$$\mathcal{E}_{\text{exch}} = - \sum_{i>j} J_{ij} \vec{m}_i \cdot \vec{m}_j \quad (\text{II.5})$$

Usually, the strength of  $J_{ij}$  decays fast with the distance between the atoms. In metals, above a certain distance, the exchange interaction does no longer result from the electron wavefunction overlap but is mediated by the conduction electrons (Ruderman-Kittel-Kasuya-Yoshida or RKKY interaction<sup>11,12,13</sup>). Above several atomic distances, the exchange coupling becomes very small and in many systems, it is even sufficient to consider the nearest-neighbor interaction, described by the coupling  $J_1$ . If  $J_1 > 0$ , a ferromagnetic order is preferred, whereas if  $J_1 < 0$ , the antiferromagnetic state is favored. If, for example, the coupling between the nearest-neighbors  $J_1$  is ferromagnetic and the coupling between the next-nearest-neighbors  $J_2$  is antiferromagnetic, the exchange can be frustrated and allows to stabilize non-collinear states. Such a frustration of the exchange can also happen for geometrical reasons, for example in the case of an antiferromagnetic coupling on a triangular lattice (see Figure II.1). In this case, the energy is minimized by a Néel state in which the angle between neighboring moments is  $120^\circ$ .

The energy term from the atomistic model in equation (II.5) can be rewritten in a micromagnetic model using a continuum approximation (valid if the angles between neighboring moments are small):

$$\tilde{\mathcal{E}}_{\text{exch}} = A \left[ \left( \frac{\partial \vec{m}}{\partial x} \right)^2 + \left( \frac{\partial \vec{m}}{\partial y} \right)^2 + \left( \frac{\partial \vec{m}}{\partial z} \right)^2 \right] \quad (\text{II.6})$$

where  $A$  is the exchange stiffness and  $\vec{m}(\vec{r})$  the normalized magnetization. The value of the exchange stiffness can be estimated from measurements of microwave absorption spectra.<sup>14</sup>

### II.1.1.3 Dzyaloshinskii-Moriya interaction

The Dzyaloshinskii-Moriya interaction (DMI) is the name given to the antisymmetric part of the bilinear interaction between two magnetic moments. It was first proposed and described by Dzyaloshinskii<sup>15</sup> and Moriya<sup>16</sup> to explain the temperature-dependent behavior of  $\alpha\text{-Fe}_2\text{O}_3$ . The corresponding energy term for two magnetic moments  $\vec{S}_A$  and  $\vec{S}_B$  can be expressed as:

$$\mathcal{E}_{\text{DM}} = \vec{D} \cdot (\vec{S}_A \times \vec{S}_B) \quad (\text{II.7})$$

where  $\vec{D}$  is the Dzyaloshinskii-Moriya vector. In contrast to the exchange interaction mentioned previously, this term favors a

non-collinear ordering of the magnetic moments. Since this interaction is antisymmetric, it vanishes if a spatial inversion symmetry is present in the system. The axis of the  $\vec{D}$  vector can be derived from the symmetry of the crystal structure. Based on the sketch in Figure II.2, the rules enunciated by Moriya<sup>17</sup> to determine the direction of  $\vec{D}$  are the following:

- If there is a mirror plane perpendicular to (AB) passing through C, then  $\vec{D}$  is orthogonal to (AB).
- If there is a mirror plane including A and B, then  $\vec{D}$  is orthogonal to this mirror plane.
- If there is a two-fold rotation axis passing through C and perpendicular to (AB), then  $\vec{D}$  is orthogonal to this axis.
- If there is a  $n$ -fold rotation axis along (AB), then  $\vec{D}$  is parallel to (AB).

The DMI is present in systems without inversion symmetry. In bulk compounds, this lack of inversion symmetry can be an intrinsic property of the crystal structure, for example in the B20 materials like MnSi<sup>18</sup> or it can be induced by some distortions of the lattice, like in some multiferroic perovskites.<sup>19</sup> For the particular B20 structure, the  $\vec{D}$  vector is oriented along the direction joining the sites where the two moments are located. This configuration is often denominated *bulk DMI*.

In ultrathin films, the symmetry breaking occurs at the interfaces and the axis of the vector  $\vec{D}$  varies depending on the symmetry of the surface. The strength of the DMI derives from the intensity of the spin-orbit coupling in the system. Therefore, systems with large *interface-induced DMI* are often constituted of interfaces between heavy metal layers and magnetic films. For each pair of magnetic moments in the magnetic layer, the DMI is mediated by a heavy atom with a large spin-orbit coupling which is located on the other side of the interface. The sum of all these contributions gives the value and orientation of the  $\vec{D}$  vector.

It is possible to derive a micromagnetic expression for the DM energy term from the atomistic model from equation (II.7). For the interface-induced DMI, the micromagnetic energy density per unit volume is:<sup>20</sup>

$$\tilde{\mathcal{E}}_{\text{DM}} = D \left[ m_z \frac{dm_x}{dx} - m_x \frac{dm_z}{dx} + m_z \frac{dm_y}{dy} - m_y \frac{dm_z}{dy} \right] \quad (\text{II.8})$$

where  $\vec{m}(\vec{r}) = (m_x(\vec{r}), m_y(\vec{r}), m_z(\vec{r}))$  is the normalized magnetization, depending on the position  $\vec{r}$ . The sign of the DMI constant  $D$  determines a preferred chirality for the rotation of the magnetic moments, either clockwise or counterclockwise.

The strength of the DMI value at the interface between a magnetic film and a heavy metal layer can be experimentally measured with several techniques. For example, it can be estimated from the asymmetric expansion of out-of-plane magnetic bubbles in the presence of an in-plane magnetic field<sup>21</sup>. Another possibility is to use Brillouin light scattering

<sup>17</sup> T. Moriya. *Physical Review* 120, 91 (1960) [20]

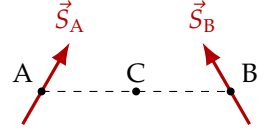


Figure II.2: Sketch of a system with two magnetic moments used to discuss the symmetry of the DMI.

<sup>18</sup> S. Mühlbauer et al. *Science* 323, 915–919 (2009) [21]

<sup>19</sup> I. Sergienko et al. *Physical Review B* 73 (2006) [22]

<sup>20</sup> A. Bogdanov et al. *Journal of Experimental and Theoretical Physics* 95, 178–182 (1989) [23]

<sup>21</sup> S.-G. Je et al. *Physical Review B* 88, 214401 (2013) [24]

22

A. Stashkevich et al. *Physical Review B* 91, 214409 (2015) [25]

23 M. Perini et al. *Physical Review B* 97, 184425 (2018) [26]

and to measure the asymmetry induced by the DMI on the dispersion of the spin waves.<sup>22</sup> It is difficult to measure precisely the strength of the DMI with SP-STM, even though an experiment similar to the bubble expansion can be realized.<sup>23</sup> However, it is possible to evaluate from SP-STM measurements if the DMI has a significant contribution in a given system by checking if the magnetic states have a unique rotational sense. The discussions of the results in the following chapters hence rely on DMI values obtained from ab initio calculations.

#### II.1.1.4 Higher-order interactions

It can happen that the above mentioned interactions are not sufficient to understand the appearance of some complex magnetic states. In this case, it is necessary to include higher-order terms in the model Hamiltonian. A typical example is the nanoskymion lattice present in the fcc Fe monolayer on Ir(111).<sup>24</sup> Further details about this systems are given in section II.4. In this case, two further terms need to be added: the four-spin interaction and the biquadratic interaction. The energy density for the four-spin interaction is written:

$$\mathcal{E}_{4\text{-spin}} = -K \sum_{ijkl} [(\vec{S}_i \cdot \vec{S}_j)(\vec{S}_k \cdot \vec{S}_l) + (\vec{S}_i \cdot \vec{S}_l)(\vec{S}_j \cdot \vec{S}_k) + (\vec{S}_i \cdot \vec{S}_k)(\vec{S}_j \cdot \vec{S}_l)] \quad (\text{II.9})$$

For simplicity, it is assumed that only diamonds of adjacent ( $ijkl$ ) lattice sites contribute and that the coupling  $K$  is the same for all of them. The expression for the biquadratic term is:

$$\mathcal{E}_{\text{biq}} = -B \sum_{ij} (\vec{S}_i \cdot \vec{S}_j)^2 \quad (\text{II.10})$$

24 S. Heinze et al. *Nature Physics* 7, 713–718 (2011) [27]

25 M. Hoffmann et al. *arXiv:1803.01315 [cond-mat]* (2018) [28]

26 A. Krönlein et al. *Physical Review Letters* 120, 207202 (2018) [29]

where again only nearest-neighbor interactions are considered. Some further higher-order terms can be derived and evaluated from ab initio calculations.<sup>25</sup> They might play a role in the stabilization of other exotic states, like the double-row-wise antiferromagnetic or  $\uparrow\uparrow\downarrow\downarrow$  state.<sup>26</sup>

### II.1.2 Non-collinear structures

The competition between the previously mentioned interactions allows to stabilize a large variety of non-collinear magnetic states. This section gives details about the structures studied in the next chapters: domain walls, spin spirals and skyrmions.

#### II.1.2.1 Domain walls

In order to reduce the demagnetization energy, ferromagnetic films break up into several domains, which are separated by domain walls. In the presence of a large interface-induced DMI, Néel domain walls are preferred to Bloch domain walls, which means that at the

boundary between two oppositely magnetized areas in an out-of-plane ferromagnetic film, the magnetic moments rotate perpendicularly to the propagation direction (see the sketch in Figure II.3). The profile of such a domain wall can be computed by minimizing the following simplified 1D micromagnetic energy density:<sup>27</sup>

$$\mathcal{E} = \int_{-\infty}^{+\infty} \left[ A \left( \frac{d\varphi}{dx} \right)^2 + D \frac{d\varphi}{dx} + K \sin^2 \varphi \right] dx \quad (\text{II.11})$$

where  $\varphi(x)$  is the angle between the plane of the film and the magnetic moment located in  $x$  ( $\varphi = 0$  means that the magnetic moment is in-plane,  $m_z$  corresponds to  $\sin \varphi$ ),  $A$  is the exchange stiffness,  $D$  the effective DMI constant and  $K$  the effective anisotropy. The boundary conditions are fixed by the ferromagnetic domains:

$$\lim_{x \rightarrow -\infty} \varphi = -\frac{\pi}{2}, \quad \lim_{x \rightarrow +\infty} \varphi = +\frac{\pi}{2} \quad (\text{II.12})$$

The functional from equation (II.11) can then be minimized. The DMI part is treated separately as it can easily be integrated and just gives a constant  $-\pi|D|$  term. The DMI thus does not influence the shape of the domain walls, only its energy. The energy minimization gives the following expression for  $\varphi(x)$ :

$$\varphi(x) = \arcsin \left( \tanh \left( \sqrt{\frac{K}{A}} x \right) \right) \quad (\text{II.13})$$

where the wall width is then  $w = 2\sqrt{A/K}$ . The shape of this profile is plotted in Figure II.4. Its energy (per unit length) is:

$$\mathcal{E}_{\text{DW}} = 4\sqrt{AK} - \pi|D| \quad (\text{II.14})$$

The rotational sense of the wall is fixed by the sign of  $D$ . In systems where the DMI needs to be considered, the walls have thus a unique rotational sense.

If the DMI interaction is large enough, the energy of the wall becomes negative. In this case, a spin spiral ground state is favorable because a spin spiral can be thought of as a close repetition of domain walls.

The previously discussed  $180^\circ$  domain walls can form pairs and become  $360^\circ$  domain walls, in particular when an out-of-plane external magnetic field is applied to an out-of-plane magnetized ferromagnetic film. In this case, one of the ferromagnetic domains shrinks and the two walls can become very close. Such a  $360^\circ$  domain wall can simply be described by the sum of two  $180^\circ$  domain walls:<sup>28</sup>

$$\varphi(x) = \arcsin \left( \tanh \left( \sqrt{\frac{K}{A}} (x + c) \right) \right) + \arcsin \left( \tanh \left( \sqrt{\frac{K}{A}} (x - c) \right) \right) \quad (\text{II.15})$$

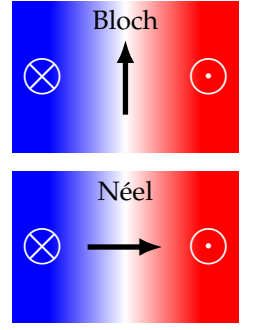


Figure II.3: Sketch of the difference between a Bloch and a Néel wall (top view).

<sup>27</sup> M. Heide et al. *Physical Review B* 78, 140403 (2008) [30]

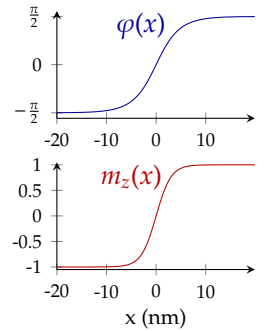


Figure II.4: Profile of a  $180^\circ$  domain wall with  $w = 6$  nm.

<sup>28</sup> A. Kubetzka et al. *Physical Review B* 67, 020401 (2003) [31]

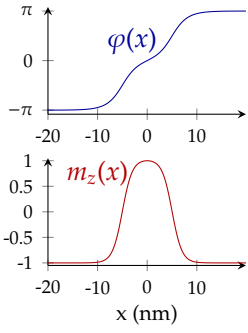


Figure II.5: Profile of a 360° domain wall with  $w = 4$  nm and  $c = 5$  nm.

For this expression,  $\varphi = 0$  means out-of-plane and thus  $m_z$  corresponds to  $\cos \varphi$  here. Besides the wall width, another parameter  $c$ , which corresponds to the spacing between the two 180° walls, is required to define the profile. The profile of a 360° domain wall with  $c = 5$  nm and  $w = 4$  nm is plotted in Figure II.5.

### II.1.2.2 Spin spirals

Spin spiral states correspond to a continuous rotation of the magnetic moments. They can be either helical or cycloidal, which means that the magnetic moments either rotate in a plane perpendicular to the propagation direction of the spiral or in a plane which contains this direction. These two configurations are drawn in Figure II.6.

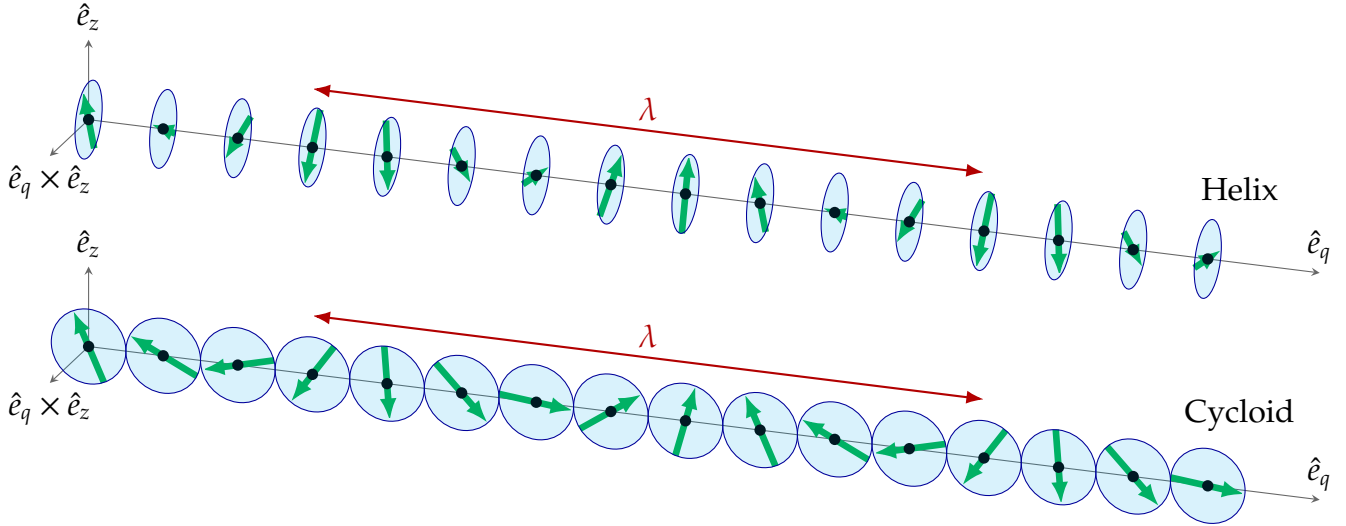


Figure II.6: Sketches of a helical and a cycloidal spin spiral.

A spin spiral is called homogeneous when the angle between two neighboring spins is fixed. This means that there is no preferred direction for the orientation of the magnetic moments. A homogeneous helical spiral can be described by the following equation:

$$\vec{S}_h(r_i) = S \left[ \cos\left(\frac{2\pi}{\lambda}r_i\right)\hat{e}_z \pm \sin\left(\frac{2\pi}{\lambda}r_i\right)(\hat{e}_q \times \hat{e}_z) \right] \quad (\text{II.16})$$

where  $\lambda$  is the period of the spiral,  $r_i$  the spatial coordinate of the moment with index  $i$  along the propagation direction  $\hat{e}_q$ , and  $\hat{e}_z$  is a unit vector in the plane perpendicular to  $\hat{e}_q$  (normal to the surface for ultrathin films). The rotational sense is given by the  $\pm$  sign. For a cycloidal spiral, if the magnetic moments rotate in a plane perpendicular to the surface, this expression becomes:

$$\vec{S}_c(r_i) = S \left[ \cos\left(\frac{2\pi}{\lambda}r_i\right)\hat{e}_z \pm \sin\left(\frac{2\pi}{\lambda}r_i\right)\hat{e}_q \right] \quad (\text{II.17})$$

To adapt this expression for a cycloid rotating in the surface plane,  $\hat{e}_z$  should be replaced by  $(\hat{e}_q \times \hat{e}_z)$ . In the case of the cycloidal spirals rotating perpendicular to the surface, there is no symmetry operation allowing to transform a spiral with one rotational sense into a spiral with the opposite rotational sense. On the contrary, the helical spirals with opposite rotational senses are related by a mirror plane, even when placed on a surface<sup>29</sup>. This is illustrated in Figure II.7. For this reason, cycloidal spirals with opposite rotational sense are not necessarily degenerate. In particular, in the presence of DMI, one of the rotational senses is energetically favorable.

Spin spirals can be stabilized by the frustration of the exchange coupling (for example because of the coexistence of a ferromagnetic nearest-neighbor coupling  $J_1$  and an antiferromagnetic next-nearest-neighbor coupling  $J_2$ ), by the DMI, or by a combination of these two effects. For spirals stabilized by DMI, the period is fixed by the ratio  $A/D$  between the exchange stiffness  $A$  and the DMI constant  $D$ . In the more general case where the effective magnetic anisotropy is included, it is possible to determine if a spin spiral is the ground state of the system and to compute its profile, for a given set of parameters  $A$ ,  $D$ ,  $K_{\text{eff}}$  and  $M_s$  (the saturation magnetization) and in the presence of an external magnetic field  $\vec{H}$ .<sup>30</sup> The considered energy density is:

$$\begin{aligned} \mathcal{W} = A & \left[ \left( \frac{\partial \vec{m}}{\partial x} \right)^2 + \left( \frac{\partial \vec{m}}{\partial y} \right)^2 + \left( \frac{\partial \vec{m}}{\partial z} \right)^2 \right] - K_{\text{eff}} m_z^2 - M_s \vec{m} \cdot \vec{B} \\ & + D \left[ m_z \frac{\partial m_x}{\partial x} - m_x \frac{\partial m_z}{\partial x} + m_z \frac{\partial m_y}{\partial y} - m_y \frac{\partial m_z}{\partial y} \right] \end{aligned} \quad (\text{II.18})$$

where  $\vec{m}$  is the normalized magnetization. This equation can be made dimensionless by the following transformation:

$$(\tilde{x}, \tilde{y}, \tilde{z}) = \frac{D}{A}(x, y, z), \quad w = \frac{A}{D^2} \mathcal{W}, \quad \beta = \frac{AK_{\text{eff}}}{D^2}, \quad \vec{h} = \frac{AM_s}{\mu_0 D^2} \vec{B} \quad (\text{II.19})$$

which leads to:

$$\begin{aligned} w = & \left[ \left( \frac{\partial \vec{m}}{\partial \tilde{x}} \right)^2 + \left( \frac{\partial \vec{m}}{\partial \tilde{y}} \right)^2 + \left( \frac{\partial \vec{m}}{\partial \tilde{z}} \right)^2 \right] - \beta m_z^2 - \vec{m} \cdot \vec{h} \\ & + \left[ m_z \frac{\partial m_x}{\partial \tilde{x}} - m_x \frac{\partial m_z}{\partial \tilde{x}} + m_z \frac{\partial m_y}{\partial \tilde{y}} - m_y \frac{\partial m_z}{\partial \tilde{y}} \right] \end{aligned} \quad (\text{II.20})$$

Assuming that the spiral propagates along the  $y$  direction and taking into account the stray field effect included in  $K_{\text{eff}}$ , it is possible to show that the spiral state is only stable if it is cycloidal and if the parameters fulfill the condition from equation (II.21).

$$1 < \frac{\pi}{4} \sqrt{\frac{D^2}{AK_{\text{eff}}}} < \frac{\pi}{4} \sqrt{\frac{2D^2}{\mu_0 AM_s^2}} \quad (\text{II.21})$$

<sup>29</sup> K. von Bergmann et al. *Journal of Physics: Condensed Matter* 26, 394002 (2014) [32]

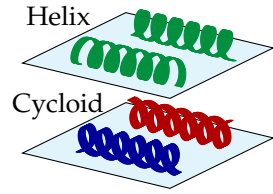


Figure II.7: Cycloidal and helical spirals with both rotational sense on a surface.

<sup>30</sup> A. Bogdanov et al. *Journal of Magnetism and Magnetic Materials* 138, 255–269 (1994) [33]

The angle  $\theta$  between the magnetization  $\vec{m}$  and the normal to the surface can be introduced in order to rewrite the energy density (II.20) and compute its average value  $\bar{w}$ :

$$\bar{w} = \frac{1}{\tilde{y}_0} \int_0^{\tilde{y}_0} \left[ \left( \frac{d\theta}{d\tilde{y}} \right)^2 + h(1 - \cos \theta) - \frac{d\theta}{d\tilde{y}} + \beta \sin^2 \theta \right] d\tilde{y} \quad (\text{II.22})$$

where  $\tilde{y}_0$  is the half period of the spiral, in reduced units. After some integration steps, it is possible to find expressions allowing to compute (numerically) both  $\tilde{y}_0$  and  $\theta(\tilde{y})$ :

$$\int_0^\pi \sqrt{h(1 - \cos \theta) + \beta \sin^2 \theta + C} d\theta = \frac{\pi}{2} \quad (\text{II.23})$$

$$\tilde{y}_0 = \int_0^\pi \frac{d\theta}{\sqrt{h(1 - \cos \theta) + \beta \sin^2 \theta + C}} \quad (\text{II.24})$$

$$\tilde{y} = \int_0^{\theta(\tilde{y})} \frac{d\theta}{\sqrt{h(1 - \cos \theta) + \tilde{\beta} \sin^2 \theta + C}}, \quad \theta(0) = 0 \quad (\text{II.25})$$

where equation (II.23) allows to obtain the value of the integration constant  $C$ .

In the absence of effective magnetic anisotropy,  $\beta = 0$ . In zero field, this means that  $C = 1/4$  and the period  $\lambda$  of the spirals is simply:

$$\lambda = 4\pi \frac{A}{D} \quad (\text{II.26})$$

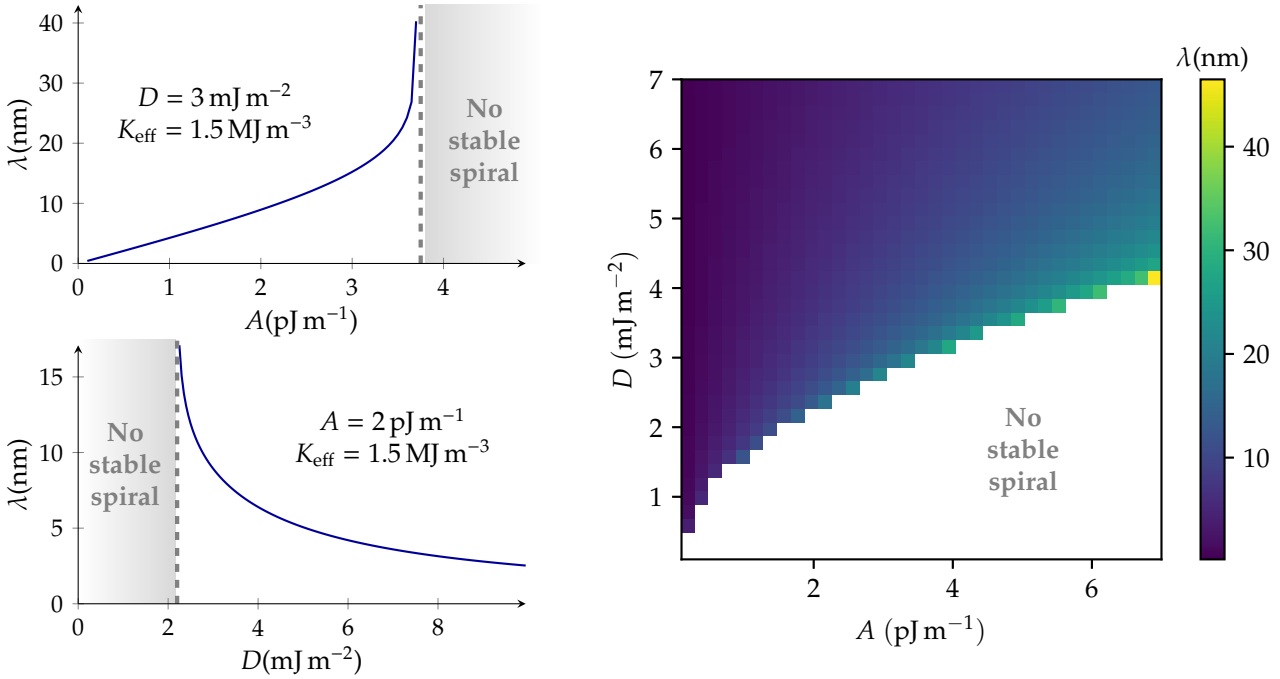


Figure II.8: Dependence of the spin spiral period  $\lambda$  on the exchange stiffness  $A$  and the DMI constant  $D$  for a fixed effective anisotropy of  $1.5 \text{ MJ m}^{-3}$ .

In a more general case, the dependence of the spin spiral period on  $A$  and  $D$  for a fixed  $K_{\text{eff}}$  is described in Figure II.8. Whereas in the absence of effective anisotropy, any couple of parameters ( $A, D$ ) corresponds to a stable spin spiral solution, when there is an out-of-plane anisotropy in the system, the spiral state is only stable in a limited range of parameters. In addition to this, the presence of an out-of-plane anisotropy leads to distortions of the spiral profile. If only the exchange coupling and the DMI are included, the spirals are homogeneous and the spiral profile is a sine function. However, because of the out-of-plane anisotropy, it becomes energetically favorable for the magnetic moments to align with the out-of-plane direction and the spirals are then inhomogeneous. This effect is illustrated in Figure II.9.

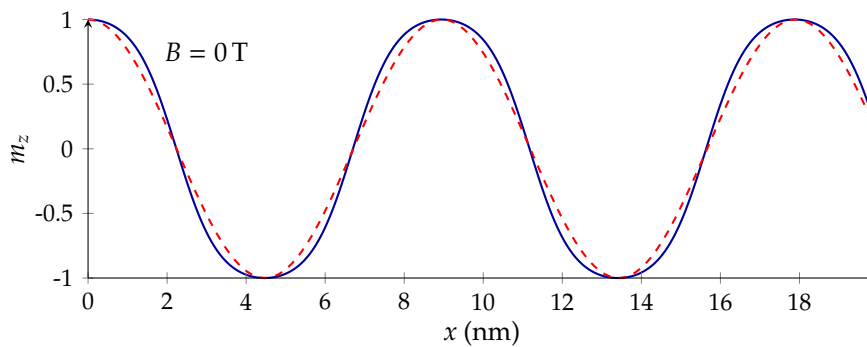


Figure II.9: Computed profile for a spin spiral using  $A = 2 \text{ pJ m}^{-1}$ ,  $D = 3 \text{ mJ m}^{-2}$ ,  $K_{\text{eff}} = 1.5 \text{ MJ m}^{-3}$  with magnetic moments of  $3\mu_B$ . The profile is compared with a fit to a sine function (red dashed line), which illustrates its inhomogeneity.

### II.1.2.3 Skyrmions

Both the previously mentioned domain walls and spin spirals are actually one-dimensional structures. The skyrmions however are the two-dimensional equivalent of the  $360^\circ$  domain walls. They are named after Tony Skyrme, who first introduced them as localized particle-like solutions of a non-linear field theory.<sup>31</sup> In the case of magnetic materials, it was predicted that in systems similar to those described in the previous section (exhibiting a DMI-induced spiral phase), a skyrmion lattice phase forms under the application of a magnetic field.<sup>32</sup> These skyrmions were previously named vortices because they are localized whirls in the spin configuration, with the center pointing in the direction opposite to the ferromagnetic background. A sketch of a skyrmion configuration is shown in Figure II.10. However, they should not be confused with the usual magnetic vortices.<sup>33</sup> In the case of a skyrmion, the magnetic moments wrap the whole unit sphere<sup>34</sup> whereas in a vortex, only one hemisphere is covered.

Motivated by this property, the skyrmions are said to be *topologically protected* because there is no continuous transformation of the magnetic state allowing to go from a skyrmion configuration to a ferromagnetic

<sup>31</sup> T. Skyrme. *Proc. R. Soc. Lond. A* 260, 127–138 (1961) [34]

<sup>32</sup> A. Bogdanov et al. *Journal of Magnetism and Magnetic Materials* 138, 255–269 (1994) [33]

<sup>33</sup> T. Shinjo et al. *Science* 289, 930–932 (2000) [35]

<sup>34</sup> R. Wiesendanger. *Nature Reviews Materials* 1, 16044 (2016) [36]

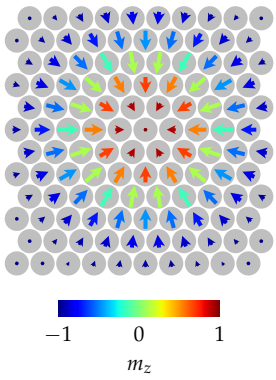


Figure II.10: Spin structure of a magnetic skyrmion, top view.

<sup>35</sup> N. Nagaosa et al. *Nature Nanotechnology* 8, 899–911 (2013) [4]

<sup>36</sup> W. Jiang et al. *Nature Physics* 13, 162–169 (2017) [37]

<sup>37</sup> M. Lee et al. *Physical Review Letters* 102 (2009) [38]

<sup>38</sup> A. V. Oosterom et al. *IEEE Transactions on Biomedical Engineering* BME-30, 125–126 (1983) [39]

<sup>39</sup> N. Romming et al. *Physical Review Letters* 114, 177203 (2015) [40]

configuration. In real systems, the atomic lattice is discrete and this topological protection means that there is an energy barrier to overcome in order to create or annihilate a skyrmion. The skyrmionic nature of a magnetic configuration can be investigated by computing its topological charge (or winding number or skyrmion number), which counts how many times the whole unit sphere is covered by the magnetic moments:<sup>35</sup>

$$Q_{\text{topo}} = \frac{1}{4\pi} \int \vec{m}(\vec{r}) \cdot \left( \frac{\partial \vec{m}}{\partial x} \times \frac{\partial \vec{m}}{\partial y} \right) d\vec{r} \quad (\text{II.27})$$

where  $\vec{m}$  is the normalized magnetization. The topological charge  $Q_{\text{topo}}$  is the integral of the solid angle: if the unit sphere is completely wrapped, the solid angle reaches  $4\pi$  and the topological charge equals 1. Because of the interaction between conduction electrons and their topologically non-trivial magnetic structure, skyrmions exhibit some particular transport properties. For example, they experience a Magnus force depending on their topological charge<sup>36</sup> and they add a contribution to the Hall effect<sup>37</sup> (the *topological Hall effect*) which can be used to detect them. In order to numerically compute the topological charge for a given structure, it is necessary to use a discretized form of equation (II.27). In an hexagonal lattice, the magnetic moments are located at the corners of equilateral triangles. For such a triangle, with the moments  $\vec{m}_1$ ,  $\vec{m}_2$  and  $\vec{m}_3$ , the solid angle  $\Omega$  is:<sup>38</sup>

$$\tan\left(\frac{\Omega}{2}\right) = \frac{\vec{m}_1 \cdot (\vec{m}_2 \times \vec{m}_3)}{1 + \vec{m}_1 \cdot \vec{m}_2 + \vec{m}_1 \cdot \vec{m}_3 + \vec{m}_2 \cdot \vec{m}_3} \quad (\text{II.28})$$

Numerically, it is necessary to use the atan2 function with the numerator and denominator of the above fraction as arguments rather than a simple atan function in order to get the proper sign. The topological charge of the whole configuration is then obtained by summing the contributions of all the triangles. This method is used in chapter V to evaluate the topological charge of the proposed magnetic structure for the nanoskyrmion lattices in the hydrogenated Fe monolayer on Ir(111).

Skyrmions are commonly axisymmetric structures and have thus a circular shape (although the skyrmions studied in chapter IV do not). In this case, their cross section is very close to a  $360^\circ$  domain wall.<sup>39</sup> There are two possibilities, either a Bloch type skyrmion (also called spiral skyrmion) or a Néel type skyrmion (also called hedgehog skyrmion). These two structures are represented in Figure II.11.

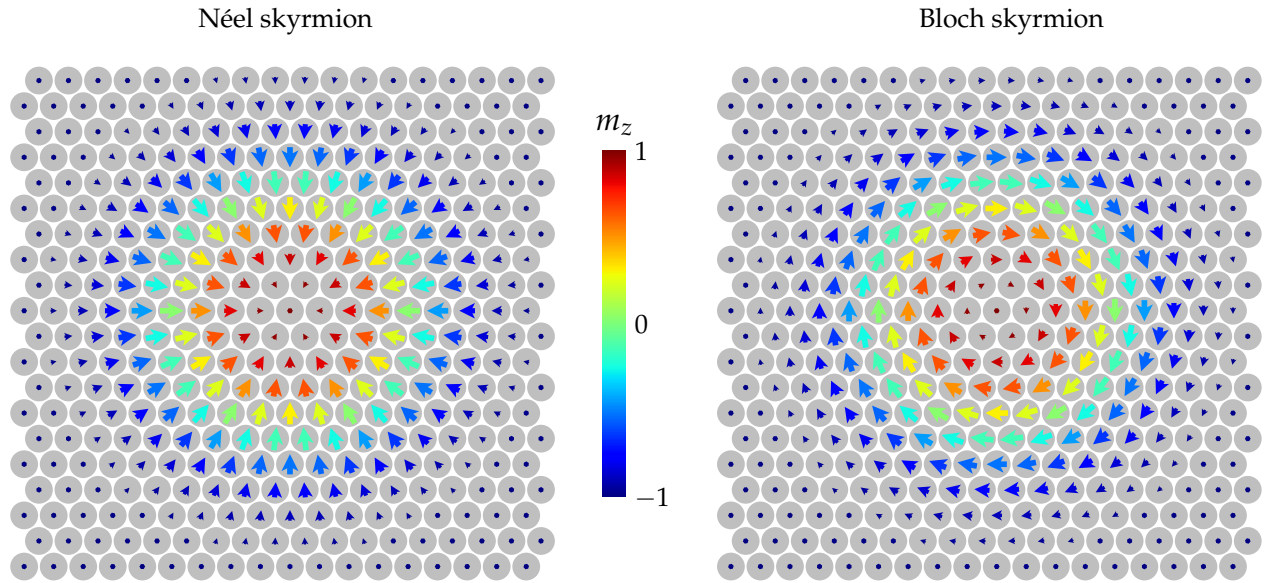


Figure II.11: Spin configuration in a Néel skyrmion (left) and a Bloch skyrmion (right). For both types of skyrmions, two rotational senses are possible, only one is represented here.

The type of skyrmions present in a magnetic material depends on the symmetry of the DMI which stabilizes them: Bloch skyrmions are found in bulk systems like MnSi<sup>40</sup> or FeGe<sup>41</sup> whereas Néel skyrmions are usually observed in ultrathin films.<sup>42</sup>

<sup>40</sup> S. Mühlbauer et al. *Science* 323, 915–919 (2009) [21]

<sup>41</sup> X. Yu et al. *Nature Materials* 10, 106–109 (2011) [41]

<sup>42</sup> L. Schmidt et al. *New Journal of Physics* 18, 075007 (2016) [42]

## II.2 Measuring non-collinear states down to the atomic scale: SP-STM

The experimental technique used in this thesis to study non-collinear magnetism is spin-polarized scanning tunneling microscopy (SP-STM). It allows to resolve the three-dimensional magnetic state at the surface of conductive samples down to the atomic scale, which makes it a well suited technique to investigate magnetism in ultrathin films exhibiting a structural pattern at the nanoscale.

This section provides a brief explanation of the working principle of a scanning tunneling microscope (invented in 1981 by Gerd Binnig and Heinrich Rohrer<sup>1</sup>) and introduces the experimental setup used, before presenting in more detail the mechanisms giving access to the magnetic state at the sample surface.

<sup>1</sup> G. Binnig et al.  
*Physical Review Letters* 49, 57–61  
(1982) [43]

### II.2.1 Scanning tunneling microscopy

#### II.2.1.1 Operation principle

STM is an imaging technique which exploits the tunnel current between two electrodes (a sharp metallic tip and a conductive sample) through a vacuum barrier. A bias voltage is applied between the two electrodes and when the tip is close enough to the sample (typically a few Å), the electrons can tunnel through the vacuum. The resulting tunnel current depends exponentially on the distance between the tip and the sample. By moving the tip over the surface it is thus possible to measure its topography. The following discussion shows that in addition, the tunnel current provides some information about the local electronic states of the surface.

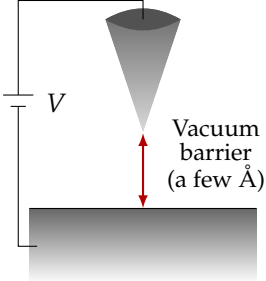


Figure II.12: Sketch of a STM tip close to a sample surface.

**Current through a planar tunnel junction** A theoretical model is needed to understand the dependence of the tunnel current on the various parameters of the experiment and thus analyze correctly the collected data. As a first step, the STM setup can be described as a planar tunnel junction. The expression for the tunnel current was found by Bardeen<sup>2</sup> using first-order perturbation theory<sup>3</sup>:

$$I = \frac{2\pi e}{\hbar} \sum_{t,s} |M_{t,s}|^2 \delta(E_t - E_s) [f(E_t - eV) - f(E_s)] \quad (\text{II.29})$$

where  $V$  is the bias voltage applied between the tip and the sample,  $M_{t,s}$  is the tunneling matrix element between the electronic states  $\psi_t$  of the tip and  $\psi_s$  of the surface (of energy  $E_t$  and  $E_s$  respectively, in the absence of tunneling) and  $f$  is the Fermi-Dirac distribution. Only elastic tunneling is considered here, as indicated by the  $\delta$  function. The unknown term in this

<sup>2</sup> J. Bardeen.  
*Physical Review Letters* 6, 57–59  
(1961) [44]

<sup>3</sup> V. Ukraintsev.  
*Physical Review B* 53, 11176 (1996)  
[45]

expression is the matrix element  $M_{t,s}$ , which can be expressed as:

$$M_{t,s} = \frac{-\hbar^2}{2m_e} \int (\psi_t^* \nabla \psi_s - \psi_s \nabla \psi_t^*) dA \quad (\text{II.30})$$

where the integral is calculated over any surface located within the vacuum barrier. The calculation of the matrix element  $M_{t,s}$  thus requires the knowledge of the wave functions  $\psi_t$  and  $\psi_s$ . However, the shape of the tip at the atomic scale is unknown, which means that the wave function  $\psi_t$  needs to be approximated.

**The Tersoff-Hamann model** In the case of the tunnel current between a tip and a sample surface, Tersoff and Hamann proposed to assume for simplicity that the tip wave function has a locally spherical geometry.<sup>4</sup>  $\psi_t$  is thus considered as an  $s$ -type wavefunction, with the center of the tip at  $\vec{r}_0$ , a curvature radius of the tip  $R$  and an effective decay constant  $\kappa$ . In the limit of low temperature, the Fermi-Dirac distribution can be replaced by a step function. In addition, if the applied bias voltage is small, the expression of the tunnel current from equation (II.29) becomes:

$$I \propto V \rho_t e^{2\kappa R} \sum_s |\psi_s(\vec{r}_0)|^2 \delta(E_s - E_F) \quad (\text{II.31})$$

$$I \propto V \rho_t e^{2\kappa R} \rho_s(\vec{r}_0, E_F) \quad (\text{II.32})$$

The current is proportional to the local density of states (LDOS) of the tip (assumed constant for simplicity) and to the local density of states  $\rho_s$  of the sample.<sup>5</sup> The wave function of the sample decays exponentially into the vacuum, which means that:

$$\rho_s \propto |\psi_s(\vec{r}_0)|^2 \propto e^{-2\kappa d} \quad (\text{II.33})$$

where  $d$  is the distance between the surface and the center of the tip at  $\vec{r}_0$  and  $\kappa = \sqrt{2m_e\phi}/\hbar$  is the decay constant corresponding to the work function  $\phi$ . This behavior of the wave function results in the exponential decay of the tunnel current with the distance between the tip and the sample.

**Generalized models** The model described above can be extended to more general situations.<sup>6</sup> In particular, the expression of the tunnel current can also be derived without considering that the bias voltage is small, which is usually not the case in the experiment. The tunnel current is then proportional to the integrated LDOS:

$$I \propto \int_{E_F}^{E_F+eV} \rho_s(\vec{r}_0, \varepsilon) d\varepsilon \quad (\text{II.34})$$

As consequence of this dependence on the LDOS of the sample, variations of the tunnel current do not necessarily occur because of

<sup>4</sup> J. Tersoff et al. *Physical Review B* 31, 805 (1985) [46]

<sup>5</sup> R. Wiesendanger. Cambridge University Press, 1994 [47]

<sup>6</sup> C. Chen. *Physical Review B* 42, 8841–8857 (1990) [48]

topographic changes but can also originate from the local electronic structure of the sample.

From the expression of the tunnel current in equation (II.34), it appears that measuring the differential conductance directly gives access to the LDOS at the applied bias voltage.

### II.2.1.2 Experimental details

Experimentally, the positioning of the tip with respect to the sample surface needs to be very precise. Indeed, the typical strength of the measured tunnel currents is between 100 pA and 10 nA, which requires a tip-sample distance of a few Å. Furthermore, the lateral position of the tip also needs to be controlled precisely in order to obtain atomic resolution. The tip is thus attached on a scanner tube made of a piezoelectric material and whose surface is separated in five electrodes: the outer surface is divided in four and the inner surface is the fifth electrode. By applying high voltages (about 100 to 150 V) between these electrodes, the tube can either be elongated (in order to precisely change the tip-sample distance) or bent in any direction (which allows to scan over the surface). The coarse approach of the tip close to the surface is realized by attaching the scanner to a sapphire prism held by piezoelectric stacks. The prism can then be moved in steps by the stacks using a stick-slip mechanism. The tunnel current is measured using a current-to-voltage amplifier. Usually, several data channels are simultaneously recorded during the measurements: the variations of the tip height, the tunnel current and the differential conductance. In addition, when scanning over a given area of the sample, the tip travels twice along the same line, forwards and backwards. These two images are recorded and are usually slightly shifted with respect to each other because of the creep in the piezoelectric material and because of the feedback loop (see below details about the constant-current measuring mode).

All the sample preparations as well as the STM measurements are performed in ultra-high vacuum (UHV), with a base pressure on the order of  $1 \times 10^{-10}$  mbar. This low pressure ensures in particular that the measurement conditions remain stable during several hours because only very few residual gas molecules adsorb on the surface.

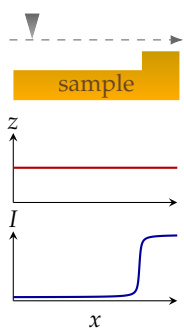


Figure II.13: Principle of a measurement in constant-height mode.

**Constant-height mode** Following the theoretical considerations presented before, the most natural procedure to obtain information about the surface of a sample would be to approach the tip close to the surface, start scanning over an area and record the variations of the tunnel current, by keeping the tip height fixed. This is called a constant-height measurement and is illustrated in Figure II.13. The map of the measured current reflects the topography of the surface as well as the changes in the LDOS. However, this measurement procedure is rarely used in practice because of the risk to crash the tip into the surface.

**Constant-current mode** Another option, safer for the tip and the sample, is the constant-current mode. In this case, a feedback loop is used to keep the tunnel current constant by adjusting the tip height during scanning. The topography of the surface is thus reflected in the variations of the tip height (see Figure II.14) and the distance between the tip and the surface is constantly adjusted which avoids tip crashes. However, the feedback loop does not work infinitely fast and the tunnel current is thus not exactly kept constant. When the tip approaches a step edge, the current increases (respectively decreases). In reaction, the feedback loop moves the tip up (respectively down) and the current goes down (respectively up) again. The crossing of the step edge appears as a step in the height data and as a peak in the current recording, as illustrated in Figure II.15. More generally, the pattern measured in the tunnel current in constant-current mode is close to the derivative of the height channel along the scanning direction.

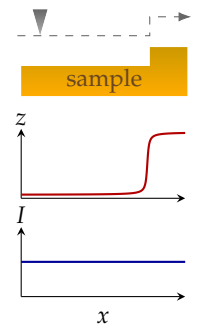


Figure II.14: Principle of a measurement in constant-current mode.

**Differential conductance measurements** The differential conductance is measured simultaneously with the constant-current height map using a lock-in amplifier. A small sinusoidal modulation is added to the applied bias voltage at a frequency of a few kHz. This frequency needs to be chosen within the bandwidth of the current amplifier avoiding the resonance frequencies of the scanner to minimize the noise level. The applied modulated bias voltage can be described as:

$$V = V_0 + v \sin \omega t \quad (\text{II.35})$$

The tunnel current, which depends on the applied voltage, will also be modulated at the same frequency. A first order Taylor expansion gives:

$$I(V) = I(V_0) + \frac{dI}{dV}(V_0) v \sin \omega t + \dots \quad (\text{II.36})$$

The lock-in amplifier allows to measure the component of the current oscillating at the frequency  $\omega$ , which is directly proportional to the differential conductance.

**UHV systems and microscopes used** The experiments reported in this thesis were performed in several UHV systems using microscopes with various features. All the systems are constituted of different chambers, allowing to separate the sample preparation from the STM chamber. The largest part of the data was measured in a large UHV system comprising dedicated chambers for each preparation step, two low temperature STMs and a room temperature STM. The latter<sup>7</sup> was only used to image the films during the optimization of the sample preparation. The low temperature STMs are both equipped with a bath cryostat which can be filled with liquid He. In the first STM setup, the measurement temperature goes down to 4 K and can even be further

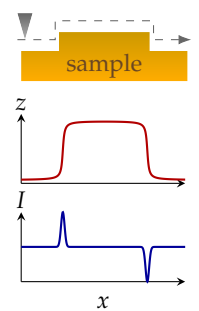


Figure II.15: Actually measured tunnel current in constant-current mode.

<sup>7</sup> C. Witt et al. *Review of Scientific Instruments* 68, 1455–1457 (1997) [49]

<sup>8</sup> O. Pietzsch et al. *Review of Scientific Instruments* 71, 424–430 (2000) [50]

<sup>9</sup> T. Eelbo. Diplomarbeit. Universität Hamburg, 2007 [51]

<sup>10</sup> S. Meckler et al. *Review of Scientific Instruments* 80, 023708 (2009) [52]

<sup>11</sup> R. Wiesendanger et al. *Physical Review Letters* 65, 247–250 (1990) [53]

<sup>12</sup> M. Julliere. *Physics Letters A* 54, 225–226 (1975) [54]

reduced down to 1 K using a Joule-Thomson expansion, but such low temperatures were not necessary for the measurements reported here. A superconducting coil present in the cryostat allows to apply out-of-plane magnetic fields up to 9 T. In the second microscope used<sup>8</sup>, the measurement temperature is about 8 K and the maximal out-of-plane magnetic field which can be applied is 2.5 T. This STM was also operated at room temperature for some experiments shown in section IV.2.2.1. The variable temperature experiments from section IV.2.2.1 were performed in another, much smaller UHV system with only two chambers. In this case, the STM<sup>9</sup> is thermally attached to a liquid He flow cryostat. By changing the He flow, it is possible to adjust the measurement temperature. It is not possible to apply an external magnetic field to the sample during the measurement in this system. Some further measurements done by Pin-Jui Hsu and Lorenz Schmidt in a third UHV system are shown in chapter III. The particularity of this system is the possibility to apply an external magnetic field in any spatial direction<sup>10</sup> during the low-temperature measurements at about 5 K.

## II.2.2 Spin-polarized scanning tunneling microscopy

The previous section described the working principle of STM, showing how it is possible to measure both the topography of the sample surface and its LDOS. When the sample is not only conductive but also magnetic, magnetoresistive effects give access to the local magnetic structure of the sample.<sup>11</sup> This section discusses the various effects involved in magnetic imaging with STM (spin-polarized STM or SP-STM), and how they can be measured, discriminated and simulated.

### II.2.2.1 Imaging mechanisms

The tunnel current between the tip and the sample can be affected by the magnetic state of the sample via several mechanisms, detailed below. They can be separated in two categories: on one hand, the tunnel magnetoresistance can only be observed if the tip is spin-polarized, whereas on the other hand, measuring tunnel anisotropic magnetoresistance, non-collinear magnetoresistance, or polarization changes do not require the utilization of a magnetic tip. Since it is often unclear which of these effects generates the observed contrast in the data when measuring with a non-magnetic tip, the generic term *electronic contrast* is used in the next chapters and refers to any combination of them.

**Tunnel magnetoresistance** The most widely used magnetoresistive effect for SP-STM measurements is the *Tunnel MagnetoResistance* or TMR. It was first measured in a planar tunnel junction made of two ferromagnetic electrodes separated by a semiconductor (Fe-Ge-Co)<sup>12</sup>: the conductance of the junction decreases when the magnetizations

of the two electrodes are antiparallel, compared to the parallel case. This phenomenon was investigated theoretically by Slonczewski<sup>13</sup> who showed that the conductance  $G$  of such a magnetic tunnel junction can be described as:

$$G \propto 1 + P_1 P_2 \cos \theta \quad (\text{II.37})$$

where  $P_1$  and  $P_2$  are the effective spin polarizations of the two electrodes and  $\theta$  the angle between their magnetization directions. In the two ferromagnetic electrodes the density of states is splitted between the electrons with spin  $\uparrow$  (noted  $\rho_{\uparrow}$ ) and the electrons with spin  $\downarrow$  (noted  $\rho_{\downarrow}$ ). The effective spin polarization can then be defined as:

$$P(\varepsilon) = \frac{\rho_{\uparrow}(\varepsilon) - \rho_{\downarrow}(\varepsilon)}{\rho_{\uparrow}(\varepsilon) + \rho_{\downarrow}(\varepsilon)} \quad (\text{II.38})$$

and is often evaluated at the Fermi level,  $\varepsilon = E_F$ . The TMR effect can be understood in the simple case of parallel and antiparallel magnetizations from the drawing in Figure II.16.

13

J. Slonczewski.  
*Physical Review B* 39, 6995–7002  
(1989) [55]

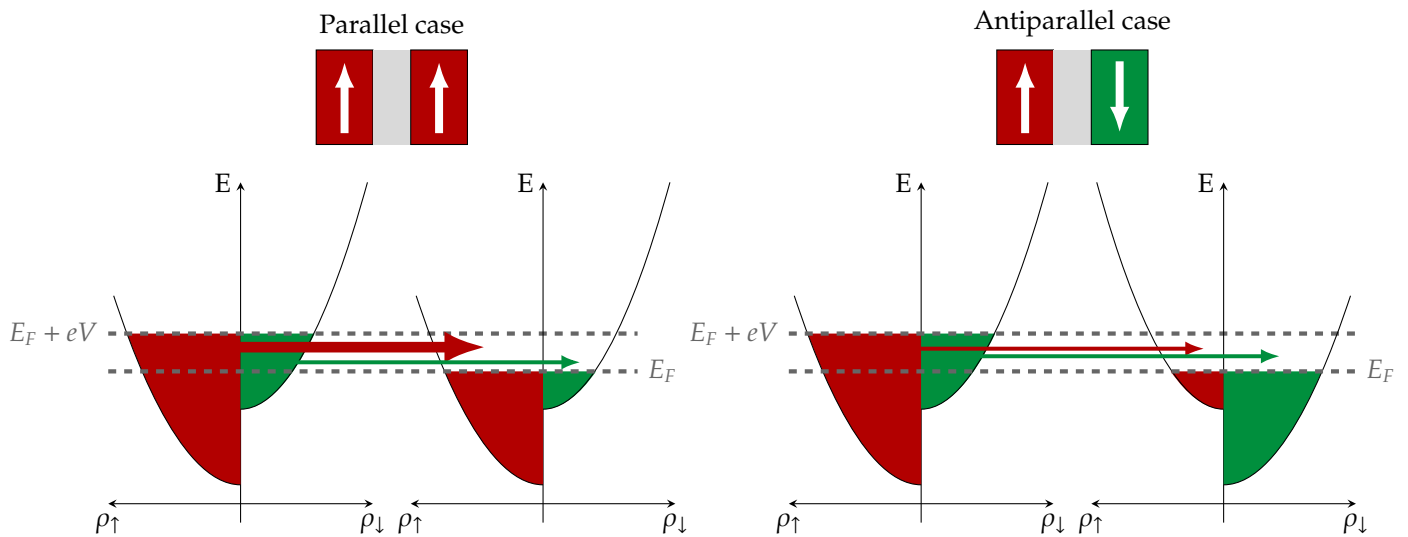


Figure II.16: Schematic explanation of the TMR between two magnetic electrodes with parallel (left) and anti-parallel (right) magnetizations. The conservation of spin and energy dictates that the spins of the tunneling electrons do not flip and that they tunnel between states of the same energy. The tunneling probability depends on the number of available states and is thus lower in the anti-parallel case, which explains the reduced conductance of the junction compared to the parallel case.

Only elastic tunneling without spin-flip is considered, which means that an electron can only tunnel into an unoccupied state of the same spin and energy. The tunnel probability depends on the number of available states into which the electron can tunnel and is thus reduced in the antiparallel case compared to the parallel case. This leads to the lower conductance measured in junctions with antiparallel magnetizations in the two electrodes compared to those with parallel magnetizations. The same situation can be reproduced in STM by using a magnetic tip to measure a magnetic sample.<sup>14,15</sup> One of the two electrodes is the tip. The

<sup>14</sup> M. Bode.  
*Reports on Progress in Physics*  
66, 523 (2003) [56]

<sup>15</sup> R. Wiesendanger.  
*Reviews of Modern Physics* 81,  
1495–1550 (2009) [57]

relevant magnetization for the calculation of the tunnel current is the one of the atom at the apex of the tip. The other electrode is the sample, in which the magnetization varies spatially. The model for the STM tunnel current discussed in section II.2.1.1 can be extended to take into account the spin-polarized tunneling.<sup>16</sup> The tunnel current can then be separated in two parts, a non-spin-polarized one and a spin-polarized one:

$$I = I_0(1 + P_t P_s \cos \theta) \quad (\text{II.39})$$

where  $P_t$  and  $P_s$  are the effective polarizations of the tip and the sample respectively and  $\theta$  the angle between the magnetization  $\vec{M}_t$  at the end of the tip and the local magnetization  $\vec{M}_s$  on the sample. Depending on the direction of  $\vec{M}_t$ , the tip is sensitive to a particular component of  $\vec{M}_s$ . By changing  $\vec{M}_t$ , it is thus possible to measure all the components of the magnetic structure of the sample and to fully understand it.  $\vec{M}_t$  can either be modified by the application of an external magnetic field or by in-situ modification of the tip apex (performed with voltage pulses or gentle contact with the sample surface). Figure II.17 shows the expected TMR contrast for a cycloidal spin spiral measured with an out-of-plane sensitive tip: an alternating pattern of bright and dark stripes separated by smooth transitions.

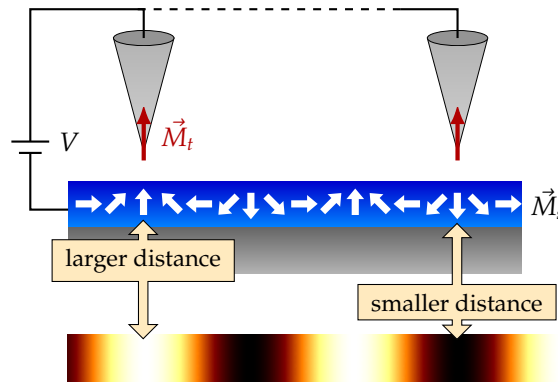


Figure II.17: Drawing showing the expected TMR contrast for a homogeneous cycloidal spin spiral measured with an out-of-plane sensitive tip. The tunnel current depends linearly on the cosine of the angle between the magnetization  $\vec{M}_t$  at the apex of the tip and the local magnetization  $\vec{M}_s$  at the sample surface. In constant-current mode, this cosine dependence is transferred to the variations of the tip height.

In constant-current mode, the dependence of the tunnel current on the relative orientations of the magnetizations of the tip and the sample is transferred to the variations of the tip height. This method allows to resolve spin structures at the atomic scale.<sup>16</sup> In addition, the magnetic states can also be investigated by measuring the differential conductance. Similarly to the previous non-magnetic case, the current (or the tip height in constant-current mode) depends on the integrated LDOS but the differential conductance gives directly access to the LDOS at the applied voltage. During a measurement, this offers the possibility to choose a

<sup>16</sup> D. Wortmann et al. *Physical Review Letters* 86, 4132–4135 (2001) [58]

bias voltage for which the magnetic contribution dominates over the non-magnetic one in order to increase the magnetic signal.<sup>17</sup>

**Tunnel anisotropic magnetoresistance** When the magnetic state is non-collinear, a further effect becomes relevant, the *Tunnel Anisotropic MagnetoResistance* or TAMR. The TAMR allows to obtain information about the magnetic state of the sample without the requirement of using a magnetic tip. It can, for example, be measured with a W tip.<sup>18,19</sup> Because of the spin-orbit coupling, the LDOS in a magnetic material depends on the local direction of the magnetization. Since the tunnel current is sensitive to the LDOS, it is thus possible to observe a contrast between areas where the magnetization is pointing out-of-plane and areas where it is oriented in the plane. This means that for a spin spiral, the measured signal has a period which is half the one measured with TMR. For domain walls, the TAMR contrast is the same on every wall, regardless of the in-plane direction of the magnetization. The TAMR thus does not allow to compare the rotational sense of two domain walls. The TAMR is not visible at all bias voltages, it is typically (but not necessarily) found at low values (below 50 mV).

**Non-collinear magnetoresistance** A third magnetoresistive effect comes into play when the non-collinearity of the magnetic state is not uniform. This happens for example in domain walls, inhomogeneous spin spirals or skyrmions. In this case, the *Non-Collinear MagnetoResistance* or NCMR (which, combined with TAMR can also be called tunnel spin-mixing magnetoresistance) needs to be considered. Like in the TAMR, the NCMR can be measured with a non-magnetic tip (for example a W tip). It was first observed<sup>20,21</sup> and identified<sup>22</sup> for the skyrmions in the PdFe bilayer on Ir(111). The NCMR originates from a mixing of the spin  $\uparrow$  and  $\downarrow$  bands for non-collinear states, which results in variations of the LDOS. For example, a different signal can be measured with a non-magnetic tip in the center of a skyrmion and in the ferromagnetic background despite the fact that in both cases the magnetic moments are pointing out-of-plane. The difference between the two areas is the local magnetic environment, which is highly non-collinear at the center of the skyrmion and collinear in the ferromagnetic background.

**Polarization effects** Another effect can contribute to the magnetic signal measured with a non-magnetic tip: variations of the induced magnetic polarization, in the substrate or in the different layers constituting the ultrathin film. For example, in the case of a film made of one magnetic layer and a non-magnetic layer (or with smaller magnetic moments than the first one), the magnetic state in the first layer can induce a spin polarization in the non-magnetic layer. When the magnetic state is not ferromagnetic, the induced moments in the non-magnetic layer may vary. This effect was predicted to occur in Fe/Rh(111)<sup>23</sup> and observed

<sup>17</sup> M. Kleiber et al. *Physical Review Letters* 85, 4606–4609 (2000) [59]

<sup>18</sup> M. Bode et al. *Physical Review Letters* 89, 237205 (2002) [60]

<sup>19</sup> K. von Bergmann et al. *Physical Review B* 86, 134422 (2012) [61]

<sup>20</sup> C. Hanneken et al. *Nature Nanotechnology* 10, 1039–1042 (2015) [62]

<sup>21</sup> A. Kubetzka et al. *Physical Review B* 95 (2017) [63]

<sup>22</sup> D. M. Crum et al. *Nature Communications* 6, 8541 (2015) [64]

<sup>23</sup> A. Al-Zubi et al. *physica status solidi (b)* 248, 2242–2247 (2011) [65]

<sup>24</sup> N. Romming et al. *Physical Review Letters* 120, 207201 (2018) [66]

in Rh/Fe/Ir(111).<sup>24</sup> In this system, the magnetic structure is close to a double-row wise antiferromagnetic state (or  $\uparrow\uparrow\downarrow\downarrow$ -state). When a Rh atom is located on top of three magnetic moments in the Fe layer pointing in the same direction, the induced moment is larger than in configurations with two moments pointing in the same direction and the third one in the opposite direction. This variation of the induced magnetic moment has an impact on the LDOS, which is then measurable with STM.

### II.2.2.2 Preparation of magnetic tips

The imaging of the magnetic states in this thesis mostly relies on the TMR effect, which means that a magnetic STM tip is required. Two types of magnetic tips were used: antiferromagnetic Cr bulk tips and ferromagnetic Fe-coated W tips.

<sup>25</sup> E. Fawcett. *Reviews of Modern Physics* 60, 209–283 (1988) [67]

**Cr bulk tips** Bulk Cr is antiferromagnetic below 311 K<sup>25</sup>, which means that the stray field generated by a Cr bulk tip is very small because the dipolar fields generated by the magnetic moments compensate each other. The sensitivity of a such an antiferromagnetic tip is determined by the state of the atom located at the tip apex.<sup>26</sup> Cr bulk tips are very useful to study magnetic systems which are modified by the application of a magnetic field. Indeed, because of the antiferromagnetic ordering, the magnetic state of the tip usually does not change in magnetic fields. Since the tip sensitivity is fixed, all the modifications in the data visible upon a change of the applied field originate from the magnetic state of the sample.

<sup>26</sup> R. Wiesendanger. *Reviews of Modern Physics* 81, 1495–1550 (2009) [57]

The Cr bulk tips used in this thesis were prepared by electrochemical etching by Christian Hanneken<sup>27</sup> and glued on a tip holder. No particular treatment is applied to the tip before inserting it in the STM (it is not possible to anneal it because of the glue). Its sharpness and magnetic sensitivity can be changed during the measurement using voltage pulses and gentle contacts with the sample surface.

<sup>27</sup> C. Hanneken. Diplomarbeit. Universität Hamburg, 2011 [68]

**Fe coated W tips** For experiments which require a controlled modification of the magnetic sensitivity of the tips, ferromagnetic tips are better suited than antiferromagnetic tips. When a magnetic field is applied, the magnetization at the tip apex aligns with the field which allows to control the magnetic sensitivity of the tip and thus measure several components of the magnetic structure of the sample. In this case, the tips used in this thesis are Fe-coated W tips. They typically have an in-plane magnetic sensitivity at zero field, which can be modified to out-of-plane by applying an out-of-plane magnetic field. For a coverage of about 30 to 50 Fe layers, they also have a better thermal stability than Cr bulk tips and are thus easier to use at elevated temperatures. However, ferromagnetic tips generate a stray field which can influence

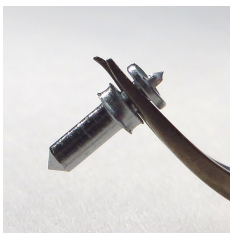


Figure II.18: W tip fixed in a tip holder.

the magnetic state of the sample and perturb the measurements, as shown in section IV.2.

The W tips were prepared by electrochemical etching of a W wire<sup>28</sup>, which is then mechanically fixed in the tip holder. A picture of such a tip is shown in Figure II.18. The tip is prepared in situ in several steps, it needs to be cleaned and then coated with Fe. The tip is first heated at high temperature for a short time (about 10 s, twice) in order to remove the surface oxide. Then Fe is deposited onto the tip, which is then post-annealed for about 5 min at 200 °C in order to get a smooth Fe film.

<sup>28</sup> J. P. Ibe et al. *Journal of Vacuum Science & Technology A* 8, 3570–3575 (1990) [69]

### II.2.2.3 Simulation of SP-STM images

In order to compare measured spin-resolved images and models of the magnetic structure, it is necessary to compute simulations of the SP-STM data. This section explains how the simulations presented in chapter V were performed, using python 3.6<sup>29</sup> and inspired from the code written by Niklas Romming<sup>30</sup>.

<sup>29</sup> [python.org](https://www.python.org)

The simulations are computed without having access to the electronic structure in the sample and thus provide only an approximation of the expected magnetic contrast. The current is estimated by assuming a spherical decay of the electronic wave functions and considering that all the atoms on the surface are identical.<sup>31</sup> Starting from a list of the normalized magnetic moments  $\vec{S}_i$  and their spatial positions  $\vec{r}_i$ , the tunnel current is estimated at the position of each pixel of the desired image. Only the TMR contribution was considered here, but the TAMR and the NCMR effects can be easily added. The tunnel current at the position  $\vec{\rho} = (x, y, z_0)$  is expressed as:

<sup>30</sup> N. Romming. PhD thesis. Universität Hamburg, 2018 [70]

<sup>31</sup> S. Heinze. *Applied Physics A* 85, 407–414 (2006) [71]

$$I(\vec{\rho}) = I_{\text{ref}} \sum_i \left[ (1 + P_t P_s \vec{S}_i \cdot \vec{S}_t) e^{-2\kappa \sqrt{(\vec{\rho} - \vec{r}_i)^2}} \right] \quad (\text{II.40})$$

where  $I_{\text{ref}}$  is a reference current value (fixed to 1 in the calculation),  $P_t P_s$  is an effective polarization factor determining the strength of the TMR,  $\vec{S}_t$  is the magnetic moment at the apex of the tip and  $\kappa = \sqrt{2m_e \phi} / \hbar$  is the decay factor depending on the work function  $\phi$ . Since the contribution of each atom decays exponentially with the distance between this atom and the position of the considered pixel, the calculation can be made faster by computing the sum only for the atoms located in a given distance range around the pixel rather than for the whole lattice. This range depends on the tip-sample distance  $z_0$ , and a typical value of  $3 z_0$  was used in the calculation. In addition, the evaluation of the decay factors is parallelized to further increase the speed of the calculation.

This procedure computes the current measured in constant height mode (at  $z_0$ ). In order to compare the simulation with the data obtained in constant-current mode, the exponential decay of the current is linearly approximated:<sup>32</sup>

<sup>32</sup> S. Heinze.  
*Applied Physics A*  
85, 407–414 (2006)  
[71]

$$\Delta z(x, y) = \frac{I(\vec{\rho}) - I_0(\vec{\rho}_0)}{2\kappa I_0(\vec{\rho}_0)} \quad (\text{II.41})$$

where  $\vec{\rho}_0$  corresponds to the center of the calculated image and  $I_0(\vec{\rho}_0)$  is the value of the current (without the magnetic contribution) at the position  $\vec{\rho}_0$ .

## II.3 Structure of epitaxial films at the nanoscale

This thesis deals with the interplay between structures formed by the atom arrangement in ultrathin films and their magnetic state. These structures have different natures and can either form spontaneously, for example to relieve epitaxial strain, or be created deliberately, which can be done by incorporating atoms from gas molecules within the film.

### II.3.1 Stacking of epitaxial ultrathin films

The crystal structure of a solid monocrystalline metal is usually one of the following: face-centered-cubic (fcc), hexagonal-close-packed (hcp) or body centered cubic (bcc). These structures are illustrated in Figure II.19. For example, bulk Ir, Pt, Ni, Pd or Rh have a fcc structure, whereas bulk Co, Ru or Re have a hcp structure and bulk Fe, Cr or W have a bcc structure. In this thesis, the magnetism of Fe films on the Ir(111) surface is studied. The fcc (111) surface is hexagonal and as shown in Figure II.20, there are various possible sites in which atoms can be placed.

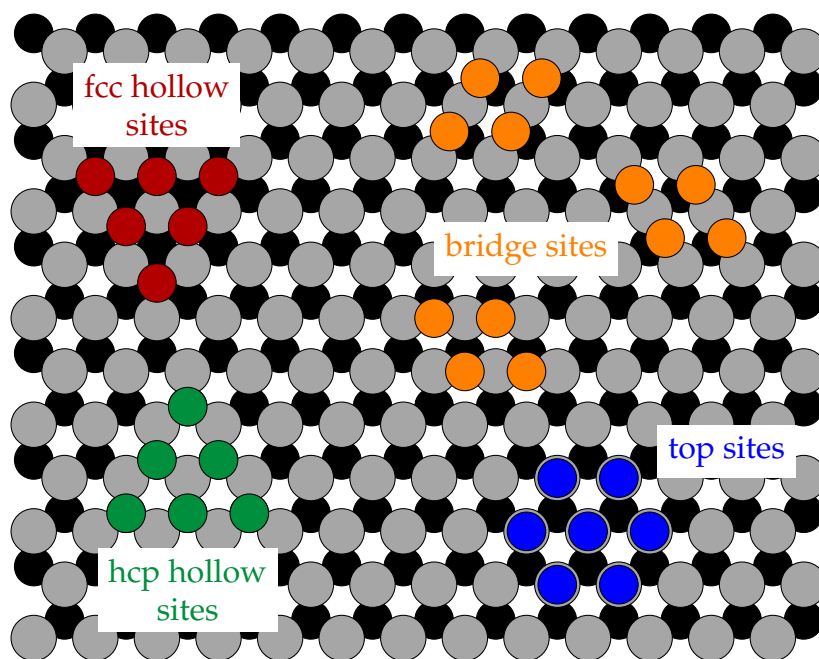


Figure II.20: Definition of the different adsorption sites on a fcc (111) layer. The gray circle mark the position of the atoms at the surfaces, the black circles indicate the position of the atoms one layer below and the colored circles correspond to the adsorbed atoms.

The gray and the black layers correspond to the substrate, the gray layer at the surface and the black layer below and the colored circles indicate the various high-symmetry adsorption sites. There are two types of hollow sites, those corresponding to fcc stacking (red) and those corresponding to hcp stacking (green). It is necessary to know the position of the black layer to decide which of the hollow sites are fcc and

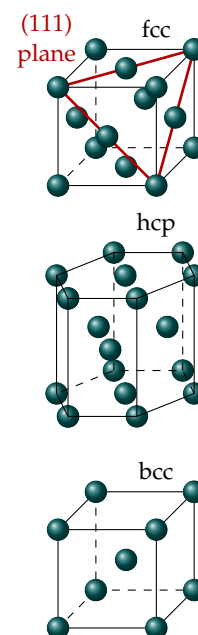


Figure II.19: Sketches of the fcc, hcp and bcc structures.

which are hcp. There are atoms of the lower layer located below the hcp sites whereas this is not the case for the fcc sites. Here, the fcc sites are at the center of down pointing triangles and the hcp sites at the center of up pointing triangles. The atoms can also be located in bridge sites, marked in orange. Top sites are marked in blue and are located on top of the surface atoms.

The structures described in the following are either formed by the positioning of the atoms of the film between these highly symmetric sites (like the dislocation lines in the Fe double layer on Ir(111), see section III.2.1), by the arrangement of the atoms in different types of states (alternating fcc, hcp and bridge sites for example, see section VI.1.2) or by the incorporation of other atoms inside the film (like H, see chapter V). Even the stacking can have a large influence on the magnetic state of an ultrathin film.<sup>1</sup> Besides this effect, the appearance of an additional pattern in the atomic arrangement creates spatial modulations of the magnetic parameters which can reshape the magnetic structure.

<sup>1</sup> K. von Bergmann et al. *Nano Letters* 15, 3280–3285 (2015) [72]

### II.3.2 Creation of superstructures

When some atoms of a different nature are incorporated in an ultrathin film, they can either form a disordered alloy or an ordered superstructure. In particular, ordered superstructures can be created by dosing a small amount of gas (for example hydrogen or oxygen) in the vacuum chamber. The atoms from the gas adsorb on the surface. Depending on the system, a subsequent post-annealing might be necessary in order to obtain a well ordered structure. For example, by adding O atoms on a Pd(110) surface it is possible to induce a row pattern in the  $[1\bar{1}0]$  direction<sup>2</sup> with a periodicity depending on the O coverage. A further example, in a magnetic system this time, is the formation of a  $p(2 \times 2)$  superstructure in Co islands on Cu(111) by the incorporation of H atoms.<sup>3</sup> Furthermore, when the amount of incorporated H increases, the surface magnetization of the Co islands is reduced<sup>4</sup>, which demonstrates that these superstructures can also drastically modify the magnetic state.

<sup>2</sup> H. Tanaka et al. *Surface Science* 327, L505–L509 (1995) [73]

<sup>3</sup> M. Sicot et al. *Surface Science* 602, 3667–3673 (2008) [74]

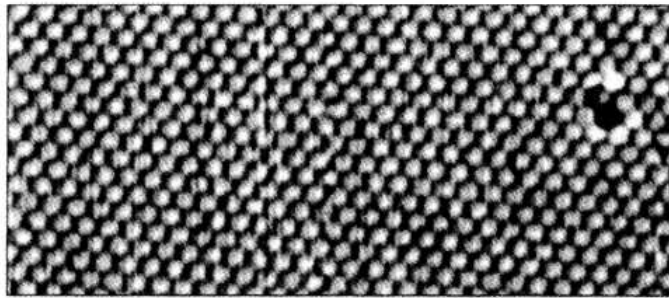
<sup>4</sup> J. Park et al. *Nano Letters* 17, 292–298 (2017) [75]

### II.3.3 Strain relief by the formation of dislocations

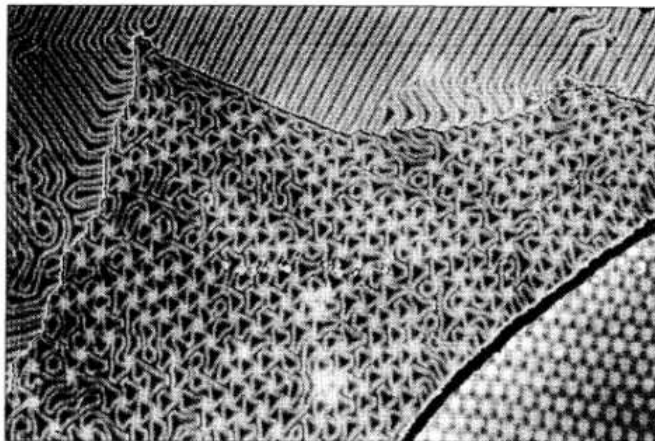
Another mechanism leading to the formation of patterns at the nanoscale in ultrathin films is the relief of epitaxial strain. When a film is grown on a substrate, it is very likely that the lattice constant of the substrate and the preferred lattice constant of the element forming the film do not match. The film is then either expanded or compressed. The film is designated as pseudomorphic when the in-plane lattice constants of the substrate and the film are the same. If the epitaxial strain is too large, a pseudomorphic growth is no longer favorable and some dislocations form in the film. Depending on the symmetry of the substrate and the preferred arrangement of the atoms in the ultrathin film, a large variety

of dislocation patterns can be found. The thickness of the film also plays a crucial role for the determination of the dislocation pattern. In Fe on Ir(111), the monolayer grows pseudomorphically whereas dislocation lines appear for higher coverages. This effect is discussed in detail in section III.2.1. Another clear example of the thickness dependence of the dislocation pattern is Cu/Ru(0001).<sup>5</sup> Figure II.21 shows four different growth modes of the Cu film, each associated with a local thickness.

<sup>5</sup> C. Günther et al. *Physical Review Letters* 74, 754–757 (1995) [76]



(a)



(b)

Figure II.21: STM images of differently thick Cu films on Ru(0001) showing four different strain relief modes. In image (a), the monolayer is pseudomorphic, fully strained (mode A), the hexagonal pattern corresponds to atomic resolution. The width of the imaged area is 7.7 nm. In image (b), three more growth modes are visible: mode B, at the top, for a local coverage of 2 layers, mode C in the middle, for 3 atomic layers and mode D at the bottom, for 4 layers. The width of the imaged area is 193 nm. Extracted with permission from [76], copyright 1995 by the American Physical Society.

At the atomic scale, the bright lines visible in the data in modes B and C correspond to atoms located on bridge sites and forming a boundary between fcc and hcp areas. A very similar behavior is found for Fe/Ir(111), Ni/Ir(111) and Ni/Fe/Ir(111), as detailed in chapters III and VI. In the mode D, the Cu layer has almost reached the lattice constant of the bulk and the observed hexagonal structure is a Moiré pattern.

### II.3.4 Surface reconstructions

Briefly, for completeness, surface reconstructions are mentioned here. At the surface of a crystal, the coordination of the atoms is reduced compared to the bulk. In the case of Ir for example, this does not have a visible effect on the (111) surface, which is perfectly flat. However, it can happen, and this is the case for Ir(001)<sup>6</sup>, that shifts of the positions of the surface atoms are energetically favorable. In Ir(001), a  $(5 \times 1)$  reconstruction forms, in which the density of atoms increases by 20%. It appears as a stripe pattern in STM. This phenomenon is not rare. The  $(7 \times 7)$  reconstruction of the Si(111) surface is very well known.<sup>7</sup> For Au(111), a *herringbone* pattern<sup>8</sup> is also visible at the surface as shown in Figure II.22. It looks very similar to the dislocation lines created in mode B of the strain relief patterns presented in Figure II.21, but here, no epitaxial strain is involved, only the surface energy.

<sup>6</sup> A. Schmidt et al. *Journal of Physics: Condensed Matter* 14, 12353 (2002) [77]

<sup>7</sup> G. Binnig et al. *Physical Review Letters* 50, 120–123 (1983) [78]

<sup>8</sup> J. Barth et al. *Physical Review B* 42, 9307–9318 (1990) [79]

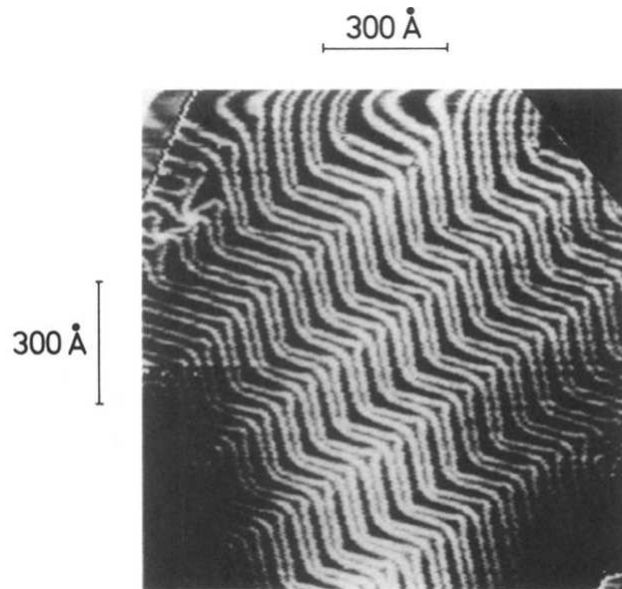


Figure II.22: STM image of reconstructed Au(111) surface showing the periodic herringbone pattern. Extracted with permission from [79], copyright 1990 by the American Physical Society.

## II.4 The Fe monolayer on Ir(111)

All the magnetic systems studied in this thesis are based on Fe films grown on an Ir(111) surface. A large DMI is indeed generated by the Fe/Ir interface, allowing to stabilize a complex two-dimensional structure called a *nanoskyrmion lattice* in the Fe monolayer. The following chapters show how this state can be modified, by adding further metallic layers on top of the Fe monolayer and incorporating H atoms in the magnetic film. Before starting these investigations, the properties of the initial Fe/Ir system are thus detailed here.

### II.4.1 Growth of the Fe monolayer

The Ir single crystals used to prepare the samples typically have the following size:  $5$  or  $7 \times 5 \times 1$  mm. They are fixed with W wires on a clean 1 mm-thick W tungsten plate (see the picture in Figure II.23).

The Ir crystal needs to be cleaned before the Fe deposition. The first step of the cleaning procedure is to sputter the crystal with  $\text{Ar}^+$  ions accelerated by a voltage of 800 V. After the sputtering, the Ir surface is rough and needs to be flattened by an annealing procedure. The crystal is heated to about 1500 K for 90 s using an electron beam heater. If there are still too many adsorbates on the surface after the annealing, the sputtering/annealing cycle is repeated.



Figure II.23: Ir single crystal fixed on a W plate.

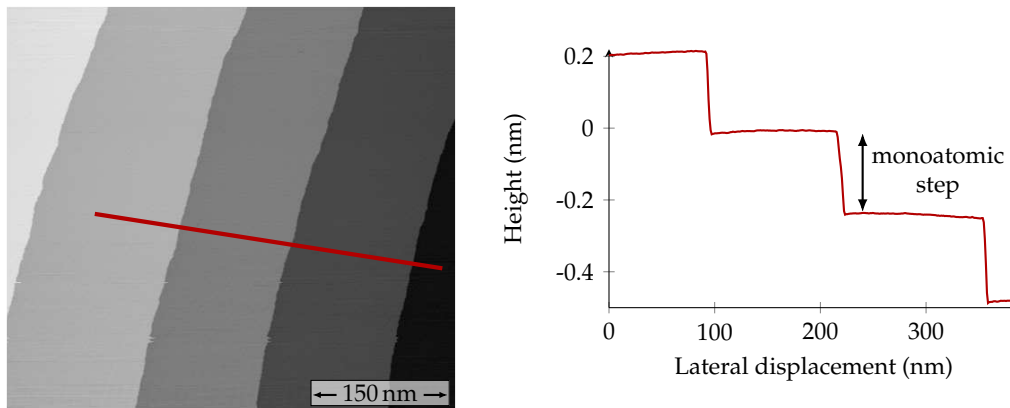


Figure II.24: STM constant-current map of a clean Ir(111) surface showing the flat terraces and the monoatomic steps. The plot displays the line profile marked in red. *Measurement parameters:* : -200 mV, 1 nA, room temperature, PtIr tip.

However, this method is not very efficient to remove C contaminations. In this case, the Ir crystal needs to be annealed in a  $\text{O}_2$  atmosphere: the elevated temperature allows the C impurities to reach the surface of the crystal where they react with the  $\text{O}_2$  gas in the chamber and form CO and  $\text{CO}_2$  which can be subsequently desorbed by increasing the temperature to 1800 K. During the  $\text{O}_2$  exposure (at a partial pressure between  $1 \times 10^{-7}$  and  $1 \times 10^{-6}$  mbar), the heating power is slowly decreased from a maximal value (allowing to reach 1800 K) to zero in cycles. Once the Ir

<sup>1</sup> K. von Bergmann et al. *New Journal of Physics* 9, 396 (2007) [80]

crystal is clean, the surface exhibits flat terraces with a step height of one atomic layer (222 pm in this case), as shown in Figure II.24.

The deposition of the Fe can be performed either at elevated temperature (shortly after the annealing) or at room temperature. When the Fe is deposited at elevated temperature, mostly step flow growth is observed and only the fcc stacking of the Fe layer is found on the surface. In contrast, when the Fe is deposited onto the surface at room temperature, triangular islands of both stackings form<sup>1</sup>, as illustrated in Figure II.25.

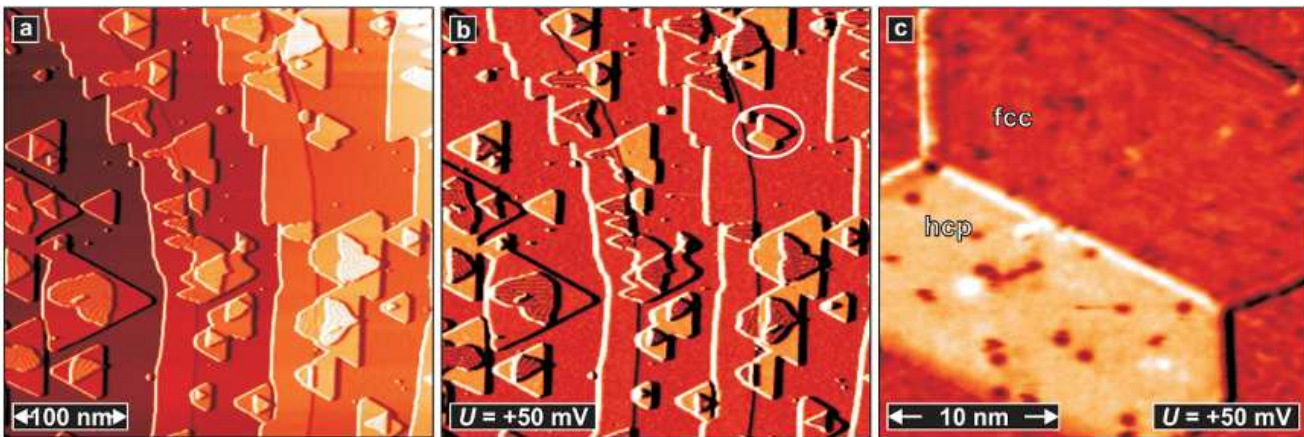


Figure II.25: STM constant-current map (a) and the simultaneously recorded differential conductance map (b) of a Fe/Ir(111) sample with a coverage of 0.7 atomic layer. A clear contrast between both stackings is visible in the differential conductance map, the hcp islands are bright whereas the fcc islands are darker. Image (c) shows a closer view of the island marked in (b) in which there is a boundary between the two stackings. Extracted from [80], licensed under [CC BY 3.0](https://creativecommons.org/licenses/by/3.0/).

## II.4.2 The incommensurate square nanoskyrmion lattice in the fcc Fe monolayer

The magnetic state of the fcc Fe monolayer is an incommensurate square nanoskyrmion lattice<sup>2</sup>, with a period of about 1 nm. A spin-resolved constant-current map of this state is shown in Figure II.26.

Since the nanoskyrmion lattice has a square symmetry and the atomic lattice in the Fe layer is hexagonal, three rotational domains are present. By comparing the observed magnetic contrast in the three rotational domains, the detailed spin structure could be determined. A sketch of this configuration is shown in Figure II.27, in the commensurate approximation.

The nanoskyrmion lattice is a superposition of spin spirals, but it cannot be described in a model containing only the exchange interactions, the DMI and the magnetic anisotropy. The four-spin and the biquadratic interactions appear to play a crucial role in its stabilization. Ab initio calculations revealed that the DMI is large at the Fe/Ir interface, with a value of  $-1.8$  meV per atom. The negative sign means that the clockwise

<sup>2</sup> S. Heinze et al. *Nature Physics* 7, 713–718 (2011) [27]

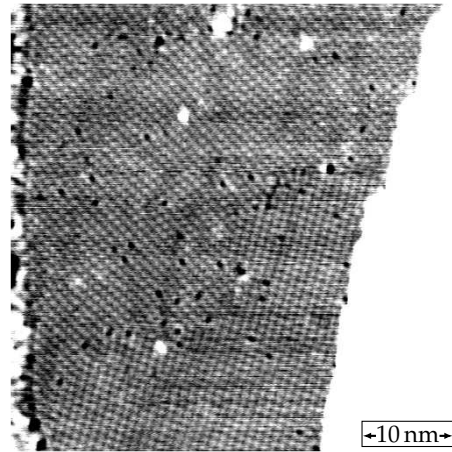


Figure II.26: Spin-resolved constant-current map of a Fe monolayer on Ir(111), in fcc stacking. The square nanoskyrmion lattice state is visible, two different rotational domains can be found in this area. *Measurement parameters:* : 50 mV, 1 nA, 4 K, 0 T, Cr bulk tip.

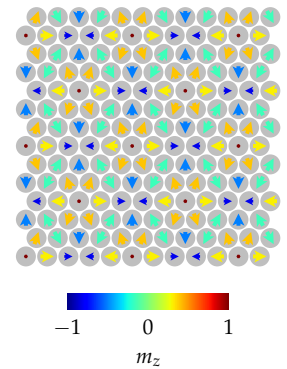


Figure II.27: Spin structure of the square nanoskyrmion lattice, in the commensurate approximation.

rotational sense of the magnetization is favored. This value will be used as a reference for the Fe/Ir interface in the following.

No change of the magnetic state occurs when an out-of-plane magnetic field is applied. This observation is compatible with the proposed spin structure: the magnetic moment is fully compensated within a magnetic unit cell in the out-of-plane direction.

Further investigations of this exotic state allowed to determine its properties. It was already found from the STM data and recently confirmed using magnetic exchange force microscopy<sup>3,4</sup> that the nanoskyrmion lattice is not commensurate with the atomic lattice. The sketch in Figure II.27 is thus only an approximation. It was also demonstrated that the orientation of the lattice is strongly coupled to the boundaries of the Fe islands<sup>5</sup>. Temperature-dependent measurements could show that the nanoskyrmion lattice vanishes at 28 K.<sup>6</sup>

### II.4.3 The hexagonal nanoskyrmion lattice in the hcp Fe monolayer

In the hcp Fe islands, the magnetic state is again a nanoskyrmion lattice, but this time it is hexagonal and commensurate with the lattice.<sup>7</sup> Hence the stacking can have an influence on the magnetic state. The period of this lattice is similar to the one of the square nanoskyrmion lattice, about 1 nm, and since the magnetic state and the atomic lattice both have an hexagonal structure, no rotational domains are present.

The corresponding spin structure is drawn in Figure II.28. There are two options to place the magnetic state (which is a superposition of three spin spirals) with respect to the atomic lattice. Either the point where the magnetic moments point in the out-of-plane direction is on a top site (on-top state) or it is on a hollow site (hollow state). These

<sup>3</sup> J. Grenz et al. *Physical Review Letters* 119, 047205 (2017) [81]

<sup>4</sup> N. Hauptmann et al. *Nano Letters* 17, 5660–5665 (2017) [82]

<sup>5</sup> J. Hagemeister et al. *Physical Review Letters* 117 (2016) [83]

<sup>6</sup> A. Sonntag et al. *Physical Review Letters* 113, 077202 (2014) [84]

<sup>7</sup> K. von Bergmann et al. *Nano Letters* 15, 3280–3285 (2015) [72]

two states cannot be distinguished with pure TMR contrast. Besides this and in contrast to the fcc case, two oppositely magnetized domains can be found. Indeed, the out-of-plane magnetic moments are not fully compensated within the magnetic unit cell of the hexagonal nanoskyrmion lattice. By inverting the direction of the magnetic moments, it is thus possible to build a different but symmetry equivalent state. These states form magnetic domains, with an up or down out-of-plane net magnetic moment. When an out-of-plane magnetic field is applied, one of these states is preferred and one of the domains switches to align with the external field.

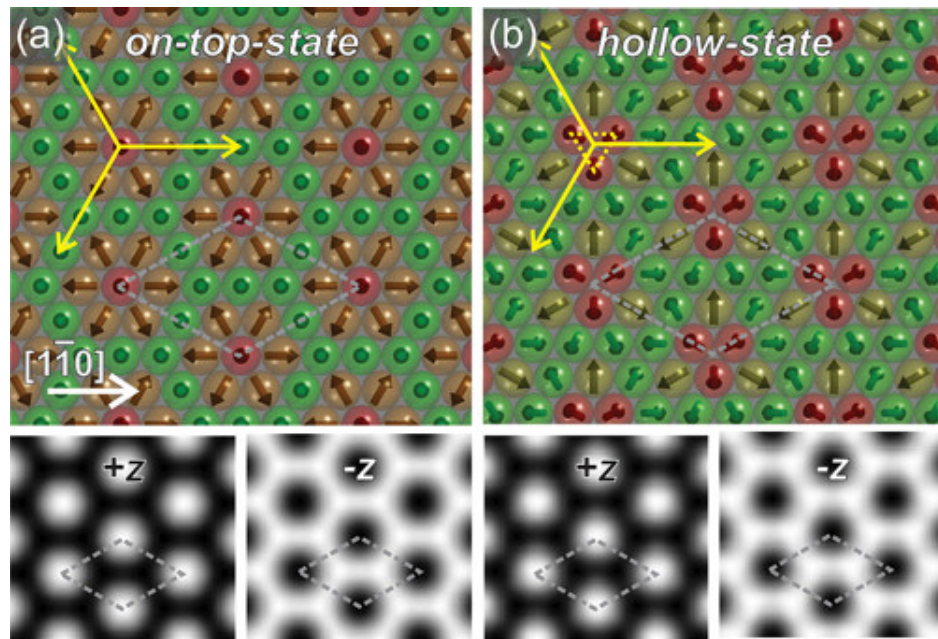


Figure II.28: Spin structure of the hexagonal nanoskyrmion lattice in the hcp Fe monolayer on Ir(111), showing the two possible configurations (on-top state and hollow state). SP-STM simulations show the expected contrast for an out-of-plane sensitive tip and for both magnetic domains for each configuration. Extracted with permission from [72], copyright 2015 by the American Chemical Society.

It is possible to determine which one of the on-top or hollow configurations is the one actually realized in the hcp Fe monolayer by measuring the TAMR signal, using a non-magnetic STM tip. The measurement is shown in Figure II.29. By comparing the measured pattern with simulations of the expected TAMR contrast, it appears that only the simulation shown on the left of panel (d) agrees with the data. It corresponds to the hollow state with a positive factor  $\gamma$ , which is a measure for the strength of the TAMR contrast.

Further simulations of the TAMR contrast also allowed to prove that unlike the square nanoskyrmion lattice, the hexagonal lattice is commensurate with the atomic lattice.

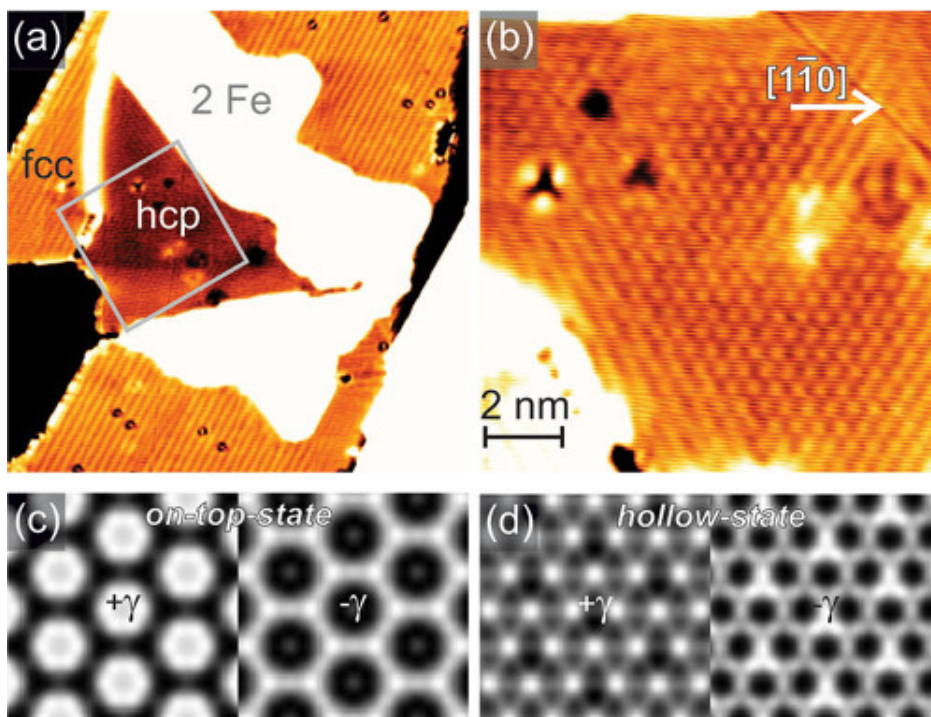


Figure II.29: STM constant-current images (a and b) showing the TAMR contrast on the hexagonal nanoskyrmion lattice in the hcp Fe monolayer on Ir(111) (and also on the square nanoskyrmion lattice in the fcc Fe monolayer). (b) is a closer view of the area marked with the square in (a). Simulations of the expected TAMR contrast for both the on-top (c) and the hollow (d) configurations are shown at the bottom for comparison, with a positive or a negative factor  $\gamma$  (measuring the strength of the TAMR effect). Only the simulation on the left in (d) agrees with the data, which demonstrates that the Fe layer is in the hollow state. Extracted with permission from [72], copyright 2015 by the American Chemical Society.

Chapter V shows how the incorporation of H in the Fe monolayer modifies the properties of the nanoskyrmion lattice, in the fcc case.



# III. Non-collinear magnetism in uniaxially relaxed Fe ultrathin films

This chapter is an introduction to the main features (in terms of growth and magnetic state) of the Fe double, triple and quadruple layers on Ir(111), before the detailed investigation of the Fe triple layer in chapter IV. Section III.1 is an overview of the structure of a typical Fe/Ir(111) sample for a coverage between 2 and 3.5 atomic layers. Because of the large lattice mismatch between Fe and Ir, the films are not pseudomorphic like the Fe monolayer but exhibit a network of dislocation lines<sup>1</sup>. These lines have a significant influence on the magnetic state of the film, which is also presented in this section. Since the details about the dislocation lines and the spin spirals in the double layer Fe are an essential prerequisite to understand the chapters IV and V, section III.2 is devoted to an extensive discussion about this topic. To conclude this chapter, the method used throughout this thesis to derive the direction of the magnetic sensitivity of the SP-STM tips is explained in section III.3. *The measurements presented in this chapter were performed jointly with Pin-Jui Hsu and Lorenz Schmidt.*

<sup>1</sup> P.-J. Hsu et al.  
*Physical Review Letters* 116, 017201  
(2016) [85]

## III.1 Overview of the Fe/Ir(111) system

### III.1.1 Growth of the Fe film

Figure III.1 is a large overview of the topography of a Fe ultrathin film on Ir(111), with a Fe coverage of about 3 atomic layers. Locally, the coverage varies from 1 to 4 layers. The Fe atoms are deposited onto the clean Ir substrate at an elevated temperature of around 200 °C at a deposition rate close to 0.3 atomic layer per min.

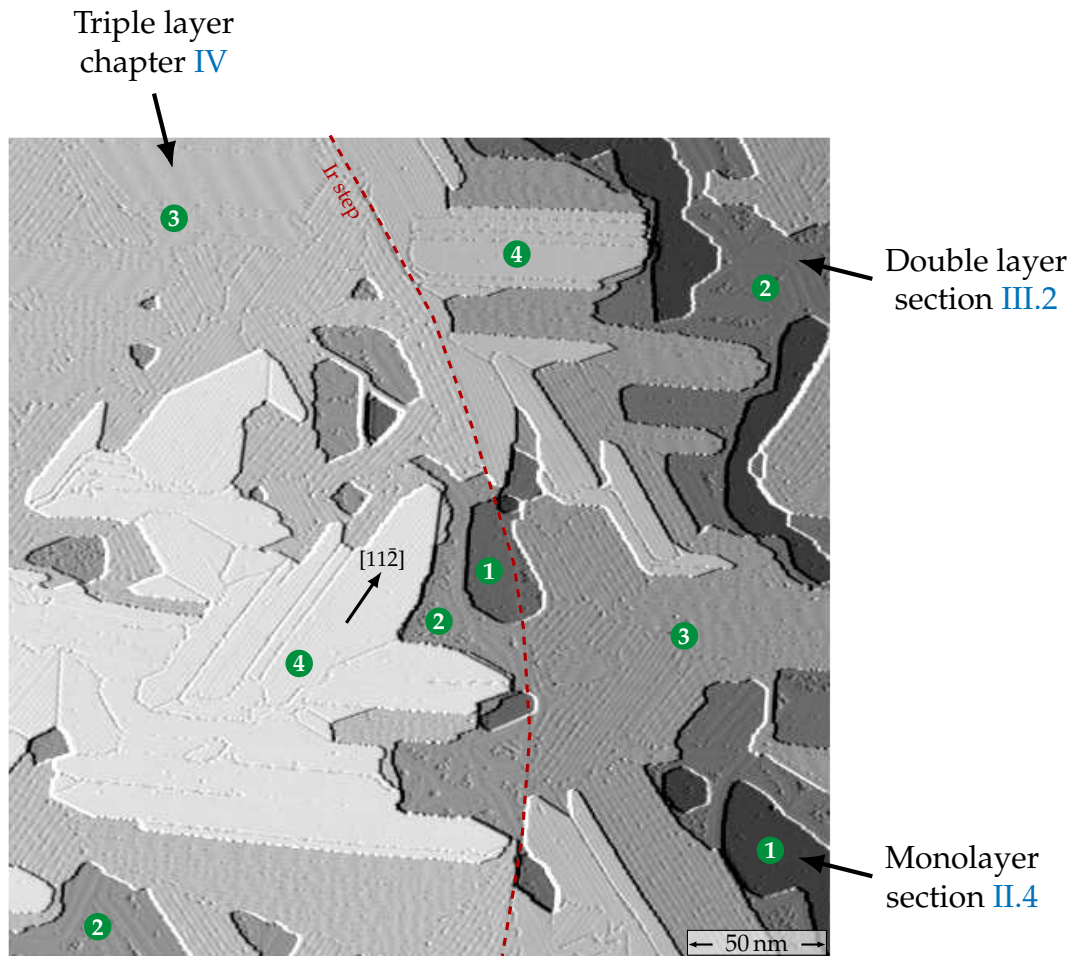


Figure III.1: STM constant-current map of a typical Fe/Ir(111) sample with a Fe coverage of about 3 atomic layers. Regions with local coverages of 1, 2, 3 and 4 atomic layers are present in the scan area and labeled with the numbers in the green circles. The data is partially differentiated along the scanning direction (horizontal) in order to improve the visibility of the dislocation lines. *Measurement parameters:* -700 mV, 1 nA, 8 K, 0 T, Cr bulk tip.

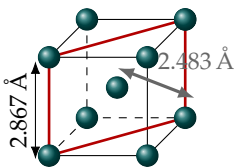


Figure III.2: Sketch of a Fe bcc cell. The (110) plane is marked in red.

As already mentioned in section II.4, the Fe monolayer grows pseudomorphically on the Ir(111) surface. These pseudomorphic areas are also visible in the image in Figure III.1. However, the lattice mismatch between Fe and Ir is very large. In the bulk state, Fe has a bcc structure and the nearest-neighbor distance on the bcc(110) surface is 2.483 Å. On the other hand, the substrate is an Ir fcc single crystal.

On the (111) surface, the atoms arrange in a hexagonal lattice with a nearest-neighbor distance of 2.715 Å. When the Fe film is grown on the Ir(111) surface, the symmetry of the atom arrangement does not correspond to a bcc structure. Previous studies have shown that when a bcc material is grown on a fcc(111) surface, it forms a bcc(110)-like structure<sup>1,2</sup> and thus in the Fe/Ir case, the lattice mismatch reaches 9%. A very large epitaxial strain is present in the Fe film. In order to relieve this strain, dislocation lines form along the  $[11\bar{2}]$  direction as soon as the local coverage exceeds one atomic layer. Whereas in the Fe double layer some pseudomorphic strained areas can still be found, the line pattern in the Fe triple layer is denser and really covers the full surface of the film. In the Fe quadruple layer, the spacing between the lines is even smaller than in the triple layer, which makes the lines rather hard to see at the scale of the image in Figure III.1. Because of the hexagonal symmetry of the surface, three symmetry equivalent rotational domains of the dislocation pattern are present.

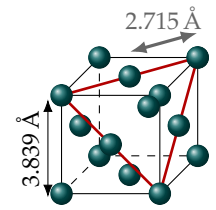


Figure III.3: Sketch of a Ir fcc cell. The (111) plane is marked in red.

### III.1.2 Non-collinear magnetic state

The magnetic state of the area displayed in Figure III.1 is depicted in Figure III.4, which shows the simultaneously recorded differential conductance map. The Cr bulk tip used here is sensitive to the out-of-plane component of the magnetization of the sample. At this scale and at the high bias voltage used, the nanoskyrmion lattice in the Fe monolayer is not detected.

**Fe double layer** In the Fe double layer, a contrast modulation is visible along the dislocation lines, with a very short period of about 1.5 nm. This pattern is induced by the presence of cycloidal spin spirals propagating along the dislocation lines.<sup>3</sup> More details are given in section III.2.

**Fe triple layer** In the Fe triple layer areas, a stripe pattern appears very clearly. Again, these stripes indicate the presence of spin spirals. Similarly to the Fe double layer case, the propagation direction of the spirals is dictated by the dislocation line network. The period of these spirals (from 3 to 10 nm) is larger than in the double layer and varies a lot between the different regions of the sample. An in-depth discussion of this observation is provided in section IV.1. The period of the spin spirals is correlated with the spacing between the dislocation lines and thus with the strain relief.<sup>4</sup>

**Fe quadruple layer** No periodic magnetic pattern is visible in the Fe quadruple layer, but rather some smooth contrast variations which seem to be influenced by the geometry of the island and the magnetic state of the surrounding triple layer areas. The ground state of the Fe quadruple layer is thus not a spin spiral but rather a ferromagnetic

<sup>1</sup> E. Bauer et al. *Physical Review B* 33, 3657–3671 (1986) [86]

<sup>2</sup> S.-H. Phark et al. *Nature Communications* 5 (2014) [87]

<sup>3</sup> P.-J. Hsu et al. *Physical Review Letters* 116, 017201 (2016) [85]

<sup>4</sup> A. Finco et al. *Physical Review B* 94, 214402 (2016) [88]

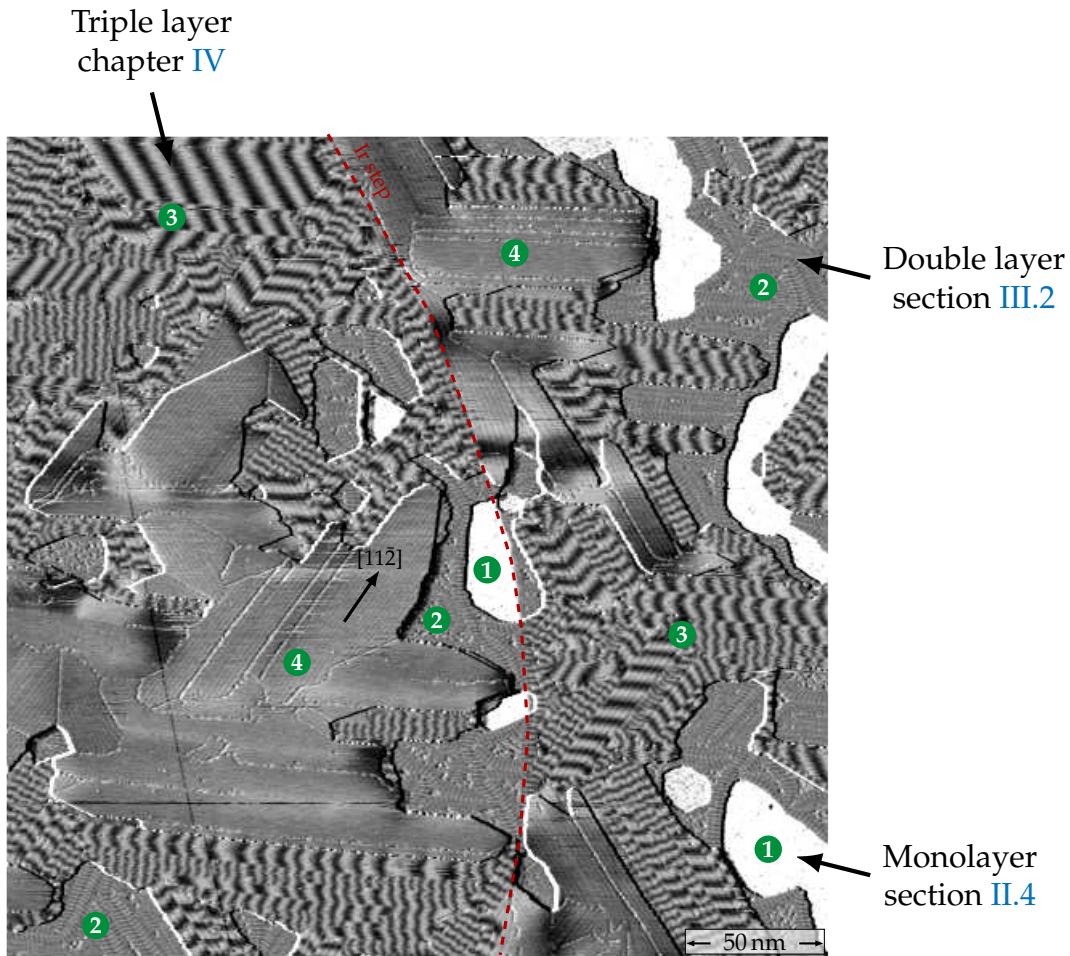


Figure III.4: Spin-resolved differential conductance map recorded simultaneously with the constant-current map from Figure III.1. The tip is sensitive to the out-of-plane component of the magnetization of the sample. Regions with local coverages of 1, 2, 3 and 4 atomic layers are present in the scan area and labeled with the numbers in the green circles. Spin spirals propagate along the dislocation lines in the Fe double and the triple layer areas. The Fe quadruple layer is ferromagnetic with a very low anisotropy. *Measurement parameters:*  $-700$  mV,  $1$  nA,  $8$  K,  $0$  T, Cr bulk tip.

<sup>5</sup> M. Perini et al. *Physical Review B* 97, 184425 (2018) [26]

<sup>6</sup> M. Hervé et al. *Nature Communications* 9, 1015 (2018) [89]

ordering. However, there is also no defined structure of oppositely magnetized domains like in Co/Ir(111)<sup>5</sup> or Ni/Fe/Ir(111) (see section VI.1). The magnetization does not have a preferred direction but rather rotates freely to form large domains without sharp boundaries in which it can be oriented in any direction. This suggests that the effective magnetic anisotropy is very small in this system. Extended films of the Fe quadruple layer are not investigated in this thesis, but a recent study of Co/Ru(0001)<sup>6</sup> showed that spin spirals and magnetic skyrmions (at very low magnetic fields) can be stabilized when the magnetic anisotropy vanishes.

## III.2 The cycloidal spin spirals in the Fe double layer on Ir(111)

This section summarizes what is known about the spin spirals in the Fe double layer on Ir(111).<sup>1</sup> The details about the dislocation line pattern and the cycloidal spin spirals provide a valuable introduction to the results presented in chapter IV about the Fe triple layer and in chapter V about hydrogenation effects.

<sup>1</sup> P.-J. Hsu et al.  
*Physical Review Letters* 116, 017201  
(2016) [85]

### III.2.1 Film morphology

Figure III.5 shows a view of the surface of a Fe double layer on Ir(111). Two types of areas are clearly visible: some pseudomorphic strained regions and some uniaxially relaxed regions. In the first case, the epitaxial strain is not relieved and the Fe double layer follows the lattice constant of the Ir substrate, like the Fe monolayer below. These areas also have a larger concentration of defects.

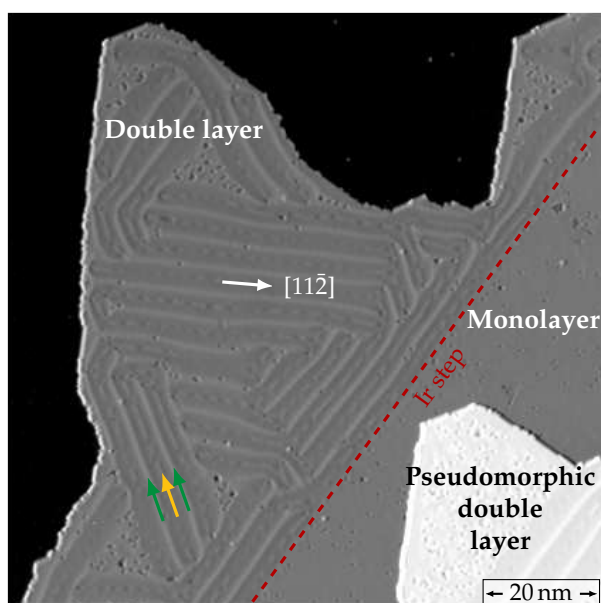


Figure III.5: Constant-current map of a Fe double layer film on Ir(111) showing the dislocation pattern and the pseudomorphic strained areas. Two types of lines alternate in the uniaxially relaxed areas (see the green and yellow arrows). The data was partially differentiated along the scanning direction to improve the visibility of the topographic features. *Measurement parameters:* 200 mV, 1 nA, 4 K, 0 T, W tip.

However, dislocation lines are present in the main part of the Fe double layer film. These lines form in order to relieve the epitaxial strain. They follow the [112] direction of the (111) surface. As indicated by the green and yellow arrows in Figure III.5, two types of lines alternate. The distance between two identical lines is 4.7 nm here. Knowing that the Fe atoms arrangement is going towards a bcc(110)-like stacking

and assuming for simplicity that the Fe monolayer below the double layer stays pseudomorphic, the emergence of this line pattern can be reproduced by a uniaxial compression of the Fe top layer. Figure III.6 shows the atomic structure model resulting from such a compression. Here 18 Fe atoms are placed on top of 17 atoms in the Fe monolayer, which corresponds to a compression of 6% perpendicularly to the  $[11\bar{2}]$  direction. Because of this compression, most of the Fe atoms (in the double layer) are not located in hollow sites. They rather follow a bcc(110)-like stacking indicated by the red unit cell in Figure III.6 and their positions slightly shift from one atom to the other. This leads to the presence of lines along the  $[11\bar{2}]$  in which the atoms are placed in hcp or fcc sites,<sup>2</sup> surrounded by the bcc(110)-like stacked regions. The hcp and fcc lines are expected to be electronically different, which explains the alternating appearance of the lines in Figure III.5. In the real system, a lateral relaxation inducing slight deviations of the positions of the atoms compared to this model is likely to occur.

<sup>2</sup> The atoms in the lines are actually not located exactly in the hollow sites but very close.

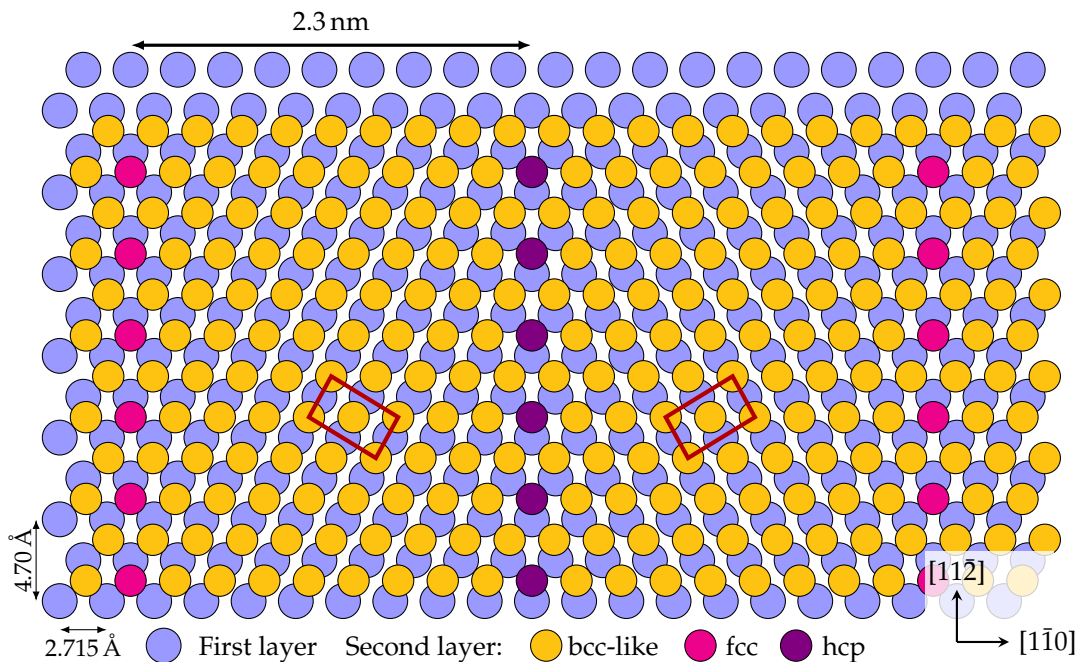


Figure III.6: Atomic structure model of the dislocation line pattern in the Fe double layer on Ir(111). The model is built by keeping the Fe first layer pseudomorphic and adding a uniaxially compressed Fe layer on top, which allows the Fe atoms to arrange in a bcc(110)-like stacking. These bcc(110)-like areas are separated by hcp and fcc lines. The red rectangles show the bcc(110)-like unit cells. In this model, 18 Fe double layer atoms are placed on top of 17 Fe monolayer atoms, which gives a line spacing of 2.3 nm and a compression rate of about 6%.

<sup>3</sup> N. Hauptmann et al. *Physical Review B* 97, 100401 (2018) [90]

<sup>4</sup> P.-J. Hsu et al. *Physical Review Letters* 116, 017201 (2016) [85]

These dislocation lines were also recently studied using a combination of SP-STM and magnetic exchange force microscopy<sup>3</sup> as well as with ab initio calculations. Some atomically resolved images of the structure could be measured and confirmed the model<sup>4</sup> proposed in Figure III.6.

## III.2.2 Details about the spin spirals

The presence of the dislocation lines has a strong influence on the magnetic state of the Fe double layer. In the uniaxially relaxed areas, spin spirals propagate along the dislocation lines whereas in the pseudomorphic strained areas, a disordered magnetic pattern is visible.

### III.2.2.1 Propagation of cycloidal spin spirals along the dislocation lines

A spin-resolved constant-current map of spin spirals in the Fe double layer on Ir(111) is presented in Figure III.8. It appears clearly that the spirals are strictly propagating along the dislocation lines, with a period of about 1.5 nm. In the displayed area, some lines are present along the three equivalent crystallographic directions and the spirals also propagate along these three directions.

The magnetic field dependence of these spirals was investigated. In this case, no change could be observed up to 9 T out-of-plane, as illustrated in Figure III.7. This indicates that there is no accessible skyrmion phase in this system.

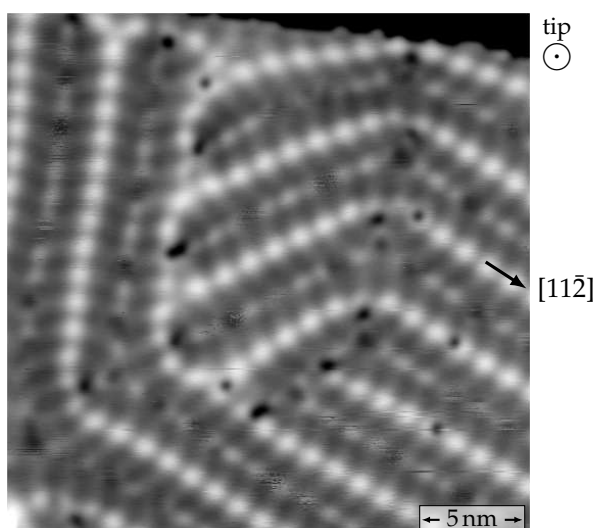


Figure III.8: Spin-resolved constant-current map of spin spirals propagating along the dislocation lines in the Fe double layer on Ir(111). There is a Fe cluster at the end of the W tip which is aligned with the out-of-plane external magnetic field and the tip is thus sensitive to the out-of-plane component of the sample magnetization. *Measurement parameters:* 200 mV, 2 nA, 4 K, 4 T, 4 T, W tip with a Fe cluster at the end.

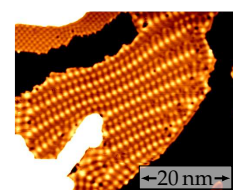


Figure III.7: Spin spirals in the Fe double layer at 9 T, 200 mV, 1 nA.

In order to gain more information about the structure of the spiral, in particular to determine if it is helical or cycloidal, it is necessary to control the magnetic sensitivity of the tip. This can be done with a ferromagnetic tip, the tip sensitivity follows the direction of the applied external magnetic field. In Figure III.8, an out-of-plane magnetic field of 4 T is used in order to measure the out-of-plane component of the

magnetic moments. The magnetic contrast has the same intensity in the three rotational domains, as expected for an out-of-plane sensitive tip.

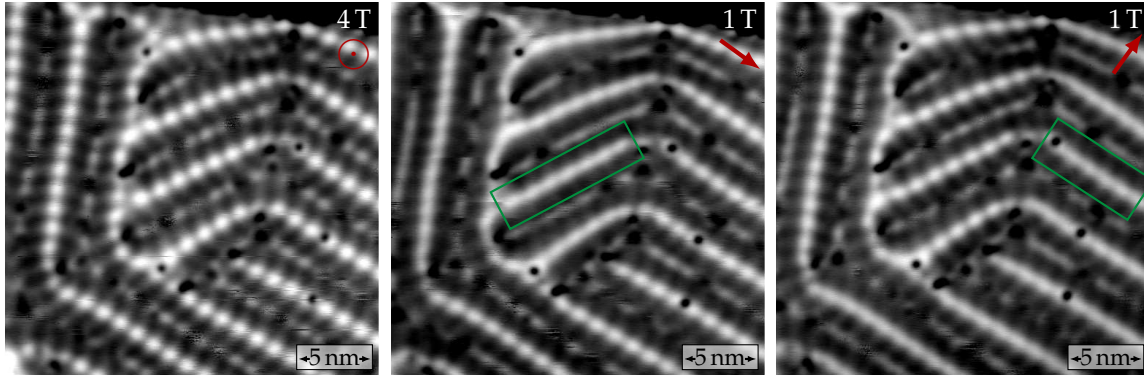


Figure III.9: Spin-resolved constant-current maps of the area displayed in Figure III.8. The direction of the magnetic field is varied from out-of-plane on the left to in-plane (in the direction of the red arrows). The magnetization of the Fe cluster present at the apex of the tip follows the magnetic field and thus the tip is sensitive to the component of the magnetization of the sample which is parallel to the magnetic field. In the images measured with the in-plane sensitive tip, the magnetic contrast vanishes in the direction perpendicular to the field (green boxes), which demonstrates that the spirals are cycloidal. *Measurement parameters:* 200 mV, 2 nA, 4 K, 4 T, W tip.

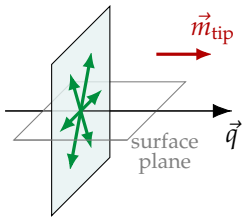


Figure III.10: Geometry of a helical spiral, with the tip magnetization corresponding to a vanishing contrast.

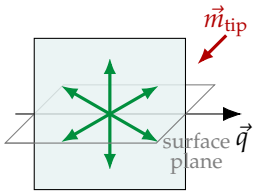


Figure III.11: Geometry of a cycloidal spiral, with the tip magnetization corresponding to a vanishing contrast.

Figure III.9 shows three similar measurements but for which the direction of the magnetic field was modified to change the direction of the tip sensitivity. By comparing the magnetic contrast measured for the three orthogonal tip sensitivity directions, it is possible to determine if the spin spiral is cycloidal or helical. As it is sketched in Figure III.10, in the helical case the magnetic moments stay in a plane which is orthogonal to the wave vector  $\vec{q}$ . The tip magnetization direction indicated here is the one for which the magnetic contrast vanishes because all the magnetic moments are perpendicular to this direction. For a helical spiral, this direction is parallel to  $\vec{q}$ . The same sketch for a cycloidal spiral is shown in Figure III.11. In this case, the magnetic moments stay in a plane which comprises the wave vector  $\vec{q}$  and thus the tip magnetization direction corresponding to a vanishing contrast is perpendicular to  $\vec{q}$ .

In the images in Figure III.9, when the magnetic field is applied in plane, dislocation lines on which the magnetic contrast is very small are marked with the green boxes. Since the tip is sensitive to the magnetization of the sample in the direction of the magnetic field, it appears that the contrast vanishes when  $\vec{m}_{\text{tip}}$  and  $\vec{q}$  are perpendicular. The spin spirals in the Fe double layer on Ir(111) are thus cycloidal. This result was expected because of the large interface-induced DMI at the Fe/Ir interface, which favors cycloids for symmetry reasons.

Not only the propagation direction but also the shape of the wave front of the spirals is influenced by the local arrangement of the Fe atoms. Figure III.12 shows two spin-resolved constant-current maps measured with an out-of-plane and an in-plane sensitive tip. In the image (c), the spirals are visible everywhere and it appears that their wave front is not

straight and perpendicular to the lines but has a zigzag shape. When the tip is in-plane sensitive in the direction shown in the image (d), half the spiral vanishes. The tip magnetization direction is indeed perfectly perpendicular to the wave vector on one side of the zigzag but not on the other side. This means that the magnetic moments rotate in a different plane (perpendicular to the wave front) depending on the branch of the zigzag. The magnetic state is not a perfect cycloidal spiral with all the moments rotating in the same plane but it is three-dimensional. A sketch of the corresponding spin structure is shown in the image (b).

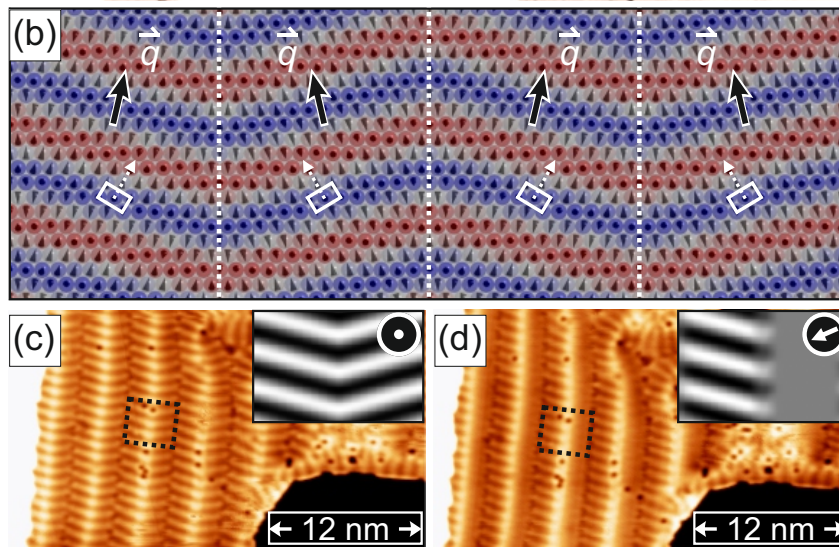


Figure III.12: (b) Sketch of the spin spiral along the dislocation lines in the Fe double layer, as deduced from the SP-STM measurements. (c),(d) Spin-resolved constant-current maps of the zigzag shape of the spin spiral wave front, measured with an out-of-plane and in-plane spin-sensitive tip, respectively. The corresponding SP-STM simulations are in the insets. *Measurement parameters:* 500 mV, 1 nA, 8 K, 2.5 T, Cr bulk tip. Extracted from [85], copyright 2016 by the American Physical Society.

This alternating direction of the wave vector  $\vec{q}$  is induced by the stacking of the Fe atoms. Coming back to the structure model from Figure III.6, it appears that there is a correlation between the canting of the wave vector  $\vec{q}$  and the orientation of the bcc-like unit cells (red rectangles) which alternate in the regions between the hcp and fcc lines. Previous works about the Fe double layer on Cu(111)<sup>5</sup> and the Fe double layer on W(110)<sup>6</sup> found that the wave vector of the spin spirals prefers to follow the rows of atoms created by the bcc(110) stacking, the bcc[001] direction. The wave vectors of the spirals in the Fe double layer on Ir(111) seem to have the same behavior.

This effect can be explained by the influence of Heisenberg exchange interactions in an anisotropic atomic arrangement<sup>7</sup> or by the direction of the DM vector<sup>8</sup>. However, in the Fe double layer on Ir(111), the wave vector does not follow exactly this crystallographic direction, probably because of the competition between the formation of a straight spiral

<sup>5</sup> S.-H. Phark et al. *Nature Communications* 5 (2014) [87]

<sup>6</sup> S. Meckler et al. *Physical Review Letters* 103, 157201 (2009) [91]

<sup>7</sup> E. Vedmedenko et al. *Physical Review Letters* 92 (2004) [92]

<sup>8</sup> M. Heide et al. *Physical Review B* 78, 140403 (2008) [30]

wave front and the alignment of  $\vec{q}$  along the bcc[001] direction.

### III.2.2.2 Magnetic modulation in the pseudomorphic strained areas

Besides the areas exhibiting dislocation lines, there are some strained pseudomorphic areas in the Fe double layer on Ir(111) (see Figure III.5). Using a spin-sensitive STM tip, a disordered magnetic structure is also visible in these regions. Figure III.13 shows an area with some dislocation lines (top of the image) and a pseudomorphic region (bottom of the image) measured with a spin-averaging tip and a spin-sensitive tip. The comparison of the two images reveals the disordered magnetic pattern in the pseudomorphic region. Here there is no line to guide the propagation of the spirals and the magnetic state is thus an assembly of randomly oriented spiral fragments. The increased density of impurities in these areas also contributes to add disorder to the structure. The period of this magnetic modulation can be estimated using a Fourier transform and appears to be slightly smaller than along the lines, around 1.2 nm. This difference might arise from the strain, which is not relaxed in these regions.

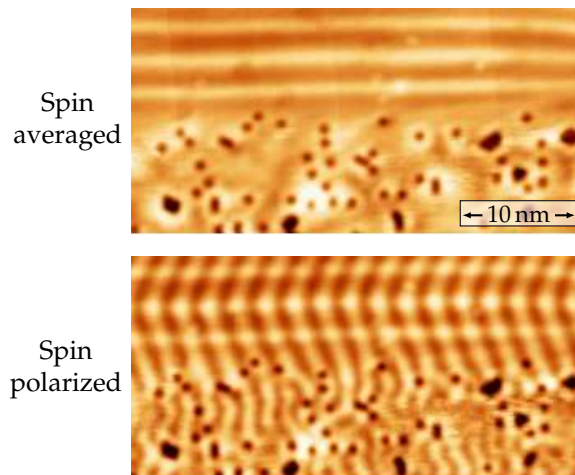


Figure III.13: Constant-current maps of some dislocation lines (top of the images) and a strained pseudomorphic area (bottom of the images) in the Fe double layer on Ir(111), using either a spin-averaging tip (top) or a spin-sensitive tip (bottom). A comparison between the two measurements shows that there is a magnetic modulation in the pseudomorphic area. *Measurement parameters:* 200 mV, 1 nA, 8 K, 1.55 T, W tip.

### III.3 Determination of the tip magnetic sensitivity using spin spirals

The reasoning explained in section III.2.2.1 allowed to demonstrate that the spin spirals are cycloidal, knowing the direction of the tip magnetization. Now that the cycloidal nature of the spirals is established, the argument can be reversed in order to determine the direction of the tip sensitivity<sup>1</sup>.

#### III.3.1 Spiral model

A further study, also making use of the ability to apply a magnetic field in any direction to control the magnetic sensitivity of the tip, demonstrated that the spirals have a clockwise rotational sense,<sup>2</sup> which is in agreement with ab initio calculations<sup>3</sup> for the Fe monolayer. A clockwise cycloidal spin spiral can be described in the following way:

$$\vec{m}(r) = \cos(qr) \hat{e}_z + \sin(qr) \hat{e}_q \quad (\text{III.1})$$

where  $\vec{m}$  is the normalized magnetic moment,  $q = 2\pi/\lambda$ , with  $\lambda$  the period of the spiral and  $\hat{e}_q$  its propagation direction. The measured SP-STM signal is proportional to the projection of the magnetization of the sample on the direction of the magnetization at the tip apex  $\vec{m}_{\text{tip}}$  (see section II.2.2). The magnetic signal measured along the propagation direction can thus be written as:

$$\vec{m}_{\text{tip}} \cdot \vec{m}(r) = \cos(qr) \sin \varphi + \sin(qr) \cos \theta \cos \varphi \quad (\text{III.2})$$

where the angles  $\theta$  and  $\varphi$  are defined in Figure III.14. In order to find the orientation of the tip magnetization (determined by  $\theta$  and  $\varphi$ ) for a given measurement, one needs to fit jointly the line profiles of the spirals along the three directions of propagation. The fitting function is the following:

$$\Delta z(r) = A [\cos(qr + \psi) \sin \varphi + \sin(qr + \psi) \cos \theta \cos \varphi] \quad (\text{III.3})$$

where  $A$  is an amplitude factor,  $q$ ,  $\theta$  and  $\varphi$  are defined as before and  $\psi$  is a phase allowing to align laterally the different profiles in the same image because the choice of the position where  $r = 0$  has to be consistent for all of them. With  $\psi = \arctan\left(\frac{\cos \theta}{\tan \varphi}\right)$ ,  $r = 0$  can be chosen as a local extremum for all the profiles. There are thus four free fitting parameters  $A$ ,  $q$ ,  $\theta$  and  $\varphi$ , the same for the three profiles measured on the image. Note that the value of  $\theta$  depends on the propagation direction of the spiral. The angle between the dislocation lines has to be extracted from the data and the value of  $\theta$  needs to be shifted accordingly for each spiral. The fitting itself is performed using a least square method.

<sup>1</sup> Only the axis of the tip sensitivity can actually be derived, one cannot decide between sensitivities corresponding to  $\pm \vec{m}_t$

<sup>2</sup> L. Schmidt. PhD thesis. Universität Hamburg, 2017 [93]

<sup>3</sup> S. Heinze et al. *Nature Physics* 7, 713–718 (2011) [27]

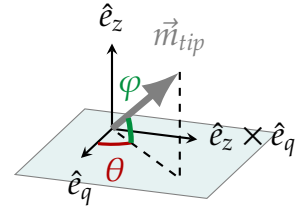


Figure III.14: Definition of  $\theta$  and  $\varphi$  in equation III.2

### III.3.2 Data fitting

The procedure explained above can be applied to the data from Figure III.9 in order to check that the Fe cluster at the end of the tip really aligns perfectly with the magnetic field. These images are reproduced in Figure III.15 and the spirals used for the fit are marked with the colored boxes.

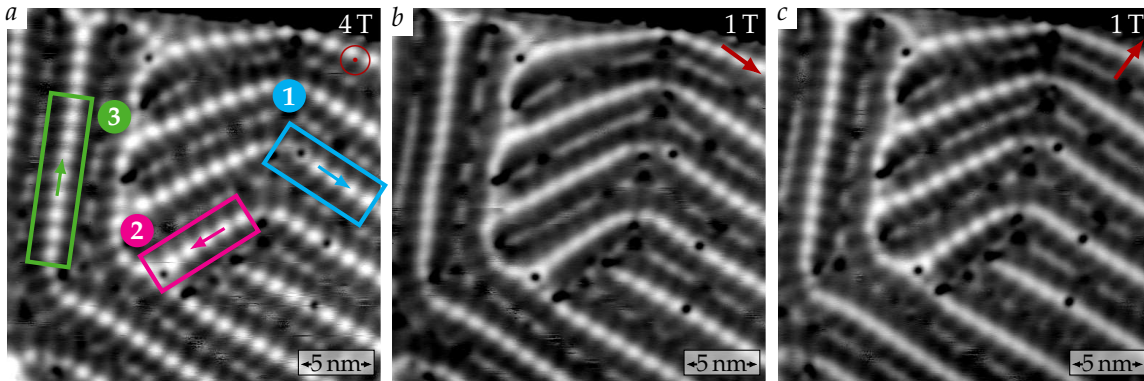


Figure III.15: Spin-resolved constant-current maps of spin spirals propagating along three directions. The direction of the magnetic field is varied from out-of-plane (*a*) to in-plane (*b, c*, field in the direction indicated by the red arrows). The spirals used for the fit are marked with the colored boxes. *Measurement parameters:* 200 mV, 2 nA, 4 K, 4 T, W tip.

The results of the fitting procedure are gathered in Figure III.16. The angle measured between the spirals 1 and 2 is  $\Delta\theta_2 = -116^\circ$  and between the spirals 1 and 3,  $\Delta\theta_3 = 114^\circ$ . They are deviating from  $120^\circ$  because the dislocation line pattern is not perfect, in particular because of the presence of defects. The values of the  $\theta$  angle of the tip magnetization are also given using the propagation direction of the spiral 1 as a reference. The fitted function gives a rather good agreement with all the profiles. The period found is the same for the three images, which is expected. The amplitude can vary because the tip might have changed between the measurements. Concerning the angles  $\theta$  and  $\varphi$ , the results of the fit indicate that the magnetization at the end of the tip really follows the applied magnetic field. In the image *a*,  $\varphi$  is close to  $90^\circ$  for an out-of-plane field whereas in the images *b* and *c*,  $\varphi$  is very small, which indicates an in-plane sensitivity, as expected. Concerning the in-plane orientation of the tip,  $\theta$  is very small in image *b*, which means that the magnetization is parallel to the propagation direction of the spiral 1. This observation is in good agreement with the indicated direction of the magnetic field. In image *c*,  $\theta$  reaches  $-112^\circ$ , which is not exactly in the direction of the magnetic field but still not too far from the correct direction. In this case the tip magnetization did not align completely with the field. The method detailed here can be used to determine the direction of the magnetic sensitivity of a tip when it is unknown, for example when no magnetic field is applied or for an antiferromagnetic Cr bulk tip. The only requirement is to have at least two, preferably three spirals with different

propagation directions imaged with the very same tip. The guiding of the spin spirals by the dislocation lines make the Fe double layer on Ir(111) a very convenient system for this type of analysis since the wave vector of the spirals remains fixed over large distances.

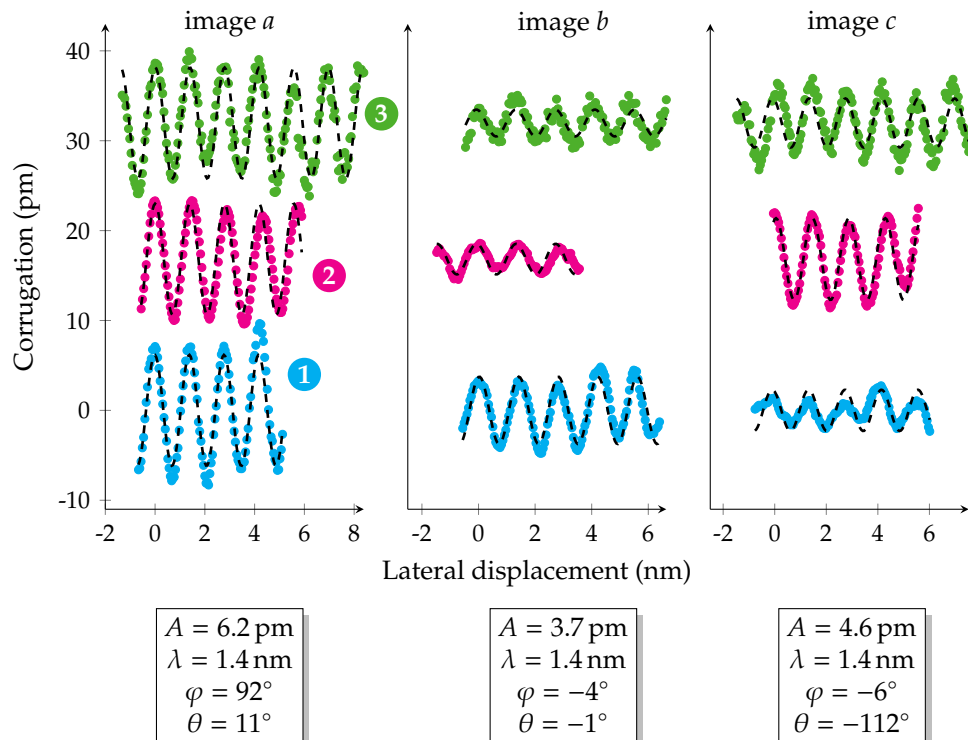


Figure III.16: Results of the fitting procedure applied to the three spirals indicated in Figure III.15. The colored dots are the data points and the black dashed line the fitted function, the profiles of the different spirals are shown with offsets. The free parameters obtained from the fit are indicated below the plots, the reference for the value of  $\theta$  is the propagation direction of the spiral 1. The direction of the tip magnetization appears to follow rather reliably the direction of the magnetic field.

In the following, the direction of the magnetic sensitivity of the tips will be determined based on this principle, although the detailed fitting is often not necessary.



## IV. Detailed investigation of the effects of strain, temperature and electric field on the triple layer Fe on Ir(111)

This chapter is devoted to the detailed study of the magnetic state in the Fe triple layer on Ir(111). Similarly to what was observed in the Fe double layer, spin spirals propagate along the dislocation lines but the situation is more complex in the triple layer because two types of lines coexist and the strain relief is not uniform.<sup>1</sup> This feature of the system will be investigated in section IV.1. Furthermore, because of the increased amount of magnetic material, the temperature stability of the magnetic state is expected to be enhanced with respect to the Fe monolayer and double layer. Section IV.2 presents an investigation of the temperature dependence of the spin spirals, which reveals that indeed they are stable up to room temperature and that their period is surprisingly largely increased.<sup>2</sup> Under the application of an out-of-plane magnetic field, the spin spirals split up into magnetic skyrmions, which can be manipulated using the electric field created by the STM tip.<sup>3</sup> This work is detailed in section IV.3.

*The low temperature measurements presented here were performed jointly with Pin-Jui Hsu and I measured the temperature dependent data. I analyzed the strain effects and the temperature dependent data. The theoretical model concerning the temperature dependence was developed by Levente Rózsa. The study about the electric field switching is a joint work, I did not perform the switching experiments but contributed to its analysis.*

<sup>1</sup> A. Finco et al. *Physical Review B* 94, 214402 (2016) [88]

<sup>2</sup> A. Finco et al. *Physical Review Letters* 119, 037202 (2017) [94]

<sup>3</sup> P.-J. Hsu et al. *Nature Nanotechnology* 12, 123–126 (2017) [95]

## IV.1 Strain relief effects

In this section, the effect of the uniaxial strain relief on the magnetic state of the Fe triple layer on Ir(111) is investigated. The Fe triple layer film exhibits a dense network of dislocation lines which dictate the propagation direction of the spin spirals, similarly to the double layer case. In the triple layer case, the spacing between the dislocation lines is not the same everywhere on the surface, which means that the strain is not equally relieved in the film. This inhomogeneity of the strain relief turns out to have a noticeable influence on the spin spiral period.<sup>1</sup>

<sup>1</sup> A. Finco et al.  
*Physical Review B*  
94, 214402 (2016)  
[88]

### IV.1.1 Known effects of strain on non-collinear magnetism

Strain can modify magnetic states through various mechanisms, in particular by making magnetic interactions anisotropic. Depending on the studied system, there are two ways to apply strain on a sample. For bulk systems, the strain is applied mechanically whereas for thin and ultrathin films, the strain is epitaxial and controlled by the choice of the substrate. It is also possible to use a piezoelectric substrate to tune the epitaxial strain by applying a voltage on the substrate<sup>2</sup>. This section gathers some results from the literature about the changes induced by strain on non-collinear states such as domain walls, spin spirals and skyrmion lattices.

<sup>2</sup> J. Cui et al.  
*Applied Physics Letters* 103, 232905  
(2013) [96]

#### IV.1.1.1 Mechanical strain

Strain can be applied to the skyrmion lattice phase in B20 compounds like FeGe or MnSi. In these experiments, the sample undergoes a physical compression or expansion along one direction.

In MnSi, compressive uniaxial strain was applied using a system of pistons.<sup>3</sup> If a transverse strain is applied at a temperature slightly below the one where the skyrmion lattice usually appears, it stabilizes the skyrmion phase. The application of a transverse strain (along the [110] direction) thus allows to increase the size of the skyrmionic phase in the phase diagram. On the contrary, when a longitudinal strain is applied (along the [001] or the [111] directions) the skyrmion phase shrinks or even collapses. In both cases, only several tens of MPa are required to induce a noticeable effect, which is achievable using the tip of a cantilever. The mechanism leading to the stabilization or annihilation of the skyrmion phase is the emergence of an in-plane effective magnetic anisotropy perpendicular to the strain axis. This effective anisotropy term arises from the magnetoelastic coupling.

<sup>3</sup> Y. Nii  
et al. *Nature Communications*  
6, 8539 (2015) [97]

A different observation was made in a thin FeGe plate under the application of uniaxial tensile strain.<sup>4</sup> The plate is attached to a Si holder and because of the different thermal expansion coefficients between FeGe and Si, a tensile strain is exerted on the FeGe plate when the setup is

<sup>4</sup> K. Shibata  
et al. *Nature Nanotechnology*  
10, 589–592 (2015)  
[98]

cooled down. Lorenz transmission electron microscopy measurements revealed that the skyrmion lattice is strongly distorted, the skyrmions are elongated in the direction of the expansion of the sample. In this case, the modification is attributed to an anisotropic modulation of the DMI strength. This interpretation is confirmed by ab initio calculations performed for  $\text{Mn}_{1-x}\text{Fe}_x\text{Ge}$ .<sup>5</sup>

#### IV.1.1.2 Epitaxial strain

Using epitaxial growth is a simple way to study the effects of strain on thin and ultrathin films, although the only way to control its strength and its orientation is to change the substrate (unless it is piezoelectric). Mössbauer and Raman spectroscopy experiments performed on thin films of the multiferroic compound  $\text{BiFeO}_3$  indicate that the cycloidal modulation of the antiferromagnetic state present in the bulk state vanishes when the film is too much strained.<sup>6</sup> The films were grown on several substrates corresponding to various lattice mismatches and the cycloid could only be observed in the cases where the lattice mismatch did not exceed 0.5%. Here the modification of the state with strain can be explained by adding a magnetoelastic energy term to the free energy which competes with the other energy terms to remove the cycloidal modulation.

In metallic ultrathin films like  $\text{Fe}/\text{Ni}/\text{W}(110)$ , the in-plane anisotropic strain resulting from the lattice mismatch induces an in-plane uniaxial magnetic anisotropy along the  $[001]$  direction via magnetoelastic coupling. This additional anisotropy term has an effect on the structure of the domain walls.<sup>7</sup> Depending on their orientation with respect to the  $[001]$  direction, the domain walls are either of Néel or Bloch type. In the case of a free-standing  $\text{Fe}(110)$  monolayer, ab initio calculations have shown that in-plane strain can induce a transition from a ferromagnetic state to a spin spiral state.<sup>8</sup> The transition is driven by the frustration of the exchange couplings in the presence of strain. This indicates that the strain can affect not only the magnetic anisotropy or the DMI but also the exchange interaction.

### IV.1.2 Two types of dislocation lines inducing changes in the shape of the spirals

#### IV.1.2.1 Structure model

As mentioned previously, a dense network of dislocation lines is created in the Fe triple layer on  $\text{Ir}(111)$  to relieve the large epitaxial strain. The lines form along the three equivalent  $[11\bar{2}]$  directions of the  $(111)$  surface, similarly to the case of the Fe double layer. However, only one type of dislocation is present in the double layer: the alternating hcp and fcc lines as described in the model from Figure III.6. In the triple layer, the situation is more complicated because there are two types of dislocation

<sup>5</sup> T. Koretsune et al. *Scientific Reports* 5, 13302 (2015) [99]

<sup>6</sup> D. Sando et al. *Nature Materials* 12, 641–646 (2013) [100]

<sup>7</sup> G. Chen et al. *Nature Communications* 6, 6598 (2015) [101]

<sup>8</sup> T. Shimada et al. *Physical Review B* 85 (2012) [102]

line patterns. Figure IV.1 shows a constant-current map of a triple layer film measured at 200 mV. Here a clear difference between two types of lines appears.

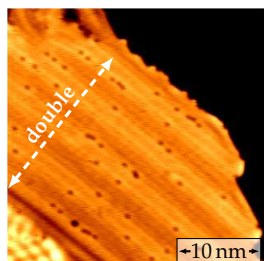


Figure IV.2:  
Zoom-in on a  
double line area  
at 200 mV, 1 nA.

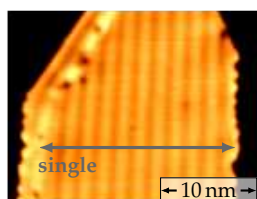


Figure IV.3:  
Zoom-in on a  
single line area  
at 200 mV, 1 nA.

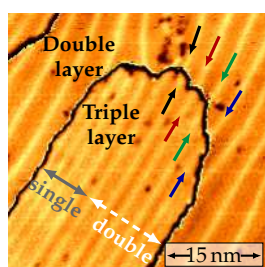


Figure IV.4:  
Alignment of the  
lines in the Fe  
double and triple  
layer. Contrast  
adjusted separately  
for the terraces,  
-700 mV, 1 nA.

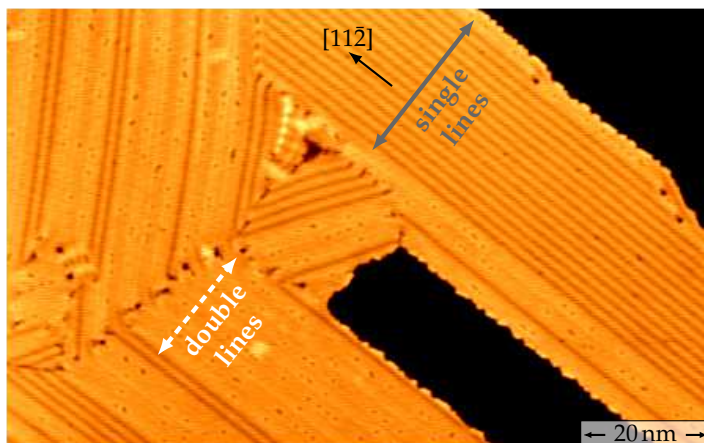


Figure IV.1: Constant-current map of a Fe triple layer film on Ir(111) showing the difference between the single and the double line areas (indicated with the arrows).  
Measurement parameters: 200 mV, 1 nA, 5 K, 3.5 T, W tip.

In the region spanned by the white dashed arrow, the lines show an alternating bright and dark contrast and a double line feature. A closer view on this type of area is shown in Figure IV.2. These lines will be named *double lines*. The spacing between them is ranging from 2.3 nm to 3 nm.

On the other hand, in the region marked with the gray arrow, all lines have the same appearance and they are denser, with a spacing between 1.8 nm and 2.2 nm. They are thus designated as *single lines*. Figure IV.3 displays a zoom-in on a single line area.

At negative sample bias voltage, the two types of lines are indistinguishable, which is the case in the constant-current map showing an overview of the film morphology in Figure III.1 in chapter III.

Atomic structure models (based on the same principle as the one proposed in Figure III.6) for the double and the single line areas are given in Figures IV.5 and IV.6, respectively. The first step is to determine the relative position of the lines in the double and in the triple layer.

Figure IV.4 displays a triple layer island on top of the Fe double layer. The contrast was adjusted separately for the two terraces in order to show that the double lines in the triple layer are exactly located on top of the lines in the double layer. In contrast, the single lines rather seem to be placed on top of pseudomorphic double layer areas.

These observations lead to the model proposed in Figure IV.5 for the double lines. The first Fe layer stays pseudomorphic and the second Fe layer is compressed uniaxially in the same way as in the model describing the lines in the double layer. Hence hcp and fcc lines are alternating. The third Fe layer is placed on top of the second layer so that the Fe atoms follow the bcc(110)-like stacking which is defined by the second layer.

The exact position of the Fe atoms at the lines (gray atoms) is not clear and was chosen to look realistic. Furthermore, the amount of impurities and defects is much larger on the lines than in the other areas, suggesting that the arrangement of the atoms might be not completely regular along these lines. On average, the stacking of the Fe atoms is getting closer to a bcc(110) stacking, but the orientation of the bcc unit cell is alternating every time a line is crossed, like in the Fe double layer. The double line regions thus have mirror planes along the dislocation lines.

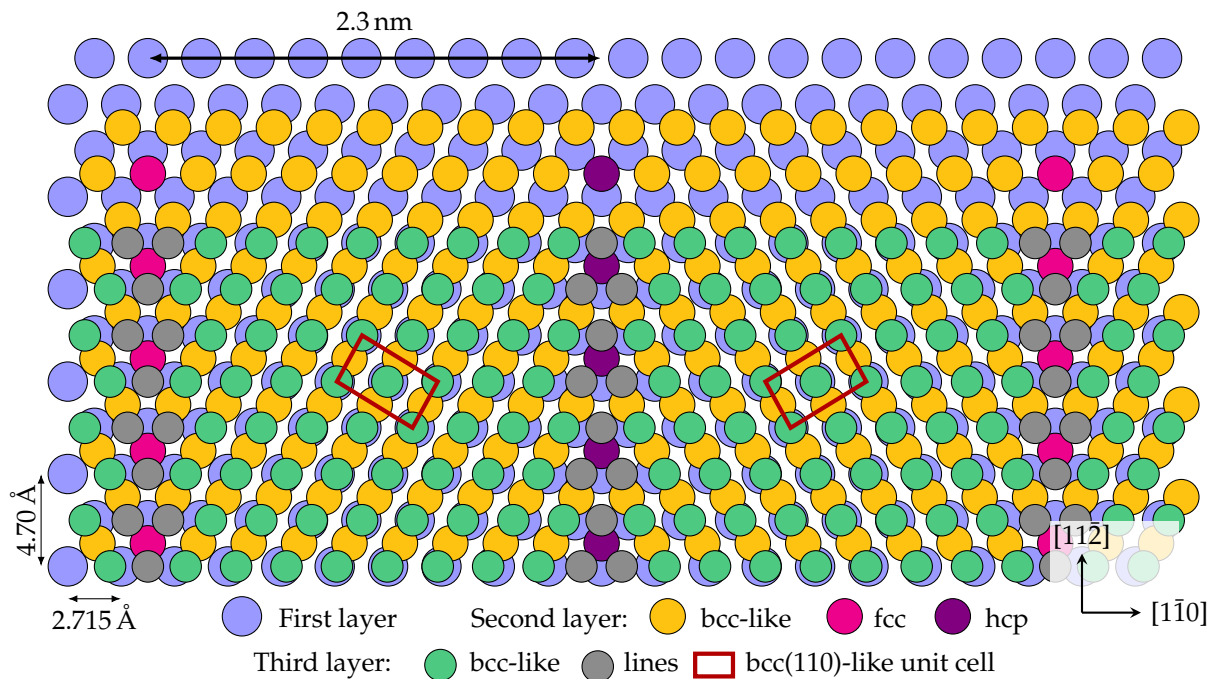


Figure IV.5: Proposed atomic structure model (top view) for the double line areas, based on the experimental observations detailed in the text.

In the case of the single line areas, the second Fe layer seems to be pseudomorphic but in the model proposed in Figure IV.6, the Fe atoms are not placed in the hollow sites but in the bridge sites, to form a bcc-like stacking. This assumption was made in order to avoid the alternating orientation of the bcc-like rows in the upper layer, which is always present if the atoms of the lower layer are placed in the hollow sites. The third Fe layer is then uniaxially compressed and in order to keep the bcc-like stacking, lateral shifts of some atoms are introduced, which form the dislocation lines. In this case, all the lines are identical. There is no mirror plane in this structure, and the bcc unit cells are all oriented in the same direction. However, a mirror symmetric structure can be formed by choosing different bridge sites for the Fe atoms in the second layer. As it will be shown in the next section using the wave front of the spin spirals, both structures can be found in the data.

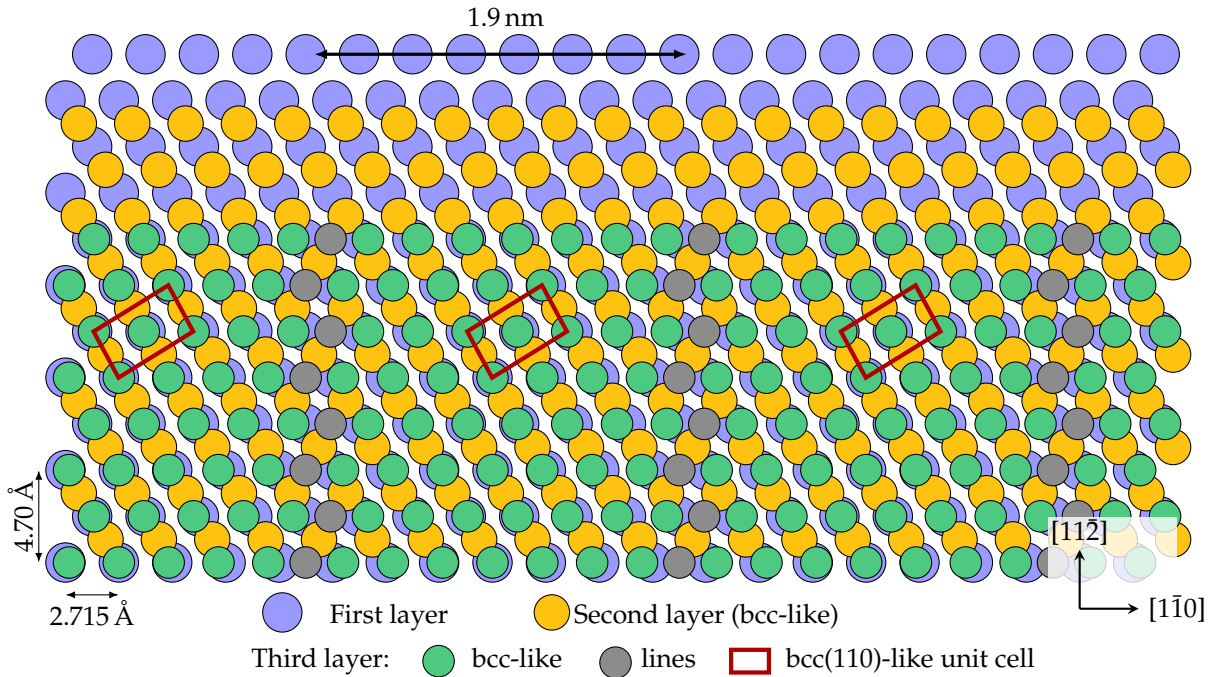


Figure IV.6: Proposed atomic structure model (top view) for the single line areas, based on the experimental observations detailed in the text.

#### IV.1.2.2 Influence of the atom arrangement on the spin spirals

Figure IV.7 shows a constant-current map and the simultaneously recorded differential conductance map of a Fe triple layer region with both double and single line areas (images *a* and *b* respectively). In the constant-current map, at  $-700$  mV, there is almost no difference between the two types of dislocation lines. However, the spirals look very different. The first striking difference is their period. In the double line areas, the period is between 3 and 4.5 nm whereas it is larger in the single line areas, between 5 and 10 nm.

Furthermore, the shape of the spiral wave front depends on the dislocation lines. In the Fe double layer, the wave front of the spirals has a zigzag shape because of the alternating orientation of the bcc unit cell (see section III.2.2.1). A similar effect is found in the double line areas, a detailed view is shown in image *c*. In the single line areas, the wave front of the spiral is straight but canted and not perpendicular to the dislocation lines. In both cases, the explanation is the same as for the Fe double layer. The wave vectors of the spirals prefer to follow the bcc[001]-like rows of atoms. In the double line structure, these rows alternate, which produces the zigzag shape of the wave front. In the single line areas, the direction of the rows is fixed but two mirror symmetric structural domains are possible and found in the data (see image *b*). The measured angle between the wave front and the dislocation lines is slightly varying depending on the considered areas and usually slightly larger than  $60^\circ$ , as indicated in Figure IV.7. For a strict coupling of

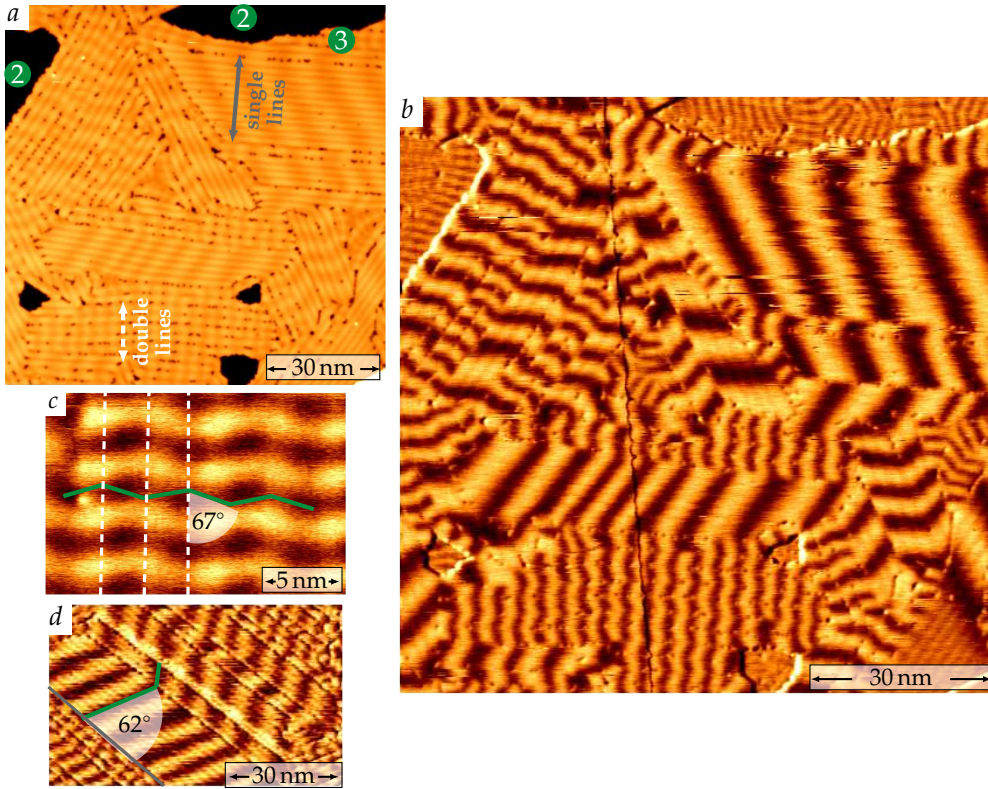


Figure IV.7: Constant-current map (image *a*) and simultaneously recorded spin resolved differential conductance map (image *b*) of a Fe triple layer film on Ir(111). The difference between the two types of dislocation lines appears clearly when looking at the spin spirals. Close views of the spirals are shown in *c* (double lines) and *d* (single lines). Their period is larger in the single line areas and the shape of their wavefront is different. *Measurement parameters:*  $-700$  mV, *a, b, d:* 1 nA, *c:* 0.75 nA, *a, b, d:* 8 K, *c:* 4 K, 0 T.

the wave vector to the bcc[001] direction, the structure models proposed in Figures IV.5 and IV.6 allow to compute the expected angle  $\alpha$  between the wave front and the lines. For both structures,

$$\tan \alpha = \frac{\sqrt{3}\delta}{\delta + a} \quad (\text{IV.1})$$

where  $\delta$  is the line spacing and  $a = 2.715 \text{ \AA}$  the nearest-neighbor distance between the atoms on the Ir(111) surface. For the single line areas, Figure IV.8 shows the comparison between the measured angle and the one predicted by this formula. Obviously, the measured angle is larger than the expected one. In the Fe double layer, a similar behavior is observed and is explained by the competition of the coupling of the wave vector to the atomic structure with the energy of the kinks in the spiral wave front. However, this argument does not apply to the single line case. Here, the deviation towards larger angles means that the wave front direction is more perpendicular to the lines than expected. This might result from boundary effects or domain-wall-like structures minimizing their length.

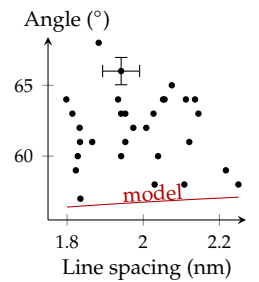


Figure IV.8: Dependence of the wave front angle on the line spacing, in single line areas. Typical error bars are given for one of the points.

### IV.1.3 Correlation between the dislocation line spacing and the spin spiral period

Besides the modification of the spin spiral wave fronts by the local arrangement of the Fe atoms, another question arises from the data presented in Figure IV.7: why does the period of the spirals vary so much in the different areas of the sample?

A first indication is given by Figure IV.9. It displays a single line area from Figure IV.7 in which the period of the spiral varies. The variation of the period seems to be correlated with the spacing between the dislocation lines, indicated by the numbers at the top. Here the line spacing is changing because of the shape of the adjacent area, dictated by the presence of defects. The period of the spiral decreases when the line spacing increases.

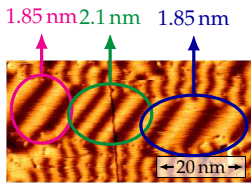


Figure IV.9: Variation of the spiral period in a single line area. The line spacing is indicated for each zone.

A more systematic study was carried out to check if there is really a clear correlation between the spiral period and the line spacing. The result is displayed in the graph from Figure IV.10: the correlation observed between the period of the spirals and the dislocation line spacing is clearly confirmed.

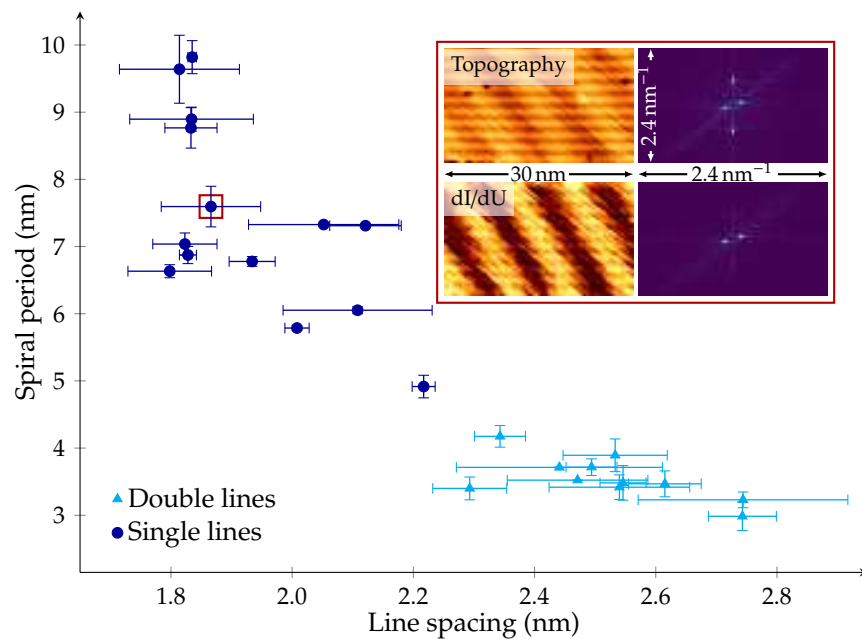


Figure IV.10: Dependence of the period of the spin spirals on the spacing between the dislocation lines, in both the double and single line regions at low temperature (4 to 8 K). The periods were extracted using 2D Fourier transformation and fits of the real-space data to sine functions. Only points with an error bar below 15% were kept. The data in the inset correspond to the point marked with the red square.

In order to produce this graph, a large number of single and double line regions were selected, from measurements performed on several different samples. The inset displays a typical selected region. The spacing between the dislocation lines is determined from the constant-current

map whereas the period of the spin spirals is obtained from the differential conductance map. In both cases, the period is measured by two methods. The first one is a 2D Fourier transform (as shown in the inset). The error bar corresponds to an interval of one pixel around the peak position in both directions. The second method is a simple fit of every row or column of the map with a sine function, and the error bar is the standard deviation. The zigzag shape of the wavefront is not included in the measurement and the period is measured along the lines. The actual wavelength along the direction of the wave vector might be 10% smaller. For the single line areas, the values on the graph take into account the angle between the spiral wave front and the lines. In the end, only the data points with an error bar below 15% were kept because for example the presence of too many defects or confinement in very small areas can create deviations.

Hence the period of the spin spirals becomes larger when the dislocation line spacing decreases. Although a precise relationship is difficult to define,<sup>9</sup> the dislocation line spacing is a measure of the strain relief in the film. A reduction of the distance between the lines corresponds to a reduction of the substrate-induced expansion of the top Fe layers. The mean value of the distance between the Fe atoms in the fcc[110] direction is thus reduced, it is 5% smaller for a line spacing of 1.8 nm than for 3 nm (from the structure models presented in Figures IV.5 and IV.6). The variation of the line spacing all over the surface shows that the strain relief is not uniform in the Fe triple layer on Ir(111). Several factors could be responsible for this non-uniformity: the amount of defects and their nature, the geometry of the islands, etc.

#### IV.1.4 Simple 1D micromagnetic analysis

The strengths of the magnetic interactions usually depend on the relative positions of the atoms, which means that the modulations of the strain relief are expected to induce modulations of the magnetic parameters.<sup>10</sup> The relevant energy contributions in the Fe triple layer on Ir(111) are those from the exchange couplings, the DMI and the effective magnetic anisotropy. The interplay between these three terms allows to stabilize non-collinear states.<sup>11</sup>

The DMI originates mainly from the interface between the Fe film and the Ir substrate.<sup>12</sup> Since the first Fe layer is pseudomorphic on the whole surface, regardless of the type or the spacing of the dislocation lines formed on top, the effect of the strain relief variation on the DMI should not be very large.

If the effective anisotropy has a pronounced effect, this should be visible in line profiles of the spin spirals. Indeed, if there is a large enough effective out-of-plane anisotropy in the system, the spirals are inhomogeneous (see section II.1.1.1) and their profile should deviate from a sine function. Figure IV.11 provides an example of a profile for an

<sup>9</sup> D. Sander et al. *Physical Review B* 57, 1406–1409 (1998) [103]

<sup>10</sup> J. Hagemeister et al. *Physical Review B* 94, 104434 (2016) [104]

<sup>11</sup> K. von Bergmann et al. *Journal of Physics: Condensed Matter* 26, 394002 (2014) [32]

<sup>12</sup> A. Fert et al. *Physical Review Letters* 44, 1538–1541 (1980) [105]

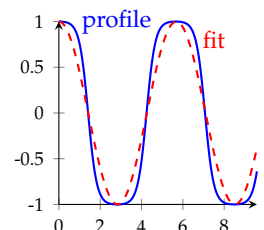


Figure IV.11: Profile of a strongly inhomogeneous spin spiral compared with a sine function.

inhomogeneous spiral compared with a sine function.

Figure IV.12 shows six line profiles of the spin spirals in the Fe triple layer extracted from the differential conductance map on the left. They correspond to various areas with different line spacings and spiral period. Each profile is fitted with a sine function and the agreement is very good. This indicates that the effective out-of-plane magnetic anisotropy does not have a large influence on the spiral state. It is thus small enough to be neglected, although it is known that epitaxial strain creates an effective anisotropy via magnetoelastic coupling in ultrathin films.<sup>13</sup>

<sup>13</sup> P. Bruno et al.  
*Applied Physics A*  
49, 499–506 (1989)  
[106]

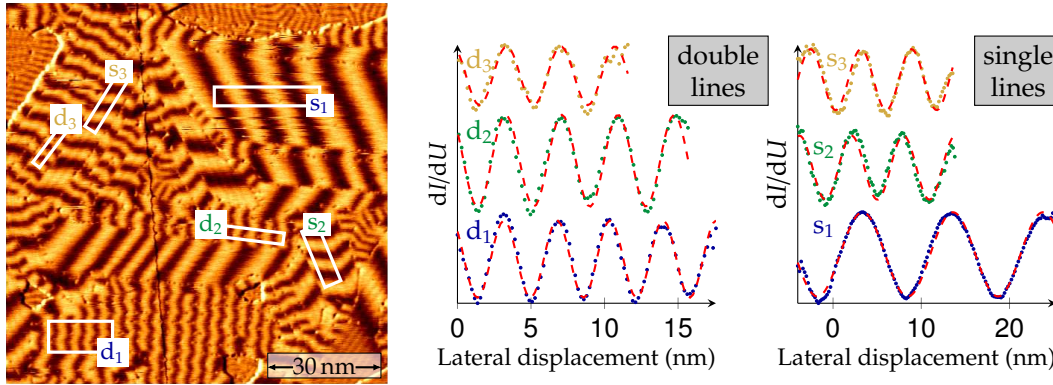


Figure IV.12: Spin resolved differential conductance map of a Fe triple layer film on Ir(111) and line profiles of the spin spirals extracted at the positions marked by the rectangles. The red dashed lines are fits to a sine function. The good agreement between the profile and the fit demonstrates that the magnetic anisotropy is negligible in the system. *Measurement parameters:*  $-700$  mV,  $1$  nA,  $8$  K,  $0$  T, Cr bulk tip.

These considerations lead to the assumption that the strain variations are modifying the exchange couplings, as it was found theoretically for a free-standing Fe layer.<sup>14</sup> The magnitude of the strain effect can be estimated from the change in the spiral period using a simplified one-dimensional micromagnetic model inspired from the one proposed by Bogdanov and Hubert to study the stabilization of skyrmions.<sup>15</sup> Only an effective isotropic exchange coupling and a DMI are included and the non-uniformity of the film is ignored. The goal is only to find how much the effective exchange needs to be modified in order to reproduce the variations of the spin spiral period. The energy density is thus:

$$\mathcal{E} = A \sum_i \left( \frac{\partial \vec{m}}{\partial x_i} \right)^2 + D \left( m_z \frac{\partial m_x}{\partial x} - m_x \frac{\partial m_z}{\partial x} \right) \quad (\text{IV.2})$$

where  $A$  is the exchange stiffness,  $D$  the DMI constant and  $\vec{m}$  the reduced dimensionless magnetization. In this particular case, there is always a stable cycloidal spin spiral state in the system and its period  $\lambda$  is simply:

$$\lambda = 4\pi \frac{A}{|D|} \quad (\text{IV.3})$$

For the monolayer Fe on Ir(111), the value of the DMI constant from ab initio calculations is  $d = -1.8$  meV per atom.<sup>16</sup> This value needs to be

<sup>14</sup> T. Shimada  
et al. *Physical Review B* 85 (2012)  
[102]

<sup>15</sup> A. Bogdanov  
et al. *Journal of Magnetism and Magnetic Materials*  
138, 255–269  
(1994) [33]

<sup>16</sup> S. Heinze  
et al. *Nature Physics* 7, 713–718  
(2011) [27]

converted in  $\text{mJ m}^{-2}$  for a three-layer-thick film. In the case of the fcc(111) surface, one has to sum the contributions over the six nearest-neighboring atoms and divide by the volume per interface atom.<sup>17</sup>  $D$  and  $d$  are thus linked by the following equation:

$$D = \frac{3\sqrt{2}d}{na^2} \quad (\text{IV.4})$$

where  $n$  is the number of atomic layers of the film and  $a$  the lattice constant ( $3.839 \text{ \AA}$  for Ir). This formula gives  $D = -2.8 \text{ mJ m}^{-2}$  for the Fe triple layer on Ir(111), starting from the calculated value of  $d = -1.8 \text{ meV}$  per atom for the Fe monolayer. From this value for  $D$  and equation IV.3,  $A$  varies between  $0.6 \text{ pJ m}^{-1}$  and  $2.2 \text{ pJ m}^{-1}$  to obtain magnetic periods ranging from  $3 \text{ nm}$  to  $10 \text{ nm}$ , which is a considerable effect. Local variations of the strain relief can very efficiently modify the magnetic properties of the ultrathin film.

## IV.1.5 Investigation of the transition magnetic field in the different areas

The effect of strain relief modulations of the magnetic configuration in the Fe triple layer on Ir(111) can be further investigated by applying an external magnetic field to the system. A comparison between the observed behavior and the prediction of the model proposed in the previous section allows to check its validity.

### IV.1.5.1 $360^\circ$ domain walls and skyrmions in magnetic field

Figure IV.13 shows the magnetic field dependence of the spin spirals in the Fe triple layer. Between  $1 \text{ T}$  and  $3 \text{ T}$ , the spirals in the double line areas transform into individual banana-shaped magnetic objects aligned in rows along the dislocation lines. These objects are magnetic skyrmions, more details about their structure can be found in section IV.3. The behavior of the spirals in the single line areas is different. No skyrmions are formed. Instead, the spiral becomes an assembly of  $360^\circ$  domain walls which become thinner as the field increases. Above  $3 \text{ T}$ , the film is almost completely ferromagnetic.

This different behavior of the two types of areas cannot be explained by the model proposed in equation (IV.2) with an additional Zeeman term. If there is no magnetic anisotropy and if the film is isotropic, there is a stable skyrmion phase for any values of  $A$  and  $D$  under the appropriate external magnetic field.<sup>18</sup> However, the film is not isotropic for the Fe triple layer on Ir(111) because of the presence of the dislocation lines which break the symmetry. The skyrmions are thus not circular, because of the arrangement of the Fe atoms, and there is no certainty that there is a stable skyrmion phase. Indeed, no skyrmions are found in the single line areas.

<sup>17</sup> H. Yang et al. *Physical Review Letters* 115 (2015) [107]

<sup>18</sup> A. Bogdanov et al. *Journal of Magnetism and Magnetic Materials* 138, 255–269 (1994) [33]

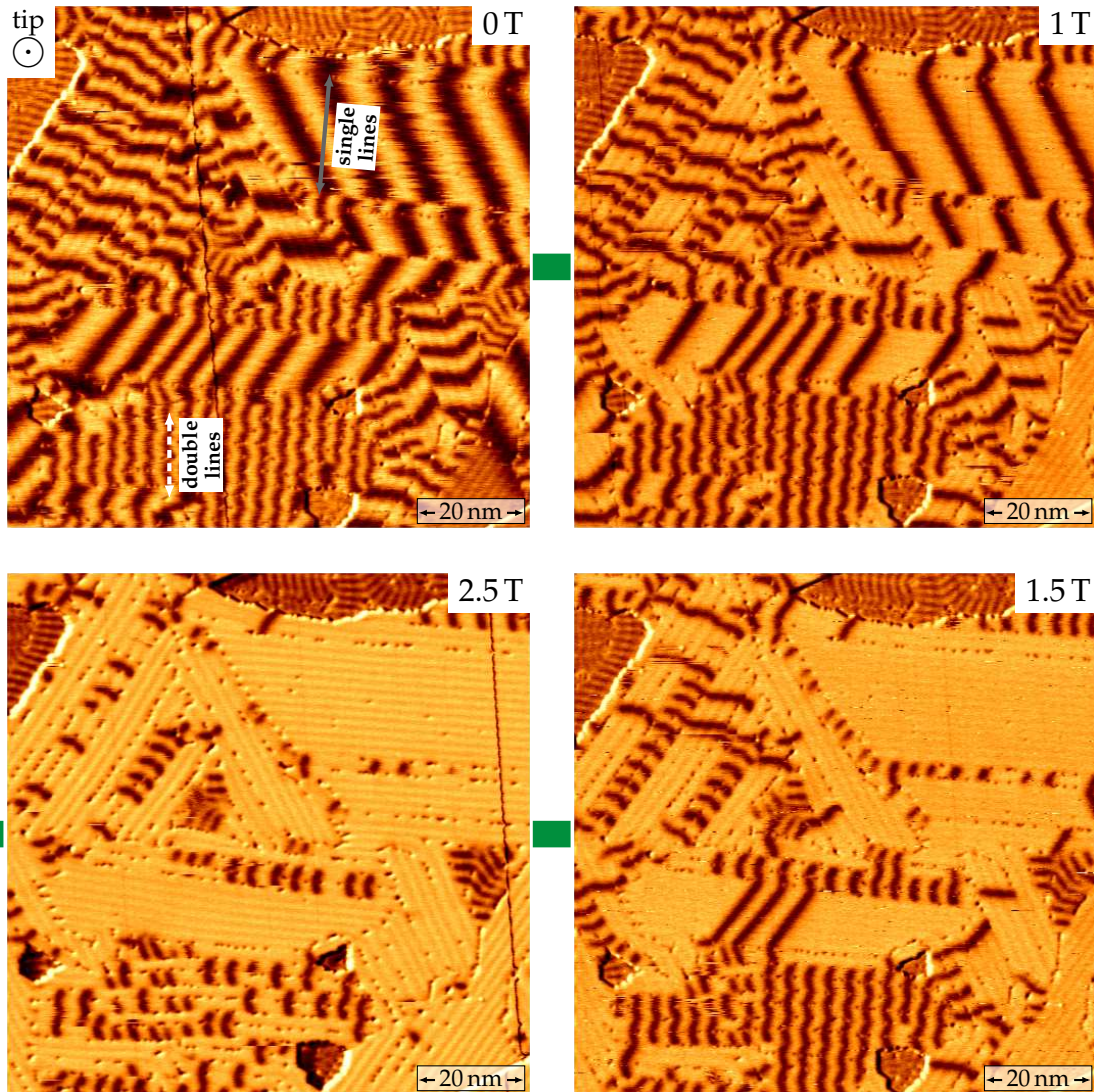


Figure IV.13: Field dependence of the spin resolved differential conductance map of a Fe triple layer film on Ir(111) measured with an out-of-plane sensitive tip. In single line areas, the spirals transform into an assembly of  $360^\circ$  domain walls already at 1 T and these walls gradually disappear when the field increases. In the double line regions, the spirals split into banana-shaped individual skyrmions around 2 T. *Measurement parameters:*  $-700$  mV, 1 nA, 8 K, Cr bulk tip.

The pinning of the magnetic structures at the dislocation lines seems to play a crucial role in the stabilization of the skyrmions. They are always placed in such a way that there is a dislocation line in their center and one line at each end. The stacking of the line at the center is thus different than the stacking of the lines at the ends because fcc and hcp lines are alternating. The skyrmions are pinned to the lines and aligned along them. This pinning effect might be induced by a spatial modulation of the magnetic interaction coupled to the dislocation pattern. Monte Carlo calculations in anisotropic environments have demonstrated that modulations of the exchange couplings and the anisotropy energy allow to reproduce the observed shapes.<sup>19</sup> However, the symmetry of the atom arrangement also plays a role for the experimental system.

<sup>19</sup> J. Hagemester et al. *Physical Review B* 94, 104434 (2016) [104]

In the single line areas, the skyrmion pinning effect is absent and only  $360^\circ$  domain walls form. A possible reason for this difference in the pinning behavior could be that the dislocation lines do not have the same structure than in the double line areas as well as the fact that they all correspond to the same stacking.

#### IV.1.5.2 Hysteresis effects and correlation with the dislocation line spacing

A more quantitative analysis of the field dependence of the magnetic state in the Fe triple layer on Ir(111) is presented in Figure IV.15. In this measurement series, the out-of-plane magnetic field was increased in 0.5 T steps from 0 T to 4 T and decreased again in the same way. When the field increases, the domain walls and the skyrmions appear, as detailed previously. At 4 T, the sample is in a ferromagnetic state (image not shown). When the field decreases again, the spirals do not reappear at the same field value than the one needed to make them vanish but at a much lower value. This hysteresis is visible in almost all the different regions of the sample. This effect appears very clearly when comparing the data measured at the same magnetic field value during the up-sweep and the down-sweep.

This observation implies that during the up-sweep the skyrmions and the  $360^\circ$  domain walls are metastable in a field range below the observed transition, as explained in the sketch from Figure IV.14. Similarly, the ferromagnetic state is metastable in a field range above the transition field during the down-sweep. The precise width of these field ranges where the states are metastable cannot be derived from the measurement shown in Figure IV.15 but their existence can be attributed to both the presence of an energy barrier between the skyrmion/domain wall state and the ferromagnetic state and to pinning effects.

The graph at the bottom of Figure IV.15 explains how the transition fields were measured in the different areas, based on the example of the four regions marked with blue ellipses. For each region, the evolution of the state is indicated at every field step. The transition field from the non-collinear state (skyrmions or assembly of domain walls) to the ferromagnetic state (and vice versa) is taken in the middle of the field step and the error bar as its height.

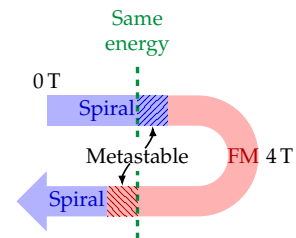


Figure IV.14: Sketch of the hysteresis for the transition from the spiral to the ferromagnetic state.

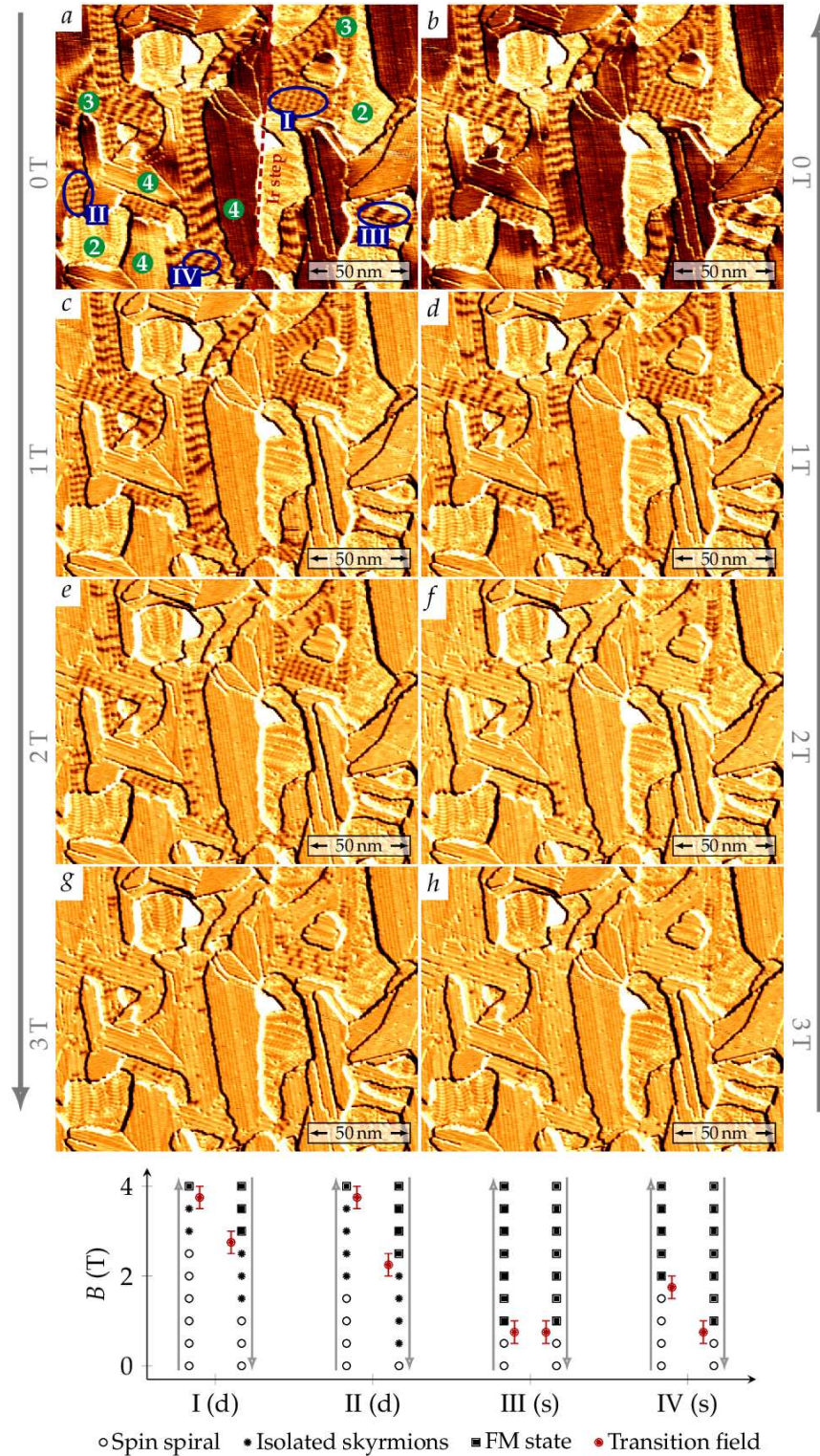


Figure IV.15: Spin resolved differential conductance maps showing the magnetic state of a Fe ultrathin film on Ir(111), measured with an out-of-plane sensitive tip. The numbers in the green circle in image *a* indicate the local Fe coverage. An out-of-plane magnetic field is increased in steps of 0.5 T up to 4 T (not shown, the sample is ferromagnetic) and then decreased back in steps to zero. The graph displays the state of the four regions marked in blue in image *a*. Areas I and II are double line regions, III and IV single line regions. *Measurement parameters:* -500 mV, 1 nA, 4 K, Cr bulk tip.

Using this procedure, the transition fields can be measured in various regions of the sample and correlated with the period of the spiral, as shown in Figure IV.16, for an up-sweep of the magnetic field. It appears clearly that higher fields are required to erase the skyrmions than the domain walls.

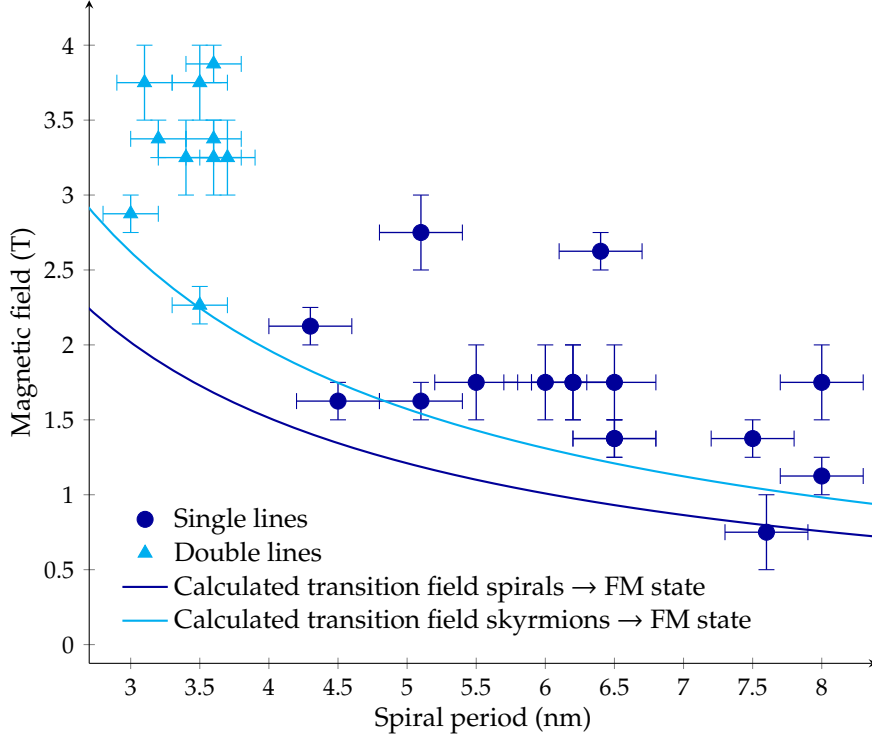


Figure IV.16: Effect of the spiral period on the magnetic fields needed to reach the ferromagnetic state during an increasing field sweep. The calculated transition fields were obtained from the phase diagram derived by Bogdanov and Hubert with the parameters from Fig. IV.10:  $|D| = 2.8 \text{ mJ m}^{-2}$  and  $K_{\text{eff}} = 0$ . The magnetic moment used is  $\mu = 2.7\mu_B$  per Fe atom.

A Zeeman term can be included in the energy density given in equation (IV.2):

$$\mathcal{E} = A \sum_i \left( \frac{\partial \vec{m}}{\partial x_i} \right)^2 + D \left( m_z \frac{\partial m_x}{\partial x} - m_x \frac{\partial m_z}{\partial x} \right) - M_s B m_z \quad (\text{IV.5})$$

with  $M_s$  the saturation magnetization and  $B$  the magnetic field. In this particular case, when the magnetic anisotropy vanishes, the transition field  $B_t$  can be easily computed using the phase diagram provided by Bogdanov and Hubert. Its expression is the following:

$$B_t = \mu_0 \frac{D^2 h_t}{A M_s} = 4\pi\mu_0 \frac{|D| h_t}{\lambda M_s} \quad (\text{IV.6})$$

where  $h_t$  is a reduced field parameter with a different value for the transition from the spirals to the ferromagnetic state and the transition

from the skyrmions to the ferromagnetic state:

$$h_t^{\text{spiral}} \simeq 0.308 \quad (\text{IV.7})$$

$$h_t^{\text{skyrmion}} \simeq 0.401 \quad (\text{IV.8})$$

The solid curves plotted in Figure IV.16 are computed with a saturation magnetization  $M_s = 1.77 \text{ MA m}^{-1}$  obtained from a magnetic moment of  $2.7\mu_B$  per atom<sup>20</sup> and assuming again that  $D = 2.8 \text{ mJ m}^{-2}$ . There is thus no free parameter, the curves are not fitted to the data. As expected from the discussion about the metastability of the states, all the data points are above the theoretical curve. The curve indeed corresponds to the green dashed line in Figure IV.14, whereas the data points are located at the boundary between the blue and red areas. Furthermore, the order of magnitude of the measured and predicted fields are very close and the general trend that smaller field are required to destroy the larger magnetic structure is found both in the experimental data and in the model. This rather good agreement (knowing that pinning plays a crucial role in the system) supports the hypothesis that the strain relief variations mostly modify the effective exchange couplings rather than the DMI. If changes in the DMI were dominant, the shape of the curve would be different.

### IV.1.5.3 Summary

The dislocation line pattern is more complicated in the Fe triple layer on Ir(111) than in the double layer, because of the coexistence of two different types of lines. The local arrangement of the Fe atoms within the film has a large influence on the spin spirals, which propagate along the dislocation lines and whose wave fronts exhibit different shapes depending on the type of dislocation line pattern. The period of the spiral depends on the spacing between the lines and thus on the local strain relief in the film. These period variations are attributed to modulations of the exchange stiffness by the strain relief. However, the DFT calculations<sup>21</sup> concerning the Fe double layer mentioned in section V.2.3 reveal that the frustration of exchange plays an important role in the stabilization of the spirals. Hence an effective exchange stiffness does not fully describe this system. The model used here to describe the Fe triple layer on Ir(111) is a simple approximation. Under the application of an out-of-plane magnetic field, the spirals either transform into skyrmions or into  $360^\circ$  domain walls. The pinning at the lines appears to play a crucial role for the stabilization of these structures. Measurements of the transition field between the non-collinear states and the ferromagnetic state show that the transition occurs at lower fields for structures with a larger magnetic length scale. A comparison between this data and the transition field computed from a micromagnetic model support the hypothesis that variations of the effective exchange are responsible for the changes of the spiral periods.

<sup>20</sup> S. Heinze et al. *Nature Physics* 7, 713–718 (2011) [27]

<sup>21</sup> P.-J. Hsu et al. *Nature Communications* 9, 1571 (2018) [108]

This analysis demonstrates how epitaxial strain relief influences non-collinear magnetism and that it can be used to induce local variations of the magnetic properties in ultrathin films. Furthermore, the patterns created by the strain relief can be used to confine magnetic objects at the nanoscale by making use of their pinning properties.

<sup>1</sup> W. Jiang et al.  
*Science* 349,  
283–286 (2015)  
[109]

<sup>2</sup> C. Moreau-Luchaire et al. *Nature Nanotechnology* 11, 444–448 (2016) [110]

<sup>3</sup> O. Boulle et al. *Nature Nanotechnology* 11, 449–454 (2016) [111]

<sup>4</sup> S. Woo et al. *Nature Materials* 15, 501–506 (2016) [5]

<sup>5</sup> A. Soumyanarayanan et al. *Nature Materials* 16, 898–904 (2017) [112]

<sup>6</sup> G. Chen et al. *Applied Physics Letters* 106, 242404 (2015) [113]

<sup>7</sup> P. Jensen et al. *Europhysics Letters* 18, 463 (1992) [114]

<sup>8</sup> C. Schneider et al. *Physical Review Letters* 64, 1059 (1990) [115]

<sup>9</sup> H. Elmers et al. *Physical Review Letters* 75, 2031 (1995) [116]

<sup>10</sup> A. Sonntag et al. *Physical Review Letters* 113, 077202 (2014) [84]

<sup>11</sup> D. Royer et al. Masson, 1996 [117]

## IV.2 Strong temperature-induced increase of the spin spiral period

Only magnetic states stable at room temperature can be used for technological applications. Improving the thermal stability of complex magnetic textures is thus a crucial issue. Increasing the amount of magnetic material in ultrathin films, by choosing the appropriate thickness for the magnetic layers or the right number of repetitions in multilayers is an efficient way to reach room temperature stability and was successful in the case of skyrmions.<sup>1,2,3,4,5,6</sup>

For various transition metal ultrathin films, it was predicted and observed that the Curie temperature becomes higher when the films become thicker.<sup>7,8,9</sup> In the Fe monolayer on Ir(111), the nanoskyrmion lattice vanishes around 28 K.<sup>10</sup> The thermal stability is expected to be enhanced for the spin spirals in the Fe double and triple layer. This section presents the measurements and the analysis of the temperature dependence of the spin spirals in the Fe double and triple layer on Ir(111). In the triple layer, they appear to be stable up to room temperature and surprisingly, their periods increase strongly with the temperature.

### IV.2.1 Calibration of the STM

#### IV.2.1.1 Geometrical considerations

Before performing a temperature-dependent STM measurement over a large temperature range, like here from 30 K to room temperature, the scanner of the STM needs to be calibrated. Indeed, the piezoelectric constants in the material which constitutes the scanner have a non-linear temperature dependence. These constants  $d_{\alpha i}$  are defined<sup>11</sup> (in the simplified case where no strain is applied on the material) by the linear relation between the deformation tensor  $S$  and the electric field  $E$ :

$$S_{\alpha} = d_{\alpha i} E_i \quad (\text{IV.9})$$

(with summation over the repeated indices). The deformation tensor is given by:

$$S_{kl} = \frac{1}{2} \left( \frac{\partial u_k}{\partial x_l} + \frac{\partial u_l}{\partial x_k} \right) \quad (\text{IV.10})$$

where  $u_k$  is the displacement in the direction  $k$ . Since it is symmetric, the indices ( $kl$ ) are not ordered and can be rewritten as  $\alpha$ , with 6 possible values: (11)  $\rightarrow$  1, (22)  $\rightarrow$  2, (33)  $\rightarrow$  3, (23) = (32)  $\rightarrow$  4, (31) = (13)  $\rightarrow$  5 and (21) = (12)  $\rightarrow$  6. The coefficients  $S_1, S_2$  and  $S_3$  describe an expansion or a compression while  $S_4, S_5$  and  $S_6$  describe shear deformations. For a uniform deformation of the scanner, induced by an electric field in this case,  $S_3 = \delta L/L$  where  $L$  is the length of the piezoelectric scanner tube.

The geometry of the scanner tube is drawn in Figure IV.17.

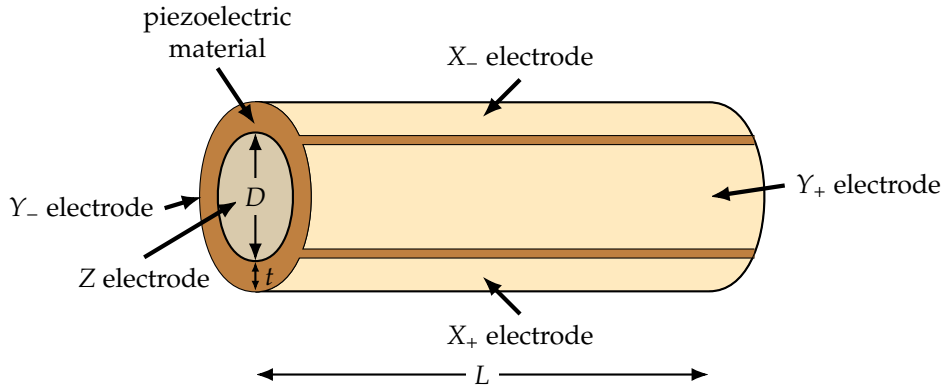


Figure IV.17: Sketch of the geometry of an STM tube scanner. When a voltage is applied to the center Z electrode, the scanner shrinks or elongates whereas when the voltage is applied on the side electrodes X<sub>+</sub>, X<sub>-</sub>, Y<sub>+</sub> or Y<sub>-</sub>, it bends.

The outer surface of the cylinder is divided into 4 electrodes, X<sub>+</sub>, X<sub>-</sub>, Y<sub>+</sub>, Y<sub>-</sub> and there is another electrode in the inner surface, Z. The electric field is only applied in the radial direction of the cylinder, the voltage is applied between the outer and the inner part. A uniform elongation is obtained by applying a voltage between the inner electrode and all the outer ones and a bending  $\Delta x$ ,  $\Delta y$  is created by applying opposite but equal voltages on the electrodes X<sub>+</sub>, X<sub>-</sub> or Y<sub>+</sub>, Y<sub>-</sub>. The tube elongates on one side and shrinks on the other one, creating the bending. In the end, only one piezoelectric constant,  $d_{31}$ , is involved in the scanning process. The elongation of the scanner is thus:<sup>12</sup>

$$\Delta L = d_{31} \frac{VL}{t} \quad (IV.11)$$

and its bending:

$$\Delta x = \Delta y = d_{31} \frac{2\sqrt{2}L^2V}{\pi Dt} \quad (IV.12)$$

where  $V$  is the voltage applied and the geometrical parameters  $D$ ,  $t$  and  $L$  are defined in Figure IV.17. Since only  $d_{31}$  depends on temperature, all the calibration coefficients should behave exactly in the same way when the measurement temperature changes. Therefore it is enough to measure the variation of the measured step height on the sample to find the calibration correction.

All the microscopes used in this thesis have scanners made of EBL4, which is a type of lead zirconate titanate (PZT). The temperature dependence of the  $d_{31}$  coefficient for this material is shown in Figure IV.18.

#### IV.2.1.2 Calibration procedure

Rather than changing the actual calibration of the STM at every temperature step, the measurements were performed using either the

12 R. Wiesendanger. Cambridge University Press, 1994 [47]

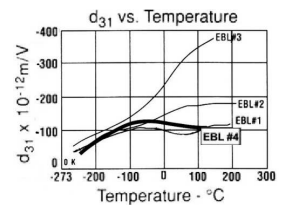


Figure IV.18: Temperature dependence of  $d_{31}$  in EBL4 (bold line), from STAVELEY Sensors Inc, East Hartford, CT, USA.

existing calibration for 40 K or the one for room temperature, and the images were recalibrated after, during the analysis. The calibration correction coefficients were extracted from the measurements of Fe ultrathin films on Ir(111) by measuring the height of the Ir steps. Only steps between terraces covered with the same number of Fe layers can be used in order to avoid variations of the measured height arising from the electronic structure. The theoretical step height for Ir(111) is 222 pm. The procedure for the step height measurements is the following:



Figure IV.19: Example of an area with two Fe double layer terraces used for the step height measurements at 200 K.

- Cut from the image a small area with the two terraces of interest.
- Fit a local plane to one of the terraces and subtract it to the data to get the terraces as flat as possible
- Draw a mask on the parts of the image which should not be taken into account like higher or lower coverage areas, areas with too many defects, etc. See the example in Figure IV.19.
- Extract the height distribution, excluding the masked regions.
- Fit two gaussian peaks to the height distribution. The difference between the positions of the centers of the peaks is the step height.
- Repeat this procedure on several different positions on the sample for each temperature in order to get a better accuracy.
- For each temperature, the selected value of the step height is the average of these results and the standard deviation is used as error bar.
- The rescaling factor for the data is then the ratio between the expected step height of 222 pm and its measured value.

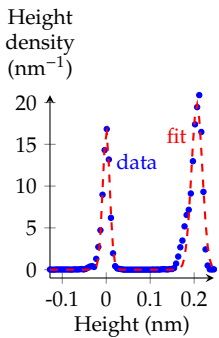


Figure IV.20: Gaussian fitting of the height distribution from Figure IV.19.

Using the height distribution gives more reliable results than simply taking line profiles because the dislocation lines distort the profiles. The results are gathered in the plot in Figure IV.21. As expected, the shape obtained is close to the one of the temperature dependence of  $d_{31}$  from Figure IV.18. The results of this calibration procedure in Figure IV.21 are used to rescale all the data presented in the following section.

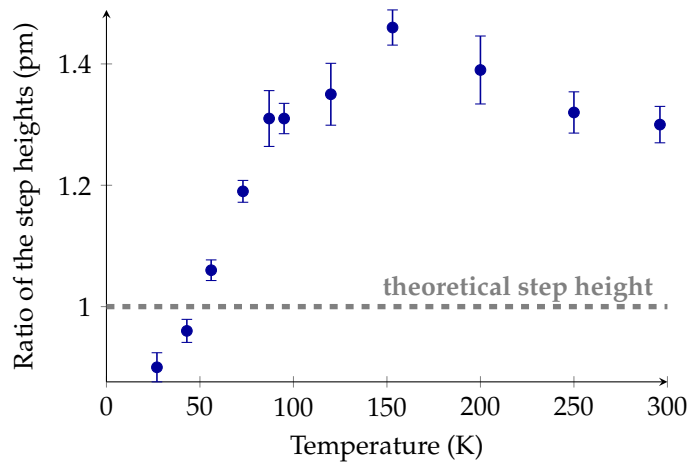


Figure IV.21: Variation of the ratio between the expected step height of 222 pm the measured value with the temperature in a variable temperature STM (with a fixed calibration). These ratios are used to recalibrate the measured data.

## IV.2.2 Stable spin spirals up to room temperature

The temperature-dependent measurements were performed mostly in the variable temperature STM (see details in section II.2.1.2), but also in a low temperature STM operated at room temperature. Because of the contamination of the sample by particles desorbing from the STM body when warming up, a new sample needs to be prepared for each temperature step. The sample preparation is explained in section III.1.1. Despite this contamination problem, the choice was made to start from measurements at low temperature because the magnetic state of the sample is known. Starting from room temperature, when no magnetic contrast is visible, it would have been more difficult to decide if the magnetic order is not present or if the tip is not polarized.

### IV.2.2.1 Measurements up to room temperature

A Fe-coated W tip was used for the first measurements. It is easier to obtain some magnetic contrast at elevated temperature using a rather thick Fe coating. The temperature was increased in several steps and the spin spirals were measured both in the Fe double layer and the Fe triple layer. Figure IV.22 shows measurements of the Fe double layer at various temperatures up to 200 K.

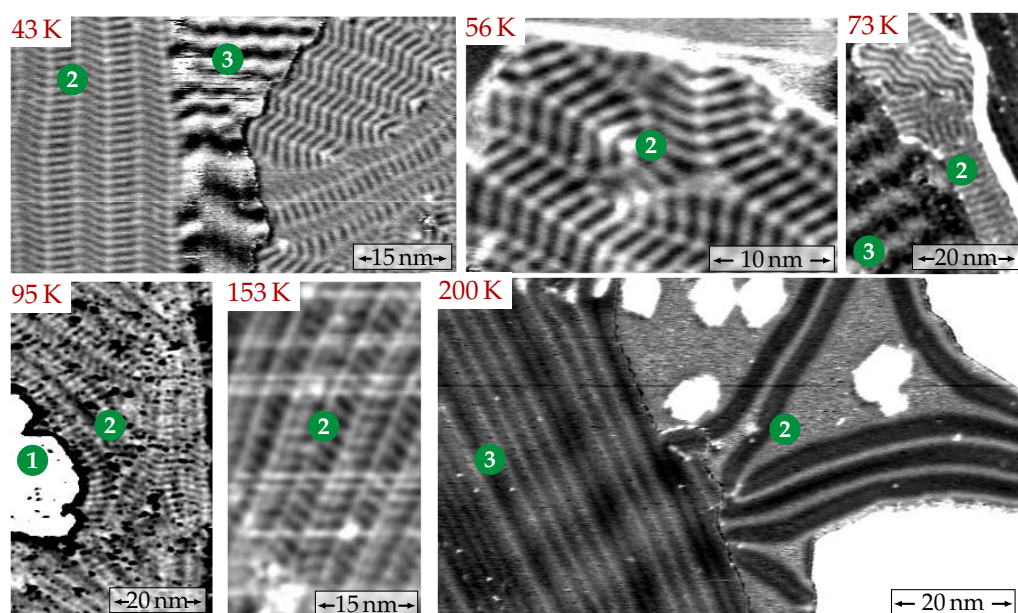


Figure IV.22: Spin resolved differential conductance maps measured with mostly out-of-plane sensitive Fe-coated W tips showing the temperature dependence of the spin spirals in the Fe double layer on Ir(111). The images measured at 73 K, 95 K and 153 K were smoothed with a Gauss filter to improve the visibility of the spiral. The numbers in the green circles indicate the local Fe coverage. *Measurement parameters:* 43 K,  $-700$  mV,  $0.7$  nA ; 56 K,  $-1$  V,  $1$  nA ; 73 K,  $-1.3$  V,  $1.5$  nA ; 95 K,  $-700$  mV,  $1$  nA ; 153 K,  $-500$  mV,  $2$  nA ; 200 K,  $-700$  V,  $2$  nA.

The spin spirals are clearly present in the double layer up to 153 K. No obvious change of the spiral shape or period with the temperature

appears on the images for the Fe double layer. At 200 K, the contrast vanishes in the Fe double layer whereas some magnetic modulation is still present on the triple layer, which indicates that the tip is spin-polarized and allows to resolve the magnetic state. Furthermore, the three possible directions of the dislocation lines are visible in the image which means that if there were spirals along the lines, at least two of them should be visible with any magnetic sensitive tip. Either the spirals disappeared at this temperature or they are fluctuating so fast that they are averaged on the timescale of the measurement (and then the actual transition temperature would be higher).<sup>13</sup> This vanishing between 150 K and 200 K represents a large improvement of the thermal stability of the magnetic state in the Fe double layer compared to the fcc Fe monolayer, in which the nanoskyrmion lattice vanishes at 28 K.<sup>14</sup>

<sup>13</sup> G. Hasselberg et al. *Physical Review B* 91, 064402 (2015) [118]

<sup>14</sup> A. Sonntag et al. *Physical Review Letters* 113, 077202 (2014) [84]

The temperature dependence up to 250 K of the spirals in the Fe triple layer is shown in Figure IV.23. Here an increase of the period of the spin spiral with temperature is very clear. Furthermore, the zigzag shape of the wavefront in the double line areas (see section IV.1.2) is not visible above 153 K.

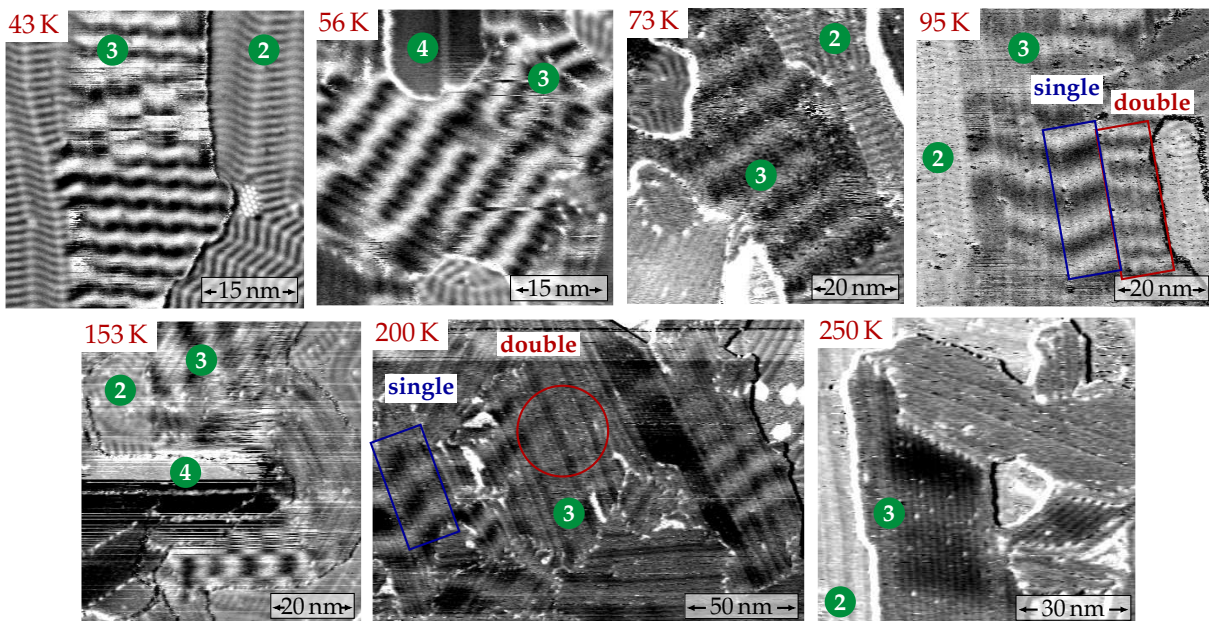


Figure IV.23: Spin resolved differential conductance maps measured with a mostly out-of-plane sensitive Fe-coated W tip showing the temperature dependence of the spin spirals in the Fe triple layer on Ir(111) up to 250 K. The numbers in the green circles indicate the local Fe coverage.

Measurement parameters: 43 K, -700 mV, 0.7 nA ; 56 K, -1 V, 1 nA ; 73 K, -1.3 V, 1.5 nA ; 95 K, -700 mV, 1 nA ; 153 K, -500 mV, 2 nA ; 200 K, -700 V, 2 nA ; 250 K, -500 V, 5 nA.

It also seems that, above 150 K, the magnetic contrast disappears in some areas where it is expected that stripes should be visible (for example in the center of the image measured at 200 K). This effect becomes critical at 250 K and even more pronounced at room temperature. Figure IV.24 shows a spin resolved differential conductance map measured with an Fe

coated tip at room temperature. A strong magnetic signal is present on the quadruple layer, indicating that the tip is spin-polarized. However, the Fe triple layer looks uniform, except in the very small area at the boundary with the quadruple layer, marked with the red box.

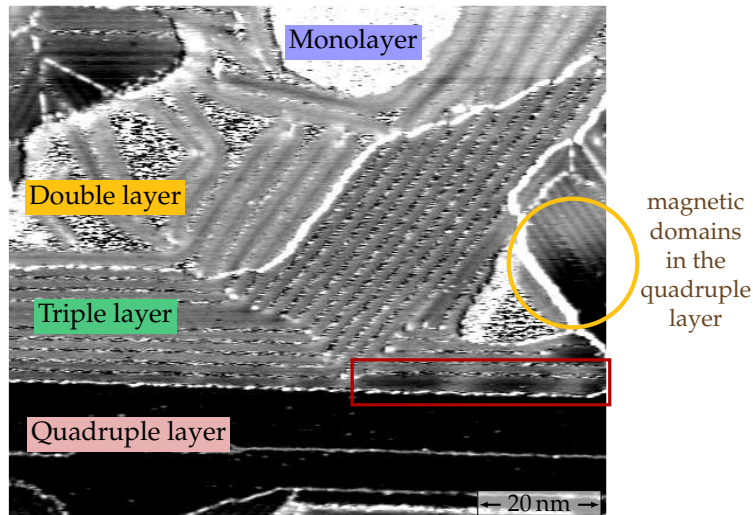


Figure IV.24: Spin resolved differential conductance maps of a Fe ultrathin film on Ir(111) measured with a Fe coated W tip at room temperature. Measurement parameters:  $-700$  mV,  $2$  nA,  $296$  K,  $0$  T, Fe coated W tip.

A possible explanation for the vanishing of the spirals in the Fe triple layer is that it is perturbed by the stray field of the ferromagnetic Fe-coated tip. In the measurement from Figure IV.24, the Fe coating is rather thick, 30 to 50 atomic layers, in order to obtain easily a spin-polarized tip. Further measurements were thus performed with an antiferromagnetic Cr bulk tip, whose stray field is largely reduced. This experiment is rather challenging since the Néel temperature of bulk Cr is  $T_N = 311$  K.<sup>15</sup> However, SP-STM measurements at room temperature using Cr bulk tips were previously reported<sup>16</sup> and could also be achieved on the Fe triple layer as shown in Figure IV.25.

A constant-current map of the area with double, triple and quadruple layer regions is displayed in the left image, and the right image shows the simultaneously recorded differential conductance map. In contrast to the measurement from Figure IV.24, in which a Fe-coated W tip was used, spirals are visible in most of the Fe triple layer regions when the measurement is performed with a Cr bulk tip. However, at the center of the image, in the area marked with the white box, the magnetic contrast is very weak. This is probably a confinement effect because the width of the Fe triple layer film is smaller than the spiral period in this area.

As observed already at  $200$  K, the spirals do not have a zigzag wave front at room temperature and the magnetic state is the same in the double and single line areas. The spirals have a straight wave front perpendicular to the dislocation lines everywhere. Their period is much larger than at low temperature. Because of the considerable thermal drift, the spiral

<sup>15</sup> E. Fawcett. *Reviews of Modern Physics* 60, 209–283 (1988) [67]

<sup>16</sup> A. Li Bassi et al. *Applied Physics Letters* 91, 173120 (2007) [119]

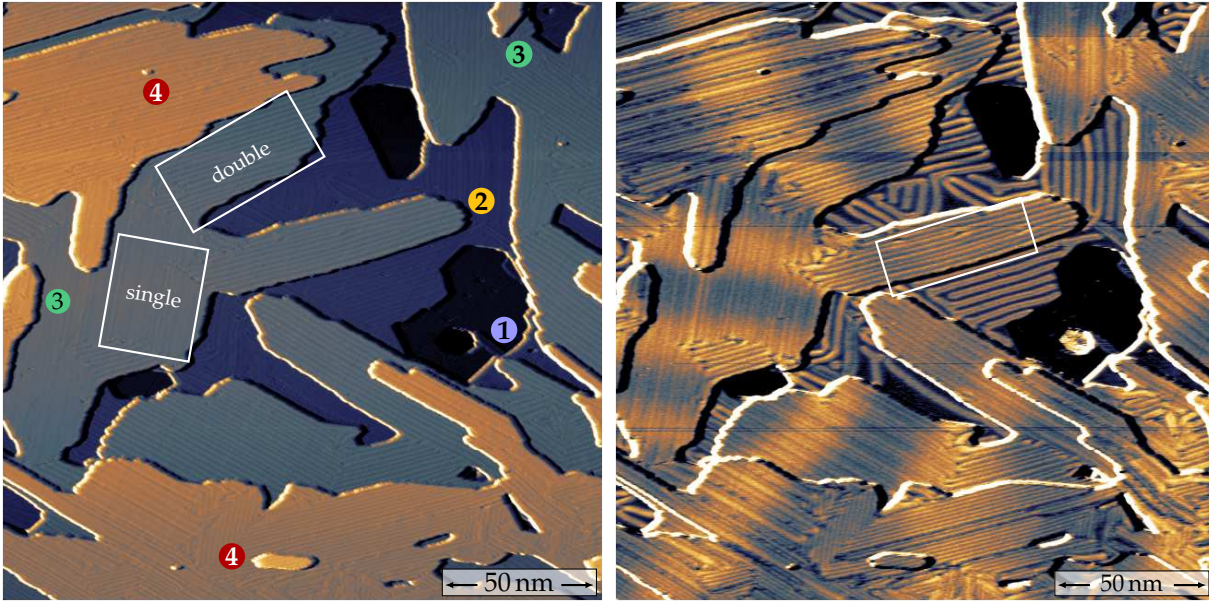


Figure IV.25: Constant-current map (left) and simultaneously measured spin resolved differential conductance map of a Fe film on Ir(111) at room temperature. The constant-current map is partially differentiated to make the dislocation lines visible and the numbers indicate the local Fe coverage. The differential conductance map reveals the presence of spirals propagating along the dislocation lines in the triple and quadruple Fe layer. The period of these spirals is much larger than at low temperature. The tip is mostly sensitive to the out-of-plane component of the sample magnetization and the pattern visible in the Fe double layer areas originates from the dislocation lines. *Measurement parameters:*  $-500$  mV,  $3$  nA,  $296$  K,  $0$  T, Cr bulk tip.

period can only be reliably measured along the scanning direction and reaches  $60$  nm to  $85$  nm, which is  $8$  to  $30$  times larger than the  $3$  nm to  $10$  nm measured at low temperature.

Another interesting observation is that at room temperature, the Fe quadruple layer regions are clearly ferromagnetically coupled to the neighboring Fe triple layer regions. This behavior is totally different from the one found at low temperature, where the Fe quadruple layer is ferromagnetic (see section III.1.2). The spirals in the Fe triple layer have a large enough period to be stabilized in the quadruple layer as well.

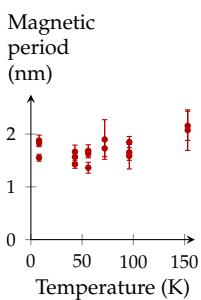


Figure IV.27: Temperature dependence of the spiral period in the Fe double layer.

#### IV.2.2.2 Large temperature-induced increase of the spin spiral period

The effect of temperature on the spirals can be estimated more quantitatively by gathering the measured spiral periods and plotting them as a function of the temperature, as it is done in Figure IV.26. The spiral period starts to increase significantly around  $150$  K and becomes very large at room temperature. For comparison, Figure IV.27 shows the same plot, measured on the same dataset, for the Fe double layer on Ir(111). In this case, a potential increase of the period cannot be distinguished from the variations of the period induced by the dislocation pattern (although the effect is smaller, the strain relief is also not fully uniform in the Fe double layer).

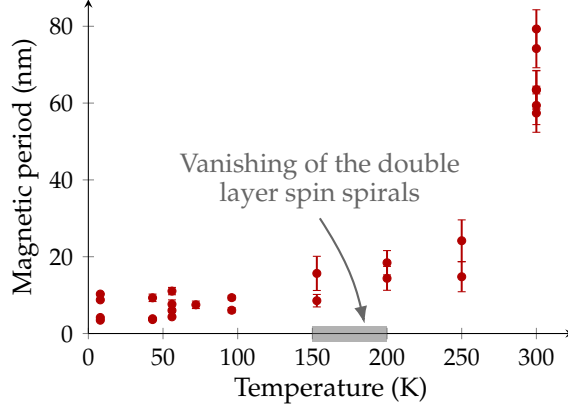


Figure IV.26: Temperature dependence of the spin spiral period in the Fe triple layer on Ir(111). The large spreading of the data points at each temperature step is caused by the variations of the strain relief (see section IV.1). The error bars reflect the resolution of the Fourier transformation used to measure the period from the experimental data as well as the thermal drift.

Such an increase of the spin spiral period with temperature is unusual for non-collinear magnetic states at the nanometer scale. Neither in the case of the nanoskyrmion lattice in the Fe monolayer,<sup>17</sup> nor for the spirals in the Mn monolayer on W(110)<sup>18</sup> or for the periodic domains in the Fe double layer on W(110),<sup>19</sup> the temperature has an influence on the magnetic length scale. Nevertheless, it was found in bulk materials that the magnetic period of non-collinear states can depend on temperature.<sup>20</sup> For example, the period decreases by about 30% in Dy and Er when the temperature increases from 20 K to 150 K or 80 K, respectively. Temperature-induced changes can be related to a coincident modification of the atom positions, like in ZnCr<sub>2</sub>Se<sub>4</sub>.<sup>21</sup> In Fe on Ir(111), the atomic structure is not modified with temperature. The lattice constant of bulk Ir does not vary between 4 and 300 K<sup>22</sup> and the constant-current maps do not show any clear change in the structure of the Fe film.

### IV.2.3 A classical model with layer dependent couplings

This significant increase can be explained using a model which considers that the three atomic Fe layers have different magnetic properties rather than using a mapping of the film on an effective single layer. This model was developed by Levente Rózsa.<sup>23</sup> In this case, the coefficients of the exchange interactions and the DMI are different in each Fe layer and the Hamiltonian is thus:

$$\mathcal{H} = \frac{1}{2} \sum_{p,q,\langle i,j \rangle} J_{pq,ij} \vec{S}_{p,i} \vec{S}_{q,j} + \frac{1}{2} \sum_{p,\langle i,j \rangle} \vec{D}_{pp,ij} (\vec{S}_{p,i} \times \vec{S}_{p,j}) \quad (\text{IV.13})$$

where the  $\vec{S}_{p,i}$  are the normalized classical magnetic moments, with  $p, q = 1, 2, 3$  the indices indicating the three Fe layers starting from the one closest to the Ir substrate and  $i, j$  the intralayer indices. The

<sup>17</sup> A. Sonntag et al. *Physical Review Letters* 113, 077202 (2014) [84]

<sup>18</sup> P. Sessi et al. *Physical Review Letters* 103, 167201 (2009) [120]

<sup>19</sup> K. von Bergmann et al. *Journal of Magnetism and Magnetic Materials* 305, 279–283 (2006) [121]

<sup>20</sup> Y. Izyumov. *Soviet Physics Uspekhi* 27, 845 (1984) [122]

<sup>21</sup> J. Akimitsu et al. *Journal of the Physical Society of Japan* 44, 172–180 (1978) [123]

<sup>22</sup> J. Arblaster. *Platinum Metals Review* 54, 93–102 (2010) [124]

<sup>23</sup> A. Finco et al. *Physical Review Letters* 119, 037202 (2017) [94]

summation only runs over the nearest-neighbors, six intralayer neighbors and three neighbors in the adjacent layers, as shown in Figure IV.28. The  $J_{pq,ij}$  coefficients describe the Heisenberg exchange interactions, both within and between the atomic layers and the  $\vec{D}_{pp,ij}$  are the Dzyaloshinsky-Moriya vectors, perpendicular to the nearest-neighbor bonds and assumed in-plane. As indicated in Figure IV.28, a perfect fcc stacking is assumed. The uniaxial distortion of the Fe layers is not included in the model for simplicity.

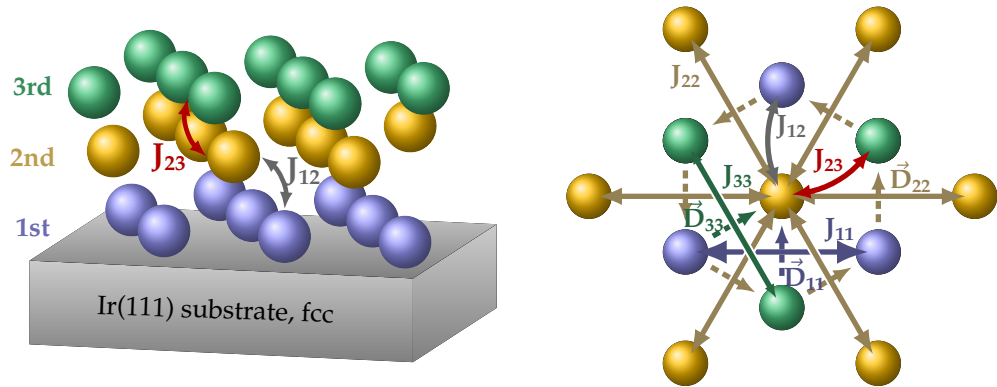


Figure IV.28: Sketch of the model system used to describe the Fe triple layer on Ir(111), considering a perfect fcc stacking and indicating the coupling constants from equation IV.13.

<sup>24</sup> K. Zakeri et al. *Nature Nanotechnology* 8, 853–858 (2013) [125]

<sup>25</sup> K. von Bergmann et al. *Physical Review Letters* 96, 167203 (2006) [126]

<sup>26</sup> E. Simon et al. *Journal of Physics: Condensed Matter* 26, 186001 (2014) [127]

<sup>27</sup> B. Dupé et al. *Nature Communications* 5 (2014) [128]

<sup>28</sup> L. Rózsa et al. *Physical Review Letters* 117 (2016) [129]

The assumption that the magnetic parameters are different in each atomic layer can be justified by two reasons. First, it usually arises from *ab initio* calculations that in general, the magnetic couplings are not the same in the different layers because of the different hybridization effects depending on their distance to the interfaces with the substrate and the vacuum.<sup>24</sup> This applies also to the Fe triple layer on Ir(111). Then even though the strain is not considered in the model, the lateral distances between the Fe atoms vary in the different atomic layers in the Fe triple layer because of the strain relief. This also supports the assumption that the magnetic interactions vary between the layers.

In order to reproduce the observed temperature dependence of the spiral period, the  $J_{pp}$  and  $D_{pp}$  couplings need to correspond to a much smaller magnetic period in the first Fe layer than in the third one. The DMI strength within a layer is expected to become weaker when the distance to the substrate increases because it mainly originates from the interface between the magnetic film and the heavy substrate. It is thus assumed that  $D_{11} > D_{22} > D_{33}$ . On the contrary, the exchange couplings are expected to increase when moving away from the interface because it was calculated that hybridization effects reduce them at the Fe/Ir interface.<sup>25,26,27,28</sup> For the exchange couplings, the assumption is thus:  $J_{11} < J_{22} < J_{33}$ .

The free energy per spin of the system described by the equation IV.13 can be computed for a spin spiral with wave vector  $k$  using a mean field approach:

$$\begin{aligned} \frac{1}{N} F_{\text{MF}}(k) = & -\frac{1}{2} \sum_{p,q} \mathcal{J}_{pq}(k) \langle S_p(k) \rangle \langle S_q(k) \rangle \\ & - \sum_p k_B T \ln \left( 4\pi \sinh \left( \frac{B_p(k)}{k_B T} \right) \frac{k_B T}{B_p(k)} \right) \end{aligned} \quad (\text{IV.14})$$

where

$$\begin{aligned} B_p(k) = & - \left[ \frac{1}{N} \sum_{q, \langle i,j \rangle} J_{pq,ij} \cos(k(x_{p,i} - x_{q,j})) \langle S_q(k) \rangle \right. \\ & \left. + D_{pq,ij} \sin(k(x_{p,i} - x_{q,j})) \langle S_q(k) \rangle \right] \end{aligned} \quad (\text{IV.15})$$

is the mean field in the layer  $p$  in energy dimensions,

$$\begin{aligned} \mathcal{J}_{pq}(k) = & \frac{1}{N} \sum_{\langle i,j \rangle} J_{pq,ij} \cos(k(x_{p,i} - x_{q,j})) \\ & + D_{pq,ij} \sin(k(x_{p,i} - x_{q,j})) \end{aligned} \quad (\text{IV.16})$$

is the Fourier transform of the interaction coefficients,  $N$  the number of atoms in each layer and  $\langle S_p(k) \rangle$  the order parameter of the spin spiral state. The spiral period is obtained by minimizing  $F_{\text{MF}}$  with respect to the wave vector  $k$ . The order parameter  $\langle S_p(k) \rangle$  decreases faster with temperature in the first and the second layer than in the third one. The contribution of the third layer to the free energy relative to the ones of the first and the second layer becomes dominant, which explains the large increase of the spiral period with temperature. By manually adjusting the coupling coefficients, the experimental data can be reproduced by the mean field theory (see Figure IV.29). However, the mean field results have to be rescaled because they overestimate the temperature. The magnetic parameters used for the calculation are gathered in Table IV.1. They were chosen in such a way that the layers do not decouple when a magnetic field is applied to the system.

In order to strengthen these results, Monte Carlo simulations were performed using the model from equation (IV.13) and the same coupling coefficients. As shown in Figure IV.29, the agreement with the experimental data is also very good. These calculations revealed in particular that the coupling  $J_{12}$  between the first and the second layers has to be stronger than the coupling  $J_{23}$  between the second and the third layer in order to reproduce the faster increase of the spiral period at higher temperatures.

$J_{11}$	-8.75 K
$J_{22}$	-70 K
$J_{33}$	-245 K
$J_{12}$	-175 K
$J_{23}$	-65.63 K
$D_{11}$	87.5 K
$D_{22}$	43.75 K
$D_{33}$	0.88 K

Table IV.1:  
Coupling coefficients used in Figure IV.29

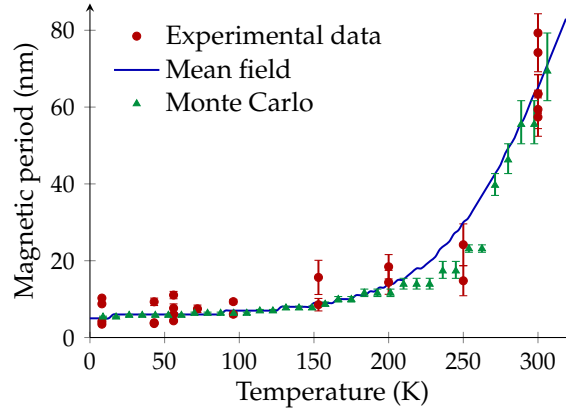


Figure IV.29: Comparison between the temperature dependence of the spin spirals in the Fe triple layer on Ir(111) obtained from the experiment, from the mean field approach and from the Monte Carlo calculations. The parameters used for the calculations are given in Table IV.1. The mean field results are rescaled by a factor 0.71 because they overestimate the temperatures. Both methods allow to obtain a good agreement between the model and the experiment.

This simplified model allows to understand the mechanism leading to the large and surprising increase of the spin spiral period with temperature. These results show that the presence of different magnetic layers and interfaces needs to be taken into account when considering temperature-dependent effects. Mapping ultrathin films onto a single layer, like in the micromagnetic model described in section IV.1.4, might fail to describe the influence of temperature on non-collinear magnetic states.

## IV.3 Electric field switching of magnetic skyrmions

In view of the development of energy-efficient spintronics devices, being able to control magnetic states using an electric field is a crucial issue. Usually, magnetic states are manipulated either with magnetic fields or with spin-transfer torques.<sup>1</sup> In both cases, currents are required, which causes a rather large energy consumption and Joule heating in the devices. Progress towards an electric control of magnetic states was made in several directions.<sup>2</sup> For example, the Curie temperature can be modified in ferromagnetic semiconductors by applying a gate voltage, which modifies the hole concentration in the system.<sup>3</sup> The magnetoelectric coupling in multiferroic materials is also widely studied, allowing to shift the frequency of spin waves<sup>4</sup> or to change the helicity of spin spirals<sup>5</sup> with electric fields. This section details the work demonstrating that it is possible to write and delete magnetic skyrmions in the Fe triple layer on Ir(111) using the electric field created by the STM tip.<sup>6</sup> A further study in Pt/Co/oxide trilayers also proved that the stability of skyrmionic bubbles can be tuned at room temperature by applying an electric field.<sup>7</sup> Combining the electric field writing and deleting of skyrmions with their detection via NCMR<sup>8</sup> makes an all-electrical skyrmion-based device possible.

### IV.3.1 Spin structure of the skyrmions

When a magnetic field is applied to the Fe triple layer on Ir(111), banana-shaped magnetic skyrmions form in the double line areas. This transition is discussed in section IV.1.5 and illustrated in Figure IV.13. However, it has not been proven yet that, despite their unusual shape, these objects are actually magnetic skyrmions. In contrast to isotropic systems in which the skyrmions are usually circular, the Fe triple layer on Ir(111) is uniaxially relaxed. It is thus very unlikely for symmetry reasons to observe circular skyrmions in such a system. The banana-shape of the skyrmions is induced by the arrangement of the Fe atoms in the film and by the spatial modulations of the magnetic parameters resulting therefrom.<sup>9</sup>

To prove their skyrmionic nature, it is necessary to show that the magnetic moments forming these objects completely wrap the unit sphere. Using SP-STM, this can be done by changing the direction of the magnetic sensitivity of the tip to measure different components of the magnetization in an area where a skyrmion is present. Figure IV.30 shows such a measurement. The direction of the tip sensitivity can be derived from the cycloidal spirals in the Fe double layer, by comparing the intensity of the magnetic contrast for the three different propagation directions (see section III.3 for details).

<sup>1</sup> J. Slonczewski. *Journal of Magnetism and Magnetic Materials* 159, L1–L7 (1996) [130]

<sup>2</sup> F. Matsukura et al. *Nature Nanotechnology* 10, 209–220 (2015) [131]

<sup>3</sup> H. Ohno et al. *Nature* 408, 944–946 (2000) [132]

<sup>4</sup> P. Rovillain et al. *Nature Materials* 9, 975–979 (2010) [133]

<sup>5</sup> M. Soda et al. *Journal of the Physical Society of Japan* 78, 124703 (2009) [134]

<sup>6</sup> P.-J. Hsu et al. *Nature Nanotechnology* 12, 123–126 (2017) [95]

<sup>7</sup> M. Schott et al. *Nano Letters* 17, 3006–3012 (2017) [135]

<sup>8</sup> C. Hanneken et al. *Nature Nanotechnology* 10, 1039–1042 (2015) [62]

<sup>9</sup> J. Hagemester et al. *Physical Review B* 94, 104434 (2016) [104]

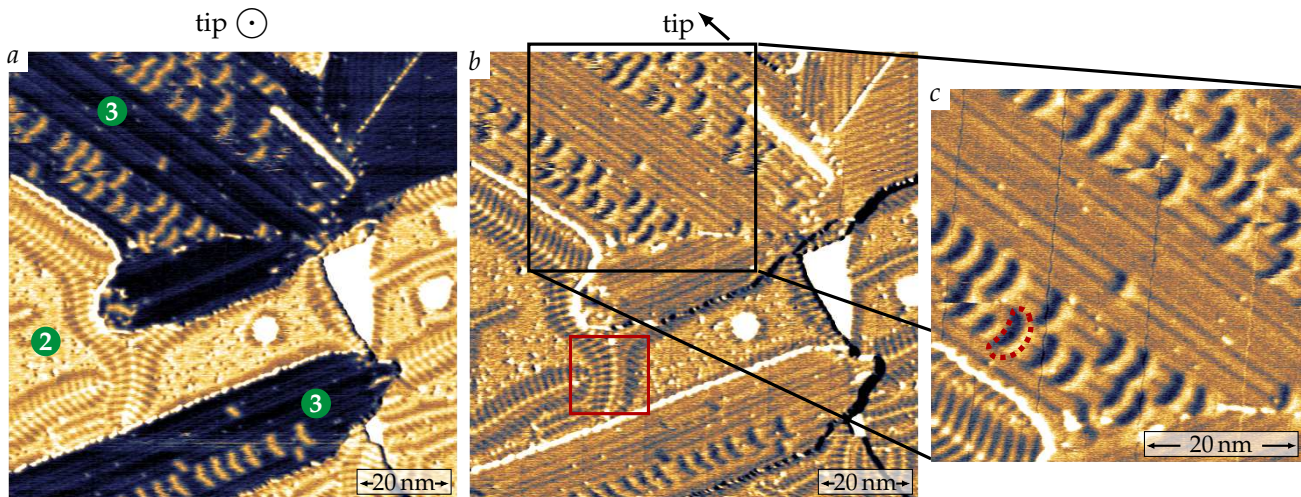


Figure IV.30: Spin resolved differential conductance maps of the skyrmions in the Fe triple layer on Ir(111), measured using tips with different magnetic sensitivities. In image *a*, the tip is sensitive to the out-of-plane component of the sample magnetization whereas in *b* and *c* the magnetization at the tip apex is canted with an in-plane component in the direction indicated by the arrow. This direction was determined by looking at the variations of the magnetic contrast of the spirals in the Fe double layer following the arguments detailed in section III.3 (see the contrast difference between the two sides of the spiral in the red box). In image *a* the skyrmions appear as bright banana-shaped objects whereas in images *b* and *c* (which is a zoom in the marked area), they have a bright and a dark lobe. The tip significantly changed between the two measurements which explains the overall contrast change between the images *a* and *b*. *Measurement parameters:*  $-700\text{ mV}$ ,  $1\text{ nA}$ ,  $8\text{ K}$ ,  $2.5\text{ T}$ , Cr bulk tip.

In image *a*, the tip is mostly out-of-plane sensitive and the skyrmions appear as bright shapes on a dark background. Between images *a* and *b*, the tip apex was modified by applying a bias pulse or touching the sample surface which resulted in a change of its magnetic sensitivity. Image *b* thus shows an in-plane component of the sample magnetization, in the direction indicated by the arrow. The appearance of the skyrmions radically differs. In this case, they are constituted of adjacent bright and dark parts which means that the magnetic moments are pointing in-plane on the sides of the skyrmions. The ordering of the bright and dark regions is the same for all the skyrmions in the same rotational domain, which proves that they have a unique rotational sense. This is expected from the presence of a large DMI in the system.

In order to determine the full three-dimensional spin structure, one further measurement with a tip also in-plane sensitive but in another direction is required. Another solution, which is more convenient, is to make use of the presence of three rotational domains in the sample, similarly to what was done for the nanoskyrmion lattice in the Fe monolayer.<sup>10</sup> The magnetic state in the different rotational domains is identical but there is a  $120^\circ$  rotation between them. Imaging the three domains with the same in-plane sensitive tip is thus equivalent to imaging one domain with three different tips sensitive to in-plane directions rotated by  $120^\circ$ .

Figure IV.31 shows the appearance of the skyrmions in the three

<sup>10</sup> S. Heinze et al. *Nature Physics* 7, 713–718 (2011) [27]

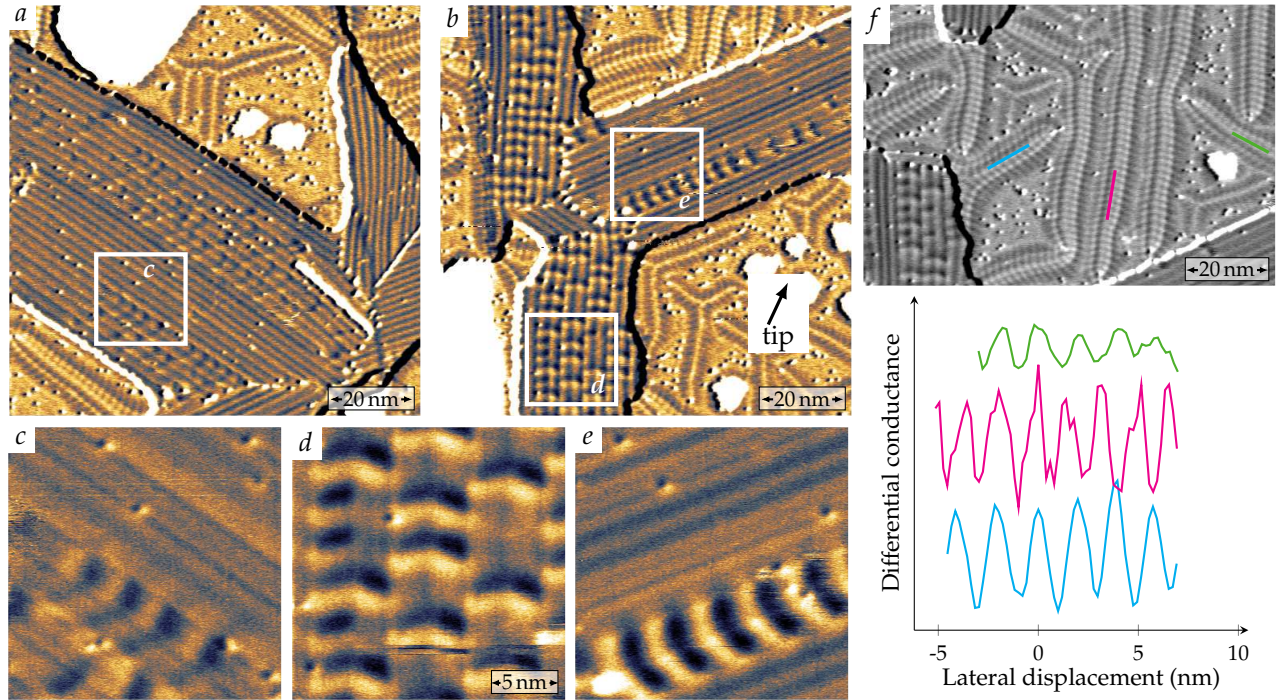


Figure IV.31: Spin resolved differential conductance maps showing the magnetic skyrmions in the Fe triple layer on Ir(111) measured with an in-plane sensitive tip (*a-e*) and a neighboring Fe double layer area used as a reference to derive the direction of the tip sensitivity (*f*) with the plotted line profiles of the spirals (see section III.3). The magnetic signal is clearly weaker in the direction of the green profile, which indicates that the tip is mostly in-plane sensitive in the direction of the arrow, with a small out-of-plane component. The images *c*, *d* and *e* show magnified views of the skyrmions in the three rotational domains. *Measurement parameters*:  $-700$  mV,  $1$  nA,  $8$  K,  $-2.5$  T, Cr bulk tip.

rotational domains for a tip sensitive to the in-plane direction marked with the arrow in image *b*. This direction was again determined using the spirals in the Fe double layer. It is clear by looking at the line profiles extracted from the image *f* that the contrast is reduced along the direction marked in green. The images *a* to *e* were measured using the very same tip in two adjacent areas on the surface. The images *a* and *b* show the orientation of the domains and the images *c* to *e* display closer views of each domain. Because the tip is dominantly in-plane sensitive, the skyrmions have very different appearances in the different domains. Since the tip sensitivity direction and the rotation angle between the domains are known, it is possible to determine the structure of the skyrmions, as shown in Figure IV.32. The images at the top of the figure show again the experimental data and the individual views of the skyrmions are compared with SP-STM simulations based on the indicated spin structure. This model was proposed by Niklas Romming and is inspired from the model describing the circular skyrmions in Pd/Fe/Ir(111).<sup>11</sup> In the case of the circular skyrmions, the skyrmion profile is assumed to be the same as the profile of a  $360^\circ$  domain wall and the structure is then extended to build an axisymmetric object. In the Fe triple layer case, the structure consists of a bent  $360^\circ$  domain wall with a half

<sup>11</sup> N. Romming et al. *Physical Review Letters* 114, 177203 (2015) [40]

circular skyrmion at each end (see sketch in Figure IV.33).

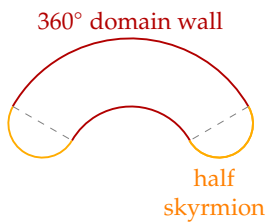


Figure IV.33: Sketch of the model used to build the spin structure of the skyrmions.

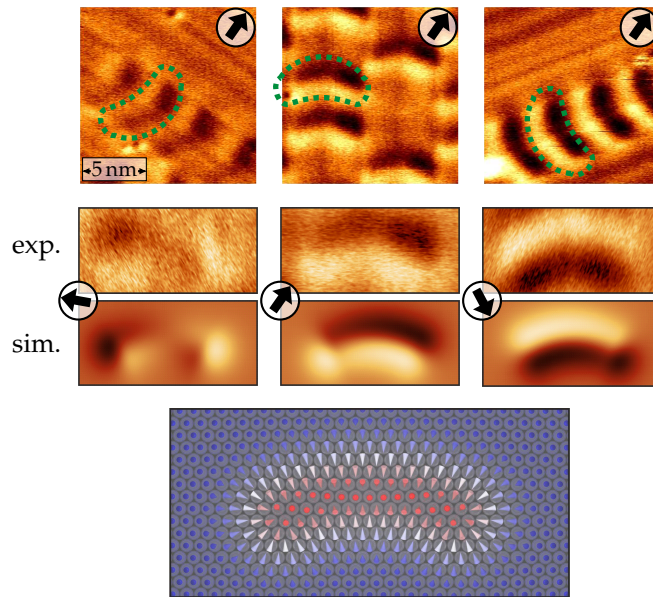


Figure IV.32: Spin-resolved difference conductance maps showing close views of the skyrmions in the three rotational domains in the Fe triple layer on Ir(111). The spin structure of the skyrmion can be determined based on this data and is shown in the sketch at the bottom. SP-STM simulations of this structure are included for comparison with the experimental data and show a very good agreement. This demonstrates that these banana-shaped magnetic objects really have the topology of magnetic skyrmions. The model was developed by Niklas Romming and André Kubetzka performed the SP-STM simulations. Adapted from [95].  
*Measurement parameters:*  $-700$  mV,  $1$  nA,  $8$  K,  $-2.5$  T, Cr bulk tip.

SP-STM simulations for this model are displayed for comparison with the experimental data. They show a very good agreement which validate the spin structure proposed and confirms that the observed banana-shaped objects have the topology of skyrmions.

### IV.3.2 Reliable writing and deleting of the skyrmions

By looking carefully again at the skyrmions in Figure IV.30, one can notice, for example in the top part of image *a*, that they are not fully stable and that some switching induced by the tip occurs. This suggests that it is possible to manipulate the skyrmions with the STM tip, following the work done on the skyrmions in Pd/Fe/Ir(111).<sup>12</sup>

A first experiment is shown in Figure IV.34. Initially, in the image at the top, there is a partially filled row of skyrmions in the area. They are stabilized by a magnetic field of  $2.5$  T and the tip is out-of-plane sensitive. The image is measured at a bias voltage of  $-700$  mV. During the next scan, in the exact same area, the bias voltage is changed to  $3$  V. In this case, the contrast is very weak in the differential conductance map and the skyrmions are hardly distinguishable. After this scan at  $3$  V, another

<sup>12</sup> N. Romming et al. *Science* 341, 636–639 (2013) [6]

scan is performed using the imaging parameters (here  $-700$  mV and  $1$  nA, which allow to measure the skyrmions without perturbing them too much). In this image, the row of skyrmions is completely filled during the first half of the scan. Two skyrmions on the right disappeared during the scan, which is not surprising because the magnetic field is rather high and probably destabilizes them. Scanning with  $3$  V thus allows to write the skyrmions.

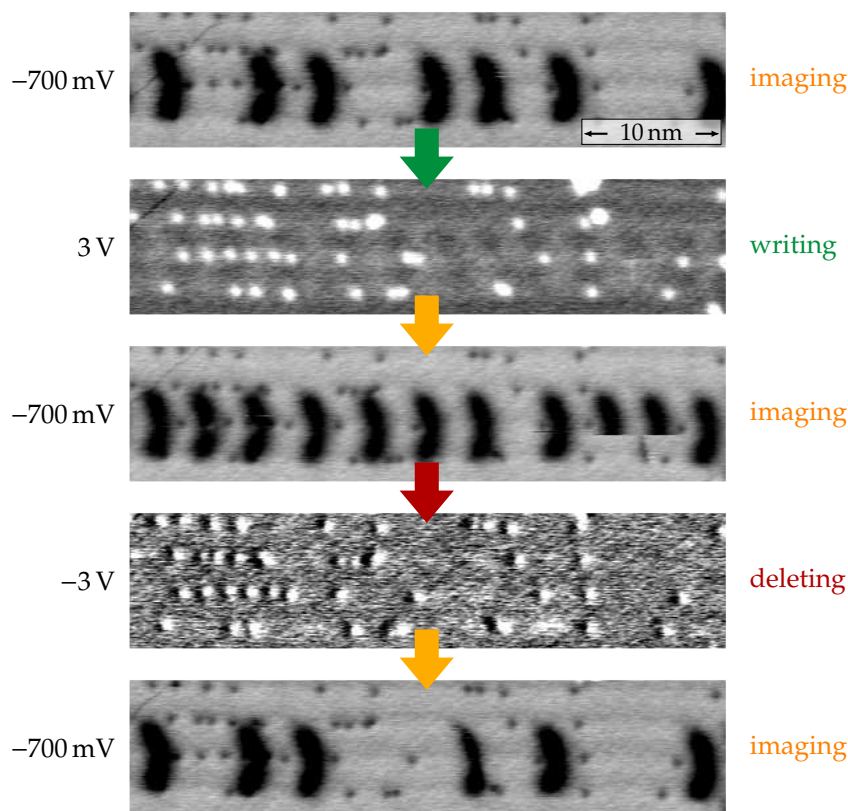


Figure IV.34: Spin resolved differential conductance maps showing how the skyrmions can be written and deleted by scanning the area at high positive (respectively negative) bias voltage. Not all the skyrmions react to the scanning procedure because some are stabilized stronger than the others (possibly by the dislocation lines and the defects). *Measurement parameters:*  $1$  nA,  $8$  K,  $2.5$  T, Cr bulk tip.

For the next scan, the bias voltage is set to  $-3$  V. Again, no magnetic signal is visible on the differential conductance map at this value but the next image is measured again with the imaging parameters and shows that the number of skyrmions is significantly reduced. This result suggests that scanning with  $-3$  V allows to erase the skyrmions. However, some of them do not react to this scanning procedure, possibly because they are more strongly stabilized (maybe by the lines and the defects) than the others.

In order to understand these observations, further switching experiments were performed. Figure IV.36 shows that the skyrmions can be individually written or deleted by applying voltage ramps. In the left column, the three skyrmions initially present are deleted one by one and

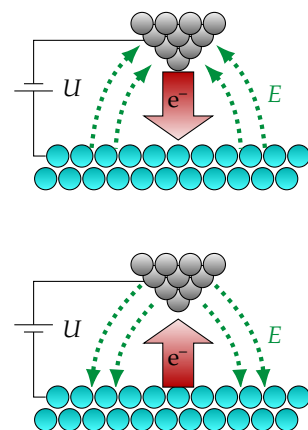


Figure IV.35: Sketch of the direction of the current and the electric field in the STM for the two opposite bias polarities during the switching experiments.

then individually written again using voltage ramps to  $-3$  V for writing and  $3$  V for deleting. For each skyrmion, the tip is stabilized in the area marked with the circle and then the bias is swept until the desired value. The area is then imaged again in order to check if the skyrmion was really written or deleted.

This strong polarity dependence for writing or deleting excludes that non-directional processes like Joule heating are dominant in the switching mechanism. It rather indicates that the electric field between the tip and the sample (see Figure IV.35) or the spin-transfer torque exerted by the spin-polarized current<sup>13</sup> play a crucial role.

13

J. Slonczewski.  
*Journal of  
Magnetism and  
Magnetic Materials*  
159, L1–L7 (1996)  
[130]

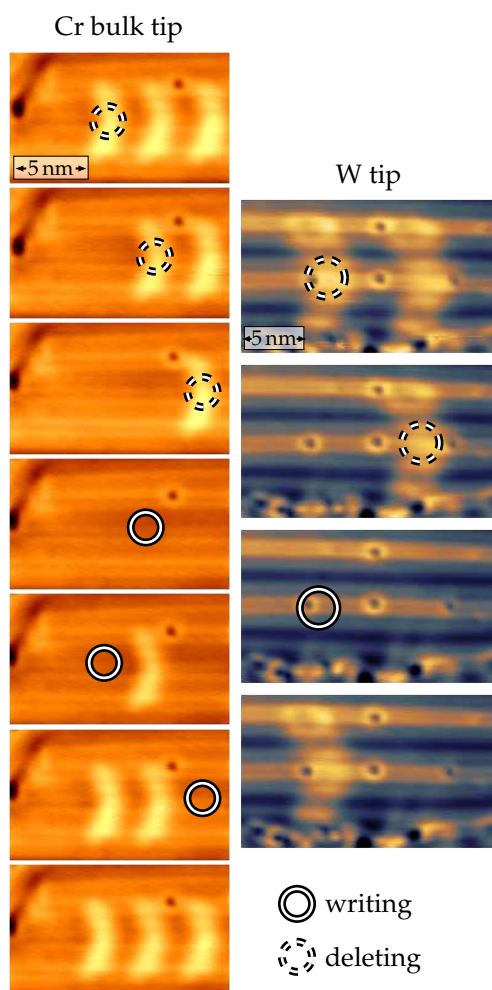


Figure IV.36: Constant-current maps showing the switching of the magnetic skyrmions using voltage ramps. On the left, the switching is performed with a spin-polarized Cr bulk tip, voltage ramps to  $3$  V are used for writing and ramps to  $-3$  V for deleting. On the right, the switching is demonstrated with a non-magnetic W tip and ramps to  $\pm 4$  V. In this case, the skyrmions are imaged using the NCMR effect. *Measurement parameters:* left:  $300$  mV,  $0.5$  nA,  $8$  K,  $2.5$  T, right:  $200$  mV,  $1$  nA,  $8$  K,  $-1.85$  T.

In the right column of Figure IV.36, the same experiment as on the left side is performed but with a non-magnetic W tip in order to gain more information. Since the tip is not spin-polarized, the skyrmions cannot

be measured with TMR as it is usually done with the Cr bulk tip. In this case, the observed contrast arises from the NCMR<sup>14</sup> (see section II.2.2.1). This time, the writing is performed with bias ramps up to 4 V, and ramps to -4 V are used for the deleting. The skyrmions can indeed be manipulated with the same procedure as with the spin-polarized Cr tip. However, a directional spin-transfer torque can be excluded when a non-spin-polarized W tip is used, which means that the switching must be electric field induced. Note that the switching is very reliable, once the appropriate value for the bias voltage is found for a particular skyrmion, every bias ramp allows to write or delete it.

<sup>14</sup> C. Hanneken et al. *Nature Nanotechnology* 10, 1039–1042 (2015) [62]

### IV.3.3 Demonstration of the role of an electric field in the switching mechanism

To support the conclusion that the skyrmion switching is really driven by the electric field, an additional experiment can be done. One should be able to show that for a given skyrmion, the writing (or the deleting) occurs at a threshold value of the electric field, independently of the current or the bias. In the simplified case where the system formed by the tip and the sample is treated as a parallel plate capacitor, the voltage  $U_{\text{th}}$  at which the skyrmion switches should depend linearly on the tip-sample distance  $d$ .<sup>15</sup> Figure IV.37 shows the expected dependence of  $U_{\text{th}}$  on  $d$  if the switching occurs at constant electric field, at constant current and at constant power. The curves shown were calculated using the following expressions relating the tip-sample distance  $d$ , the tunnel current  $I$ , the bias voltage  $U$ , the electric field  $E$  and the power  $P$ :

<sup>15</sup> L. Gerhard et al. *Nature Nanotechnology* 5, 792–797 (2010) [136]

$$E = \frac{-U}{d} \quad (\text{IV.17})$$

$$I \propto Ue^{-\kappa d} \quad (\text{IV.18})$$

$$P = UI \propto U^2 e^{-\kappa d} \quad (\text{IV.19})$$

Here the electric field pointing away from the surface is chosen negative. By measuring such a curve, one can thus discriminate between the different switching mechanisms.

#### IV.3.3.1 Measurement of the tip-sample distance

During constant-current STM measurements, the relative variations of the tip-sample distance are recorded. These are controlled by the feedback loop and are known with high precision. However, in order to estimate the electric field between the tip and the sample, it is necessary to know the absolute distance between them. This distance depends on the exact shape of the tip at the atomic scale and changes every time the apex of the tip is modified. There are two ways to measure this distance. In both cases, the dependence of the tunnel current on the tip-sample distance needs to be recorded. If the tip enters in contact with the surface

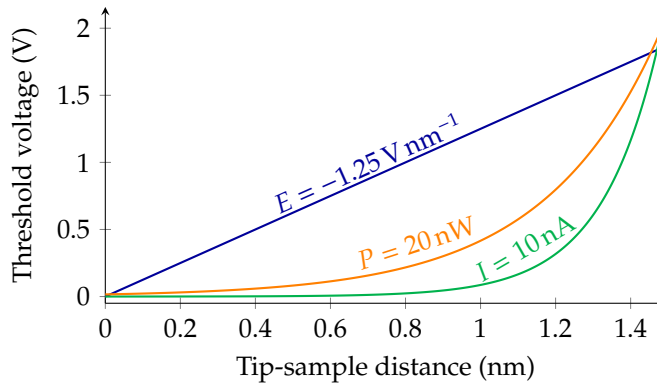


Figure IV.37: Expected dependence of the switching threshold voltage on the tip-sample distance if the switching occurs at a constant electric field, at a constant current or at a constant power. These curves were calculated as examples in order to show their different shapes and assuming that  $\kappa = 6.5 \text{ nm}^{-1}$  with a resistance at the contact between the tip and the sample of  $13 \text{ k}\Omega$ .

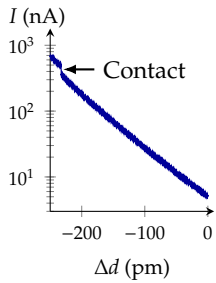


Figure IV.38: Variation of the tunnel current with the tip-sample distance at  $10 \text{ mV}$  showing the current jump at the contact point.

during such a measurement, a jump is visible in the data, as illustrated in Figure IV.38.

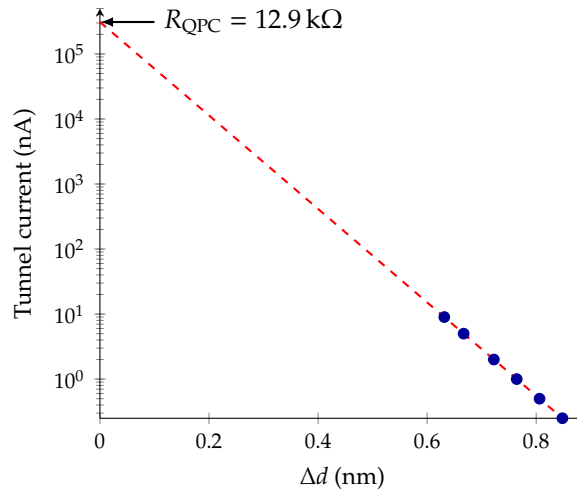


Figure IV.39: Dependence of the tunnel current on the relative tip-sample distance for the tip used in the switching experiment detailed in Figure IV.41, measured at  $4 \text{ V}$ . The expression of the tunnel current from equation IV.20 is fitted to the data points in order to estimate the absolute tip-sample distance, here  $(764 \pm 17 \text{ pm})$  at  $1 \text{ nA}$ .

The position of this jump allows to directly measure the absolute tip-sample distance. Nevertheless, there is a risk that the tip apex is modified during this procedure. Unfortunately, this curve was not measured for the exact tip used in the experiment shown in Figure IV.41. Another option is to use the current and relative tip-sample distance values available from the data at one fixed bias voltage and fit the curve using the following expression for the tunnel current, valid for intermediate bias voltages:<sup>16</sup>

$$I = \frac{U}{R_{\text{QPC}}} e^{-\kappa d} \quad (\text{IV.20})$$

<sup>16</sup> J. Simmons.  
*Journal of Applied Physics* 34,  
1793–1803 (1963)  
[137]

where  $\kappa = 2\sqrt{2m_e\phi}/\hbar$  is the decay constant of the tunnel current, depending on the work function  $\phi$ , and  $R_{\text{QPC}} = 12.9 \text{ k}\Omega$  is the quantum point contact resistance corresponding to the conductance quantum  $G_0 = 2e^2/h$ . This fit is shown in Figure IV.39 for the tip used in the experiment from Figure IV.41.

### IV.3.3.2 Calculation of the electric field from the parallel plate model

Once the distance between the tip and the sample is known, the voltage at which the switching occurs needs to be measured, using the procedure described in Figure IV.40. The tip is stabilized at 4 V on top of a skyrmion and the voltage is swept until  $-4 \text{ V}$ . During this sweep, the feedback is turned off: the tip-sample distance does not change but the tunnel current varies. The value of the current is recorded during the whole sweep and at the voltage at which the skyrmion is deleted, a jump is visible. Similarly, the voltage is swept back up to 4 V and another jump is visible when the skyrmion is written again.

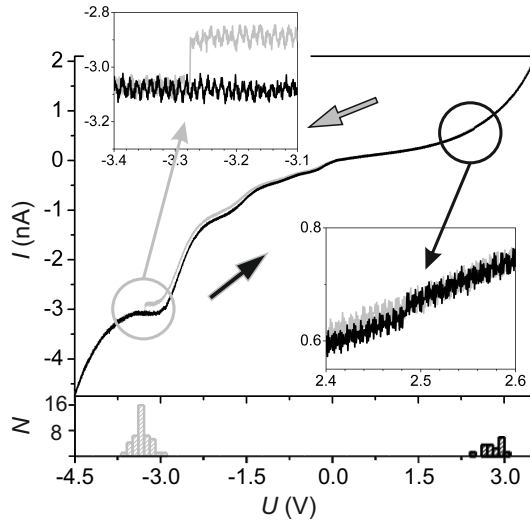


Figure IV.40: Measured tunnel current during a voltage ramp used for writing and deleting a magnetic skyrmion in the Fe triple layer on Ir(111). When the skyrmion switches, a jump is visible in the current, both for writing and for deleting. The threshold voltages correspond to these jumps. The histogram at the bottom shows the scattering of the threshold voltage for 42 repetitions of this experiment. The W tip was stabilized at 4 V, 1 nA, 8 K,  $-1.75 \text{ T}$  before starting the ramp shown here. Extracted from [95].

The threshold voltages for writing and deleting were measured for several values of the tip-sample distance using this procedure, with exactly the same tip (otherwise the data cannot be compared). These values are gathered in Figure IV.41, for two different magnetic field strengths.

The threshold voltages clearly have a linear dependence on the tip-sample distance, as expected for a switching induced by the electric field (see Figure IV.37). The values of the electric field are estimated by

fitting the data with a linear model, the obtained slope is simply the electric field in the parallel plate model. These values of a few  $\text{V nm}^{-1}$  are upper bounds because of the parallel plate approximation. Furthermore, the slope of the curve corresponding to the writing increases when the magnetic field intensity increases, whereas the slope of the deleting curve decreases. This effect is fully compatible with the variations of the stability of the magnetic states induced by the magnetic field. If the magnetic field increases, the ferromagnetic state is favored compared to the skyrmion state and thus it is easier to delete the skyrmions than to write them.

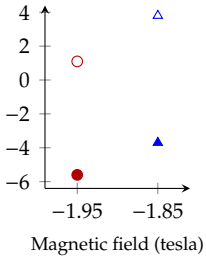
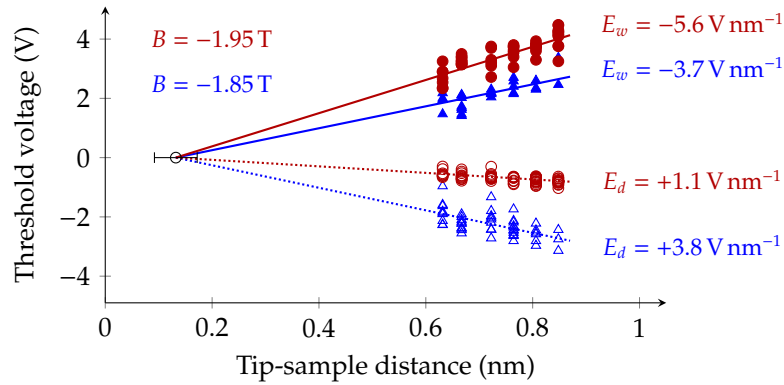


Figure IV.41: Dependence of the switching threshold voltage (see Figure IV.40) on the tip-sample distance for two values of the magnetic field. The data is linearly fitted using the parallel plate model in order to extract the value of the electric field needed to switch. Since the ferromagnetic state is favored by the magnetic field, a larger (respectively smaller) electric field is required to write (respectively delete) the skyrmions when the magnetic field increases.

Figure IV.42: Variation of the electric field required for the skyrmion switching with the magnetic field.

Figure IV.42 shows the variation of the electric field needed to switch the skyrmion with the magnetic field. From this, it is possible to estimate that  $1 \text{ V nm}^{-1}$  corresponds to a variation of 40 mT. The major difference is that in our STM setup, the application of a magnetic field modifies the global energy landscape of the system whereas the electric field switching allows to change locally the magnetic state.

### IV.3.3.3 Beyond the parallel plate model

Using the parallel plate approximation, the previous section demonstrates that the switching of the skyrmions is mainly driven by the electric field. This model also allows to estimate an upper bound of the electric field required to write or delete the skyrmion<sup>17</sup>, and this value depends on the magnetic field. However, this approximation might seem rough because the tip is in principle rather sharp. A further model is thus discussed here, the plane-sphere capacitor.

The electric field generated between a metallic sphere and a metallic plane, in the vicinity of the center of the sphere, is described by the

<sup>17</sup> A. Sonntag et al. *Physical Review Letters* 112, 017204 (2014) [138]

following expression<sup>18</sup>:

$$\vec{E} = -\frac{U}{d} \frac{\sqrt{d/R(1+d/R)}}{\ln\left(\sqrt{d/R} + \sqrt{1+d/R}\right)} \hat{e}_z \quad (\text{IV.21})$$

where  $U$  is the applied voltage and the geometrical parameters are defined in Figure IV.43. This is of course again an approximation of the electric field value, especially because the electric field value which matters for the switching is the value at the surface of the plane.

Figure IV.44 shows the dependence of the bias voltage on the tip-sample distance in order to keep a constant electric field of  $-5 \text{ V nm}^{-1}$  for various radii of the sphere (plot *a*) as well as for various electric field values and a sphere radius of 5 nm (plot *b*).

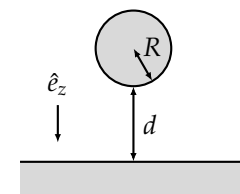


Figure IV.43: Geometry of the plane-sphere capacitor model.

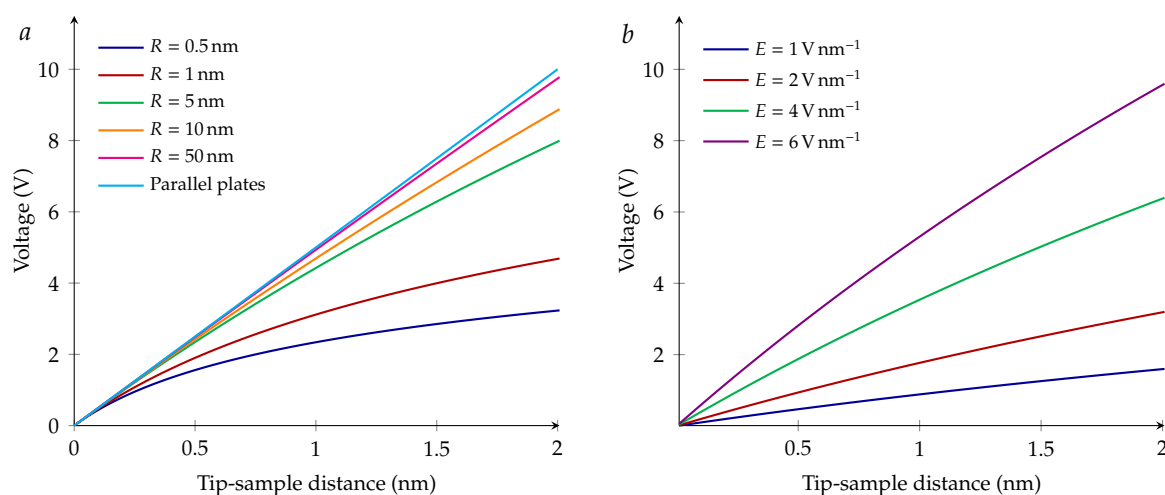


Figure IV.44: Variation of the bias voltage with the tip-sample distance in order to keep a constant electric field of  $-5 \text{ V nm}^{-1}$  for various radii of the sphere (plot *a*) and for various electric field values and a sphere radius of 5 nm (plot *b*), and comparison with the parallel plate model.

Already for a radius value of 50 nm, for the typical tip-sample distances used in the experiment, the difference to the parallel plate model is very small. Since the typical curvature radius at the end of an electrochemically etched W tip is a few tens of nm<sup>19</sup> and that in addition the tip used here is coated with an Fe film, the sphere-plane capacitor model does not allow to improve the estimation of the electric field value compared to the parallel plate model.

#### IV.3.3.4 Summary

Under the application of a magnetic field, the spin spirals from the double line areas transform into a skyrmion phase. These skyrmions are not axisymmetric but distorted because of the local arrangement of the Fe atoms. SP-STM measurements allow to prove that the direction of the magnetic moments wraps the whole unit sphere and confirm their

<sup>19</sup> I. Ekvall et al. *Measurement Science and Technology* 10, 11–18 (1999) [140]

skyrmionic nature. Using voltage ramps, the magnetic skyrmions can be locally switched. There is a clear polarity dependence of the switching which suggests that non-directional processes like Joule heating can be excluded for its driving mechanism. Furthermore, this switching can also be reliably performed using a non-magnetic W tip which also excludes spin transfer torque effects. The linear dependence of the electric field on the tip-sample distance also proves that the electric field is indeed dominant in the switching procedure. The demonstration of this local manipulation of skyrmions is a first step towards the development of energy-efficient spintronics devices because the writing and deleting processes do not require electrical currents.

# V. Tuning of non-collinear magnetism in Fe ultrathin films on Ir(111) by hydrogenation

In the previous chapters, the large influence of strain relief and of the corresponding dislocations on the magnetic state was demonstrated in Fe ultrathin films. Another way to modify the magnetic couplings within the film, besides adding a cover layer, is to incorporate H atoms. Indeed, it is known that the presence of H can modify the magnetic properties of single atoms<sup>1,2</sup> or ultrathin films<sup>3</sup>. This chapter will show that in the case of Fe on Ir(111), the hydrogenation increases the period of the spin spirals and modifies the nanoskyrmion lattice.

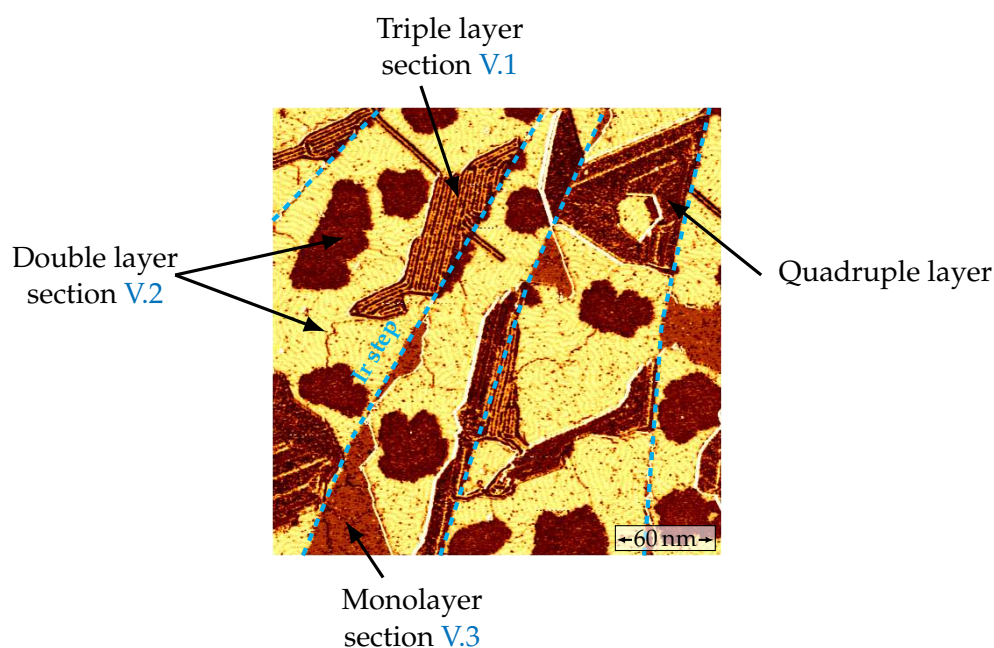


Figure V.1: Differential conductance map of an hydrogenated Fe film on Ir(111). The sample was hydrogenated in two cycles of H exposure at  $2 \times 10^{-8}$  mbar for 4 min and subsequent post-annealing at 300 °C for 10 min. Coverages from the monolayer to the quadruple layer are present in the scan area. *Measurement parameters:* 1 V, 1 nA, 4 K, 0 T.

Figure V.1 displays the differential conductance map of an hydrogenated Fe film. Different films thicknesses, from one to four Fe layers, are visible. The most striking effect of the H incorporation on the film structure is the vanishing of the dislocation lines in the Fe double layer. At the nanoscale, the H atoms form superstructures in the monolayer and the double layer and adsorb on the dislocation lines in the triple layer.

The first part (section V.1) of this chapter is a brief discussion about the

<sup>1</sup> Q. Dubout et al. *Physical Review Letters* 114, 106807 (2015) [141]

<sup>2</sup>

A. Khajetoorians et al. *Nature Nanotechnology* 10, 958–964 (2015) [142]

<sup>3</sup> B. Santos et al. *Physical Review B* 85, 134409 (2012) [143]

<sup>4</sup> P.-J. Hsu  
et al. *Nature  
Communications* 9,  
1571 (2018) [108]

effect of the incorporation of a small amount of H atoms on the period of the spin spirals in the Fe triple layer. The second part (section V.2) summarizes the results about the hydrogenation of the Fe double layer, in which a skyrmionic phase can be stabilized in a magnetic field<sup>4</sup>. Finally, a detailed analysis of the changes of the nanoskyrmion lattice occurring in the Fe monolayer is presented in the third part (section V.3).

*The data concerning the double and triple layer as well as about a third of the data about the monolayer were measured by Pin-Jui Hsu, who also analyzed the double layer data. The ab initio calculations concerning the hydrogenated double layer were done by Levente Rózsa. I measured the rest of the monolayer data and did the analysis for the monolayer and the triple layer.*

## V.1 Effect of hydrogenation on the triple layer spin spirals

In the absence of H atoms, two types of dislocation lines are present in the Fe triple layer on Ir(111) and spin spirals propagate along these lines,<sup>1</sup> as previously explained in detail in section IV.1. The following short discussion shows how these spirals are affected by the incorporation of H atoms.

<sup>1</sup> A. Finco et al.  
*Physical Review B*  
94, 214402 (2016)  
[88]

### V.1.1 Incorporation of the H atoms at the dislocation lines

Figure V.2 presents the morphology and the magnetic state of three different samples. The first one, column *a*, consists simply of a pristine Fe film on Ir(111) and is shown as a reference. Both single line and double line areas of the Fe triple layer are visible but they are hardly distinguishable in the constant-current map (top) at this bias voltage of  $-700$  mV.

This sample shown in column *b* was exposed to atomic H for 2 min at  $2 \times 10^{-8}$  mbar at room temperature and then post-annealed at  $300$  °C for 10 min. The atomic H is obtained by cracking H molecules at elevated temperature in a H source. In the constant-current map, the difference between the single and the double lines appears clearly although the bias voltage is the same as in column *a*. The double lines become darker than the single lines which indicates that the H atoms prefer to adsorb on them. This is reminiscent of the observation made on the pristine Fe triple layer that much more defects are located on the double lines than on the single lines (see Figure V.3). When the H amount is further increased, the sample can reach the state displayed in column *c*. In this case, the sample was exposed to atomic H for 4 min in two steps, with a post-annealing of 10 min at  $300$  °C after each exposure. The triple layer film becomes disordered but the position of the lines is still visible. The corrugation reaches  $60$  pm on the lines, which should be compared to the  $10$  pm corrugation at  $-1$  V on the pristine film.

The magnetic states of these three samples is shown in the bottom images of Figure V.2. The spin spirals are still present, even on sample *c* and they still propagate along the dislocation lines. However, some differences can be noticed. In sample *b*, the spin spirals on the single line areas are not really affected by the H atoms but on the double line areas, the period seems a little larger. Furthermore, the zigzag shape of the spin spiral wavefront disappeared. On sample *c*, the period is even larger and the difference between the single and the double lines is not clear anymore.

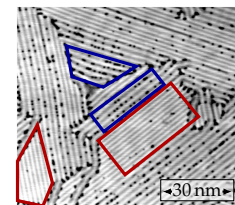


Figure V.3:  
Constant-current map at  $-500$  mV,  $1$  nA showing that more defects are located on the double line areas (blue) than on the single line areas (red).

### V.1.2 Increase of the spin spiral period

The apparent increase of the period of the spin spirals can be studied in the same way as for the pristine triple layer Fe on Ir(111). Indeed,

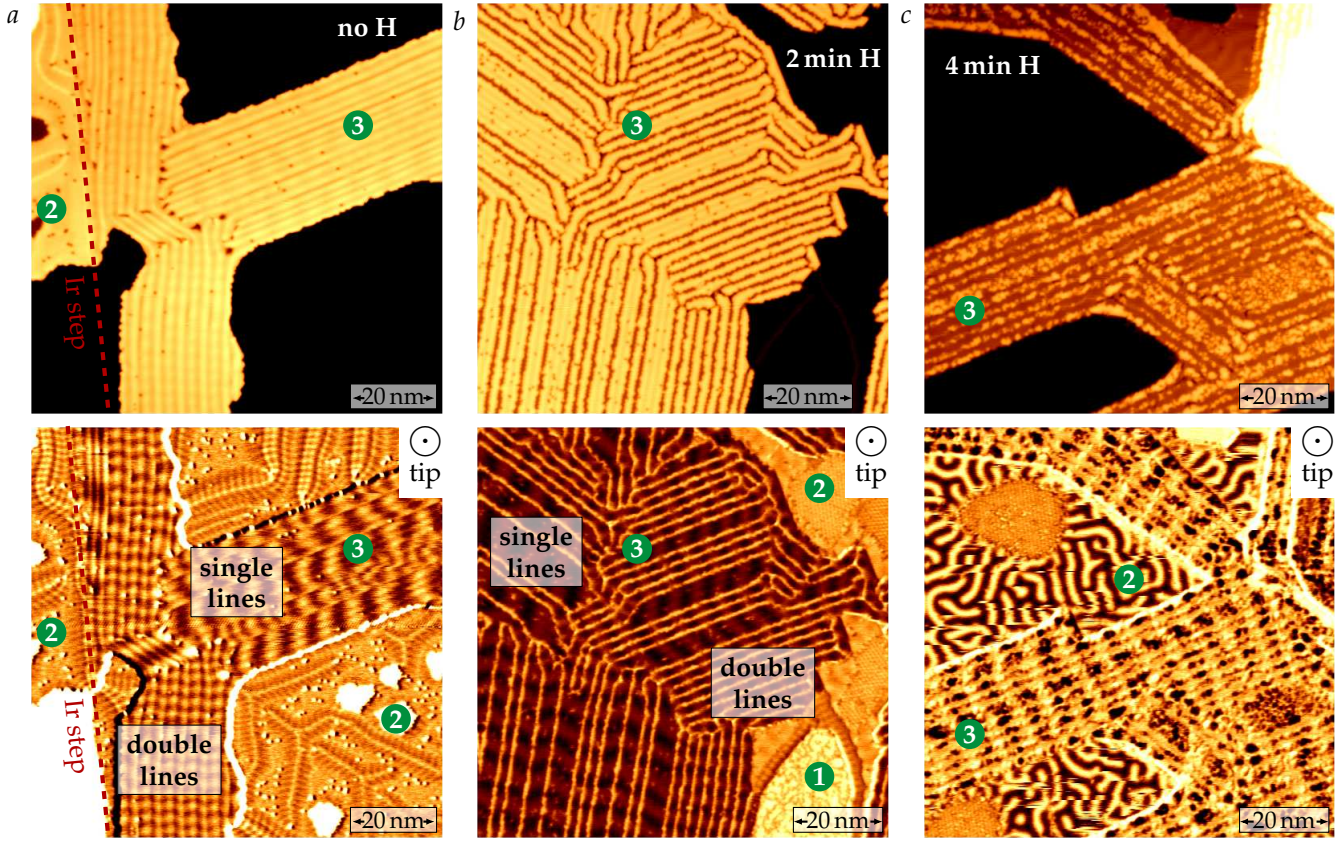


Figure V.2: Constant-current maps (top) and spin-resolved differential conductance maps (bottom) of three Fe on Ir(111) samples. The numbers in the green circles indicate the local Fe coverage (number of atomic layers). In column *a*, the pristine Fe film is visible whereas columns *b* and *c* present samples exposed to atomic H for respectively 2 min and 4 min at  $2 \times 10^{-8}$  mbar and subsequently post-annealed. The H atoms adsorb preferentially on the double lines and when the amount of H is large, the film becomes rather disordered. Nevertheless the spin spirals are still visible in the differential conductance maps *b* and *c*. *Measurement parameters: a, b: -700 mV, c: -1 V, 1 nA, a: 8 K, b, c: 4 K, 0 T, Cr bulk tip.*

the spiral period might depend again on the dislocation line spacing. Hence the best way to compare the hydrogenated and the pristine Fe triple layers is to measure the spin spiral period and the line spacing for various areas on a hydrogenated sample and then plot all the data together. Figure V.5 shows this plot. The sample considered is not strongly hydrogenated, it was only exposed to H for 45 s at  $2 \times 10^{-8}$  mbar (and subsequently post-annealed). Constant-current and differential conductance maps of a typical area can be found in Figure V.4. The double layer is not fully hydrogenated, some dislocation lines are remaining. On the triple layer, H atoms are located only on the double lines.

The script used to analyze the data is the same for the hydrogenated layer as the one used previously for the pristine layer (see section IV.1). Sufficiently large areas not obviously influenced by defects and neighboring spirals were chosen and both the spiral period and the dislocation line spacing were measured, either by Fourier transformation

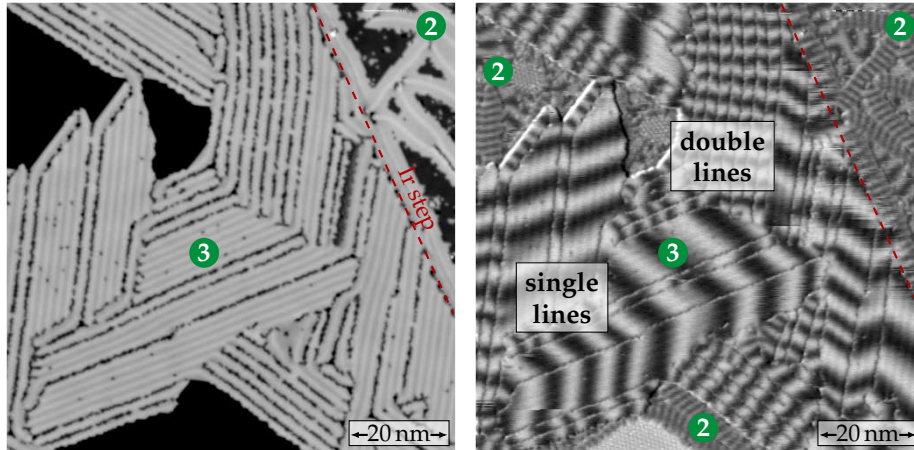


Figure V.4: Constant-current map (left) and spin-resolved differential conductance map (right) of a typical area on the sample used to measure the spin spiral period with respect to the dislocation line spacing in the hydrogenated triple layer Fe on Ir(111). The numbers in the green circles indicate the local Fe coverage (number of atomic layers). This sample was exposed to atomic H for 45 s and post-annealed 10 min at 300 °C. *Measurement parameters:* -700 mV, 1 nA, 4 K, 0 T, Cr bulk tip.

or fitting to a sine function. The data points with an error bar larger as 15% were removed.

The plot from Figure V.5 demonstrates that the period of the spin spirals actually increases in the double line areas. In the pristine sample, the period is about 3.5 nm whereas in the slightly hydrogenated one, the period is about 5 nm. This corresponds to an increase of 40%. Another observation is that there is not much dependence of the spin spiral period on the dislocation line spacing in double line areas. This effect might be related to a modification of the strain relief in the Fe film by the adsorption of the H atoms on the lines.

Concerning the single line areas, no clear effect is visible. The period does not seem to change much, which is expected since the H atoms do not adsorb in these areas. However, two data points correspond to a much lower period than usually observed. These periods are even similar to the ones found in the double layer areas. Figure V.6 shows one of the areas corresponding to these points.

The reason why the period of this spiral is lower than expected appears clearly: the period is coupled with the one of the neighboring double line area. The increase of the spin spiral period in the double line areas makes the periods in the two neighboring areas close enough for this phenomenon to be energetically favorable. The energy lost on the single line area because of the period being too small must be compensated by the energy gained in avoiding to break the spiral wave front.

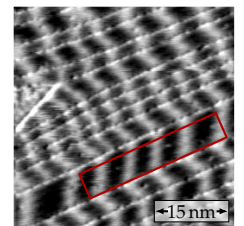


Figure V.6: Differential conductance map at -700 mV, 1 nA of one of the areas (in red) corresponding to the small periods in the single line areas.

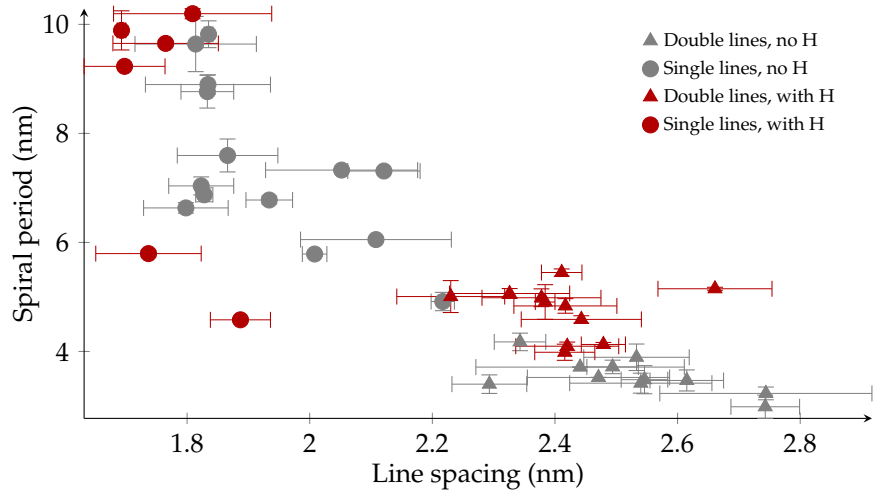


Figure V.5: Dependence of the spiral period on the spacing of the dislocation lines for the hydrogenated triple layer Fe on Ir(111). The data points corresponding to the pristine Fe triple layer are shown as a reference. The comparison between these two data sets shows that the period of the spin spirals increases by about 40% in the double line areas, where the H atoms adsorb. On the contrary, in the single line areas, no effect is observed which is expected since no H atoms are visible there.

In summary, atomic H can be incorporated in the triple layer Fe on Ir(111) to tune the magnetic state. The H atoms preferentially adsorb on the double lines and induce an increase of the spin spiral period. This effect is large: the increase reaches already 40% for a rather low H amount. The adsorption of the H atoms might modify the epitaxial strain relief within the Fe film.

## V.2 Emergence of a skyrmionic phase in the hydrogenated Fe double layer

In the double layer Fe, the presence of the H atoms has a much larger effect both on the film structure and its magnetic state than in the triple layer. Some hexagonal superstructures form, the period of the spin spirals is considerably increased and a skyrmionic phase is created under the application of an external magnetic field.

### V.2.1 Morphology of the hydrogenated film

As it was already discussed in section III.2, dislocation lines form in the Fe double layer on Ir(111) in order to relieve the epitaxial strain. Some pseudomorphic strained areas coexist with the lines. A constant-current map of such a surface of pristine Fe double layer is shown in Figure V.7, image *a*. When such a sample is exposed to atomic H for several minutes at a measured pressure of  $2 \times 10^{-8}$  mbar at room temperature and then post-annealed at 300 °C for 10 min, its structure changes drastically. As depicted on the map *b* in Figure V.7, almost all the dislocation lines disappear (in contrast to the Fe triple layer case discussed in section V.1) and two different hexagonal phases can be distinguished. They will be designated as H1 and H2 in what follows.

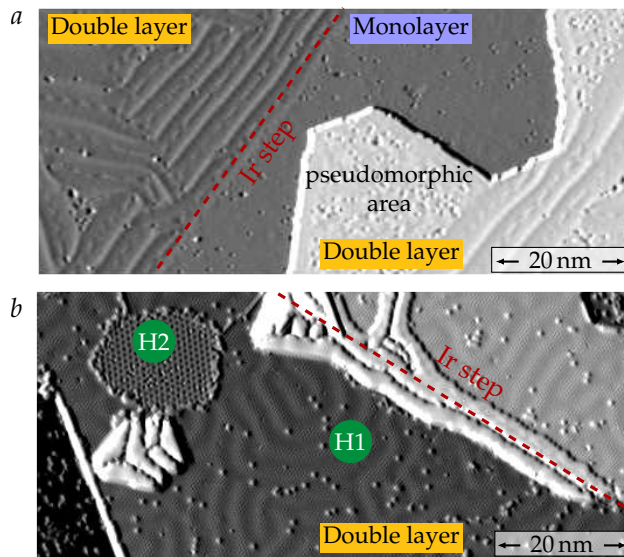


Figure V.7: STM constant-current maps of a pristine (image *a*) and a hydrogenated (image *b*) Fe double layer on Ir(111). The sample *b* was exposed to atomic H at  $2 \times 10^{-8}$  mbar for 4 min and post-annealed 10 min at 300 °C. The incorporation of H atoms allows to remove the dislocation lines and creates two phases, H1 and H2 exhibiting different hexagonal superstructures. The stripe pattern in the area H1 has a magnetic origin. The images were partially differential along the scanning direction to improve the visibility of the topographic features. *Measurement parameters: a: 200 mV, b: -200 mV, 1 nA, 4 K, 0 T, a: W tip, b Cr bulk tip.*

### V.2.1.1 A $p(2 \times 2)$ superstructure: the H1 phase

A closer view on the H1 superstructure is shown in Figure V.8 as well as two possible structure models for the position of the H atoms. The superstructure is hexagonal, with a size of 0.54 nm, which corresponds to twice the lattice constant of the Ir(111) surface. Furthermore, the superstructure is aligned with the surface and is thus a  $p(2 \times 2)$  superstructure. From the STM measurements, the vertical position (on top, between the Fe layers or at the Fe/Ir interface) of the H atoms is unknown.

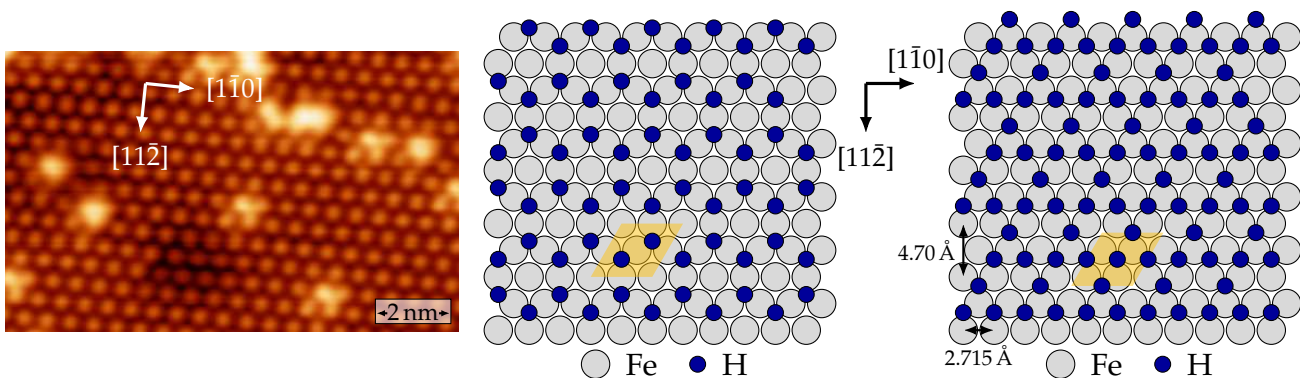


Figure V.8: High-resolution STM constant-current map of the H1 phase on the hydrogenated Fe double layer on Ir(111). The  $p(2 \times 2)$  superstructure is clearly visible. Two possible models indicating the positions of the H atoms are also shown. Adapted from [108].

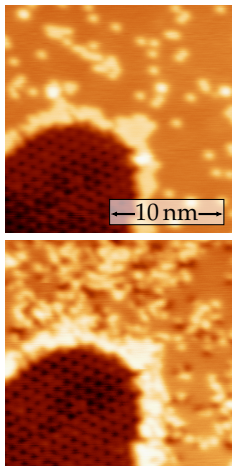


Figure V.10: Constant-current map measured with 1 V and 1 nA of the boundary between the H1 and H2 phase before and after a scan at 8 V and 9 nA.

### V.2.1.2 A larger and rotated hexagonal superstructure: the H2 phase

Whereas most of the Fe double layer is covered by the H1 phase, some islands with a larger hexagonal superstructure are always present. Figure V.9 shows the details of the structure. The corrugation is higher on this superstructure than on the H1 phase. The period of the hexagonal lattice is 0.98 nm. This time, the structure is not aligned with the high-symmetry lines of the Ir(111) surface, there is a  $14^\circ$  angle between the rows of dots in the H2 phase and in the H1 phase. Two possible models of the superstructure are depicted in Figure V.9.

The transition between the H1 and the H2 phase is very sharp and always clearly visible. Furthermore, Figure V.10 shows constant-current maps recorded at a boundary between the two phases before and after it was scanned at 8 V and 9 nA. The H1 phase becomes disordered whereas the H2 phase is not much modified and the limit between them remains sharp and clear. This suggests that the H atoms in the H2 phase are located deeper inside the film than in the H1 phase.

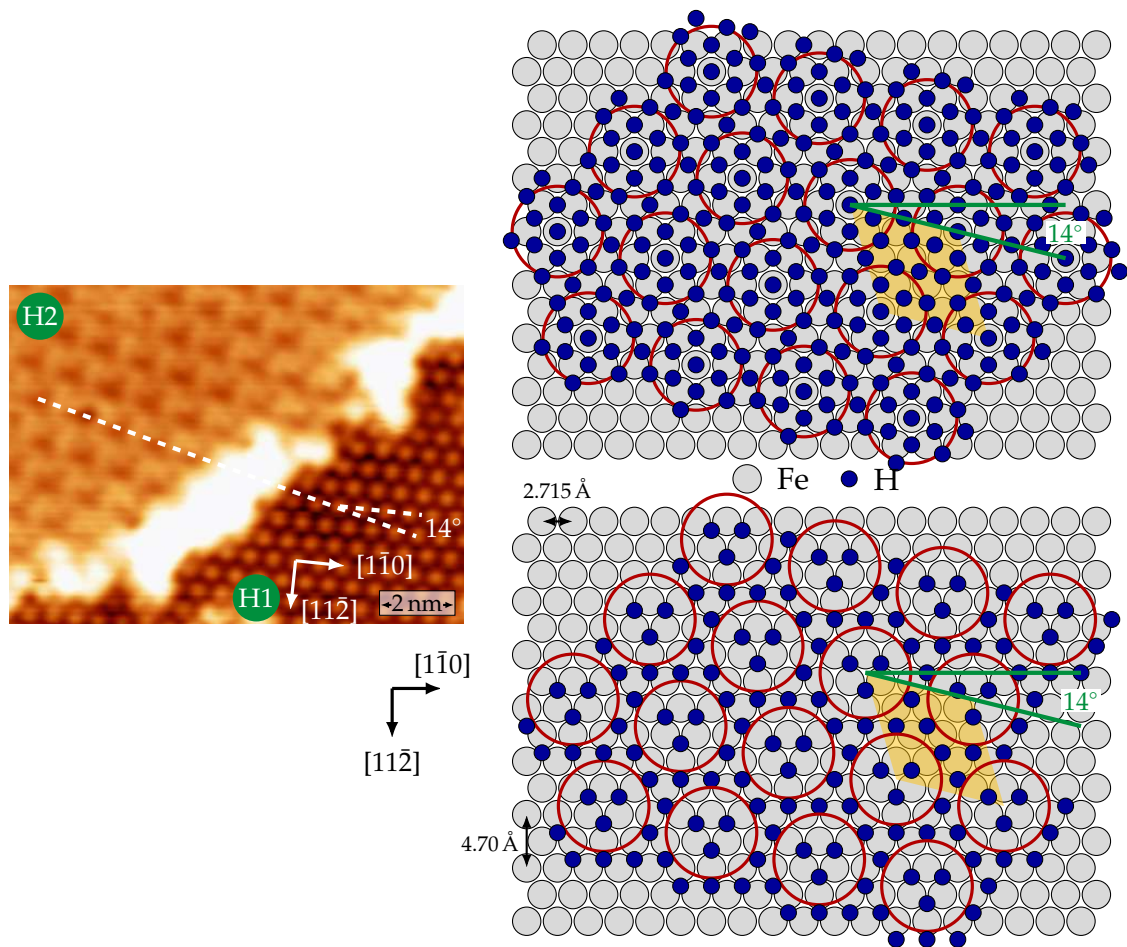


Figure V.9: High-resolution STM constant-current map of the hydrogenated Fe double layer on Ir(111), showing the hexagonal superstructures H1 and H2. The  $14^\circ$  angle between the two lattices is visible here. Two possible models indicating the positions of the H atoms in the H2 phase are also shown. Adapted from [108].

## V.2.2 Magnetism in the two hydrogenated phases

### V.2.2.1 Spin spirals and ferromagnetic islands

Spin-resolved measurements reveal the magnetic state in the two hydrogenated phases. Figure V.11 shows a constant-current map measured on an area containing both phases with an out-of-plane sensitive Cr bulk tip. The two H2 islands appear uniform (except for the pattern of the superstructure) but with different heights. This indicates a ferromagnetic state and the two islands have opposite magnetization directions. The H1 areas exhibit a stripe pattern which is very similar to the one observed in Pd/Fe/Ir(111)<sup>1</sup> and corresponds to a spin spiral. In this case, the propagation direction of the spiral can vary within the area because it is not guided by dislocation lines anymore. The typical period of this spiral is 3.5 nm, much larger than the 1.2 nm period measured in the strained pseudomorphic pristine Fe double layer film or the 1.5 nm to 2 nm period of the guided spirals<sup>2</sup>.

<sup>1</sup> N. Romming et al. *Science* 341, 636–639 (2013) [6]

<sup>2</sup> P.-J. Hsu et al. *Physical Review Letters* 116, 017201 (2016) [85]

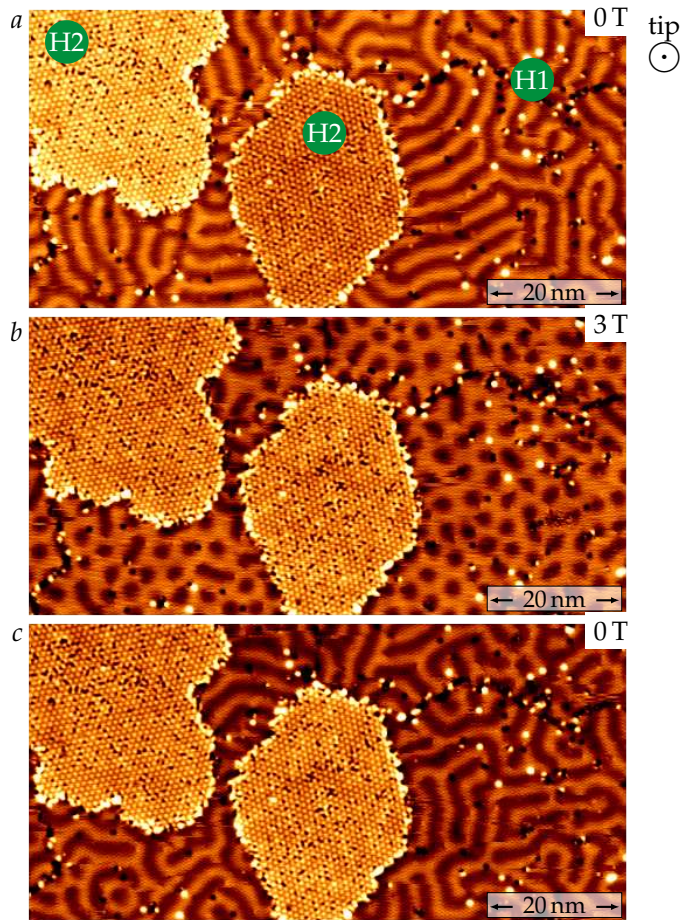


Figure V.11: STM constant-current maps showing the magnetic state of the two hydrogenated phases H1 and H2. Image *a* was measured at zero field. The magnetic field was increased to 3 T in image *b* and decreased again to zero for image *c*. One of the ferromagnetic H2 islands switched with the magnetic field and some skyrmions form in the H1 phase at 3 T. The tip is sensitive to the out-of-plane component of the magnetization. Adapted from [108]. *Measurement parameters*:  $-700$  mV, 1 nA, 4 K, Cr bulk tip.

When an out-of-plane magnetic field of 3 T is applied to the sample, the apparent height of one of the H2 islands decreases (as shown on the image *b*) and becomes the same as on the other island. This behavior confirms that the H2 islands are ferromagnetic, the island on the left aligned with the magnetic field. On the H1 phase, the spirals almost disappear at 3 T and some circular objects form. The next section will show that these objects are magnetic skyrmions. When the field is decreased again to zero, the magnetic state of the H2 islands remains unchanged and the spin spirals reappear in the H1 phase.

### V.2.2.2 Formation of magnetic skyrmions in magnetic field

In order to check that the circular objects observed in the H1 phase at 3 T are skyrmions, the in-plane component of the magnetization needs to be measured. Figure V.12 presents such a measurement with an in-plane

sensitive tip. Instead of appearing as dark dots like in Figure V.11, the magnetic objects present a bright and a dark lobe, as expected for magnetic skyrmions imaged with an in-plane sensitive tip. Furthermore, the dark lobe is on the left and the bright lobe on the right for all of them, which indicates that they are indeed skyrmions with a unique rotational sense. When the magnetic field increases, the number of skyrmions and their size decreases, as illustrated by the images *b* and *c*. This behavior is expected for magnetic skyrmions and was previously observed and investigated in detail for the Pd/Fe/Ir(111) system.<sup>3</sup>

<sup>3</sup> N. Romming et al. *Physical Review Letters* 114, 177203 (2015) [40]

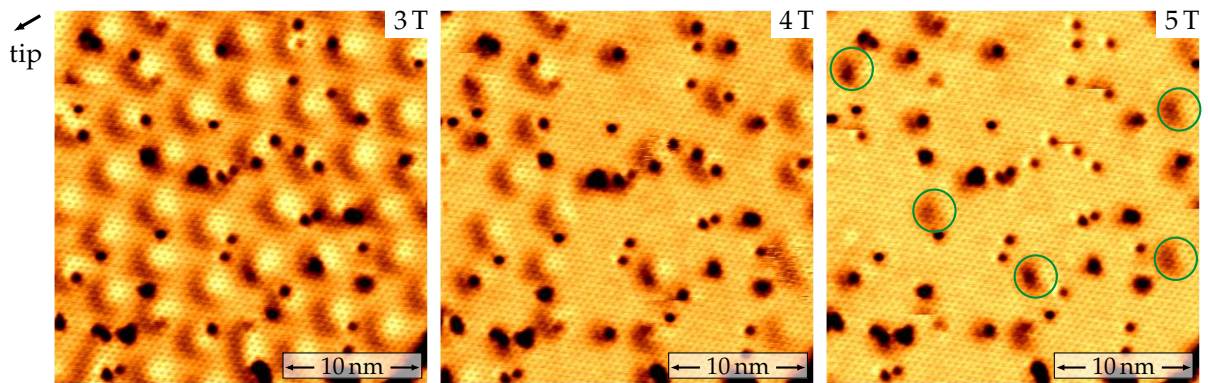


Figure V.12: Spin-resolved differential conductance maps of the magnetic state in the H1 phase in the Fe double layer under magnetic field. The tip is sensitive to the indicated in-plane component of the sample magnetization. All the magnetic objects exhibit the same contrast consisting of a dark and a bright lobe, which indicates that they are skyrmions with a unique rotational sense. When the magnetic field increases, their number and their size decrease. In the image *c*, only very few skyrmions are left and marked with green circles, the other dark dots are defects. Adapted from [108]. *Measurement parameters*:  $-200$  mV,  $1$  nA,  $4$  K.

### V.2.3 Ab initio calculations

In order to provide a complete analysis of the system, the results of ab initio calculations performed for the hydrogenated Fe double layer are summarized in this section. All the details can be found in the published article<sup>4</sup> on this topic.

The effect of the presence of H atoms in different vertical positions and concentrations was investigated with density functional theory calculations. The results are gathered in Figure V.13. For the pristine pseudomorphic Fe double layer (i.e. without any H atoms), the calculated period of the spin spirals is  $1.4$  nm which is very close to the measured period of  $1.2$  nm in the pseudomorphic areas.<sup>5</sup> If a layer of H atoms is placed on top of the Fe bilayer, almost no effect is found for the spiral period. In contrast, when the H atoms are located in the octahedral sites between the two Fe layers, the calculated period of the spin spirals reaches  $9.2$  nm and when they are at the Fe/Ir interface, the ground state is ferromagnetic. This indicates that in the H2 phase, the H atoms are probably placed at the Fe/Ir interface and in the H1 phase, between the two Fe layers.

<sup>4</sup> P.-J. Hsu et al. *Nature Communications* 9, 1571 (2018) [108]

<sup>5</sup> P.-J. Hsu et al. *Physical Review Letters* 116, 017201 (2016) [85]

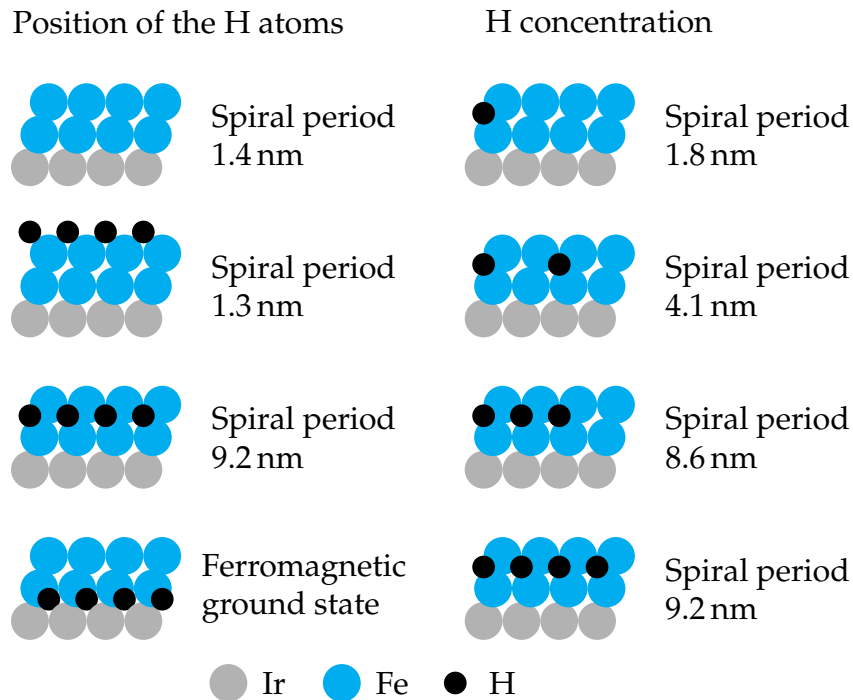


Figure V.13: Sketch gathering the values of the spin spiral period obtained from ab initio calculations for a Fe double layer on Ir(111) with H atoms incorporated at different vertical positions and with different concentrations. From these results, the H atoms would be located at the Fe/Ir interface in the H2 phase. In the H1 phase, half a layer of H atoms would be positioned between the two Fe layers.

This large change of the obtained spin spiral period occurs because the hybridization between the atoms in the different layers is modified by the variation of the distances between the layers. In particular, the distance between the Fe layers increases when the H atoms are placed between them. When the H atoms are at the interface, both the distance between the Fe layers and the distance between the Fe and the substrate are increased.

The effect of the H concentration was also investigated in the case where the H atoms are placed between the Fe layers. The spin spiral period becomes larger when the H amount increases. This is also linked to the increase of the distance between the Fe layers when more H atoms are incorporated, but there is also an effect of the hybridization of the Fe and H orbitals. For a concentration of 0.5 atomic layer, the calculated period of 4.1 nm is close to the measured 3.5 nm.

Further calculations were performed in order to evaluate the influence of the H incorporation on the strength of the magnetic interactions. The used spin model includes the nearest- and next-nearest-neighbor exchange interactions, the DMI and the on-site magnetic anisotropy and was applied to the pristine layer, to the probable H1 phase with 0.5 layer of H atoms between the Fe layers and to the probable H2 phase with the H atoms at the interface. From this calculations, it appears that the frustration of the exchange interaction plays a crucial role for

the stabilization of the spin spiral in the pristine Fe double layer. This frustration is reduced in the H1 phase, where the spin spiral state is stabilized by the DMI. In the H2 phase, the DMI is nearly quenched by the presence of the H atoms at the interface and the ground state is thus ferromagnetic.

In summary, the hydrogenation of the Fe double layer allows to remove the dislocation lines which form to relieve the epitaxial strain, and creates two different hexagonal superstructures. One of them exhibits a ferromagnetic ground state whereas spin spirals are observed in the other one in the absence of a magnetic field. The period of these spirals (3.5 nm) is much larger than in the pristine Fe double layer (1.2 nm). When a magnetic field is applied, the spirals disappear and transform into magnetic skyrmions, which is not the case for the pristine Fe double layer. The incorporation of atomic H in ultrathin films is thus demonstrated to be an efficient way to tune non-collinear magnetic states.

## V.3 Modification of the nanoskyrmion lattice in the Fe monolayer by hydrogenation

Since the hydrogenation of the Fe double layer on Ir(111) has such a large impact on the magnetic state, allowing to stabilize a skyrmionic phase around 3 T, the next step is to investigate the hydrogenated monolayer. As it was previously detailed in section II.4, the magnetic state of the pristine fcc Fe monolayer is a square nanoskyrmion lattice<sup>1</sup>. The goal of the following study is to explore the effect of hydrogenation on this complex two-dimensional magnetic structure.

<sup>1</sup> S. Heinze et al. *Nature Physics* 7, 713–718 (2011) [27]

### V.3.1 Formation of two superstructures

#### V.3.1.1 The hexagonal superstructure

When a Fe/Ir(111) sample is exposed to atomic H and then post-annealed in order to prepare the hydrogenated double layer, some H atoms are also incorporated in the Fe monolayer. This hydrogenation of the monolayer occurs only once the double layer is fully covered by the H1 and H2 phases. When the supplied amount of H is not sufficient to cover the complete monolayer, some small patches of hydrogenated Fe film form. They appear as regularly distributed darker areas on the constant-current map of Figure V.14, like the one marked with a white circle.

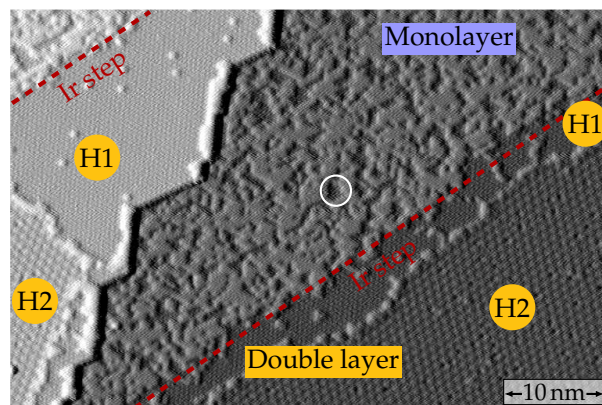


Figure V.14: Constant-current map of a hydrogenated Fe film on Ir(111). This sample was exposed to H for 15 min at  $2 \times 10^{-8}$  mbar for a Fe coverage of about 1.5 atomic layers. The double layer areas are covered with the H1 and H2 phases created by H exposure whereas the H amount was not sufficient to fully hydrogenate the monolayer. Some darker areas are thus visible on the monolayer (like the one marked with a white circle), which correspond to the areas where the H atoms are incorporated into the Fe film. The image was partially differentiated along the scanning direction in order to improve the visibility of the topographic features. *Measurement parameters:*  $-700$  mV, 1 nA, 8 K, 0 T, Fe coated W tip.

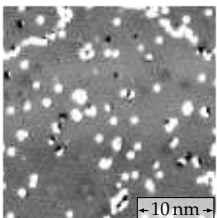


Figure V.15: Fully hydrogenated Fe monolayer, after 10 min H exposure at  $2 \times 10^{-8}$  mbar.

In order to obtain a fully hydrogenated monolayer, the sample preparation needs to be optimized. The Fe/Ir(111) sample is exposed to

atomic H at room temperature, which means that the sample is kept at least one hour in the vacuum chamber after the last annealing or after it was taken out of a cold microscope before the H dosage. Since the Fe is deposited at elevated substrate temperature, the pristine monolayer grows from the step edges in fcc stacking.<sup>2</sup> The pressure measured by the ion gauge during the H exposure is about  $2 \times 10^{-8}$  mbar. The exact amount of H needed depends on the Fe coverage. From the sample shown in Figure V.15, for a Fe coverage slightly below 1 AL without double layer areas, an exposure of 10 min is required to get a uniform hydrogenated monolayer. After the H exposure, the sample is post-annealed. The temperature should not be too high to avoid that the H desorbs. Therefore, low power (0.3 W) was used for 10 min in our electron beam heater setup. The estimated corresponding temperature is 300 °C, by extrapolation of the curve measured with a pyrometer (see Figure V.16) which is not accurate at this low power.

The samples can be prepared either in a single hydrogenation step or with subsequent steps. It is indeed possible to add more H to the Fe film when the amount is not sufficient, by simply exposing the sample to atomic H at room temperature and post-annealing again. For example, starting from the sample in Figure V.14, after exposing the sample to atomic H for 5 additional minutes and post-annealing, the Fe monolayer can be fully hydrogenated, as shown in Figure V.17. With this amount of H, a very regular hexagonal superstructure is formed, which has the same size and orientation than the H1 superstructure in the hydrogenated double layer (see section V.2.1).

<sup>2</sup> S. Heinze et al. *Nature Physics* 7, 713–718 (2011) [27]

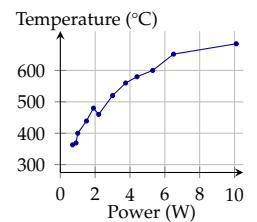


Figure V.16: Measured temperature of the sample depending on the heating power.

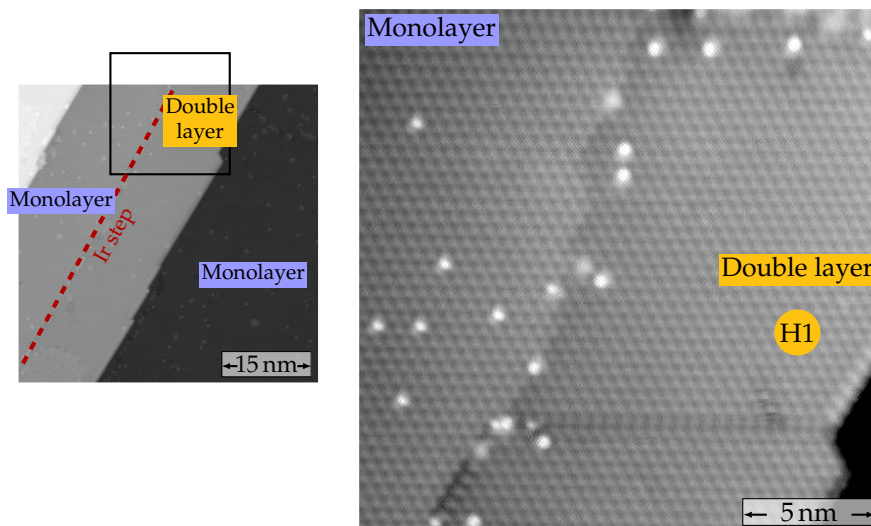


Figure V.17: Constant-current maps of a fully hydrogenated Fe film on Ir(111). This sample is the one in Figure V.14, exposed to H for 5 min more at  $2 \times 10^{-8}$  mbar and post-annealed. A hexagonal superstructure is formed on the monolayer, very similarly to the H1 phase in the double layer, as shown on the zoom-in. *Measurement parameters:*  $-700$  mV, 1 nA, 8 K, 0 T, Fe coated W tip.

The constant-current map of Figure V.19 reveals a different appearance

<sup>3</sup> P.-J. Hsu et al. *Nature Communications* 9, 1571 (2018) [108]

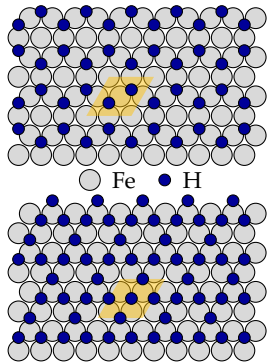


Figure V.18: Two atomic structure models proposed for the H1 phase in the double layer [108].

of the H superstructure in the monolayer and the double layer. It displays the interface between the two superstructures imaged at a different bias voltage. In this case, the superstructure in the double layer appears as an arrangement of bright protrusions. A detailed analysis leads to the conclusion that these bright protrusions correspond to H vacancies.<sup>3</sup> Two possible atomic structure models are thus proposed for this superstructure (see Figure V.18). Note that in the double layer, the H atoms are probably located between the two Fe layers.

In the case of the monolayer, the superstructure appears as a hexagonal pattern of dark dots. Since the transition from the superstructure in the double layer to the one in the monolayer is very smooth and no phase domain wall is visible, there must be a continuous transition from one superstructure to the other. This suggests that the dark dots indicate the lateral positions of H atoms. The H concentration would thus be lower in the monolayer superstructure. One cannot conclude from the STM data if the atoms are located on top of the Fe layer or at the Fe/Ir interface. The corresponding atomic structure model is drawn in Figure V.19.

In addition, as indicated with the red and blue lines on the zoomed area in Figure V.19, the rows of bright protrusions in the double layer are not aligned with the rows of dark dots in the monolayer. The two lattices are shifted by a distance corresponding to a third of the spacing between two rows. This observation allows to exclude one of the models proposed for the arrangement of the H atoms in the double layer superstructure, as it is explained in Figure V.20. This figure shows some schematics of the transition between this model and the two possible models for the double layer.

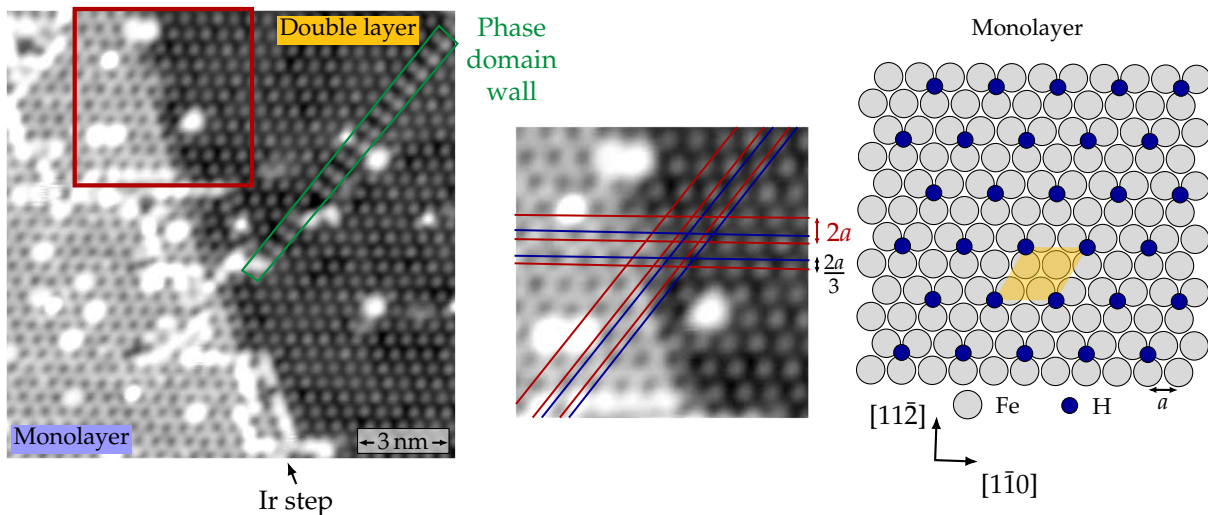


Figure V.19: Constant-current map of the interface between the H superstructures in the monolayer and in the double layer Fe. At this bias voltage, the superstructure appears as bright protrusions on the double layer and dark dots on the monolayer. The two structures have obviously the same size and the same orientation, they are both  $p(2 \times 2)$  structures. The zoom-in allows to see their precise respective alignment. The red lines mark the rows of bright dots, the blue lines the rows of dark dots. A possible atomic structure model for the H superstructure of the monolayer Fe is also shown. *Measurement parameters:* 50 mV, 1 nA, 8 K, 0 T, Fe coated W tip.

In model *b*, all the H atoms as well as the center of the bright dots in the double layer are located at equivalent lattice sites. The rows of H atoms in the monolayer are exactly in the center between the rows of bright dots in the double layer, in contradiction with the data. The model *b* can thus be excluded. On the other side, in model *a*, the H atoms are placed either in hcp or fcc sites and the bright dots on top sites. In this case, the rows of H atoms in the monolayer are not in the center between the rows of bright dots but shifted, which is in agreement with the experimental observation.

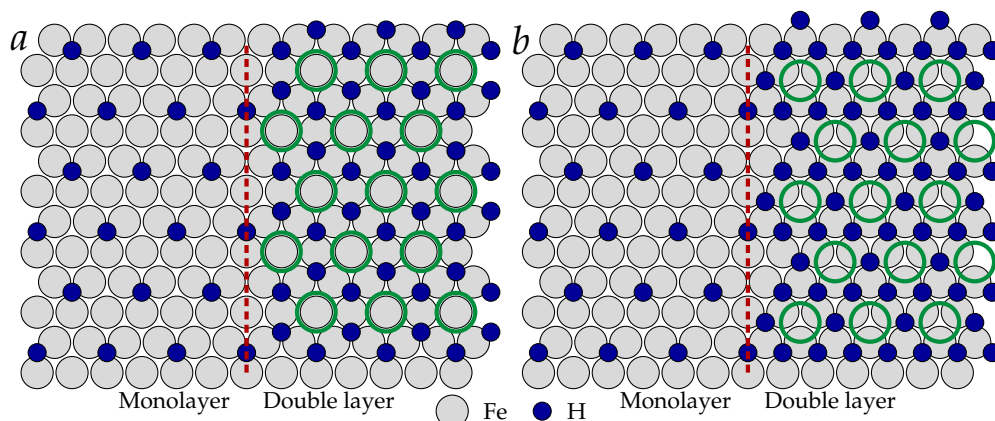


Figure V.20: Transition between the model for the monolayer from Figure V.19 and the models shown in Figure V.18. The positions of the bright dots are marked with green circles. The dark dots in the monolayer correspond to the H atoms. The precise alignment between the two structures allows to exclude the model *b* because the rows of dark dots in the monolayer are not centered between the rows of bright dots. They are rather at a third of the distance between two rows, which is compatible with model *a*.

### V.3.1.2 The square superstructure

If even more atomic H is added to the Fe film, a new H superstructure appears. As it was seen for the transition from the pristine film to the hexagonal superstructure, some regularly distributed small areas with a presumably higher H concentration and a new superstructure form in the already hydrogenated monolayer.

The emergence of this new phase is visible in Figure V.21, on which the Fe monolayer was exposed to atomic H for 4 min at  $2 \times 10^{-8}$  mbar and subsequently post-annealed at the usual temperature about 300 °C for 10 min, twice, for a Fe coverage of about 0.9 atomic layer. If a sufficient amount of H is provided, the complete monolayer Fe can exhibit this new superstructure which will be called the *square superstructure* in the following even though the pattern is not exactly square but only close to a square pattern. From the various sample preparations performed, none of them allowed to obtain this square superstructure after only one cycle of H exposure and post-annealing. At least two of these cycles seem to be required, which suggests that it is easier to build the square superstructure once the hexagonal one is already formed.

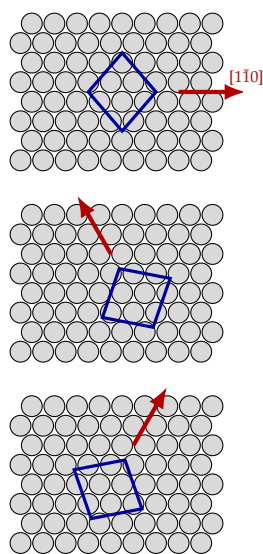


Figure V.22: The three symmetry equivalent orientations of the superstructure on the (111) surface.

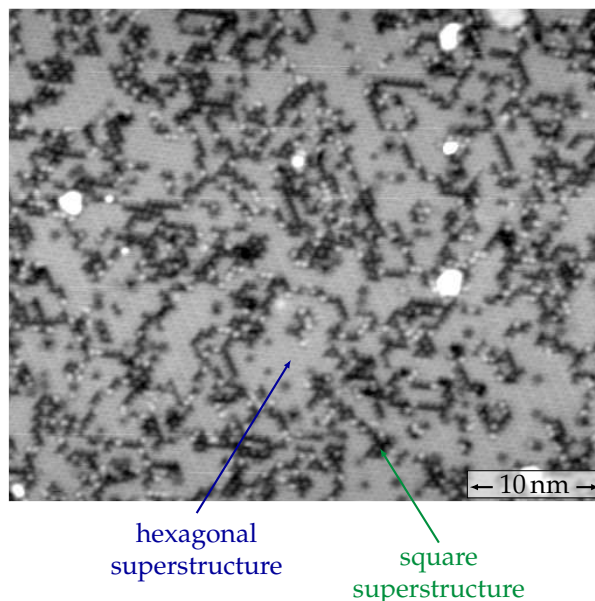
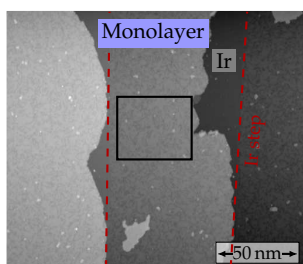


Figure V.21: Constant-current map of a hydrogenated Fe film on Ir(111) showing the emergence of a new square H superstructure. The Fe coverage is about 0.9 atomic layer and the sample was exposed twice to H during 4 min at  $2 \times 10^{-8}$  mbar and post-annealed after each exposure. The irregular shape at the bottom is a double layer island. *Measurement parameters:* 1 V, 1 nA, 4 K, 0 T, Cr bulk tip.

A sample exhibiting a monolayer Fe fully covered by the square superstructure is presented in Figure V.23. As expected from symmetry arguments, three rotational domains are found and marked with A, B and C. One direction of the diagonals of the square is oriented along the close-packed rows of the (111) surface. This is visible here from the direction of the straight edges of the double layer island, straight edges usually follow high-symmetry directions. There are thus three equivalent possibilities for the orientation of the superstructure (see Figure V.22), leading to the presence of three rotational domains.

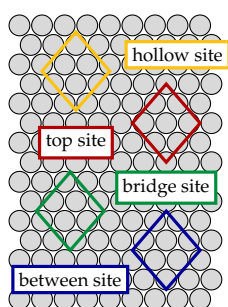


Figure V.24: Sketch of various positions for the unit cell of the superstructure.

The position of the unit cell in the sketch of Figure V.23 is rather unusual. Neither the corner nor the center is located on a top, a hollow or a bridge site of the atomic lattice. This choice was made for symmetry reasons. Indeed, if a corner is placed on a top or a hollow site, the other corners of the unit cell are not located at symmetry equivalent positions, as depicted in Figure V.24 (yellow and red position). If a bridge site is selected as a corner, the system does not have a mirror symmetry (green position). However, such a symmetry is present in the data. The chosen position with the corners between the rows of atoms (blue position) allows to define a lattice of points located on similar sites, with a mirror symmetry. The superstructure is not fully regular and this is already visible in the overview of Figure V.23. Besides the presence of many defects and the merging of some protrusions (marked with the green circles), the size of the protrusions is varying and their positions are not exactly periodic. From the closer view, it becomes clear that the superstructure

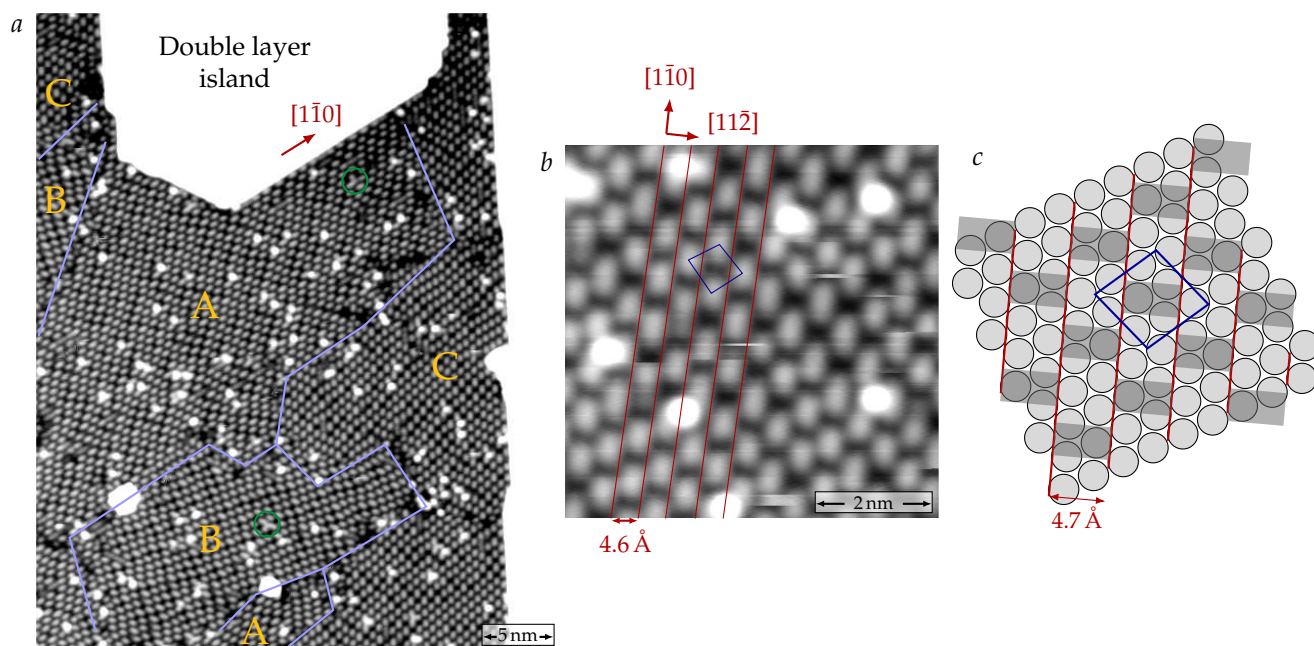


Figure V.23: Constant-current maps of a hydrogenated Fe film exhibiting the square superstructure on the monolayer and sketch of a possible structure model. The three rotational domains are visible in the overview *a* and the straight edges of the double layer island indicate the direction of the close-packed rows of the (111) surface. The closer view *b* reveals the details of the structure and its irregularity. In the sketch *c*, the darker areas on the constant-current map are marked in gray. *Measurement parameters:* *a*: -800 mV, *b*: 500 mV, 1 nA 4 K, 0 T, Cr bulk tip.

is commensurate with the substrate along the  $[11\bar{2}]$  direction, but shows a variable length along the other diagonal, the  $[1\bar{1}0]$  direction. Each row of bright protrusions corresponds to two rows of Fe atoms as depicted in the sketch. The bright protrusions are elongated along these rows and their length and spacing is not fixed. In the most regular areas like the lower left corner of the zoom-in, the average distance between the protrusions along the close-packed row is 8.1 Å, which means three times the lattice constant of 2.7 Å. In the more irregular areas, this distance can be larger. Furthermore, since this superstructure probably has a larger H concentration than the hexagonal one and appears usually lower in the topography (see the mixed structure in Figure V.21), more H atoms might be located in the dark areas between the protrusions than in the protrusions. The sketch of the unit cell presented in Figure V.23 is derived from all these observations but represents an ideal regular structure. The exact number of H atoms and their positions remain unknown.

The square superstructure is also very mobile. Some movement of the bright protrusions is induced by the tip, even at moderated bias voltages below 1 V as shown in Figure V.25. Note that some jumps are already visible at 500 mV in Figure V.23. One can relate this to the absence of proper ordering of the H atoms on the surface. Since the H atoms are not located on well-defined positions, nothing really prevents their movement. It could also indicate that some of the H atoms are adsorbed

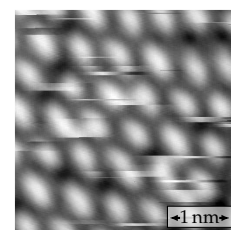


Figure V.25: Tip-induced movement on the square superstructure at -800 mV, 1 nA.

on top of the Fe film rather than at the Fe/Ir interface where they would be less sensitive to the influence of the tip. Nevertheless, the H atoms cannot be very easily desorbed from the surface: scanning with  $-3\text{ V}$  and  $60\text{ nA}$  is not enough to damage the superstructure, only to induce more movement. Higher voltage and current values were not tested.

## V.3.2 The hexagonal nanoskyrmion lattice in the $p(2\times 2)$ superstructure

### V.3.2.1 A commensurate hexagonal pattern

Going back to the hexagonal  $p(2\times 2)$  superstructure, its magnetic state can now be discussed. Figure V.26 shows a constant-current map of such an hydrogenated Fe monolayer as well as the simultaneously recorded spin-resolved differential conductance map.

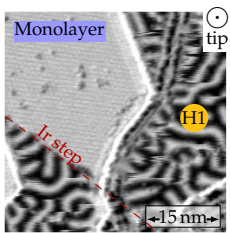


Figure V.27: Differential conductance map used as a reference to determine the tip sensitivity in Figure V.26 using the spin spirals of the H1 phase of the double layer.

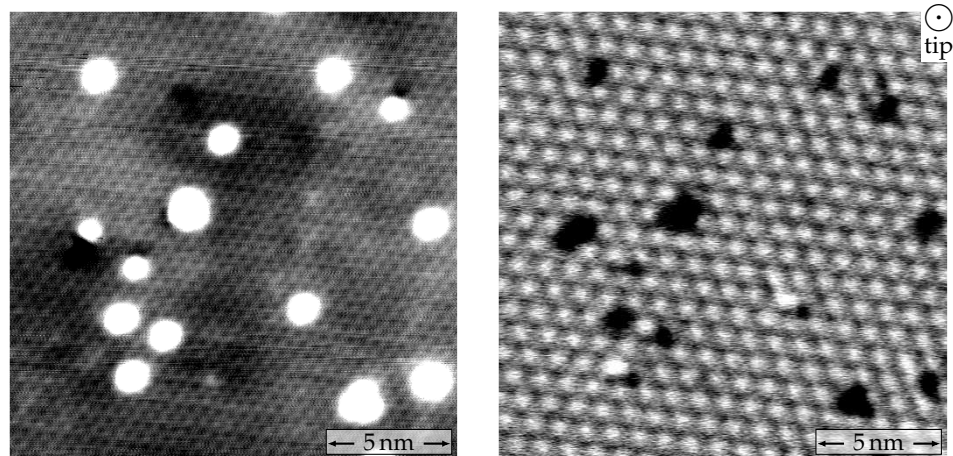


Figure V.26: Constant-current map (left) and simultaneously recorded spin-resolved differential conductance map (right) of an hydrogenated Fe monolayer exhibiting the  $p(2\times 2)$  superstructure. An hexagonal pattern larger than the superstructure is visible in the differential conductance map, which reveals the out-of-plane component of the sample magnetization. The two images were shifted in the scanning direction according to the difference between the forward and the backward scans in order to check the matching of the two structures. *Measurement parameters:*  $-1\text{ V}$ ,  $1\text{ nA}$ ,  $4\text{ K}$ ,  $0\text{ T}$ , Cr bulk tip.

The H superstructure appears as a lattice of dark dots on the constant-current map and a larger hexagonal pattern of bright dots is visible on the differential conductance map. The tip sensitivity was determined using the spin spirals of the H1 phase of the hydrogenated double layer also present on the sample as a reference. Since the intensity of the magnetic contrast is the same irrespective of the propagation direction of the spiral (see Figure V.27), the tip is sensitive to the out-of-plane component of the sample magnetization.

The hexagonal magnetic pattern in the differential conductance map has the same orientation as the H superstructure and is two times larger, with a period of  $1.08\text{ nm}$  determined from the Fourier transform of

Figure V.28. The magnetic unit cell would then simply be twice the unit cell of the  $p(2 \times 2)$  superstructure and form a  $p(4 \times 4)$  structure. In order to check that the magnetic state is really commensurate and aligned with the H superstructure, it is possible to correlate the data from the constant-current map with the simultaneously recorded differential conductance map. To measure the differential conductance, the component of the current at the modulation frequency is extracted using lock-in technique. This requires to integrate the signal over time, which is not the case for the topography measurement. Hence the two maps might be shifted even though they were measured at the same time and this shift needs to be corrected. First, the difference in lateral position is evaluated along the scanning direction between the forward and the backward scan for both channels. A difference of 4 pixels is found for the topography, whereas for the differential conductance it reaches 12 pixels. This indicates that the two channels are indeed slightly misaligned. Both maps were then shifted to the middle position and cut to display the very same area. Then the two images in Figure V.26 can be carefully compared. This analysis confirms that the magnetic unit cell is commensurate with the H superstructure and has the double size.

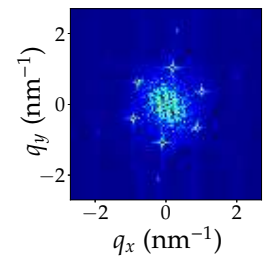


Figure V.28: Zoom in on the central region of the Fourier transform from the differential conductance map in Figure V.26.

### V.3.2.2 Switching of domains in out-of-plane magnetic field

Whereas no rotational domains are present in the hexagonal H superstructure, two opposite magnetic domains can be found. Figure V.29 shows again the magnetic data from Figure V.26 as well as the magnetic state in another area, imaged with the same tip sensitive to the out-of-plane component of the sample magnetization. The magnetic pattern is not made of bright dots anymore but of dark dots on a bright background: the magnetic contrast is inverted.

The next step is to apply an out-of-plane magnetic field to the sample and see if one of the domains switches. This experiment is shown in Figure V.30 where two adjacent domains are visible in the absence of magnetic field. At the beginning, the tip is mostly sensitive to an in-plane component of the sample magnetization. In the insets on each domain, the image was smoothed with a gaussian filter in order to make the difference between the two domains more obvious. When the out-of-plane magnetic field is applied, the tip becomes mostly sensitive to the out-of-plane component of the magnetization. This behavior is not expected for an antiferromagnetic Cr bulk tip and suggests that there is an Fe cluster at its end and that the magnetization of this cluster aligns with the magnetic field. Although the magnetic state is not affected by the field up to 6 T, this modification of the tip sensitivity allows to distinguish more clearly the two opposite domains. At 9 T, the left domain switches. This switching confirms that the two magnetic domains found are oppositely magnetized and indicates that the out-of-plane magnetic moment is not compensated within the magnetic unit cell, similarly to what was observed for the hexagonal nanoskyrmion lattice in the hcp

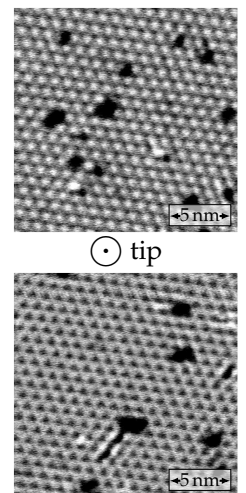


Figure V.29: Differential conductance maps showing the two opposite magnetic states imaged with  $-1$  V,  $1$  nA,  $0$  T.

pristine monolayer Fe on Ir(111).

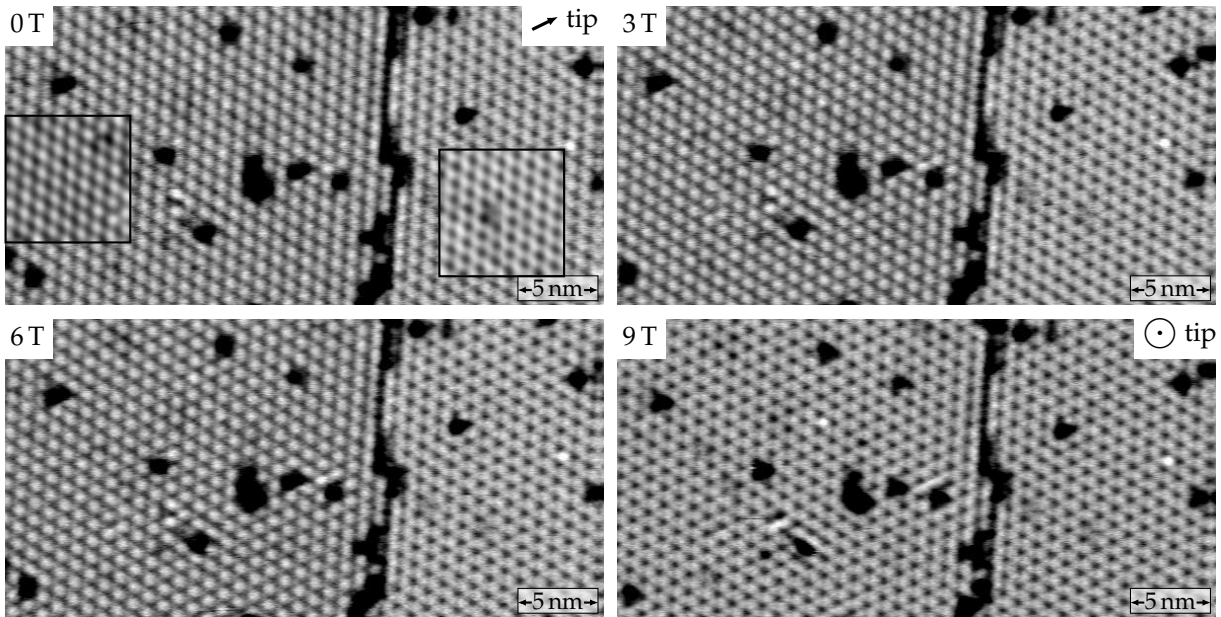


Figure V.30: Spin-resolved differential conductance maps of a hydrogenated Fe monolayer covered with the hexagonal superstructure. At zero field, the tip is mostly sensitive to an in-plane component of the magnetization (but a small out-of-plane component is also visible) and two opposite magnetic states are present in this area. The image was smoothed with a Gauss filter in the areas marked with squares in order to enhance the difference between the domains. An out-of-plane magnetic field is applied to the sample and increased in several steps. The magnetization of the apex of the Cr bulk tip unexpectedly gradually aligns with the field which suggests that there might be an Fe cluster at the end of the tip. This allows to better see the difference between the two domains up to 6 T. At 9 T, the domain on the left switches. *Measurement parameters:*  $-700$  mV, 1 nA, 4 K, Cr bulk tip.

### V.3.2.3 Two possible nanoskyrmion lattice states

The information about the magnetic state of the  $p(2 \times 2)$  hydrogenated Fe monolayer derived from the previous observations can be summarized:

- the state is a hexagonal lattice with a size of 1.08 nm,
- commensurate and aligned with both the Fe lattice and the H superstructure,
- and with a net out-of-plane magnetic moment within the unit cell.

This immediately suggests that a hexagonal nanoskyrmion lattice like the one present in the hcp pristine monolayer<sup>4</sup> would be a good candidate to be the actual magnetic state. The hexagonal nanoskyrmion lattice consists of the superposition of three symmetry-equivalent spin spirals. In the case of the hydrogenated monolayer, the cycloidal spin spirals used for the superposition propagate along the  $[11\bar{2}]$  direction, which means perpendicular to the close-packed rows, with a period of four rows. These three spirals with the same rotational sense are depicted in Figure V.31. The state obtained by adding the three spirals together is drawn in Figure V.32. The magnetic unit cell contains 16 atoms. The size of the magnetic moments is kept constant on every lattice site by

<sup>4</sup> K. von Bergmann et al. *Nano Letters* 15, 3280–3285 (2015) [72]

normalizing the moments after adding the spirals together. There is still a degree of freedom concerning the position of the magnetic structure with respect to the atomic lattice. Since the magnetic state appears to have at least a three-fold symmetry, the point where the magnetic moment is oriented in the out-of-plane direction can only be either on a top site or a hollow site of the atomic lattice.

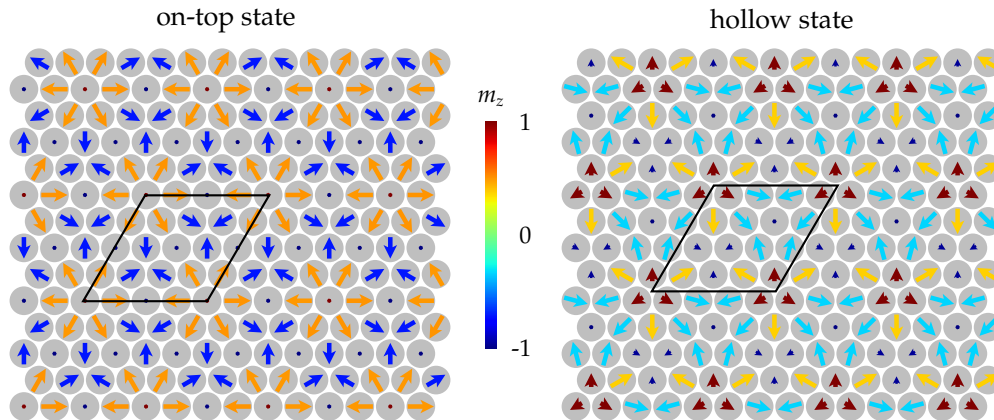


Figure V.32: Representations of the two possible hexagonal nanoskyrmion lattice states obtained by adding the three spin spirals from Figure V.31 and normalizing the magnetic moments. In order to keep at least the three-fold symmetry, the points where the magnetic moments are oriented out-of-plane have to be located either on top sites of the atomic lattice or on hollow sites.

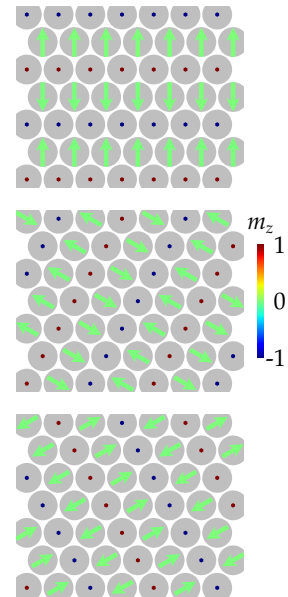


Figure V.31: The three spirals added to create the nanoskyrmion lattice.

These two possibilities lead to the two states shown in Figure V.32. They both have a topological charge of  $\pm 1$  per magnetic unit cell which justifies their designation as nanoskyrmion lattices. For the hollow configuration, there are two inequivalent possibilities: the hollow site on the atomic lattice can either be a fcc or a hcp site which means that the point of maximum out-of-plane magnetization is located in the center of an up-pointing or a down-pointing triangle of atoms. Since these sites are not equivalent, these two states might have different energies and it is not necessary that they coexist on the sample. Only one of them is represented in Figure V.32.

Both the on-top and the hollow configurations can be inverted in a symmetry equivalent state (in the absence of a magnetic field) which allows the formation of two opposite magnetic domains. The two states have a net out-of-plane magnetic moment. For the configurations shown in Figure V.32 with normalized magnetic moments, the net moment of the on-top configuration is  $-3.24$  per unit cell of 16 atoms and  $-2.75$  per unit cell for the hollow configuration. A magnetic field can thus break the symmetry and favor one of the domains, leading to the observed switching.

### V.3.2.4 Comparison with the data

<sup>5</sup> S. Heinze.  
*Applied Physics A*  
 85, 407–414 (2006)  
 [71]

In order to check if the on-top state and/or the hollow state corresponds to the data, one can use SP-STM simulations<sup>5</sup> (see section II.2.2.3) and compare them to the magnetic pattern obtained for various directions of the tip sensitivity. Figure V.33 shows this comparison for the out-of-plane tip sensitivity. Only the TMR effect is taken into account in the simulations. The images corresponding to both the on-top and the hollow states reproduce the hexagonal pattern of bright or dark dots and look very close.

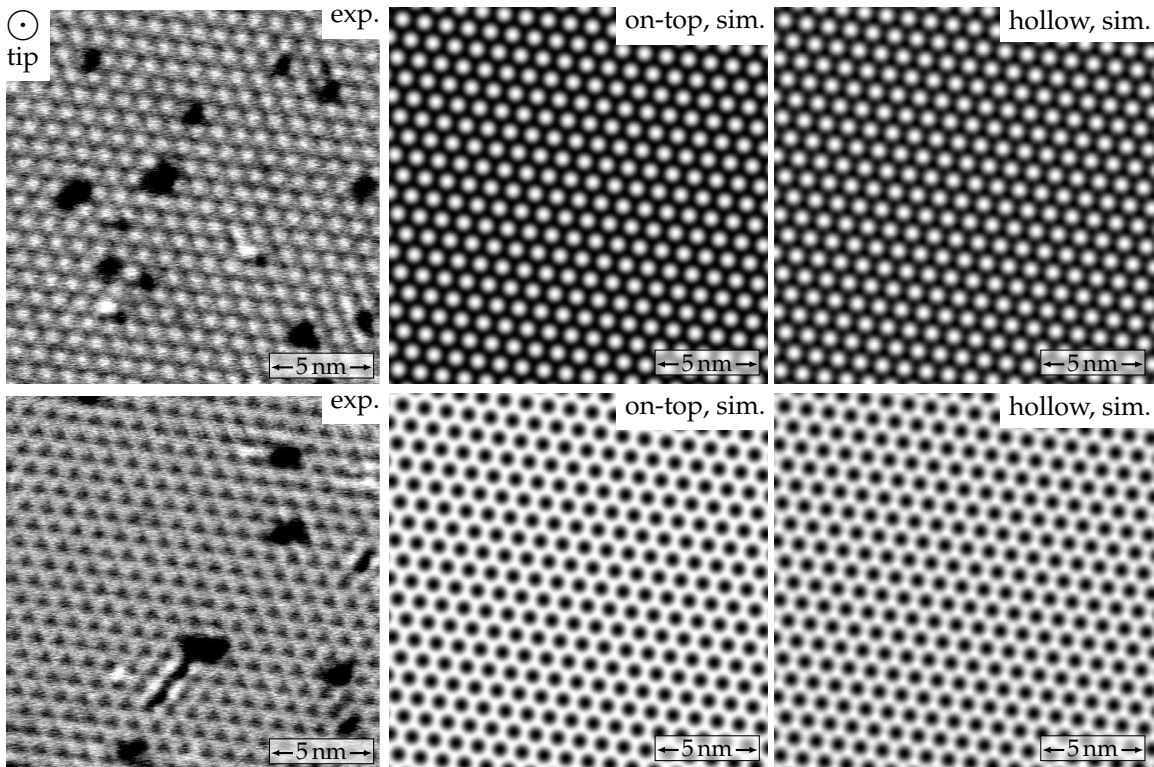


Figure V.33: Comparison between spin-resolved differential conductance maps on the left and SP-STM simulations on the right for the two magnetic domains in the hydrogenated Fe monolayer on Ir(111) presenting the hexagonal superstructure. The tip is sensitive to the out-of-plane component of the sample magnetization in both the experiments (see Figure V.27) and the simulations. The hexagonal patterns of bright or dark dots are reproduced by the on-top and the hollow state. The simulations were performed with the following realistic parameters: tip-sample distance  $z_0 = 600$  pm, work function  $\psi = 4.8$  eV and polarization  $P_s P_t = 0.2$ .  
*Measurement parameters:*  $-1$  V,  $1$  nA,  $4$  K,  $0$  T, Cr bulk tip.

However, one can already notice some small discrepancies, like for example the slightly triangular shape of the dark dots in the experimental data which is not visible in the simulations. This effect is probably caused by the H atoms and will be discussed later in section V.3.2.5.

The comparison also needs to be done with tips sensitive to in-plane magnetization components in order to cover the full magnetic structure. Usually, the direction of the magnetic moment at the apex of the Cr bulk tip is not fully in-plane but canted. Therefore, a small out-of-plane

angle is added to the direction of the magnetization at the tip apex in the simulations in order to reproduce better the data. Figure V.34 displays the comparison with a mostly in-plane sensitive tip, again for the two opposite magnetic domains. The in-plane direction of the tip sensitivity is indicated, perpendicular to one direction of close-packed rows and there is an additional angle of  $20^\circ$  outside the plane, otherwise the two domains would be indistinguishable (for this in-plane direction). In this case, the sensitivity of the tip could not be derived from the data and was determined using the simulations. The distorted checkerboard pattern is again well reproduced by both the on-top and the hollow state.

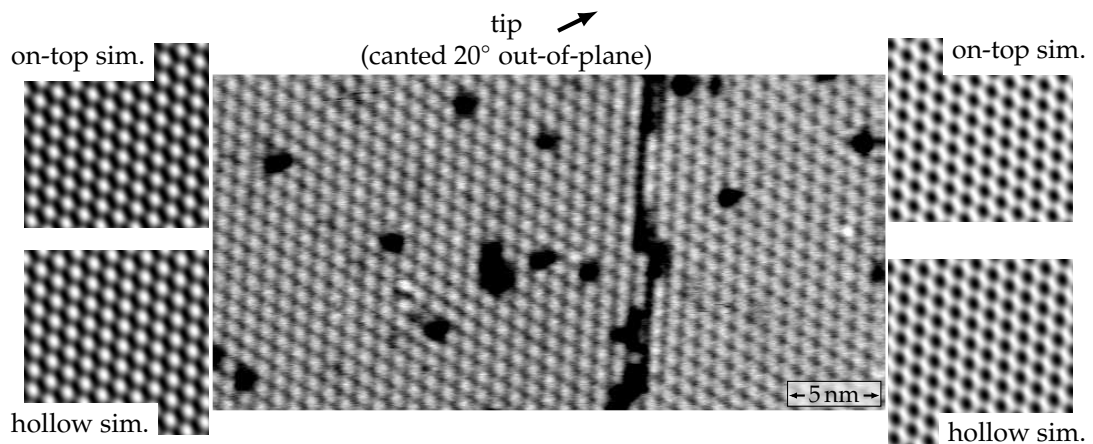


Figure V.34: Comparison between a spin-resolved differential conductance map (in the center) and SP-STM simulations for the two magnetic domains in the hydrogenated Fe monolayer on Ir(111) presenting the hexagonal H superstructure. The tip is mostly sensitive to the in-plane component of the sample magnetization indicated with the arrow, with an additional angle of  $20^\circ$  outside the plane in both the experiment and the simulations. Both the on-top and the hollow state reproduce the checkerboard pattern visible in the experimental data. The simulations were performed with the following realistic parameters: tip-sample distance  $z_0 = 600$  pm, work function  $\psi = 4.8$  eV and polarization  $P_s P_t = 0.2$ . *Measurement parameters:*  $-700$  mV,  $1$  nA,  $4$  K,  $0$  T, Cr bulk tip.

When the tip is sensitive to another in-plane component of the sample magnetization, along a close-packed row this time, the magnetic pattern is triangular, as illustrated in the overview of Figure V.35. Here the tip sensitivity was determined using the spin spirals in the H1 phase of the hydrogenated double layer Fe as a reference. When the spiral propagates in the indicated tip sensitivity direction, the magnetic contrast is stronger than when it propagates along the perpendicular direction. Here the contrast almost disappears. For this in-plane sensitive tip, the SP-STM simulations reproduce again the data quite well. The results for the on-top and for the hollow configurations are also very close in this case.

From these comparisons between experiments and simulations considering the full three-dimensional structure, it appears that the proposed hexagonal nanoskyrmion lattice states are compatible with the actual magnetic state of the hydrogenated monolayer.

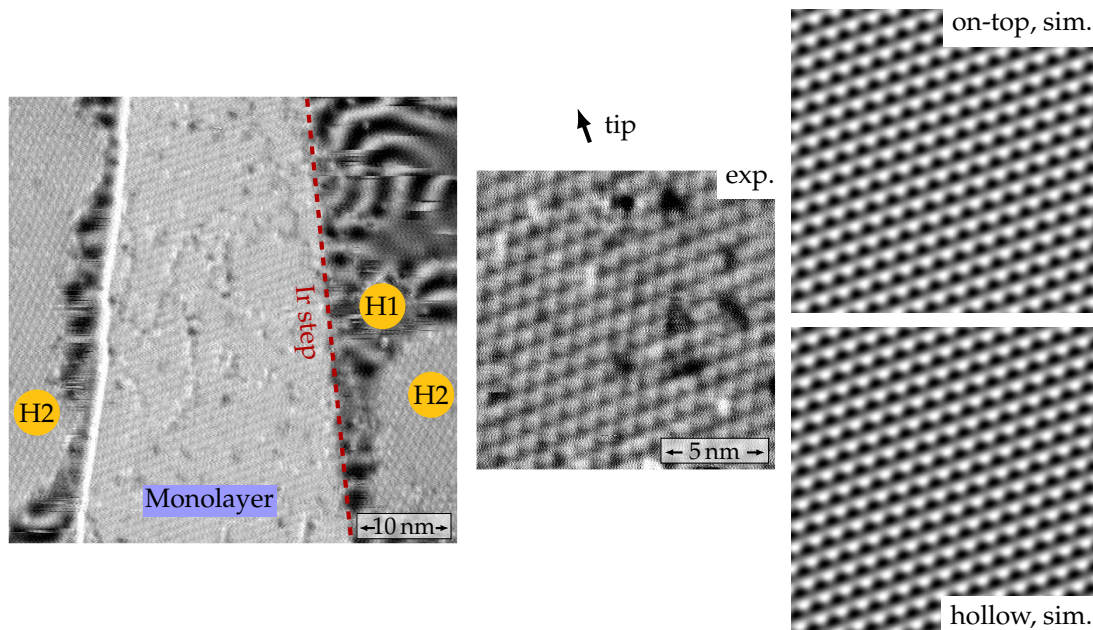


Figure V.35: Comparison between a spin-resolved differential conductance map (on the left) and SP-STM simulations (on the right) of the hydrogenated Fe monolayer on Ir(111) presenting the hexagonal H superstructure. The tip sensitivity can be derived from the contrast of the spin spiral in the H1 phase on the double layer. The magnetic contrast is stronger when the spiral propagates in the indicated tip direction than in the perpendicular direction. In this case, the magnetic pattern is an assembly of triangles. For the given tip direction, the SP-STM simulations reproduce the data for one of the domains, both for the on-top state and the hollow state. The simulations were performed with the following realistic parameters: tip-sample distance  $z_0 = 600$  pm, work function  $\psi = 4.8$  eV and polarization  $P_s P_t = 0.2$ . *Measurement parameters:*  $-1$  V, 1 nA, 8 K, 0 T, Fe-coated W tip.

### V.3.2.5 Position of the H atoms with respect to the magnetic state

When the tip is not sensitive to the magnetic state of the hydrogenated Fe monolayer, the hexagonal H superstructure appears as an arrangement of dark dots, not only in the constant-current maps but also in the differential conductance maps at  $-1$  V, which is the bias voltage usually used to image the magnetic state. An example of this pattern of dark dots is visible in Figure V.36, where the magnetic state is still partially visible but not dominant. This pattern is always present in the data, even though it might be hardly visible if the magnetic contrast is very strong. As it was mentioned previously, some features of the pattern corresponding to the out-of-plane component of the magnetic state cannot be reproduced in the SP-STM simulations. These are reproduced again in Figure V.37. Since the H superstructure always appears as dark dots, the effect of their superposition on the magnetic pattern is different for the two magnetic domains. On the left-hand side, where the magnetic state is depicted as bright dots on a dark background, some smaller and darker dots are visible between the bright dots. On the right-hand side, the dark dots on the bright background have a triangular shape.

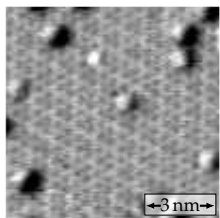


Figure V.36: Effect of the H superstructure on the differential conductance map at  $-1$  V, 1 nA in the absence of dominant magnetic contrast.

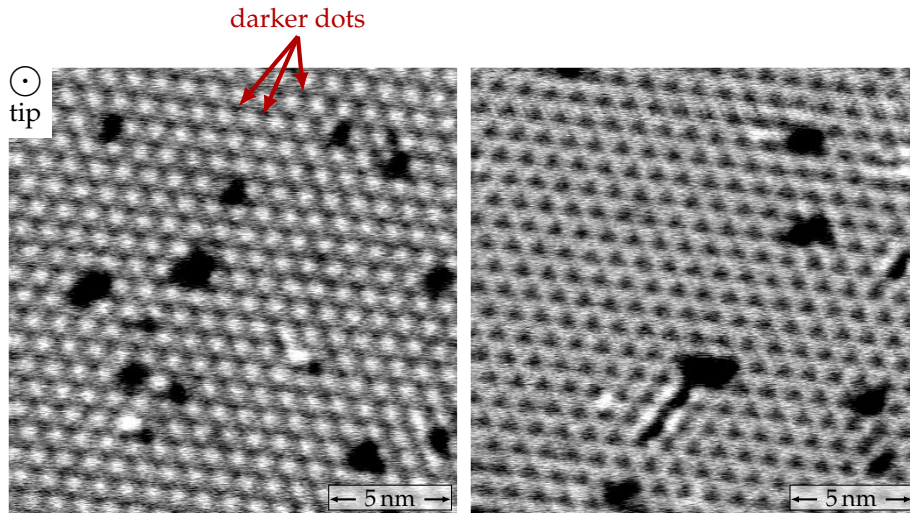


Figure V.37: Spin-resolved differential conductance maps of the nanoskyrmion lattice in the hydrogenated Fe monolayer covered with the hexagonal H superstructure. The tip is sensitive to the out-of-plane component of the sample magnetization and the two images show the two opposite magnetic domains in different areas. The H superstructure is actually also visible on this data: some small darker dots are visible in the dark background of the left image whereas the dark dots look triangular in the right picture. *Measurement parameters: -1 V, 1 nA, 4 K, 0 T.*

For symmetry reasons, the H atoms are assumed to be located on hollow lattice sites. Taking the periodicity of the H superstructure into account, the 32 possible hollow sites represent eight possibilities to place the H atoms in the magnetic unit cell. These positions are illustrated and numbered in Figure V.38 for the on-top and the hollow state. In both cases, the corners of the unit cell correspond to the magnetization pointing out-of-plane,  $m_z = 1$ .

In order to investigate the modification of the magnetic pattern by the H superstructure, a STM simulation (not spin-polarized!) of a lattice with twice the lattice constant of the Ir(111) surface was calculated. The image is then inverted in order to get dark dots instead of bright ones. It is shown in Figure V.39. The obtained pattern is properly shifted and added to the regular SP-STM simulation of the nanoskyrmion lattice with an arbitrary amplitude factor chosen in a way that the magnetic pattern is modified but still dominant. This procedure was applied to the eight possible shifts for both the on-top and the hollow state. The full set of data is shown in Figure V.40.

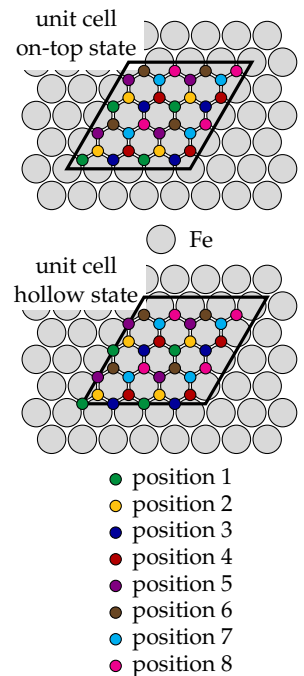


Figure V.38: Schematics and numbering of the eight possible positions of the H atoms in the magnetic unit cell of the hexagonal nanoskyrmion lattice.

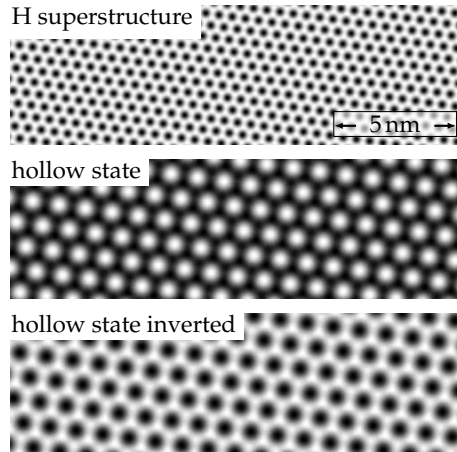


Figure V.39: Simulated pattern of the H superstructure obtained by simulating a lattice with twice the lattice constant of Ir(111) (without magnetic contrast) and inverting the picture. The simulated magnetic pattern for the two domains of the hollow state are given for comparison. The simulations were performed with the following realistic parameters: tip-sample distance  $z_0 = 600$  pm, work function  $\psi = 4.8$  eV and polarization  $P_s P_t = 0.2$ .

Most of the obtained configurations break the three-fold symmetry and are thus not realistic. The images obtained with position 4 on the on-top state and position 8 on the hollow state have a six-fold symmetry and do not agree with the experimental data. The couples of magnetic configuration and H position reproducing the structure measured in the data for both domains are marked in red. They correspond to the on-top state with the H atoms in position 7 or 2 (see Figure V.38 for the positions) or to the hollow state with the H atoms in position 1. Note that position 7 and position 2 give similar results for the top state, the pattern is just rotated by  $180^\circ$ . The difference between them is that the H atoms are located in fcc or hcp sites. They are thus not energetically equivalent. This calculation does not allow to choose between the on-top and the hollow state but determines the position of the H atoms with respect to the magnetic state. A drawing of the magnetic structure with the positions of the H atoms for both states is shown in Figure V.41 as well as the SP-STM simulation of the top state with the H atoms on position 7 and the hollow state with the H atoms in position 1, next to the experimental data for a closer comparison.

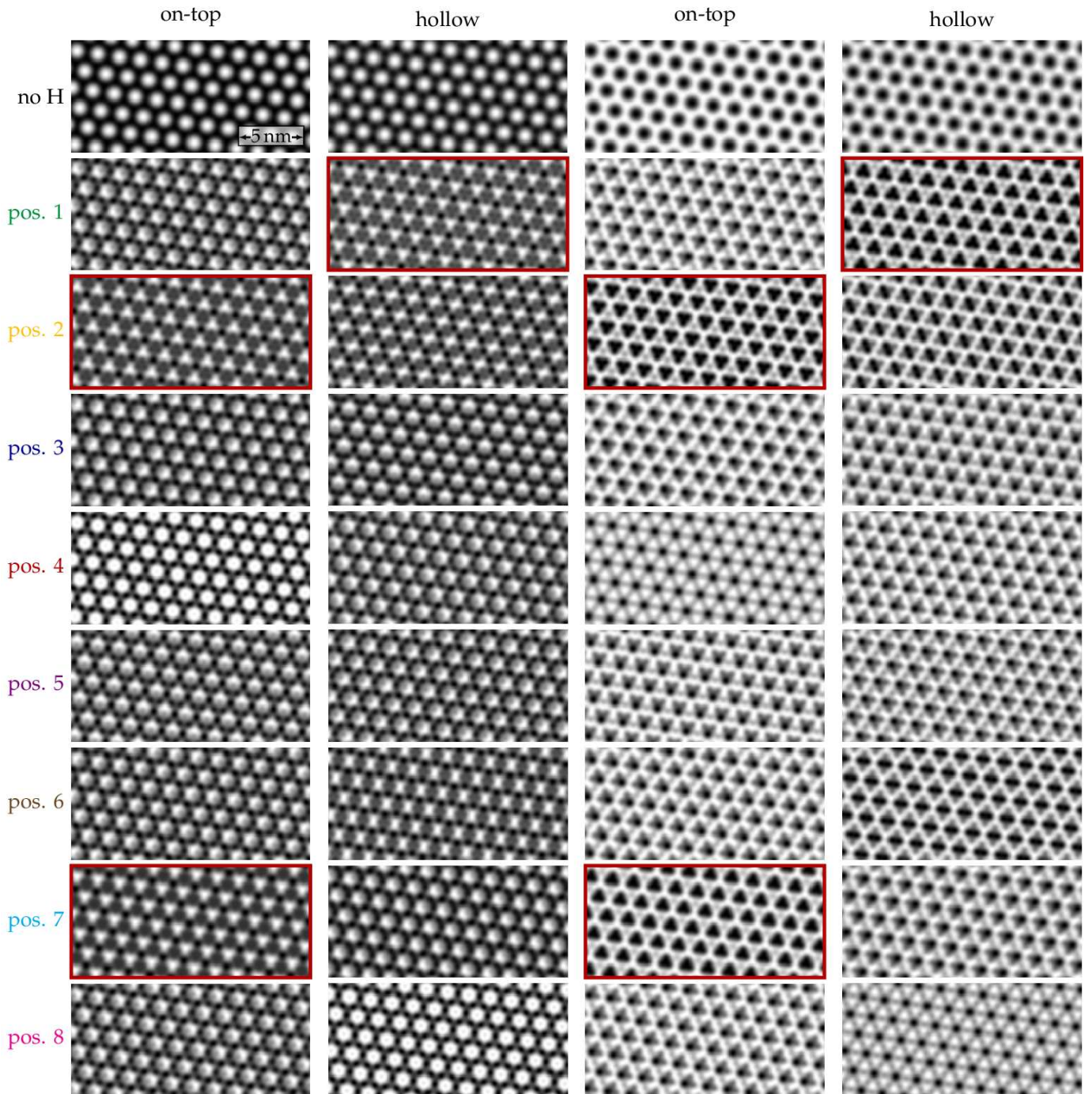


Figure V.40: Complete set of data obtained by adding the hexagonal pattern of dark dots representing the H superstructure to the SP-STM simulations for both domains of each configuration (on-top or hollow). The positions of the dots with respect to the magnetic unit cell are shown in Figure V.38. Most of the obtained patterns break the three-fold symmetry and are thus not compatible with the data. The configurations marked in red reproduce the features observed in the experimental data. The H superstructure was computed as the STM simulation of a two times larger atomic lattice. The picture was inverted to get dark dots instead of bright ones and added with a 0.1 coefficient to the SP-STM simulation in order to modify the magnetic pattern without becoming dominant. The simulations were performed with the following realistic parameters: tip-sample distance  $z_0 = 600$  pm, work function  $\psi = 4.8$  eV and polarization  $P_s P_t = 0.2$ .

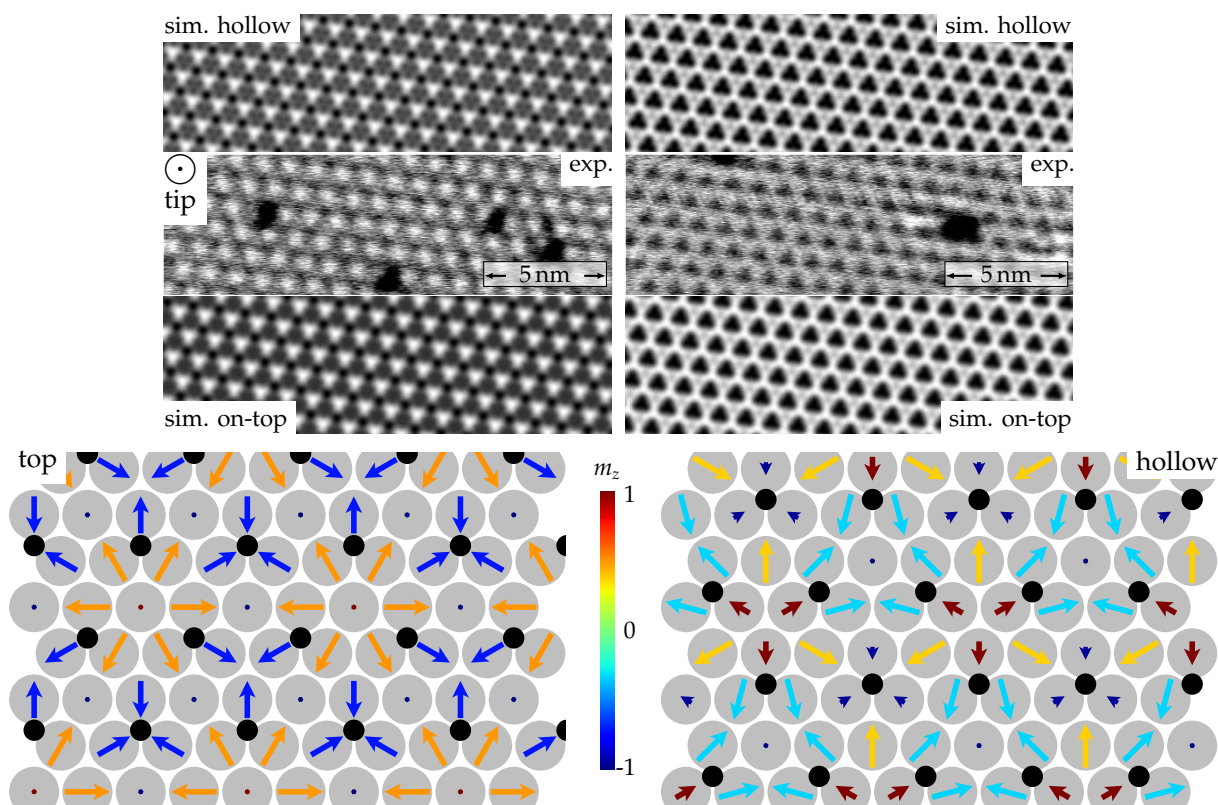


Figure V.41: Close comparison between the spin-resolved differential conductance maps from Figure V.33 and the SP-STM simulations of the on-top state with the H superstructure added on position 7 and the hollow state with the H superstructure on position 1 from Figure V.40. The H atoms are located at the position displayed on the magnetic structure models at the bottom.

### V.3.2.6 On-top or hollow state?

From the previous analysis, it cannot be decided if the magnetic state is the on-top state or the hollow state. In the case of the hexagonal nanoskyrmion lattice of the pristine hcp Fe monolayer, the assignment could be done using TAMR data.<sup>6</sup> For the present system, this data is not available because no magnetic pattern could be observed at low bias voltages where the TAMR contrast is likely to be found. The pattern of the H superstructure is strongly dominating.

<sup>6</sup> K. von Bergmann et al. *Nano Letters* 15, 3280–3285 (2015) [72]

Another option is to compare the energies of the two states. The strengths of the magnetic interactions are not known but for each interaction, the energy contribution of the states can be compared. The calculations of the energy contributions were performed by André Kubetzka assuming that all the magnetic parameters are equal to 1 meV per atom. Therefore, the comparisons have to be done for each contribution, a global comparison does not make any sense. The results are gathered in the Table V.1.

Interaction		On-top state	Hollow state
Exchange energy	$J_1$	-1.98	-1.93
	$J_2$	1.61	1.65
	$J_3$	1.44	1.62
	$J_4$	3.21	3.29
	$J_5$	-1.98	-1.93
	$J_6$	1.44	1.62
	$J_7$	-3.96	-3.86
	$J_8$	-6	-6
Anisotropy energy		0.53	0.44
Dzyaloshinskii-Moriya energy		3.19	3.21
4-spin energy		-6.36	-6.35
Biquadratic energy		-1.51	-1.43

Table V.1: Energy contributions corresponding to the various magnetic interactions for the on-top and the hollow state. All the parameters were set to 1 meV per atom and thus the comparisons can only be done for each interaction separately. All the values are given in meV per atom.

It appears that the on-top state is more favorable for the exchange and the biquadratic interactions whereas the magnetic easy-axis anisotropy favors the hollow state. The DMI and the 4-spin energies are very close for the two states. This does not allow to draw a clear conclusion and to decide which of the two states is the most probable.

To summarize, the magnetic structure of the hydrogenated Fe monolayer on Ir(111) with the hexagonal H superstructure is a hexagonal nanoskyrmion lattice. The magnetic unit cell comprises 16 atoms and has a net out-of-plane magnetic moment which leads to the presence of two opposite magnetic domains. Finally, the exact position of the H atoms constituting the superstructure with respect to the magnetic state could be derived from the data. The strong coupling between the magnetic state and the H superstructure suggests that the magnetic parameters, for example the magnetocrystalline anisotropy, could be locally modulated by the presence of the H atoms.

### V.3.3 Another two-dimensional magnetic lattice in the square superstructure

#### V.3.3.1 Observation of a square magnetic pattern

From the previous study of the magnetic state of the hexagonal superstructure in the hydrogenated Fe monolayer, one can expect that the square superstructure will again modify the nanoskyrmion lattice.

Figure V.43 shows both a constant-current map and a spin-resolved differential conductance map displaying the H superstructure with a small modulation coming from the magnetic state. Since the bias voltage needed to distinguish this magnetic pattern is rather high (1.4 V), the H superstructure is not very clear in the constant-current map. Nevertheless, some bright protrusions are visible. A schematic of the square H superstructure is given in Figure V.42 as a reminder. The red lines indicate the double rows of atoms along the  $[1\bar{1}0]$  direction which constitute the fixed part of the structure. With the help of these lines, one can see that the dark dots in the differential conductance map correspond to the bright protrusions of the structure.

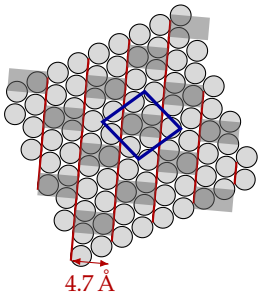


Figure V.42: Schematics of the square H superstructure.

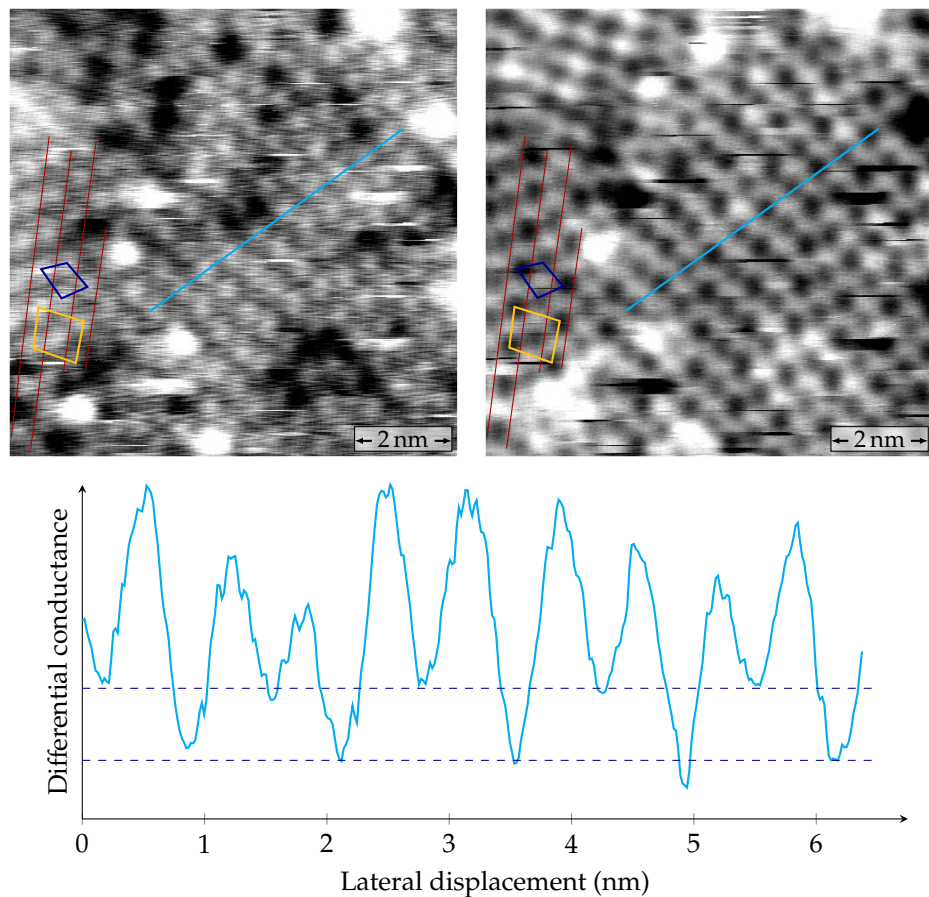


Figure V.43: Constant-current (left) and spin-resolved differential conductance (right) maps of the square superstructure on the hydrogenated Fe monolayer on Ir(111). Even though the superstructure is not very clear in the constant-current map, the positions of the bright protrusions are visible and correspond to the dark dots in the differential conductance map. A reminder of the schematics of the superstructure is shown by Figure V.42 and the close-packed rows are indicated with the red lines. In the differential conductance map, the magnetic pattern is visible: every second dot appears darker. This is also shown on the line profile taken along the blue line. The corresponding magnetic unit cell is drawn in yellow. The direction of the tip magnetic sensitivity is unknown. *Measurement parameters:* 1.4 V, 3 nA, 4 K, 0 K, Cr bulk tip.

Furthermore, every second row of these dark dots appears darker, as it is also shown by the profile taken along the blue line. This additional pattern comes from the magnetic state. Unfortunately, the direction of the tip magnetic sensitivity is unknown. The amount of H atoms needed to create the square superstructure on the monolayer is so large that the double layer becomes disordered and the spin spirals are not present anymore as a reference. The magnetic unit cell defined by the magnetic modulation of the dark dots is thus again rectangular, close to a square and rotated by  $45^\circ$  with respect to the H superstructure (see the yellow mark in Figure V.43).

When an out-of-plane magnetic field of 9 T is applied to the sample, no domain switching occurs. Spin-resolved differential conductance maps showing the three rotational domains are presented in Figure V.44, first in the absence of a magnetic field and then when successively 9 T and  $-9$  T are applied. Since the tip induces the movement of defects, the comparison between the differential conductance images is rather difficult. However, some impurities and defects appear much more clearly in the constant-current maps (not shown because only the defects are visible) and did not move between the scans (because their respective positions are unchanged). Six of these are marked with colored dots in the three images and allow to compare them. Their positions were identified in the constant-current maps and transferred to the differential conductance images. No change in the magnetic pattern can be found between the data measured at 0 T and 9 T which means that the magnetic state did not react to the application of the magnetic field. Between 9 T and  $-9$  T, the magnetic pattern globally reverses. The colored dots which were located on a row of dark dots at 9 T are between the rows at  $-9$  T and vice versa. Since this change is visible in the whole scan area, which comprises several rotational domains, it is caused by the switching of the magnetization of the tip following the magnetic field. The field was indeed ramped directly from 9 to  $-9$  T for this measurement. It is not unusual that such a switching occurs even with a Cr bulk tip for this large magnetic field strength. Hence the magnetic state stays unchanged under the application of magnetic fields up to  $\pm 9$  T. This absence of reaction to the magnetic field indicates that, in contrast to the hexagonal nanoskyrmion lattice but similarly to the square nanoskyrmion lattice in the pristine Fe monolayer, there is no net magnetic moment within the magnetic unit cell, it is fully compensated.

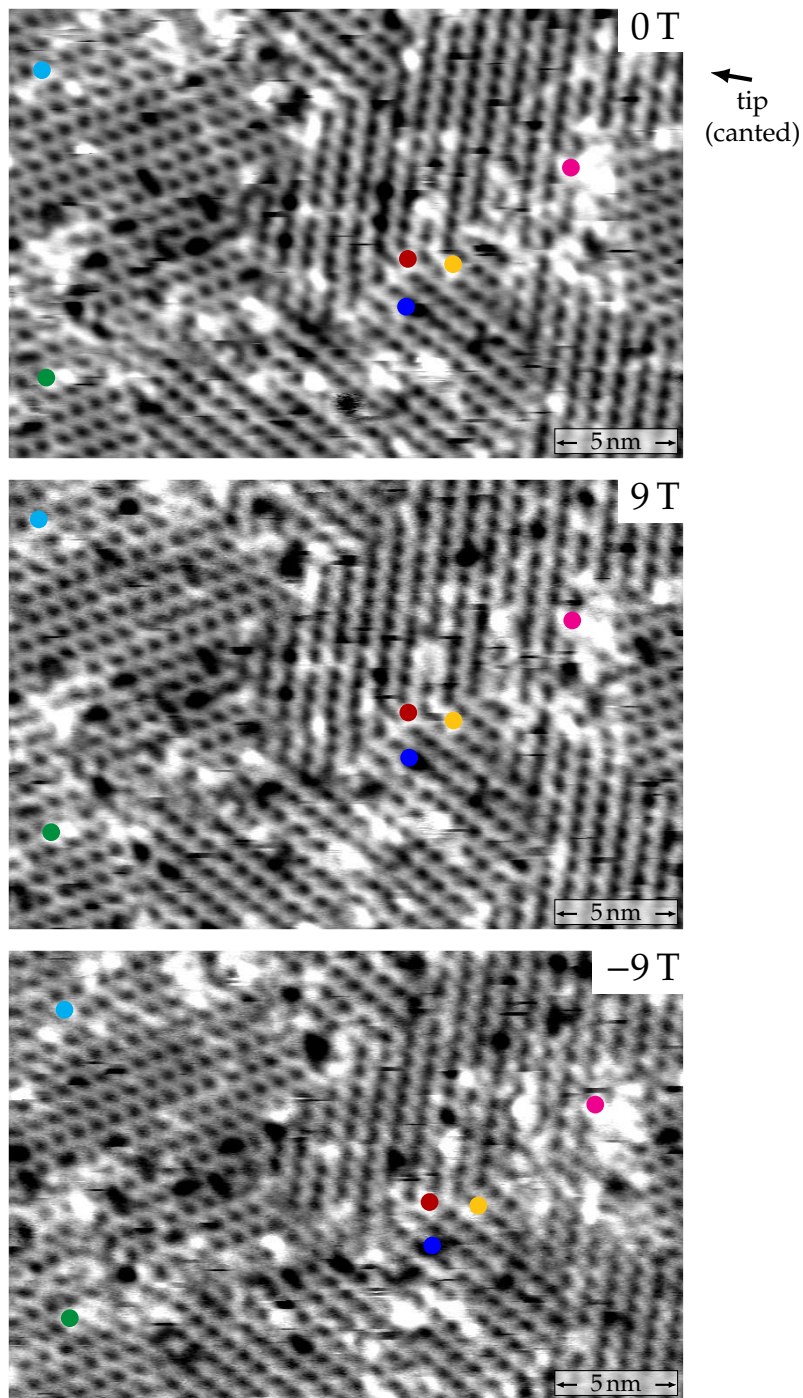


Figure V.44: Spin-resolved differential conductance maps of the magnetic state of the square H superstructure of the Fe monolayer on Ir(111). The three rotational domains are visible in this area. Some fixed defects are marked with colored circles in order to compare the images. No change of the magnetic state is visible upon the application of an out-of-plane magnetic field of  $\pm 9$  T but the out-of-plane component of the direction of the tip sensitivity switched between 9 and  $-9$  T. This induces a global phase shift of the magnetic pattern, the same for all the rotational domains. The direction of the tip sensitivity is derived from the magnetic structure model described later. *Measurement parameters:* 1.4 V, 3 nA, 4 K, Cr bulk tip.

### V.3.3.2 A square magnetic lattice commensurate with the H superstructure

From the previous analysis, it is now known that the magnetic state is again a two-dimensional lattice. The magnetic unit cell is strongly linked to the H superstructure and the out-of-plane magnetic moment is compensated within this cell. From these observations, it is possible to model the magnetic structure presented in Figure V.45. The magnetic unit cell is indicated with the rectangle. The construction of this state is similar to the one of the hexagonal nanoskyrmion lattice. Here, the two spin spirals depicted in Figure V.46 are added together and the magnetic moments normalized. The propagation direction of these spirals as well as their period is dictated by the size and the orientation of the magnetic unit cell.

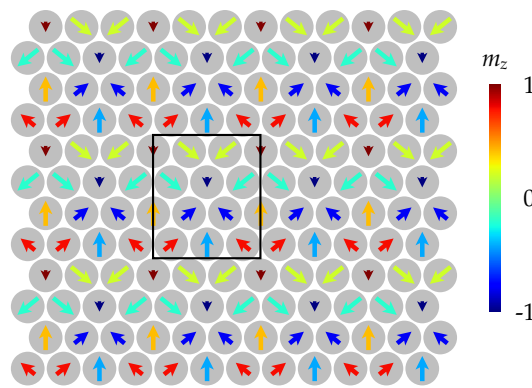


Figure V.45: Representation of a magnetic state compatible with the observations made for the hydrogenated Fe monolayer on Ir(111) exhibiting the square superstructure. This state is a superposition of the two spirals with the same rotational sense shown in Figure V.46. The position of the magnetic configuration with respect to the atomic lattice was chosen in order to have a mirror symmetry.

The position of the magnetic structure with respect to the atomic lattice is rather free as well as the phase shift between the spirals. However, some of the configurations can be excluded for symmetry reasons. For example, if the spirals are not shifted with respect to each other and the up pointing position of the moments is on a bridge site, there is no mirror symmetry in the magnetic structure (see configuration *a* in Figure V.47). If it is placed on a hollow site (configuration *b*), the out-of-plane magnetic moment is not compensated within the unit cell, which is also not compatible with the data. If the up pointing position of the magnetic moment is located on a top site of the lattice, the magnetic moment goes to zero on some lattice sites (configuration *c*). This solution is not expected but cannot be excluded, the moments could be fluctuating on some sites. The structure presented in Figure V.45 with the up pointing position on sites between the rows was chosen in order to have the corners and the center of the magnetic unit cell, which are symmetry equivalent positions of the magnetic state, on symmetry-equivalent

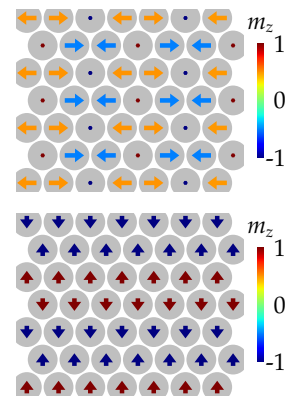


Figure V.46: The two spin spirals superposed to build the state from Figure V.45.

positions on the atomic lattice. With this solution, the magnetic moments can be normalized, the out-of-plane magnetic moment is compensated within the unit cell and it exhibits a mirror symmetry. In this case, there is no topological charge within the magnetic unit cell.

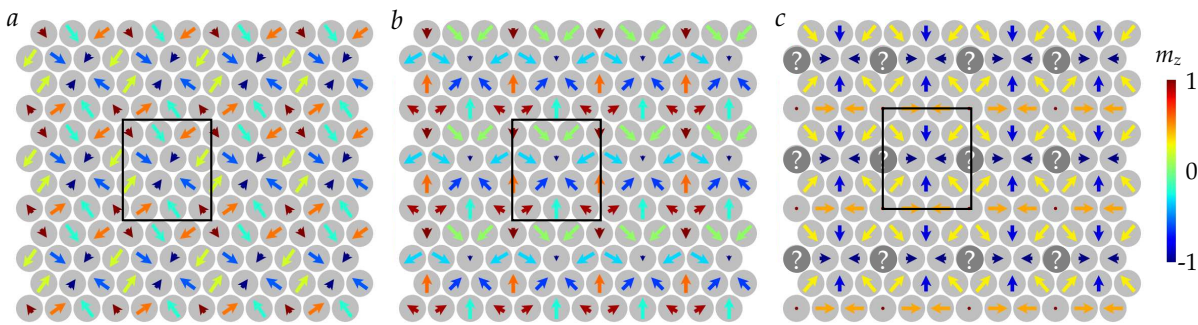


Figure V.47: Representation of some magnetic states obtained by shifting the superposition of spirals on the atomic lattice. In the state *a*, the point where the magnetic moment is pointing up is located on a bridge site, for configuration *b* on a hollow site and for configuration *c* on a top site.

### V.3.3.3 Comparison with the data

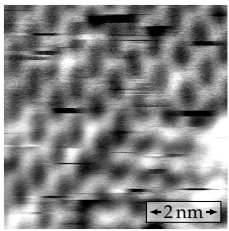


Figure V.48: Differential conductance map measured at 1.4 V, 2 nA and showing the distortion of the magnetic pattern in a zigzag shape because the H superstructure is also visible.

The validity of the proposed magnetic state has to be checked by comparing SP-STM simulations to the measured data. Since there is no area on the sample which could be used as a reference, the direction of the magnetic sensitivity of the tip is a priori not known. Therefore, areas with the three rotational domains are used to find the tip direction which allows to reproduce the three magnetic patterns at the same time. Figure V.49 shows again the zero-field data from Figure V.44 with a zoom in on each domain and the corresponding SP-STM simulation using the magnetic structure described above (Figure V.45).

The magnetic pattern can be reproduced by the simulations, although the agreement is not perfect. The discrepancies are probably related to the H superstructure which might add a non-magnetic (and not fully periodic!) component to the data, similarly to the effect observed with the hexagonal superstructure. Unfortunately, since the pattern created by the superstructure is not exactly known and not periodic, repeating the procedure applied to the hexagonal superstructure is not possible. The presence of the H superstructure is also possibly responsible for the formation of a zigzag shape in some data (see Figure V.48), which cannot be generated using only the magnetic state.

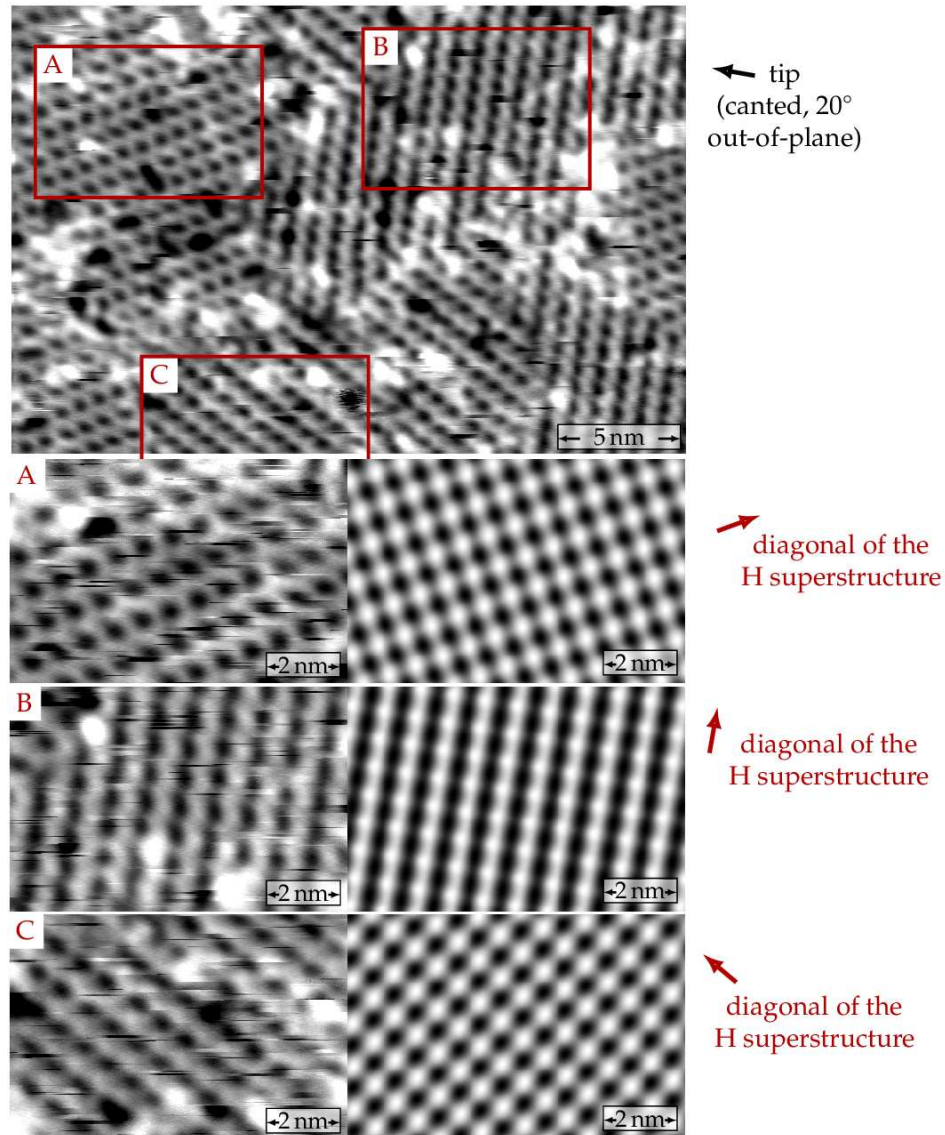


Figure V.49: Spin-resolved differential conductance map showing the magnetic state in the three rotational domains of the hydrogenated Fe monolayer on Ir(111) exhibiting the square superstructure. Zooms on the three domains are shown at the bottom (left) as well the corresponding SP-STM simulations for the indicated tip sensitivity direction. The general pattern is reproduced by the data. The simulations were performed with the following arbitrarily chosen parameters: tip-sample distance  $z_0 = 600$  pm, work function  $\psi = 4.8$  eV and polarization  $P_s P_t = 0.2$ . *Measurement parameters:* 1.4 V, 3 nA, 4 K, 0 T, Cr bulk tip.

### V.3.4 Summary

This investigation of the effect of hydrogenation on the Fe monolayer on Ir(111) reveals that two different H superstructures can be formed depending on the amount of atomic H supplied and that the presence of these superstructures has a large impact on the magnetic state. The square incommensurate nanoskyrmion lattice from the pristine fcc Fe monolayer is transformed either into a commensurate hexagonal nanoskyrmion lattice or into another roughly square two-dimensional state commensurate with the superstructure. The H superstructures

thus allow to tune the state in terms of size, symmetry and topology. The Table V.2 assembles the various magnetic states observed in the system consisting of a Fe monolayer on Ir(111), hydrogenated or not. The exact mechanism leading to the transformation of the nanoskyrmion lattice cannot be determined with SP-STM experiments but it is expected that the magnetic interactions will be modified by the presence of the H atoms like in the double layer case.<sup>7</sup> They would then be periodically modulated within the magnetic unit cell. Since the pristine Fe monolayer on Ir(111) is already a very complicated system, understanding the hydrogenated monolayer appears to be a challenging and exciting task for ab initio calculations.

<sup>7</sup> P.-J. Hsu et al. *Nature Communications* 9, 1571 (2018) [108]

	Pristine Fe monolayer		Hydrogenated Fe monolayer	
structure of the film	pseudomorphic fcc	pseudomorphic hcp	hexagonal $p(2 \times 2)$ H superstructure	square irregular H superstructure
typical size			4 Fe atoms per unit cell	about 6 Fe atoms per unit cell
magnetic state	square incommensurate nanoskyrmion lattice	hexagonal commensurate nanoskyrmion lattice	hexagonal commensurate nanoskyrmion lattice	roughly square 2D lattice commensurate with the superstructure
typical size	13 to 15 Fe atoms per unit cell	12 Fe atoms per unit cell	16 Fe atoms per unit cell	about 12 Fe atoms per unit cell

Table V.2: Summary of the various structures and magnetic states observed in the Fe monolayer (hydrogenated or not) on Ir(111).

## VI. Effect of metallic cover layers on the Fe monolayer on Ir(111)

In the previous chapter, the effect of hydrogenation on non-collinear magnetism was demonstrated in the case of Fe ultrathin films on Ir(111). However, a more frequent way to modify the properties of magnetic ultrathin films is interface engineering. By adding further layers of different materials, magnetic or not, the system is influenced by the presence of new interfaces. This approach is widely used in the case of sputtered magnetic multilayers and allowed in particular to stabilize magnetic skyrmions at room temperature.<sup>1,2,3,4,5</sup>

Adding metallic cover layers on top of the Fe monolayer on Ir(111) also proved to be a very efficient way to tune the magnetic state. In the Pd/Fe bilayer on Ir(111), individual magnetic skyrmions are stabilized in an external magnetic field.<sup>6</sup> Other elements than Pd can have an influence on the magnetism of the Fe monolayer, in particular Ni. Section VI.1 will focus on the Ni/Fe bilayer on Ir(111). The magnetic state of extended films is investigated, starting from a previous work about nanoislands.<sup>7</sup> Section VI.2 presents a comparison between the results obtained for various cover layers made of Fe, Pd, Ni, Rh and Pb.

*In this chapter, I only measured and analyzed the data about the extended Ni/Fe bilayer on Ir(111). The other results are gathered from various other published works and used for comparison.*

<sup>1</sup> W. Jiang et al. *Science* 349, 283–286 (2015) [109]

<sup>2</sup> C. Moreau-Luchaire et al. *Nature Nanotechnology* 11, 444–448 (2016) [110]

<sup>3</sup> O. Boulle et al. *Nature Nanotechnology* 11, 449–454 (2016) [111]

<sup>4</sup> S. Woo et al. *Nature Materials* 15, 501–506 (2016) [5]

<sup>5</sup> A. Soumyanarayanan et al. *Nature Materials* 16, 898–904 (2017) [112]

<sup>6</sup> N. Romming et al. *Science* 341, 636–639 (2013) [6]

<sup>7</sup> D. Iaia et al. *Physical Review B* 93, 134409 (2016) [144]

## VI.1 Strong domain wall pinning in Ni/Fe/Ir(111)

In this section, the role of a Ni cover layer on Fe/Ir(111) is investigated. Ni is indeed isoelectronic to Pd but bulk Ni is ferromagnetic (unlike Pd, which just misses the Stoner criterion). The Ni/Fe interface was previously studied in Fe/Ni/Cu(001).<sup>1</sup> In this case, homochiral domain walls are created by the DMI. Although the DMI is rather weak in this system because of the weak spin-orbit coupling, some magnetic skyrmions can also be stabilized using the coupling to a thick ferromagnetic layer underneath, which acts as an effective magnetic field.<sup>2</sup> SP-STM measurements already revealed that Ni nanoislands on Fe/Ir(111) are ferromagnetic.<sup>3</sup> This work is summarized in section VI.1.1. Some further details about the growth of extended Ni/Fe films on Ir(111) are given in section VI.1.2 and the unusual behavior of the domain walls is analyzed in section VI.1.3.

<sup>1</sup> G. Chen et al.  
*Physical Review Letters* 110, 177204 (2013) [145]

<sup>2</sup> G. Chen et al.  
*Applied Physics Letters* 106, 242404 (2015) [113]

<sup>3</sup> D. Iaia et al.  
*Physical Review B* 93, 134409 (2016) [144]

<sup>4</sup> S. Heinze et al.  
*Nature Physics* 7, 713–718 (2011) [27]

<sup>5</sup> F. Meier et al.  
*Physical Review B* 74, 195411 (2006) [146]

### VI.1.1 Previous work: ferromagnetic nanoislands

The growth and magnetic state of Ni/Fe nanoislands on Ir(111) was studied using SP-STM.<sup>3</sup> The samples were prepared by depositing first about 0.8 atomic layer of Fe on a clean Ir(111) single crystal at elevated temperature. In this case, the Fe film grows from the step edge in fcc stacking.<sup>4</sup> Afterwards, about 0.3 atomic layer of Ni was deposited onto the Fe film.

There is a large lattice mismatch between bulk fcc Ni and bulk fcc Ir, about 8% but only a few dislocation lines form in the Ni monolayer on Ir(111), which grows mostly pseudomorphically. However, the Ni islands on the pseudomorphic Fe layer (which is strained and has thus the same in-plane lattice constant as Ir) exhibit a triangular network of dislocation lines.

Figure VI.1 shows the constant-current STM map as well as the differential conductance map of such an island. This triangular pattern is reminiscent of the one observed in Co islands on Pt(111).<sup>5</sup> The structure is an assembly of triangular hcp and fcc areas separated by bridge lines. The hcp and fcc areas have similar sizes which indicates that the two stackings are roughly energetically equivalent. The main difference is that the fcc stacking is preferred at the edges.

Spin-resolved measurements reveal that the islands have a ferromagnetic state. Figure VI.2 shows the magnetic field dependence of two islands. Image (a) displays their magnetic state at 1 T, which is the same as their initial zero-field state. One of the islands appears brighter and the other one darker in the differential conductance map, they have opposite out-of-plane magnetization directions.

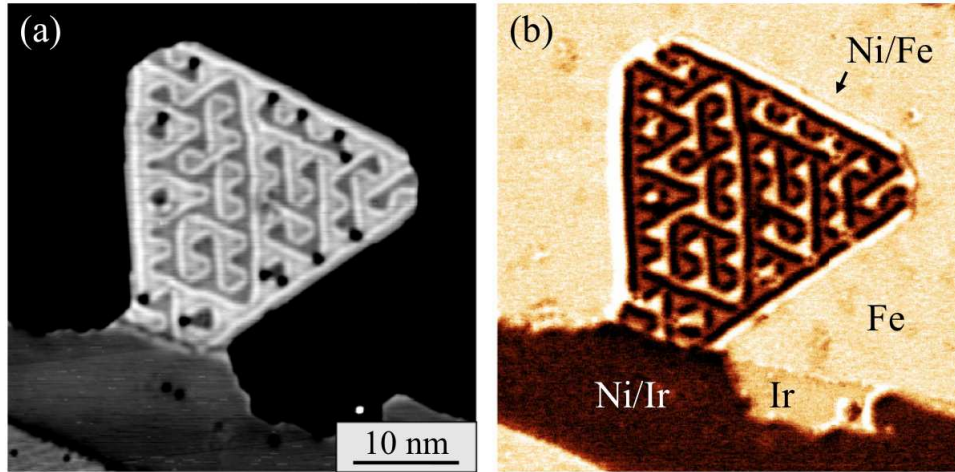


Figure VI.1: STM constant-current map (a) and differential conductance map (b) of a Ni island on Ir(111). The dislocation line network is clearly visible. The lines separate triangular hcp and fcc areas. *Measurement parameters:* 500 mV, 1 nA, 8 K, Fe coated W tip. Extracted with permission from [144], copyright 2016 by the American Physical Society.

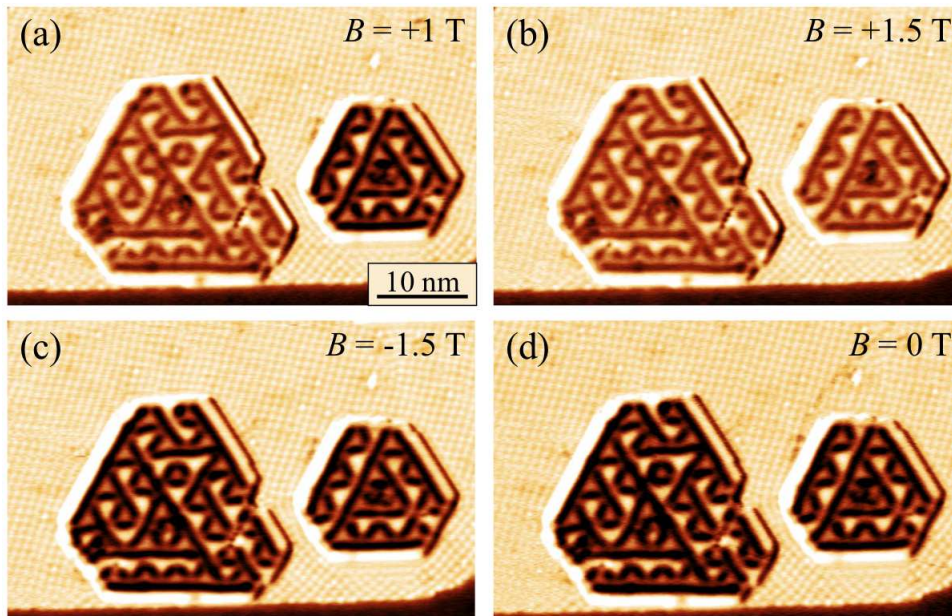


Figure VI.2: Field dependence of the spin-resolved differential conductance maps of two Ni islands on Fe/Ir(111). At the chosen bias voltage, the magnetic contrast is mostly visible on the bridge lines. Initially, the islands are oppositely magnetized. The magnetization of the small island is switched with a field of 1.5 T (image (b)). The magnetization direction of both islands aligns with the field at  $-1.5$  T (image (c)). The nanoskyrmion lattice is also visible in the fcc Fe layer. *Measurement parameters:* 500 mV, 1 nA, 8 K, Cr bulk tip. Extracted with permission from [144], copyright 2016 by the American Physical Society.

When the magnetic field is increased in steps, the magnetization of the islands switches to become parallel to the field direction. The field needed for the switching depends on the size and the geometry of the island. When the magnetic field is reversed from 1.5 T to  $-1.5$  T,

the magnetization of both islands in Figure VI.2 is also inverted. This behavior confirms that the islands are really ferromagnetic with out-of-plane anisotropy.

## VI.1.2 Growth of extended Ni/Fe films

The width of the larger islands studied previously is about 30 nm. They are all ferromagnetic, with only a single domain in each island. One cannot exclude that no domain wall could be found in the islands because of confinement effects and that larger complex magnetic structures could form in extended films. A study of the growth of extended Ni/Fe films on Ir(111) is presented in this section.

### VI.1.2.1 Sample morphology

**Typical preparation procedure** Extended areas of Ni/Fe on Ir(111) were prepared by depositing between 0.8 and 1.2 atomic layers of Fe on the clean Ir substrate at elevated temperature, between 5 and 7 min after the annealing. The Fe layer thus grows from the step edges in fcc stacking.<sup>6</sup> Between 0.6 and 0.8 atomic layer of Ni was subsequently deposited onto the Fe film 40 min after the annealing of the Ir crystal. The morphology of a typical sample prepared with this procedure is shown in Figure VI.3.

<sup>6</sup> S. Heinze et al.  
*Nature Physics* 7,  
713–718 (2011)  
[27]

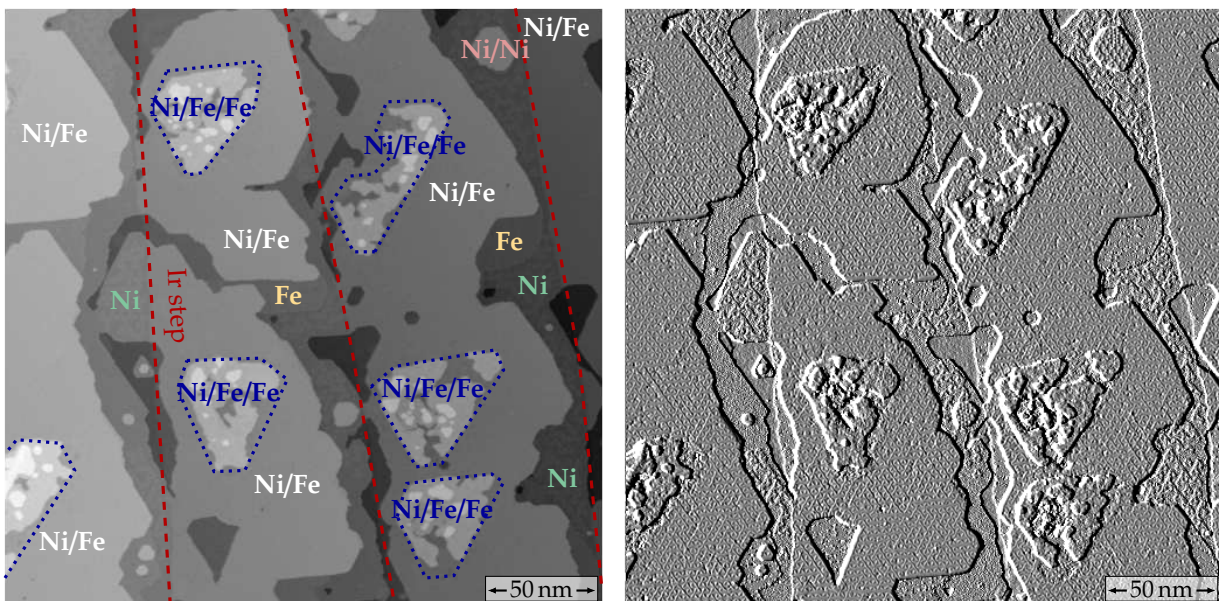


Figure VI.3: STM constant-current map (left) and simultaneously recorded current map of a typical Ni/Fe/Ir(111) sample. Some extended Ni/Fe areas can be prepared, despite the presence of Fe double layer islands embedded in the Ni/Fe bilayer. *Measurement parameters:* 100 mV, 1 nA, 4 K, 0 T, Cr bulk tip.

The Fe layer is mostly covered by Ni which forms some nicely extended areas of Ni/Fe bilayer. The same triangular pattern of alternating fcc and hcp areas separated by bridge lines as in the nanoislands can be observed. A zoomed view of this structure is displayed in Figure VI.4.

The size of the triangles is about 3 nm and they are not perfectly aligned in a hexagonal lattice.

Some Ni also grows on the bare Ir from the Fe step edges. The Ni layer on Ir(111) is pseudomorphic with some triangular stacking defects.<sup>7</sup> These triangular features can be distinguished in the current map. Some roughly triangular islands of Fe double layer also formed during the Fe deposition and were embedded in the Ni/Fe bilayer when the Ni layer was deposited. These islands are also partly covered with Ni. The Ni growth on these Fe double layer islands is significantly less smooth than on the Fe monolayer. The Ni layer is fragmented and some tiny Ni double layer islands are present. A close view of this type of area is shown in Figure VI.5. The surface of the Fe double layer island appears very rough, some intermixing between the Fe and the Ni layers must be occurring there. However, no clear indication of intermixing was found in the Ni/Fe bilayer.

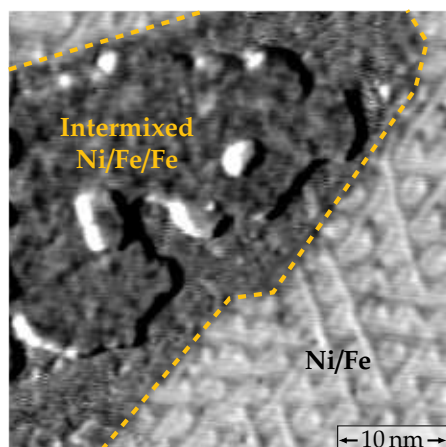


Figure VI.5: Differential conductance map of the boundary between an embedded Fe double layer island with a Ni island on top and the Ni/Fe film. *Measurement parameters:* 100 mV, 1 nA, 4 K, 0 T, Cr bulk tip.

**Effect of post-annealing** Figure VI.6 shows a sample with a larger Ni coverage, around 1.3 atomic layers. On the left image, which is a STM constant-current map of the sample as initially prepared, the second layer Ni forms small round shaped islands on top of the Ni/Fe film with the triangular dislocation pattern. To see if these Ni islands could coalesce, the sample was post-annealed for 10 min at about 300 °C. A differential conductance map of the obtained sample is shown in the right image of Figure VI.6. Here some large darker islands which seem to exhibit a triangular pattern are embedded in a rather uniform film. A few islands of higher coverage are also present. The exact nature of these different areas cannot be determined for sure. Since the structure of the film is unclear and intermixing between Fe and Ni is possible in this sample, post-annealing should be avoided during the preparation of Ni/Fe/Ir(111) samples.

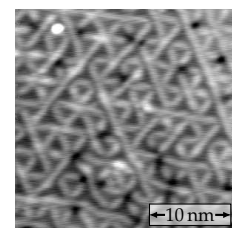


Figure VI.4: Topography of the triangular pattern on the Ni/Fe bilayer (100 mV, 1 nA).

<sup>7</sup> D. Iaia et al. *Physical Review B* 93, 134409 (2016) [144]

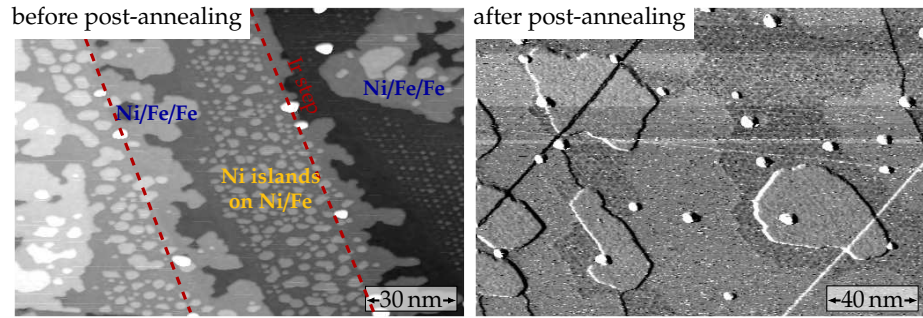


Figure VI.6: STM constant-current map (left) of a Ni/Fe/Ir(111) sample with a larger Ni coverage than the one shown in Figure VI.3 and differential conductance map (right) of the same sample after 10 min post-annealing at around 300 °C. Different areas can be distinguished on the film but their nature remains unclear. The bright dots are impurities present on the not perfectly clean Ir substrate. The straight lines on the differential conductance map were induced by a collision between the tip and the sample surface after the sample preparation. *Measurement parameters:* -100 mV, 1 nA, 296 K, 0 T, Cr bulk tip.

### Growth of Ni on the Fe double layer areas with dislocation lines

As mentioned previously, small Ni islands can grow on top of small pseudomorphic Fe double layer islands and show some indications of intermixing. These areas are those marked in blue in Figure VI.3 or shown in Figure VI.5. However, when the Fe double layer area below is large enough and exhibits a regular dislocation line pattern, a well ordered Ni layer grows on top.

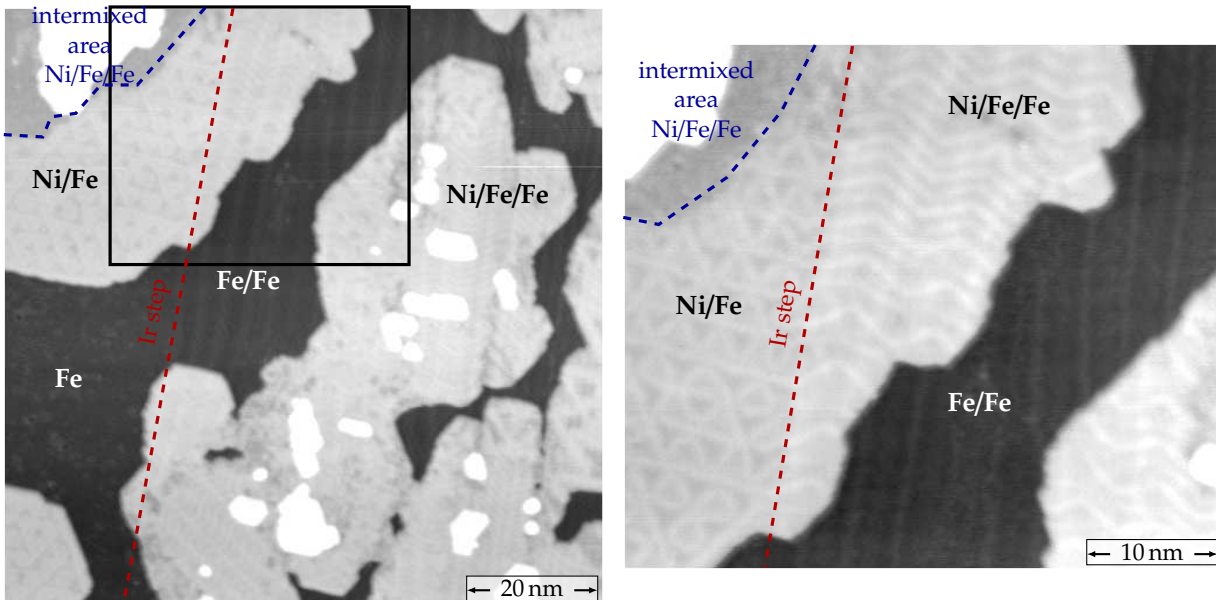


Figure VI.7: STM constant-current maps of a Ni layer grown on the Fe double layer on Ir(111). The zoom (right image) shows that the dislocation line pattern becomes very complex. The parallel dislocation lines from the Fe double layer are visible in the Ni layer and some additional lines form a zigzag pattern perpendicular to them in the Ni film. *Measurement parameters:* -200 mV, 1 nA, 31 K, 0 T, Cr bulk tip.

Figure VI.7 shows a close view of a Ni film on a Fe double layer area with parallel dislocation lines. The Ni film grown on top of the Fe double layer in the areas with dislocation lines in the Fe looks much more regular and less intermixed with the Fe than the one which is growing on top of small Fe double layer islands surrounded by Ni/Fe. The dislocation lines from the Fe layer are also found in the Ni layer on top, with an additional pattern. Zigzag dislocation lines form perpendicularly to the straight Fe dislocation lines which creates a rather complicated pattern. The Ni/Fe/Fe/Ir(111) system was not investigated further.

### VI.1.2.2 An irregular dislocation pattern

A model for the atomic structure of the triangular dislocation pattern in Ni/Fe was proposed for the nanoislands<sup>8</sup> and is reproduced in Figure VI.8. The Fe layer is pseudomorphic on top of the Ir(111) substrate. In the Ni layer, the atoms are mostly located either in hcp or fcc hollow sites. The dislocation pattern is made of triangular areas of each stacking, regularly ordered and separated by two rows of atoms located in bridge sites (marked in blue in Figure VI.8). At the border of the islands, the Ni atoms are preferably placed in the fcc hollow sites.

<sup>8</sup> D. Iaia et al.  
*Physical Review B*  
93, 134409 (2016)  
[144]

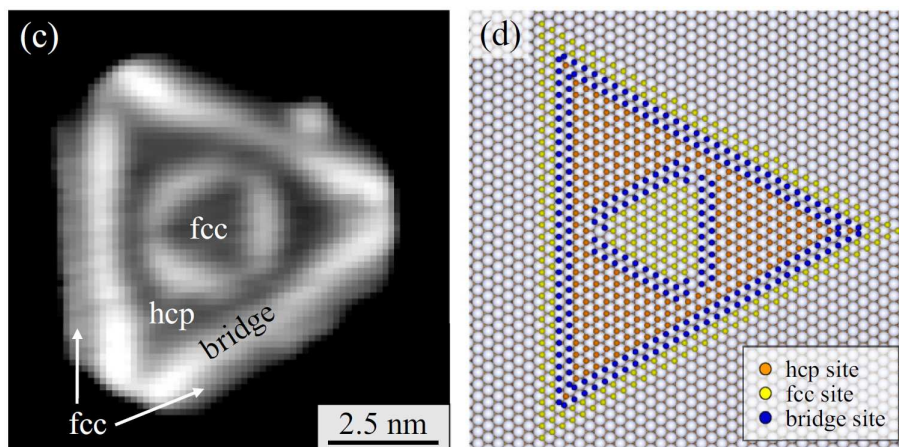


Figure VI.8: STM constant-current map of a very small Ni island on Fe/Ir(111) and the corresponding atomic structure model. *Measurement parameters:* 20 mV, 1 nA, 8 K, Cr bulk tip. Extracted with permission from [144], copyright 2016 by the American Physical Society.

Using the triangular stacking defects in the Ni monolayer on Ir(111), it is possible to decide which of the triangles are the fcc and the hcp ones. Indeed, as it is shown in Figure VI.9, the Ni monolayer grows from the Fe step edges and thus very probably in fcc stacking. This means that the triangular defects created in the layer to relieve the strain are hcp areas surrounded by bridge lines. In the image from Figure VI.9, the up-pointing triangles are hence the hcp areas. By looking carefully at the structural pattern in the Ni/Fe bilayer, it appears that the arrangement of the triangular areas is not fully regular.

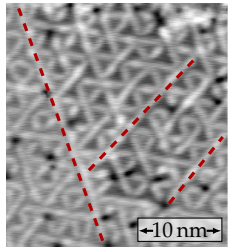


Figure VI.10: Topography of the dislocation pattern in Ni/Fe/Ir(111), measured at 100 mV, 1 nA. Some long bridge lines are marked in red.

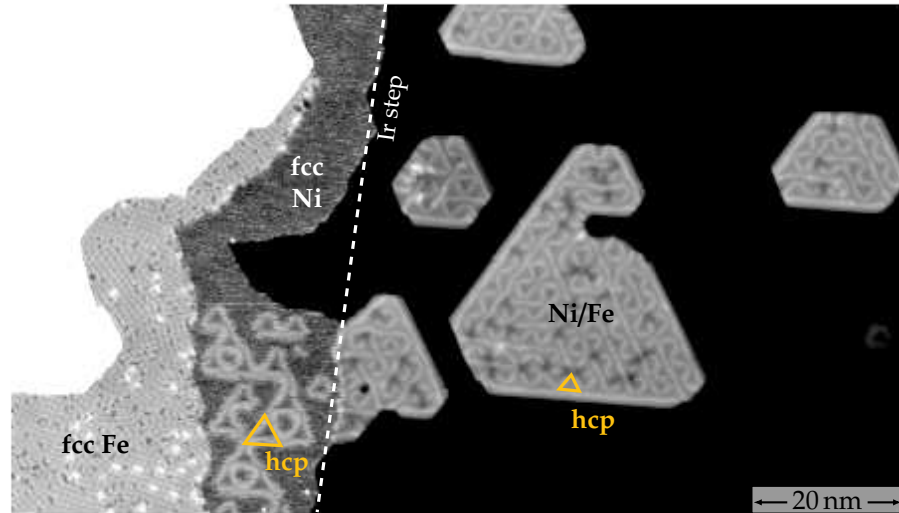


Figure VI.9: STM constant-current map of a Ni/Fe/Ir(111). The stacking defects in the Ni monolayer on Ir(111) allow to identify which of the triangular areas correspond to the hcp and the fcc stacking in the Ni/Fe bilayer. *Measurement parameters:* 100 mV, 1 nA, 4 K, 0 T, Cr bulk tip.

Figure VI.10 shows some details of the structure. Most of the time, the triangular areas are attached together and the bridge lines continue along several triangles. Some of these long lines are marked in red in Figure VI.10. It will be shown in the next section that these lines have a large influence on the magnetic state of the film.

No clear effect of the temperature of the substrate during the Ni deposition could be found concerning the regularity of the pattern, for Ni depositions between 30 min and 80 min after the annealing of the Ir(111) crystal.

Based on the precise structure of each area and following the model proposed in Figure VI.8, one can build a model which easily reproduces the data as shown in Figure VI.11. One can also check that the width of the bridge lines really corresponds to two rows of atoms by taking a line profile and fitting a gaussian peak to find its width (see Figure VI.12).

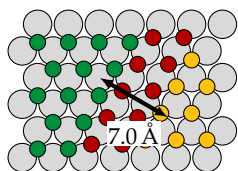
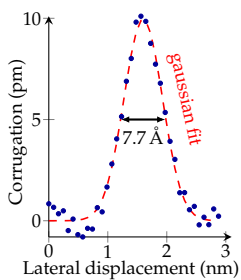


Figure VI.12: Profile of a bridge line fitted with a gaussian peak to measure its width, which corresponds to two rows of atoms.

### VI.1.3 Pinning of the domain walls to the bridge lines

Spin-resolved STM measurements reveal that also the Ni/Fe bilayer on Ir(111) is ferromagnetic with out-of-plane anisotropy, in agreement with the previous work about nanoislands. However, many magnetic domains are visible in extended films, whereas domain walls were not found in the nanoislands. The dislocation pattern turns out to have again a large influence on the magnetic state since the domain walls follow the long bridge lines found in the structure.

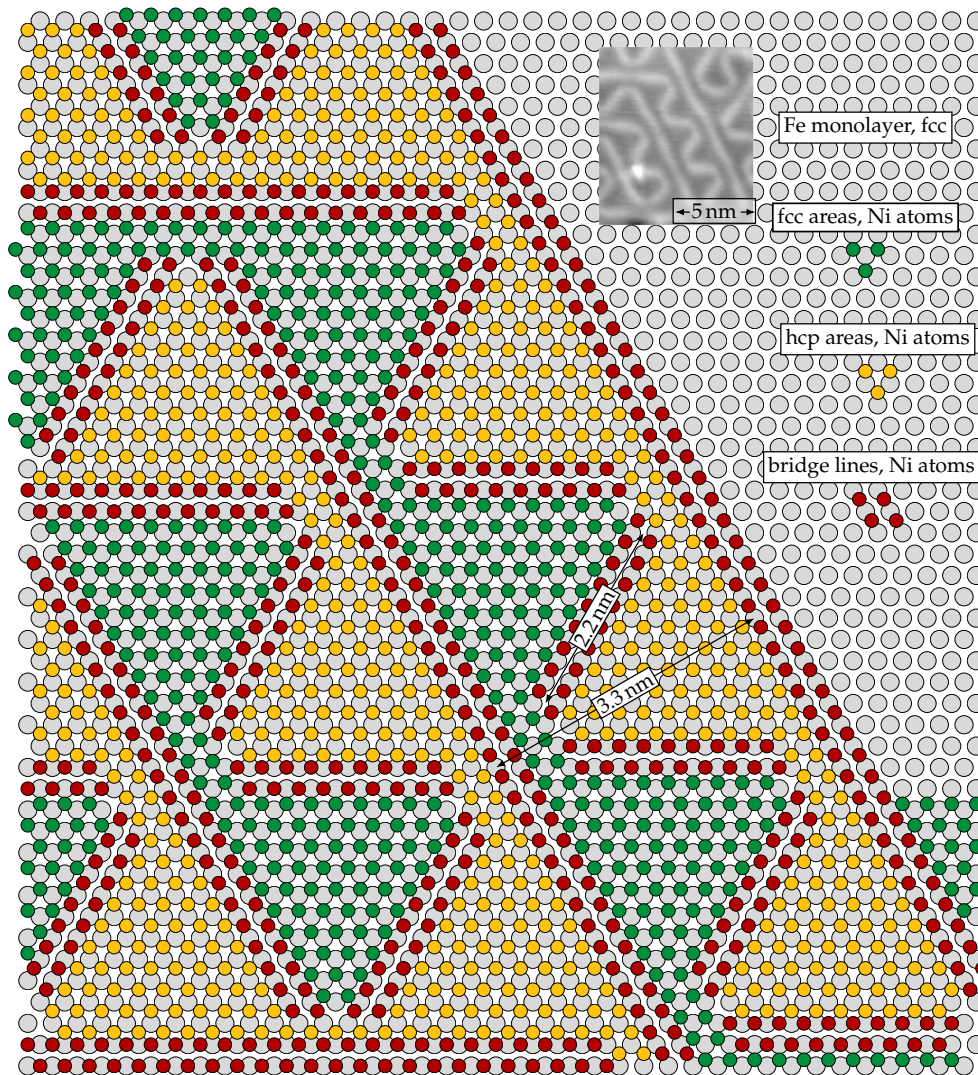


Figure VI.11: Structure model of most of the area shown in the inset exhibiting the triangular pattern of the Ni/Fe bilayer on Ir(111) with some long bridge lines.

### VI.1.3.1 Ferromagnetic domains with out-of-plane anisotropy

Figure VI.13 shows a constant-current map and the simultaneously recorded spin-resolved differential conductance map of a Ni/Fe/Ir(111) sample.

The structures mentioned in section VI.1.2 are, as expected, still present: large Ni/Fe areas, small regions of Ni or Fe monolayer on bare Ir(111) as well as Fe double layer islands embedded in the Ni/Fe film and covered with Ni. However, an additional pattern of magnetic origin is clearly visible in the differential conductance map. The Ni/Fe bilayer is ferromagnetic and oppositely magnetized domains appear dark or bright. Their sizes lie between 30 nm and 100 nm which explains why only single magnetic domains were observed in the nanoislands.<sup>9</sup> Usually, since the formation of a domain wall requires some energy, their length is minimized: they are thus typically straight and often

<sup>9</sup> D. Iaia et al. *Physical Review B* 93, 134409 (2016) [144]

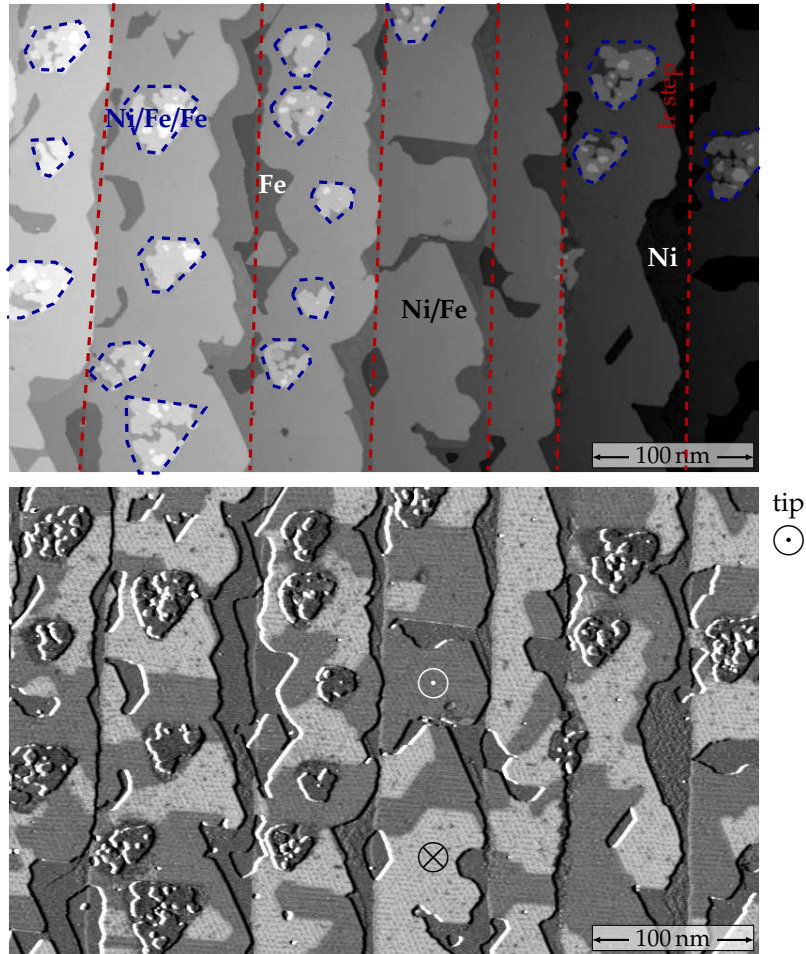


Figure VI.13: STM constant-current map (top) and spin-resolved differential conductance map (bottom) of a Ni/Fe/Ir(111) sample. Oppositely magnetized out-of-plane domains with boundaries following the dislocation pattern appear dark and bright in the Ni/Fe bilayer in the differential conductance map. The domain sizes are mostly between 30 nm and 100 nm. *Measurement parameters:* 100 mV, 1 nA, 4 K, 0 T, Cr bulk tip.

<sup>10</sup> F. Meier et al.  
*Physical Review B*  
 74, 195411 (2006)  
 [146]

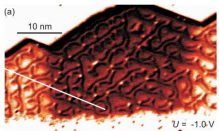


Figure VI.14: Domain walls in Co/Pt(111). Extracted with permission from [146], copyright 2006 by the American Physical Society.

located in geometrical constrictions of the magnetic layer. For example, a differential conductance map showing two domain walls in Co on Pt(111)<sup>10</sup> is reproduced in Figure VI.14. In the case of the Ni/Fe bilayer on Ir(111), the shape of the domains walls is more complicated and rather surprising. They are not straight lines but follow some complex paths. The difference to the Co/Pt(111) system is that the position of the walls is dictated by the dislocation pattern. The walls are pinned at the bridge lines. This pinning effect will be discussed in detail in section VI.1.3.3.

### VI.1.3.2 Unique rotational sense of the domain walls

Since the DMI is large at the Fe/Ir interface, it is expected that the domain walls in the Ni/Fe bilayer have a unique rotational sense. In order to check this, the same area containing a reasonably large number of

domain walls needs to be measured with an out-of-plane and an in-plane sensitive magnetic tip. The correlation between these data allows to check if the rotational sense is the same for all the walls but not to find the absolute rotational sense. Indeed, the direction of the magnetization at the tip apex cannot be fully determined without a vectorial magnetic field, the  $\vec{m}_t$  and  $-\vec{m}_t$  cases are not distinguishable.

### Observation of electronic contrast

At 100 mV, which is the bias mostly used to measure the magnetic contrast in the Ni/Fe bilayer in the following discussion, not only the TMR contrast is visible, there is also an electronic contribution (for details, see section II.2.2.1). Consequently, the data showing the in-plane magnetization components of the domain walls do not look as clear and simple as when only TMR contrast is visible. With only TMR contrast, some walls should appear bright and the others dark depending on their in-plane components. In the case of the Ni/Fe bilayer, this bright/dark contrast arising from the TMR is still present but there is an additional contribution visible at 100 mV which reduces the signal of the domain walls compared to the ferromagnetic surrounding in the differential conductance map. Some of the walls appear thus dark and the others are not visible because the bright contrast of the TMR is compensated. This effect is illustrated in Figure VI.15.

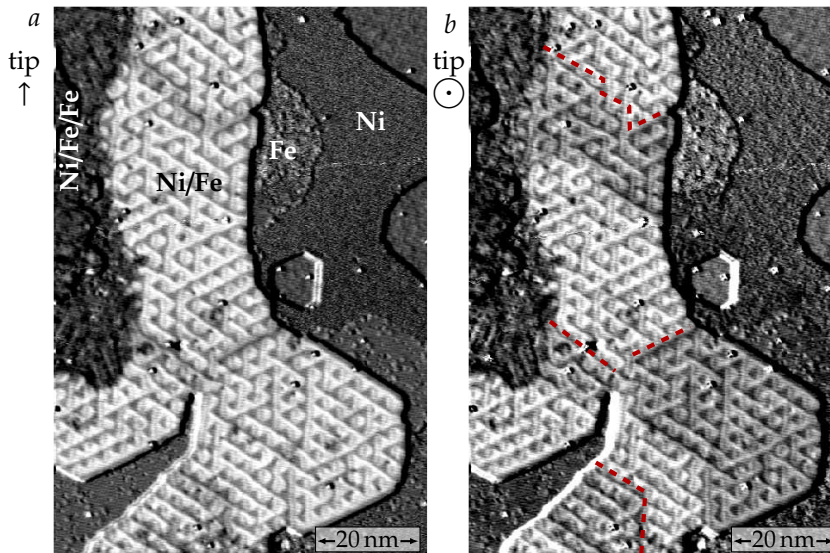


Figure VI.15: Spin-resolved differential conductance maps of a Ni/Fe bilayer on Ir(111). In image *a*, the tip is sensitive to an in-plane component of the sample magnetization (probably the one indicated with the arrow, assuming that the domain walls are Néel walls) and in *b* there is some additional weak out-of-plane contrast. Because the effect of the TMR and the electronic contributions add up, some walls appear very dark (marked in red in image *b*) and some others are hardly visible in image *a*. *Measurement parameters: a: 100 mV, b: 50 mV, 1 nA, 4 K, 0 T, Cr bulk tip.*

### Alternating contrast on the domain walls

Figure VI.16 shows a spin resolved differential conductance map similar to the ones from Figure VI.15 but on a larger area in order to get enough statistics about the domain walls. Here the tip sensitivity direction is not fully in-plane or fully out-of-plane but canted and thus both the out-of-plane domains and the in-plane contrast on the walls are visible. The observed contrast is explained in the sketch. With only the TMR effect and such a canted magnetization at the tip apex, one should see some brighter and darker domains separated by brighter and darker walls. The additional electronic contrast reduces the signal at the position of the domain walls. In the sum, one can thus see the out-of-plane domains, one type of domains walls looks very dark and the other type of walls can hardly be distinguished from the ferromagnetic background.

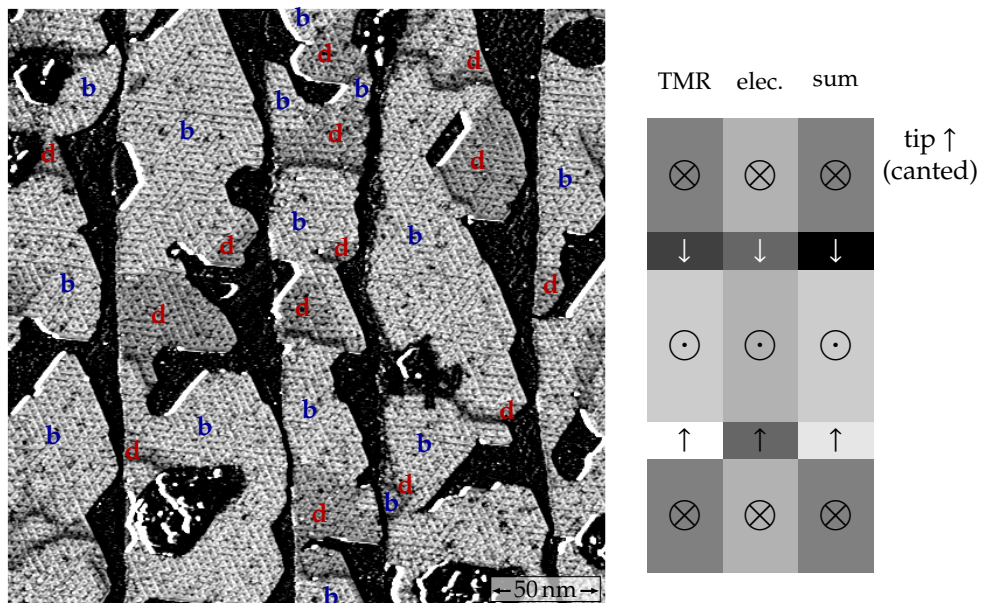


Figure VI.16: Spin-resolved differential conductance map of a Ni/Fe bilayer on Ir(111). The tip is sensitive to both the out-of-plane and the in-plane components of the sample magnetization: the out-of-plane magnetized domains (marked with **d** and **b**) as well as the domain walls are visible. The sketch explains the observed contrast. Note that the contrast induced by the electronic contributions (second column) is the same for the two walls, despite the optical illusion. Because of the presence of this additional electronic contrast at the bias voltage used, half of the walls appear very dark whereas the other half is only slightly bright and thus hardly visible. These two types of walls are alternating which demonstrates that they have a unique rotational sense. *Measurement parameters:* 100 mV, 1 nA, 4 K, 200 mT, Cr bulk tip.

Concerning the rotational sense of the domain walls, the important point is their ordering. In the image from Figure VI.16, starting from the top and going down, one crosses a bright domain, then an invisible domain wall and enters a dark domain. Going further down, the next domain wall is very dark and one reaches a bright domain after crossing it. This ordering bright domain - invisible wall - dark domain - very dark wall - bright domain (from the top to the bottom) is the same in the whole

scan area. This indicates that all the observed walls in this image have the same rotational sense.

If the two possible rotational senses are energetically equivalent, i.e. if they have the same probability to appear, the probability to observe more than 7 domain walls with the same rotational sense is below 1%. Since the number of domain walls in Figure VI.16 is around 20, this measurement demonstrates that the domain walls all have the same unique rotational sense in Ni/Fe/Ir(111).

This finding is not surprising since homochiral domain walls were already observed in Fe/Ni/Cu(001),<sup>11</sup> a system in which the DMI is rather weak because of the small spin-orbit coupling in the substrate. For Ni/Fe/Ir(111), it is already known that the DMI is very large at the Fe/Ir(111) interface. Therefore this result confirms the expectations about the unique rotational sense of the domain walls.

<sup>11</sup> G. Chen et al.  
*Physical Review Letters* 110, 177204  
(2013) [145]

### VI.1.3.3 Strong pinning at the bridge lines

#### Pinning at the long bridge lines

As it was previously mentioned, the domain walls in the Ni/Fe bilayer have an unusual shape. They do not follow straight lines to minimize their length but rather follow the dislocation pattern. Figure VI.17 gathers close views on 10 different walls. For each of these sample areas, the long bridge lines located at the position of the domain walls are marked in red. It shows clearly that the domain walls prefer to stay along the long bridge lines. When the lines are interrupted, the direction of the wall is likely to change.

It seems that the energy gained by having the domain walls along the lines compensates the energy lost of having longer domain walls. This suggests that the magnetic parameters are modulated within the Ni/Fe bilayer because of the stacking variations in the dislocation pattern. For example, a reduced out-of-plane magnetic anisotropy on the bridge lines would decrease the energy cost of the rotation of the magnetic moments in the domain walls and could thus explain this strong pinning effect.

#### Position of the domain walls

It would be interesting to know where the domain walls are exactly located, for example if the rotation of the moments starts at the bridge line or if the line is exactly at the center of the wall. The procedure used to measure this exact position is the following:

- Mark the position of the bridge line on which the wall is pinned in the constant-current map.
- Note the positions of points located on bridge lines on both sides of the domain wall at various distances from the marked bridge line.

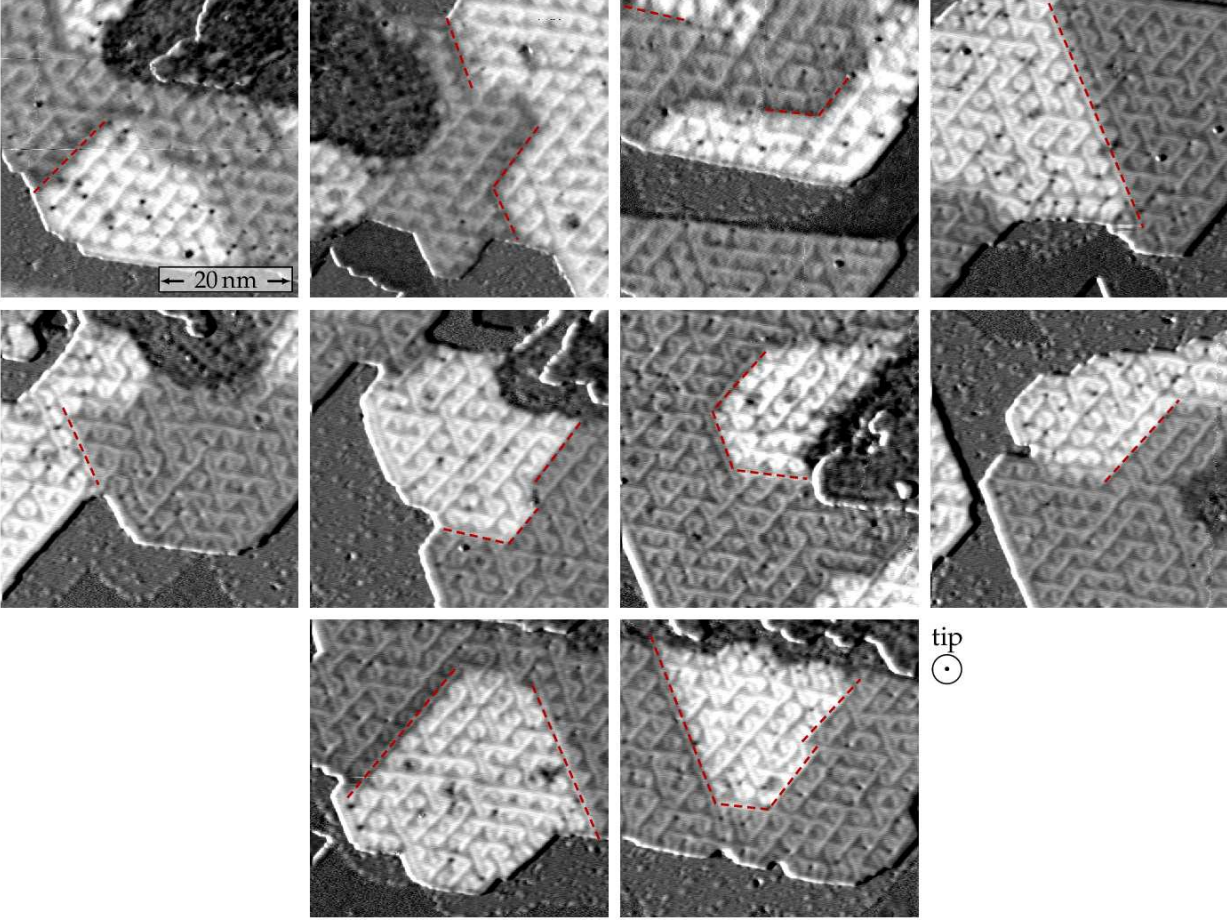


Figure VI.17: Spin-resolved differential conductance maps of 10 different domain walls in the Ni/Fe bilayer on Ir(111). The position of long bridge lines are marked in red, which reveals that the domain walls are pinned at these lines. *Measurement parameters:* 100 mV, 1 nA, 4 K, Cr bulk tip.

- Plot the values of the differential conductance at these points as a function of the distance to the marked bridge line. The differential conductance value is averaged in a square of  $3 \times 3$  pixels centered at the point on the bridge line.
- Fit a domain wall profile in this data and check the position of the center. Here the tip magnetization direction is fixed out-of-plane to avoid deviations originating from the oscillations present in the data and induced by the dislocation pattern.

This procedure was applied to a wall pinned at a very long bridge line and for which the additional electronic contrast is not visible in the differential conductance map. The result is shown in Figure VI.18.

The fit is done using equation II.13 and the fit procedure is defined by:

$$\varphi_{180^\circ DW}(x) = \arcsin\left(\tanh\left(\frac{x-c}{w/2}\right)\right) \quad (\text{VI.1})$$

$$y_{fit} = A \cos(\varphi_{180^\circ DW}(x) + \theta) + y_0 \quad (\text{VI.2})$$

where  $x$  is the spatial coordinate along the profile,  $c$  is the position of the

center of the wall,  $w$  its width,  $A$  the amplitude of the measured signal,  $y_0$  its offset and  $\theta$  the polar angle of the tip magnetization, fixed to  $\pi/2$ .

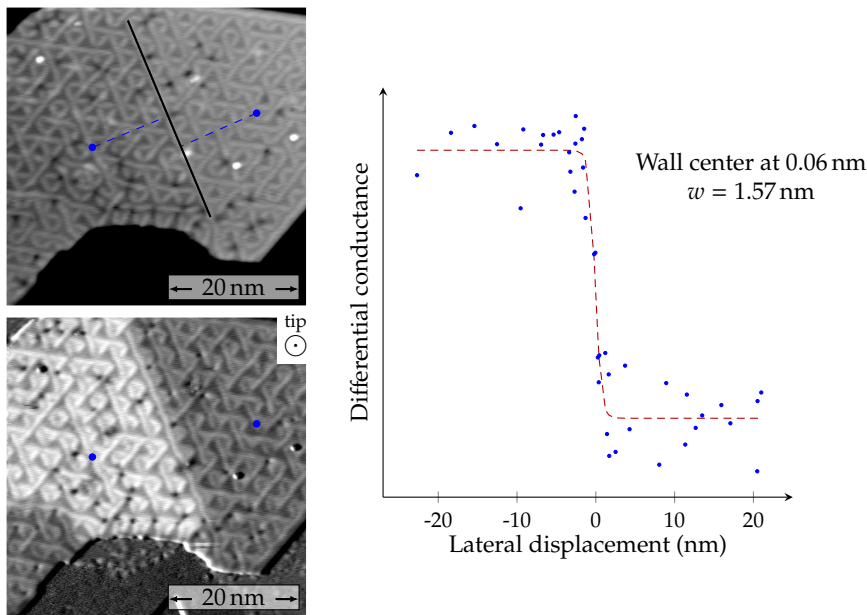


Figure VI.18: Differential conductance values at points located on the bridge lines in the bottom image, plotted as a function of their distance to the long bridge line marked in the constant-current map (top). A domain wall profile (red dashed line) was fitted to the data (blue dots) in order to find the position of the center of the wall.

The center of this wall is located exactly on the bridge line. The wall width obtained is small but here the curve is not as smooth as a line profile, the shape of the wall is not well reproduced in the data and thus the width value is not very accurate. Because of the strength of the signal arising from the dislocation pattern, no reliable measurement of the wall width could be achieved. The presence of the additional electronic contrast on the wall can also make the fitting unreliable, finding a suitable wall for this analysis is therefore complicated. More statistics would help to draw a stronger conclusion but the center of the wall seems to be located on the bridge line. This observation would be compatible with a reduction of the out-of-plane magnetic anisotropy on the bridge line, facilitating the rotation of the magnetic moments towards in-plane directions at the center of the wall.

### **Movement in external magnetic field**

When an external out-of-plane magnetic field is applied to the sample, the domains aligned with the field direction grow, which means that the domain walls are moving. However, because of the strong pinning, this movement consists of jumps from one bridge line to another. Figure VI.19 displays a series of measurements in the same area with an increasing magnetic field.

The domain on the left, in which the magnetization is aligned with the field, is growing. At every field step, the domain wall jumps to another

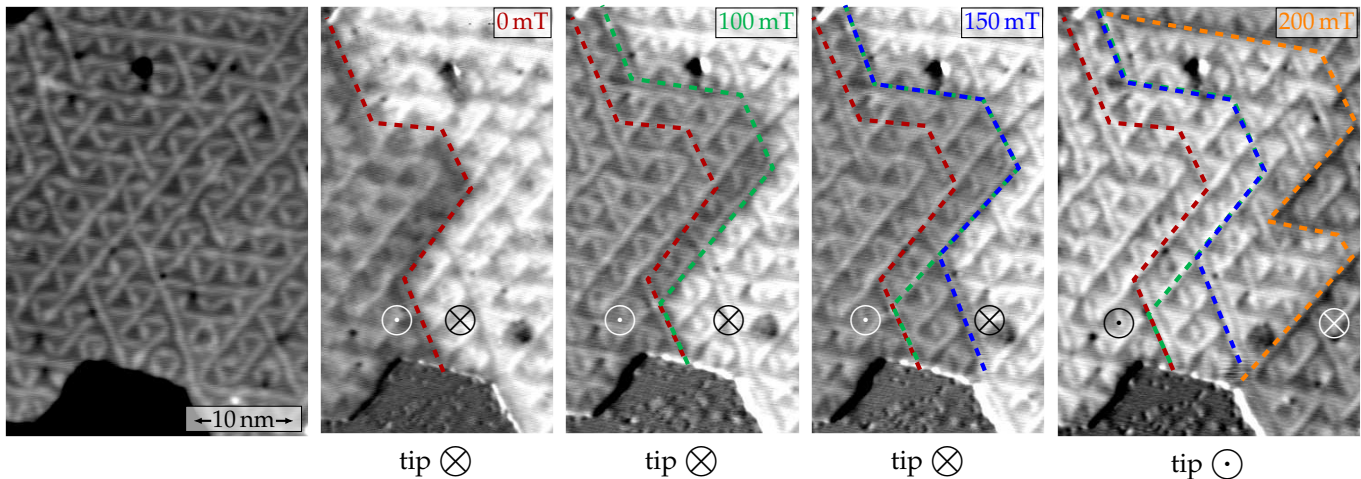


Figure VI.19: Constant-current map (left) and spin-resolved differential conductance maps showing the field dependence of a domain wall in Ni/Fe/Ir(111). The constant-current map shows the details of the dislocation pattern. When the field increases, the domain on the left grows. The domain wall jumps from a bridge line to the next which demonstrates again the strong pinning of the walls to the bridge lines. The tip is sensitive to the out-of-plane component of the sample magnetization and it switched between 150 mT and 200 mT, which caused a contrast inversion. *Measurement parameters:* 100 mV, 1 nA, 4 K, Cr bulk tip.

bridge line, illustrating again the strong pinning of the walls to the long bridge lines.

Note that the magnetization at the tip apex reversed between 150 mT and 200 mT which explains the contrast inversion in the image at 200 mT. Some walls even start to move at 50 mT and the pinning effect varies from line to line (probably depending on the length of the line and on the presence of defects). At 1 T, the sample is fully polarized and stays remanent when the field is decreased again to zero.

Figure VI.20 shows a series a differential conductance maps with out-of-plane spin sensitivity measured in the same area at the same magnetic field and the time interval between the scans is indicated. Nothing was done (no scanning) during the 40 min between the first and the second scan. The third scan was performed right after the second one. During the 4 h between the third and the fourth scan, measurements were only performed in the yellow marked area. Some movements of the walls occurred between the scans, while the magnetic field was kept constant at 200 mT, even in areas which were not scanned. This observation allows to exclude that the movement is dominantly induced by the tip and rather suggests that the movement of the wall is thermal. The presence of the magnetic field breaks the symmetry and favors one of the domains but at 200 mT, the pinning effect is still very large. Thermal energy is thus needed to overcome the pinning barriers and move the walls.

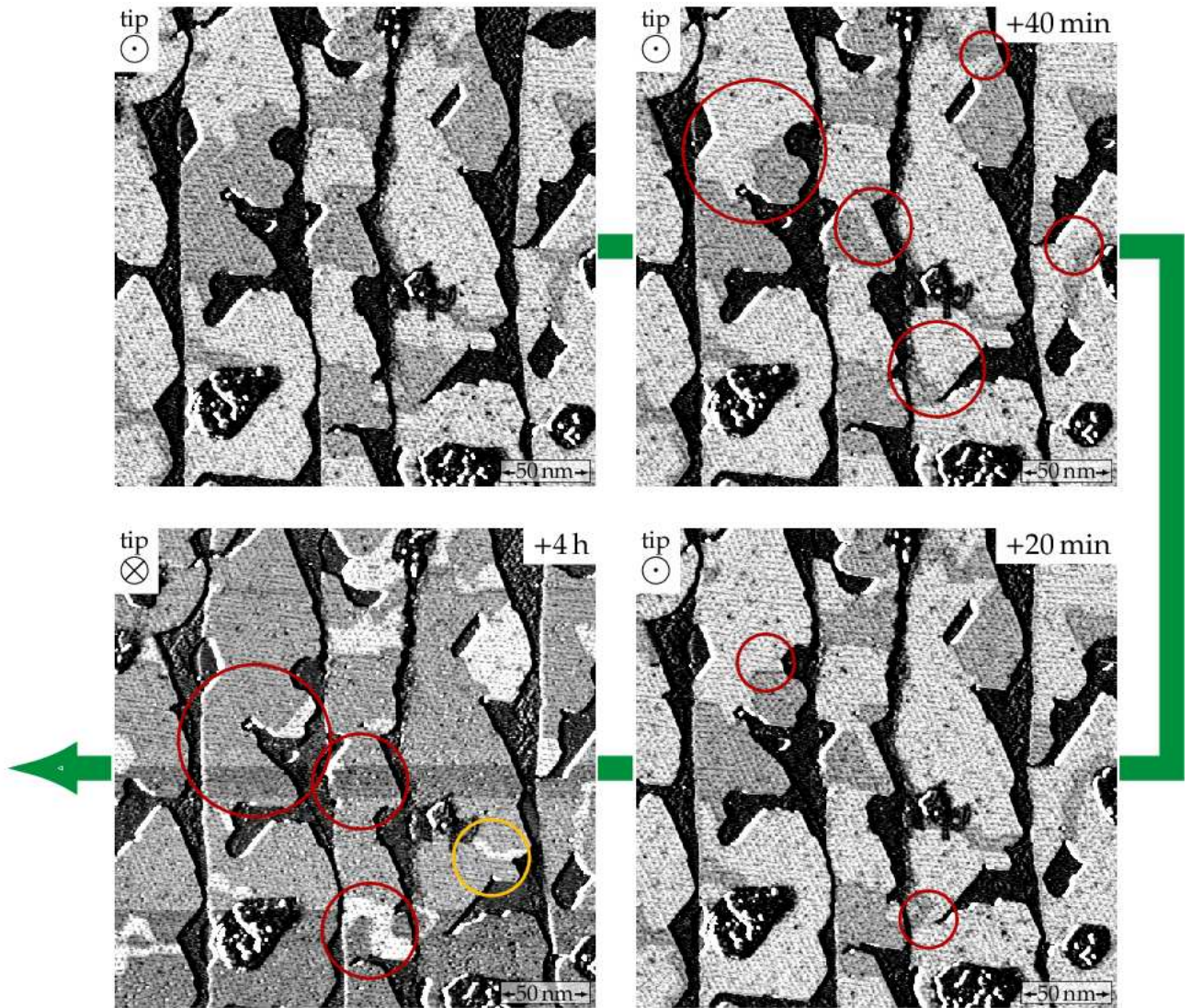


Figure VI.20: Spin-resolved differential conductance maps of a Ni/Fe bilayer on Ir(111) imaged with the same parameters with various time intervals between the scans. The areas where the walls moved are marked in red and the duration indicated on the images corresponds to the time elapsed since the previous scan shown. Between the third and the fourth image, only the area marked in yellow was scanned. *Measurement parameters:* 100 mV, 1 nA, 4 K, 200 mT, Cr bulk tip.

### VI.1.4 Summary

The Ni/Fe bilayer on Ir(111) exhibits a dislocation pattern composed of triangular hcp and fcc areas separated by bridge lines. The Ni nanoislands on Fe/Ir(111) are ferromagnetic.<sup>12</sup> In extended films, out-of-plane magnetic domains with a size between 30 nm and 100 nm alternate. The domain walls have a unique rotational sense and follow long bridge lines from the dislocation pattern. The pinning of the walls to these bridge lines is very strong and is probably induced by a spatial modulation of magnetic parameters, for example the out-of-plane magnetic anisotropy.

<sup>12</sup> D. Iaia et al. *Physical Review B* 93, 134409 (2016) [144]

## VI.2 Comparison between the various systems based on the Fe/Ir interface

In the previous chapters and sections, the effects of the addition of a Fe or a Ni layer on top of the monolayer on Ir(111) were discussed. In this section, these results are compared with the influence of a Pd, a Rh or a Pb layer. These various examples demonstrate the high tunability of the magnetic state in Fe ultrathin films on Ir(111) via the addition of metallic layers on top of the Fe monolayer. Starting from the complex square nanoskyrmion lattice in the Fe monolayer, a large variety of magnetic structures can be reached by interface engineering.

**Fe/Fe/Ir(111)** When a second Fe layer is grown on top of the Fe monolayer, dislocation lines form to relieve the epitaxial strain and spin spirals propagate along these lines<sup>1</sup> (section III.2). The period of the spirals is very small, about 1.5 nm, which remains close to the 1 nm-size of the magnetic unit cell of the nanoskyrmion lattice. This short wavelength is stabilized in the Fe double layer case both by the large DMI at the Fe/Ir interface and a large frustration of the magnetic exchange<sup>2</sup>.

<sup>1</sup> P.-J. Hsu et al. *Physical Review Letters* 116, 017201 (2016) [85]

<sup>2</sup> P.-J. Hsu et al. *Nature Communications* 9, 1571 (2018) [108]

**Pd/Fe/Ir(111)** When a non-magnetic pseudomorphic Pd layer is added on top of the Fe monolayer, the period of the spin spiral reaches 6 nm and in contrast to the double layer Fe, the Pd/Fe bilayer reacts to the application of an external magnetic field by forming a skyrmion phase around 3 T.<sup>3</sup> In the case of hcp Pd on fcc Fe, the magnetic state can be nicely described using a micromagnetic model considering effective exchange interactions, the DMI and the effective magnetic anisotropy.

<sup>3</sup> N. Romming et al. *Science* 341, 636–639 (2013) [6]

**Ni/Fe/Ir(111)** Although Ni is isoelectronic to Pd (but ferromagnetic in bulk!), the effect of a Ni overlayer on the Fe monolayer on Ir(111) is very different. Because of the large lattice mismatch, the epitaxial strain is relieved by the creation of a triangular dislocation pattern. The Ni/Fe bilayer is ferromagnetic with out-of-plane magnetized domains and the domain walls are strongly pinned to the dislocation pattern. Nevertheless, the effect of the DMI is still noticeable: the domain walls have a unique rotational sense.

**Rh/Fe/Ir(111)** In the case of a Rh overlayer, depending on the stacking, either a short period spin spiral (1.5 nm, similar to the Fe double layer) or a canted  $\uparrow\uparrow\downarrow$ -state is measured.<sup>4</sup> The spiral state is stabilized by the frustration of exchange interaction. However, in order to understand to emergence of the canted  $\uparrow\uparrow\downarrow$ -state, one needs to consider the competition between the DMI and higher-order exchange couplings.

<sup>4</sup> N. Romming et al. *Physical Review Letters* 120, 207201 (2018) [66]

**Pb/Fe/Ir(111)** The influence of a Pb layer was also investigated and is mentioned here for completeness. The Pb growth on the Fe monolayer is different than for the previous elements, it forms a honeycomb lattice.<sup>5</sup> However, no magnetic contrast could be observed in the Pb/Fe bilayer on Ir(111).

The addition of a metallic overlayer turns out to be a very efficient way to modify the subtle balance between the various magnetic interactions in ultrathin films and thus to precisely control their magnetic states and properties.

<sup>5</sup> J. Sassmanshausen. Master thesis. Universität Hamburg, 2016 [147]



## VII. Summary

In this thesis, three types of non-collinear magnetic structures in ultrathin films were studied using SP-STM:

- spin spirals in the Fe double and triple layers on Ir(111);
- skyrmions in the Fe triple layer on Ir(111) and nanoskyrmion lattices in the hydrogenated Fe monolayer on Ir(111);
- domain walls in the NiFe bilayer on Ir(111).

They illustrate the large variety of states which can be stabilized in Fe-based films on Ir(111) as well as the broad range of efficient means to tune non-collinear magnetism.

The investigations were especially focused on the interplay between these complex states and the structural properties of the epitaxial films. The spatial resolution of STM, which can go down to the atomic scale indeed allows to gain detailed information about the structural patterns which can form at the surface of epitaxial films. They can for example be induced by strain relief or the incorporation of H atoms in the film. The presence of structural patterns introduces a spatial modulation of the magnetic properties which have a clear influence on the observed magnetic states.

This way, cycloidal spin spirals propagating along the dislocation lines were found in the uniaxially relaxed Fe double and triple layers on Ir(111). In addition, local variations of the strain relief in the Fe triple layer have a considerable impact on the period of these spirals, ranging from 3 nm to 10 nm. Using a simple micromagnetic model, this change induced by the strain relief was attributed to a modulation of the effective exchange coupling within the film. When a magnetic field is applied to this system, skyrmions are created, aligned along the dislocation lines. They can reliably be switched using the STM tip and a detailed investigation allowed to conclude that this switching is mainly driven by an electric field. The electric field is then a further parameter which can be used to tune magnetic states, and it could be very useful for the development of energy-efficient devices. Temperature-dependent measurements revealed that the period of the spin spirals in the Fe triple layer on Ir(111) increases strongly between 4 K and room temperature. This observation was interpreted with a model in which the magnetic interactions are different in the three atomic Fe layers. Such an effect indicates that using effective magnetic parameters which correspond to the whole layer might not be suited to describe thermal effects in systems made of different magnetic layers. A further study demonstrated that H atoms can be incorporated in the Fe monolayer and double layer on Ir(111) to form superstructures. The presence of the H atoms changes both the atom arrangement and the vertical spacing between the different layers. These structural modifications have a direct effect on the magnetic state, allowing to stabilize skyrmions in the Fe double layer, which is not possible for the pristine film, and modifying the symmetry of the nanoskyrmion lattice in the monolayer. The incorporation of H atoms is thus a controlled way to tune the magnetic state of the Fe/Ir(111) samples.

The domain walls in the ferromagnetic NiFe bilayer on Ir(111) were also investigated. They exhibit a very strong pinning to the dislocation pattern which forms in the layer to relieve the strain. This observation suggests that because of the dislocation pattern, the energy required to form domain walls is reduced at some specific positions, which would explain the observed pinning. The patterning of the film (here spontaneously realized to relieve the strain) consequently allows to tune the magnetic configuration of the sample.

This work throws light upon the magnetic behavior of thin films which are neither perfectly pseudomorphically epitaxial nor as disordered as sputtered films. This fundamental study on model type systems provides insight into some very general phenomena, which might be useful for a better understanding of the mechanisms inducing pinning in the sputtered films. Further possible means to control non-collinear magnetism were also indicated, in particular local strain variations or the incorporation of H atoms.

# Bibliography

- [1] S. Wolf, D. Awschalom, R. Buhrman, J. Daughton, S. von Molnár, M. Roukes, A. Chtchelkanova, and D. Treger. [Spintronics: A Spin-Based Electronics Vision for the Future](#). *Science* 294, 1488–1495 (2001).
- [2] S. Parkin, M. Hayashi, and L. Thomas. [Magnetic Domain-Wall Racetrack Memory](#). *Science* 320, 190–194 (2008).
- [3] A. Fert, V. Cros, and J. Sampaio. [Skyrmions on the track](#). *Nature Nanotechnology* 8, 152–156 (2013).
- [4] N. Nagaosa and Y. Tokura. [Topological properties and dynamics of magnetic skyrmions](#). *Nature Nanotechnology* 8, 899–911 (2013).
- [5] S. Woo, K. Litzius, B. Krüger, M.-Y. Im, L. Caretta, K. Richter, M. Mann, A. Krone, R. Reeve, M. Weigand, P. Agrawal, I. Lemesch, M.-A. Mawass, P. Fischer, M. Kläui, and G. Beach. [Observation of room-temperature magnetic skyrmions and their current-driven dynamics in ultrathin metallic ferromagnets](#). *Nature Materials* 15, 501–506 (2016).
- [6] N. Romming, C. Hanneken, M. Menzel, J. Bickel, B. Wolter, K. von Bergmann, A. Kubetzka, and R. Wiesendanger. [Writing and Deleting Single Magnetic Skyrmions](#). *Science* 341, 636–639 (2013).
- [7] C. Hanneken, A. Kubetzka, K. von Bergmann, and R. Wiesendanger. [Pinning and movement of individual nanoscale magnetic skyrmions via defects](#). *New Journal of Physics* 18, 055009 (2016).
- [8] X. Zhang, M. Ezawa, and Y. Zhou. [Magnetic skyrmion logic gates: conversion, duplication and merging of skyrmions](#). *Scientific Reports* 5, 9400 (2015).
- [9] D. Prychynenko, M. Sitte, K. Litzius, B. Krüger, G. Bourianoff, M. Kläui, J. Sinova, and K. Everschor-Sitte. [Magnetic Skyrmion as a Nonlinear Resistive Element: A Potential Building Block for Reservoir Computing](#). *Physical Review Applied* 9, 014034 (2018).
- [10] S. Blundell. *Magnetism in Condensed Matter*. Oxford University Press, 2001.
- [11] P. Bruno. Physical origins and theoretical models of magnetic anisotropy. *Magnetismus von Festkörpern und Grenzflächen*. Forschungszentrum Jülich: IFF-Ferienkurs, 1993, 24.1–24.28.
- [12] L. Néel. [Anisotropie magnétique superficielle et surstructures d’orientation](#). *Journal de Physique et le Radium* 15, 225–239 (1954).
- [13] B. Tudu and A. Tiwari. [Recent Developments in Perpendicular Magnetic Anisotropy Thin Films for Data Storage Applications](#). *Vacuum* 146, 329–341 (2017).

- [14] S. Ikeda, K. Miura, H. Yamamoto, K. Mizunuma, H. Gan, M. Endo, S. Kanai, J. Hayakawa, F. Matsukura, and H. Ohno. [A perpendicular-anisotropy CoFeB–MgO magnetic tunnel junction](#). *Nature Materials* 9, 721–724 (2010).
- [15] M. Ruderman and C. Kittel. [Indirect Exchange Coupling of Nuclear Magnetic Moments by Conduction Electrons](#). *Physical Review* 96, 99–102 (1954).
- [16] T. Kasuya. [A Theory of Metallic Ferro- and Antiferromagnetism on Zener’s Model](#). *Progress of Theoretical Physics* 16, 45–57 (1956).
- [17] K. Yosida. [Magnetic Properties of Cu-Mn Alloys](#). *Physical Review* 106, 893–898 (1957).
- [18] S. Klingler, A. Chumak, T. Mewes, B. Khodadadi, C. Mewes, C. Dubs, O. Surzhenko, B. Hillebrands, and A. Conca. [Measurements of the exchange stiffness of YIG films using broadband ferromagnetic resonance techniques](#). *Journal of Physics D: Applied Physics* 48, 015001 (2015).
- [19] I. Dzyaloshinskii. [A thermodynamic theory of “weak” ferromagnetism of antiferromagnetics](#). *Journal of Physics and Chemistry of Solids* 4, 241–255 (1958).
- [20] T. Moriya. [Anisotropic superexchange interaction and weak ferromagnetism](#). *Physical Review* 120, 91 (1960).
- [21] S. Mühlbauer, B. Binz, F. Jonietz, C. Pfleiderer, A. Rosch, A. Neubauer, R. Georgii, and P. Böni. [Skyrmion lattice in a chiral magnet](#). *Science* 323, 915–919 (2009).
- [22] I. Sergienko and E. Dagotto. [Role of the Dzyaloshinskii-Moriya interaction in multiferroic perovskites](#). *Physical Review B* 73 (2006).
- [23] A. Bogdanov and D. Yablonskii. Thermodynamically stable "vortices" in magnetically ordered crystals. The mixed state of magnets. *Journal of Experimental and Theoretical Physics* 95, 178–182 (1989).
- [24] S.-G. Je, D.-H. Kim, S.-C. Yoo, B.-C. Min, K.-J. Lee, and S.-B. Choe. [Asymmetric magnetic domain-wall motion by the Dzyaloshinskii-Moriya interaction](#). *Physical Review B* 88, 214401 (2013).
- [25] A. Stashkevich, M. Belmeguenai, Y. Roussigné, S. Cherif, M. Kostylev, M. Gabor, D. Lacour, C. Tiusan, and M. Hehn. [Experimental study of spin-wave dispersion in Py/Pt film structures in the presence of an interface Dzyaloshinskii-Moriya interaction](#). *Physical Review B* 91, 214409 (2015).
- [26] M. Perini, S. Meyer, B. Dupé, S. von Malottki, A. Kubetzka, K. von Bergmann, R. Wiesendanger, and S. Heinze. [Domain walls and Dzyaloshinskii-Moriya interaction in epitaxial Co/Ir\(111\) and Pt/Co/Ir\(111\)](#). *Physical Review B* 97, 184425 (2018).
- [27] S. Heinze, K. von Bergmann, M. Menzel, J. Brede, A. Kubetzka, R. Wiesendanger, G. Bihlmayer, and S. Blügel. [Spontaneous atomic-scale magnetic skyrmion lattice in two dimensions](#). *Nature Physics* 7, 713–718 (2011).

- [28] M. Hoffmann and S. Blügel. [Systematic derivation of realistic spin-models for beyond-Heisenberg solids from microscopic model](#). *arXiv:1803.01315 [cond-mat]* (2018).
- [29] A. Krönlein, M. Schmitt, M. Hoffmann, J. Kemmer, N. Seubert, M. Vogt, J. Küspert, M. Böhme, B. Alonazi, J. Kügel, H. A. Albrithen, M. Bode, G. Bihlmayer, and S. Blügel. [Magnetic Ground State Stabilized by Three-Site Interactions: Fe/Rh\(111\)](#). *Physical Review Letters* 120, 207202 (2018).
- [30] M. Heide, G. Bihlmayer, and S. Blügel. [Dzyaloshinskii-Moriya interaction accounting for the orientation of magnetic domains in ultrathin films: Fe/W\(110\)](#). *Physical Review B* 78, 140403 (2008).
- [31] A. Kubetzka, O. Pietzsch, M. Bode, and R. Wiesendanger. [Spin-polarized scanning tunneling microscopy study of 360° walls in an external magnetic field](#). *Physical Review B* 67, 020401 (2003).
- [32] K. von Bergmann, A. Kubetzka, O. Pietzsch, and R. Wiesendanger. [Interface-induced chiral domain walls, spin spirals and skyrmions revealed by spin-polarized scanning tunneling microscopy](#). *Journal of Physics: Condensed Matter* 26, 394002 (2014).
- [33] A. Bogdanov and A. Hubert. [Thermodynamically stable magnetic vortex states in magnetic crystals](#). *Journal of Magnetism and Magnetic Materials* 138, 255–269 (1994).
- [34] T. Skyrme. [A non-linear field theory](#). *Proc. R. Soc. Lond. A* 260, 127–138 (1961).
- [35] T. Shinjo, T. Okuno, R. Hassdorf, K. Shigeto, and T. Ono. [Magnetic Vortex Core Observation in Circular Dots of Permalloy](#). *Science* 289, 930–932 (2000).
- [36] R. Wiesendanger. Nanoscale magnetic skyrmions in metallic films and multilayers: a new twist for spintronics. *Nature Reviews Materials* 1, 16044 (2016).
- [37] W. Jiang, X. Zhang, G. Yu, W. Zhang, X. Wang, M. Benjamin Jungfleisch, J. Pearson, X. Cheng, O. Heinonen, K. L. Wang, Y. Zhou, A. Hoffmann, and S. te Velthuis. [Direct observation of the skyrmion Hall effect](#). *Nature Physics* 13, 162–169 (2017).
- [38] M. Lee, W. Kang, Y. Onose, Y. Tokura, and N. Ong. [Unusual Hall Effect Anomaly in MnSi under Pressure](#). *Physical Review Letters* 102 (2009).
- [39] A. V. Oosterom and J. Strackee. [The Solid Angle of a Plane Triangle](#). *IEEE Transactions on Biomedical Engineering* BME-30, 125–126 (1983).
- [40] N. Romming, A. Kubetzka, C. Hanneken, K. von Bergmann, and R. Wiesendanger. [Field-Dependent Size and Shape of Single Magnetic Skyrmions](#). *Physical Review Letters* 114, 177203 (2015).
- [41] X. Yu, N. Kanazawa, Y. Onose, K. Kimoto, W. Zhang, S. Ishiwata, Y. Matsui, and Y. Tokura. [Near room-temperature formation of a skyrmion crystal in thin-films of the helimagnet FeGe](#). *Nature Materials* 10, 106–109 (2011).

- [42] L. Schmidt, J. Hagemester, P.-J. Hsu, A. Kubetzka, K. von Bergmann, and R. Wiesendanger. [Symmetry breaking in spin spirals and skyrmions by in-plane and canted magnetic fields](#). *New Journal of Physics* 18, 075007 (2016).
- [43] G. Binnig, H. Rohrer, C. Gerber, and E. Weibel. [Surface Studies by Scanning Tunneling Microscopy](#). *Physical Review Letters* 49, 57–61 (1982).
- [44] J. Bardeen. [Tunnelling from a Many-Particle Point of View](#). *Physical Review Letters* 6, 57–59 (1961).
- [45] V. Ukraintsev. [Data evaluation technique for electron-tunneling spectroscopy](#). *Physical Review B* 53, 11176 (1996).
- [46] J. Tersoff and D. Hamann. [Theory of the scanning tunneling microscope](#). *Physical Review B* 31, 805 (1985).
- [47] R. Wiesendanger. *Scanning probe microscopy and spectroscopy. Methods and applications*. Cambridge University Press, 1994.
- [48] C. Chen. [Tunneling matrix elements in three-dimensional space: The derivative rule and the sum rule](#). *Physical Review B* 42, 8841–8857 (1990).
- [49] C. Witt, U. Mick, M. Bode, and R. Wiesendanger. [An ultrahigh vacuum scanning tunneling microscope for in situ studies of thin-film growth](#). *Review of Scientific Instruments* 68, 1455–1457 (1997).
- [50] O. Pietzsch, A. Kubetzka, D. Haude, M. Bode, and R. Wiesendanger. [A low-temperature ultrahigh vacuum scanning tunneling microscope with a split-coil magnet and a rotary motion stepper motor for high spatial resolution studies of surface magnetism](#). *Review of Scientific Instruments* 71, 424–430 (2000).
- [51] T. Eelbo. Construction of a new Ultra-High Vacuum Variable-Temperature Scanning Tunneling Microscope. Diplomarbeit. Universität Hamburg, 2007.
- [52] S. Meckler, M. Gyamfi, O. Pietzsch, and R. Wiesendanger. [A low-temperature spin-polarized scanning tunneling microscope operating in a fully rotatable magnetic field](#). *Review of Scientific Instruments* 80, 023708 (2009).
- [53] R. Wiesendanger, H.-J. Güntherodt, G. Güntherodt, R. Gambino, and R. Ruf. [Observation of vacuum tunneling of spin-polarized electrons with the scanning tunneling microscope](#). *Physical Review Letters* 65, 247–250 (1990).
- [54] M. Julliere. [Tunneling between ferromagnetic films](#). *Physics Letters A* 54, 225–226 (1975).
- [55] J. Slonczewski. [Conductance and exchange coupling of two ferromagnets separated by a tunneling barrier](#). *Physical Review B* 39, 6995–7002 (1989).
- [56] M. Bode. [Spin-polarized scanning tunnelling microscopy](#). *Reports on Progress in Physics* 66, 523 (2003).
- [57] R. Wiesendanger. [Spin mapping at the nanoscale and atomic scale](#). *Reviews of Modern Physics* 81, 1495–1550 (2009).

- [58] D. Wortmann, S. Heinze, P. Kurz, G. Bihlmayer, and S. Blügel. [Resolving Complex Atomic-Scale Spin Structures by Spin-Polarized Scanning Tunneling Microscopy](#). *Physical Review Letters* 86, 4132–4135 (2001).
- [59] M. Kleiber, M. Bode, R. Ravlić, and R. Wiesendanger. [Topology-Induced Spin Frustrations at the Cr\(001\) Surface Studied by Spin-Polarized Scanning Tunneling Spectroscopy](#). *Physical Review Letters* 85, 4606–4609 (2000).
- [60] M. Bode, S. Heinze, A. Kubetzka, O. Pietzsch, X. Nie, G. Bihlmayer, S. Blügel, and R. Wiesendanger. [Magnetization-Direction-Dependent Local Electronic Structure Probed by Scanning Tunneling Spectroscopy](#). *Physical Review Letters* 89, 237205 (2002).
- [61] K. von Bergmann, M. Menzel, D. Serrate, Y. Yoshida, S. Schröder, P. Ferriani, A. Kubetzka, R. Wiesendanger, and S. Heinze. [Tunneling anisotropic magnetoresistance on the atomic scale](#). *Physical Review B* 86, 134422 (2012).
- [62] C. Hanneken, F. Otte, A. Kubetzka, B. Dupé, N. Romming, K. von Bergmann, R. Wiesendanger, and S. Heinze. [Electrical detection of magnetic skyrmions by tunnelling non-collinear magnetoresistance](#). *Nature Nanotechnology* 10, 1039–1042 (2015).
- [63] A. Kubetzka, C. Hanneken, R. Wiesendanger, and K. von Bergmann. [Impact of the skyrmion spin texture on magnetoresistance](#). *Physical Review B* 95 (2017).
- [64] D. M. Crum, M. Bouhassoune, J. Bouaziz, B. Schweflinghaus, S. Blügel, and S. Lounis. [Perpendicular reading of single confined magnetic skyrmions](#). *Nature Communications* 6, 8541 (2015).
- [65] A. Al-Zubi, G. Bihlmayer, and S. Blügel. [Modeling magnetism of hexagonal Fe monolayers on 4d substrates](#). *physica status solidi (b)* 248, 2242–2247 (2011).
- [66] N. Romming, H. Pralow, A. Kubetzka, M. Hoffmann, S. von Malottki, S. Meyer, B. Dupé, R. Wiesendanger, K. von Bergmann, and S. Heinze. [Competition of Dzyaloshinskii-Moriya and Higher-Order Exchange Interactions in Rh/Fe Atomic Bilayers on Ir\(111\)](#). *Physical Review Letters* 120, 207201 (2018).
- [67] E. Fawcett. [Spin-density-wave antiferromagnetism in chromium](#). *Reviews of Modern Physics* 60, 209–283 (1988).
- [68] C. Hanneken. Development and Characterization of Cr Bulk Tips for SP-STM. Diplomarbeit. Universität Hamburg, 2011.
- [69] J. P. Ibe, P. P. Bey, S. L. Brandow, R. A. Brizzolara, N. A. Burnham, D. P. DiLella, K. P. Lee, C. R. K. Marrian, and R. J. Colton. [On the electrochemical etching of tips for scanning tunneling microscopy](#). *Journal of Vacuum Science & Technology A* 8, 3570–3575 (1990).
- [70] N. Romming. [Discovery and Manipulation of Individual Skyrmions in Ultrathin Magnetic Films](#). PhD thesis. Universität Hamburg, 2018.

- [71] S. Heinze. [Simulation of spin-polarized scanning tunneling microscopy images of nanoscale non-collinear magnetic structures](#). *Applied Physics A* 85, 407–414 (2006).
- [72] K. von Bergmann, M. Menzel, A. Kubetzka, and R. Wiesendanger. [Influence of the Local Atom Configuration on a Hexagonal Skyrmion Lattice](#). *Nano Letters* 15, 3280–3285 (2015).
- [73] H. Tanaka, J. Yoshinobu, and M. Kawai. [Oxygen-induced reconstruction of the Pd\(110\) surface: an STM study](#). *Surface Science* 327, L505–L509 (1995).
- [74] M. Sicot, O. Kurnosikov, H. Swagten, and B. Koopmans. [Hydrogen superstructures on Co nanoislands and Cu\(111\)](#). *Surface Science* 602, 3667–3673 (2008).
- [75] J. Park, C. Park, M. Yoon, and A.-P. Li. [Surface Magnetism of Cobalt Nanoislands Controlled by Atomic Hydrogen](#). *Nano Letters* 17, 292–298 (2017).
- [76] C. Günther, J. Vrijmoeth, R. Hwang, and R. Behm. [Strain Relaxation in Hexagonally Close-Packed Metal-Metal Interfaces](#). *Physical Review Letters* 74, 754–757 (1995).
- [77] A. Schmidt, W. Meier, L. Hammer, and K. Heinz. [Deep-going reconstruction of Ir\(100\)-5 × 1](#). *Journal of Physics: Condensed Matter* 14, 12353 (2002).
- [78] G. Binnig, H. Rohrer, C. Gerber, and E. Weibel. [7 × 7 Reconstruction on Si\(111\) Resolved in Real Space](#). *Physical Review Letters* 50, 120–123 (1983).
- [79] J. Barth, H. Brune, G. Ertl, and R. Behm. [Scanning tunneling microscopy observations on the reconstructed Au\(111\) surface: Atomic structure, long-range superstructure, rotational domains, and surface defects](#). *Physical Review B* 42, 9307–9318 (1990).
- [80] K. von Bergmann, S. Heinze, M. Bode, G. Bihlmayer, S. Blügel, and R. Wiesendanger. [Complex magnetism of the Fe monolayer on Ir\(111\)](#). *New Journal of Physics* 9, 396 (2007).
- [81] J. Grenz, A. Köhler, A. Schwarz, and R. Wiesendanger. [Probing the Nano-Skyrmion Lattice on Fe/Ir\(111\) with Magnetic Exchange Force Microscopy](#). *Physical Review Letters* 119, 047205 (2017).
- [82] N. Hauptmann, J. Gerritsen, D. Wegner, and A. Khajetoorians. [Sensing Noncollinear Magnetism at the Atomic Scale Combining Magnetic Exchange and Spin-Polarized Imaging](#). *Nano Letters* 17, 5660–5665 (2017).
- [83] J. Hagemester, D. Iaia, E. Vedmedenko, K. von Bergmann, A. Kubetzka, and R. Wiesendanger. [Skyrmions at the Edge: Confinement Effects in Fe/Ir\(111\)](#). *Physical Review Letters* 117 (2016).
- [84] A. Sonntag, J. Hermenau, S. Krause, and R. Wiesendanger. [Thermal Stability of an Interface-Stabilized Skyrmion Lattice](#). *Physical Review Letters* 113, 077202 (2014).

- [85] P.-J. Hsu, A. Finco, L. Schmidt, A. Kubetzka, K. von Bergmann, and R. Wiesendanger. [Guiding Spin Spirals by Local Uniaxial Strain Relief](#). *Physical Review Letters* 116, 017201 (2016).
- [86] E. Bauer and J. van der Merwe. [Structure and growth of crystalline superlattices: From monolayer to superlattice](#). *Physical Review B* 33, 3657–3671 (1986).
- [87] S.-H. Phark, J. A. Fischer, M. Corbetta, D. Sander, K. Nakamura, and J. Kirschner. [Reduced-dimensionality-induced helimagnetism in iron nanoislands](#). *Nature Communications* 5 (2014).
- [88] A. Finco, P.-J. Hsu, A. Kubetzka, K. von Bergmann, and R. Wiesendanger. [Tailoring noncollinear magnetism by misfit dislocation lines](#). *Physical Review B* 94, 214402 (2016).
- [89] M. Hervé, B. Dupé, R. Lopes, M. Böttcher, M. Martins, T. Balashov, L. Gerhard, J. Sinova, and W. Wulfhekel. [Stabilizing spin spirals and isolated skyrmions at low magnetic field exploiting vanishing magnetic anisotropy](#). *Nature Communications* 9, 1015 (2018).
- [90] N. Hauptmann, M. Dupé, T.-C. Hung, A. Lemmens, D. Wegner, B. Dupé, and A. Khajetoorians. [Revealing the correlation between real-space structure and chiral magnetic order at the atomic scale](#). *Physical Review B* 97, 100401 (2018).
- [91] S. Meckler, N. Mikuszeit, A. Preßler, E. Vedmedenko, O. Pietzsch, and R. Wiesendanger. [Real-Space Observation of a Right-Rotating Inhomogeneous Cycloidal Spin Spiral by Spin-Polarized Scanning Tunneling Microscopy in a Triple Axes Vector Magnet](#). *Physical Review Letters* 103, 157201 (2009).
- [92] E. Vedmedenko, A. Kubetzka, K. von Bergmann, O. Pietzsch, M. Bode, J. Kirschner, H. Oepen, and R. Wiesendanger. [Domain Wall Orientation in Magnetic Nanowires](#). *Physical Review Letters* 92 (2004).
- [93] L. Schmidt. [Magnetic skyrmions and spin spirals in ultrathin films and canted magnetic fields](#). PhD thesis. Universität Hamburg, 2017.
- [94] A. Finco, L. Rózsa, P.-J. Hsu, A. Kubetzka, E. Vedmedenko, K. von Bergmann, and R. Wiesendanger. [Temperature-Induced Increase of Spin Spiral Periods](#). *Physical Review Letters* 119, 037202 (2017).
- [95] P.-J. Hsu, A. Kubetzka, A. Finco, N. Romming, K. von Bergmann, and R. Wiesendanger. [Electric-field-driven switching of individual magnetic skyrmions](#). *Nature Nanotechnology* 12, 123–126 (2017).
- [96] J. Cui, J. Hockel, P. Nordeen, D. Pisani, C.-y. Liang, G. Carman, and C. Lynch. [A method to control magnetism in individual strain-mediated magnetoelectric islands](#). *Applied Physics Letters* 103, 232905 (2013).
- [97] Y. Nii, T. Nakajima, A. Kikkawa, Y. Yamasaki, K. Ohishi, J. Suzuki, Y. Taguchi, T. Arima, Y. Tokura, and Y. Iwasa. [Uniaxial stress control of skyrmion phase](#). *Nature Communications* 6, 8539 (2015).

- [98] K. Shibata, J. Iwasaki, N. Kanazawa, S. Aizawa, T. Tanigaki, M. Shirai, T. Nakajima, M. Kubota, M. Kawasaki, H. Park, D. Shindo, N. Nagaosa, and Y. Tokura. [Large anisotropic deformation of skyrmions in strained crystal](#). *Nature Nanotechnology* 10, 589–592 (2015).
- [99] T. Koretsune, N. Nagaosa, and R. Arita. [Control of Dzyaloshinskii-Moriya interaction in  \$Mn\_{1-x}Fe\_xGe\$ : a first-principles study](#). *Scientific Reports* 5, 13302 (2015).
- [100] D. Sando, A. Agbelele, D. Rahmedov, J. Liu, P. Rovillain, C. Toulouse, I. Infante, A. Pyatakov, S. Fusil, E. Jacquet, C. Carrétéro, C. Deranlot, S. Lisenkov, D. Wang, J.-M. Le Breton, M. Cazayous, A. Sacuto, J. Juraszek, A. K. Zvezdin, L. Bellaiche, B. Dkhil, A. Barthélémy, and M. Bibes. [Crafting the magnonic and spintronic response of BiFeO<sub>3</sub> films by epitaxial strain](#). *Nature Materials* 12, 641–646 (2013).
- [101] G. Chen, A. N'Diaye, S. P. Kang, H. Y. Kwon, C. Won, Y. Wu, Z. Qiu, and A. Schmid. [Unlocking Bloch-type chirality in ultrathin magnets through uniaxial strain](#). *Nature Communications* 6, 6598 (2015).
- [102] T. Shimada, J. Okuno, and T. Kitamura. [Ab initio study of spin-spiral noncollinear magnetism in a free-standing Fe\(110\) monolayer under in-plane strain](#). *Physical Review B* 85 (2012).
- [103] D. Sander, C. Schmidhals, A. Enders, and J. Kirschner. [Stress and structure of Ni monolayers on W\(110\): The importance of lattice mismatch](#). *Physical Review B* 57, 1406–1409 (1998).
- [104] J. Hagemester, E. Vedmedenko, and R. Wiesendanger. [Pattern formation in skyrmionic materials with anisotropic environments](#). *Physical Review B* 94, 104434 (2016).
- [105] A. Fert and P. Levy. [Role of Anisotropic Exchange Interactions in Determining the Properties of Spin-Glasses](#). *Physical Review Letters* 44, 1538–1541 (1980).
- [106] P. Bruno and J.-P. Renard. [Magnetic surface anisotropy of transition metal ultrathin films](#). *Applied Physics A* 49, 499–506 (1989).
- [107] H. Yang, A. Thiaville, S. Rohart, A. Fert, and M. Chshiev. [Anatomy of Dzyaloshinskii-Moriya Interaction at Co / Pt Interfaces](#). *Physical Review Letters* 115 (2015).
- [108] P.-J. Hsu, L. Rózsa, A. Finco, L. Schmidt, K. Palotás, E. Vedmedenko, L. Udvardi, L. Szunyogh, A. Kubetzka, K. von Bergmann, and R. Wiesendanger. [Inducing skyrmions in ultrathin Fe films by hydrogen exposure](#). *Nature Communications* 9, 1571 (2018).
- [109] W. Jiang, P. Upadhyaya, W. Zhang, G. Yu, M. Benjamin Jungfleisch, F. Fradin, J. Pearson, Y. Tserkovnyak, K. Wang, O. Heinonen, S. te Velthuis, and A. Hoffmann. [Blowing magnetic skyrmion bubbles](#). *Science* 349, 283–286 (2015).

- [110] C. Moreau-Luchaire, C. Moutafis, N. Reyren, J. Sampaio, C. a. F. Vaz, N. V. Horne, K. Bouzehouane, K. Garcia, C. Deranlot, P. Warnicke, P. Wohlhüter, J.-M. George, M. Weigand, J. Raabe, V. Cros, and A. Fert. [Additive interfacial chiral interaction in multilayers for stabilization of small individual skyrmions at room temperature](#). *Nature Nanotechnology* 11, 444–448 (2016).
- [111] O. Boulle, J. Vogel, H. Yang, S. Pizzini, D. de Souza Chaves, A. Locatelli, T. O. Mentes, A. Sala, L. D. Buda-Prejbeanu, O. Klein, M. Belmeguenai, Y. Roussigné, A. Stashkevich, S. M. Chérif, L. Aballe, M. Foerster, M. Chshiev, S. Auffret, I. M. Miron, and G. Gaudin. [Room-temperature chiral magnetic skyrmions in ultrathin magnetic nanostructures](#). *Nature Nanotechnology* 11, 449–454 (2016).
- [112] A. Soumyanarayanan, M. Raju, A. Gonzalez Oyarce, A. Tan, M.-Y. Im, A. Petrović, P. Ho, K. Khoo, M. Tran, C. Gan, F. Ernult, and C. Panagopoulos. [Tunable room-temperature magnetic skyrmions in Ir/Fe/Co/Pt multilayers](#). *Nature Materials* 16, 898–904 (2017).
- [113] G. Chen, A. Mascaraque, A. T. N’Diaye, and A. K. Schmid. [Room temperature skyrmion ground state stabilized through interlayer exchange coupling](#). *Applied Physics Letters* 106, 242404 (2015).
- [114] P. Jensen, H. Dreyssé, and K. Bennemann. [Calculation of the film-thickness-dependence of the Curie temperature in thin transition metal films](#). *Europhysics Letters* 18, 463 (1992).
- [115] C. Schneider, P. Bressler, P. Schuster, J. Kirschner, J. De Miguel, and R. Miranda. [Curie temperature of ultrathin films of fcc-cobalt epitaxially grown on atomically flat Cu \(100\) surfaces](#). *Physical Review Letters* 64, 1059 (1990).
- [116] H. Elmers, J. Hauschild, H. Fritzsche, G. Liu, U. Gradmann, and U. Köhler. [Magnetic frustration in ultrathin Fe films](#). *Physical Review Letters* 75, 2031 (1995).
- [117] D. Royer and E. Dieulesaint. *Ondes élastiques dans les solides. Tome 1, propagation libre et guidée*. Masson, 1996.
- [118] G. Hasselberg, R. Yanes, D. Hinzke, P. Sessi, M. Bode, L. Szunyogh, and U. Nowak. [Thermal properties of a spin spiral: Manganese on tungsten\(110\)](#). *Physical Review B* 91, 064402 (2015).
- [119] A. Li Bassi, C. Casari, D. Cattaneo, F. Donati, S. Foglio, M. Passoni, C. Bottani, P. Biagioni, A. Brambilla, M. Finazzi, F. Ciccacci, and L. Duò. [Bulk Cr tips for scanning tunneling microscopy and spin-polarized scanning tunneling microscopy](#). *Applied Physics Letters* 91, 173120 (2007).
- [120] P. Sessi, N. Guisinger, J. Guest, and M. Bode. [Temperature and Size Dependence of Antiferromagnetism in Mn Nanostructures](#). *Physical Review Letters* 103, 167201 (2009).

- [121] K. von Bergmann, M. Bode, and R. Wiesendanger. [Coverage-dependent spin reorientation transition temperature of the Fe double-layer on W\(110\) observed by scanning tunneling microscopy](#). *Journal of Magnetism and Magnetic Materials* 305, 279–283 (2006).
- [122] Y. Izyumov. [Modulated, or long-periodic, magnetic structures of crystals](#). *Soviet Physics Uspekhi* 27, 845 (1984).
- [123] J. Akimitsu, K. Siratori, G. Shirane, M. Iizumi, and T. Watanabe. [Neutron Scattering Study of ZnCr<sub>2</sub>Se<sub>4</sub> with Screw Spin Structure](#). *Journal of the Physical Society of Japan* 44, 172–180 (1978).
- [124] J. Arblaster. [Crystallographic Properties of Iridium](#). *Platinum Metals Review* 54, 93–102 (2010).
- [125] K. Zakeri, T.-H. Chuang, A. Ernst, L. Sandratskii, P. Buczek, H. Qin, Y. Zhang, and J. Kirschner. [Direct probing of the exchange interaction at buried interfaces](#). *Nature Nanotechnology* 8, 853–858 (2013).
- [126] K. von Bergmann, S. Heinze, M. Bode, E. Vedmedenko, G. Bihlmayer, S. Blügel, and R. Wiesendanger. [Observation of a Complex Nanoscale Magnetic Structure in a Hexagonal Fe Monolayer](#). *Physical Review Letters* 96, 167203 (2006).
- [127] E. Simon, K. Palotás, B. Ujfalussy, A. Deák, G. Stocks, and L. Szunyogh. [Spin-correlations and magnetic structure in an Fe monolayer on 5 \*d\* transition metal surfaces](#). *Journal of Physics: Condensed Matter* 26, 186001 (2014).
- [128] B. Dupé, M. Hoffmann, C. Paillard, and S. Heinze. [Tailoring magnetic skyrmions in ultra-thin transition metal films](#). *Nature Communications* 5 (2014).
- [129] L. Rózsa, A. Deák, E. Simon, R. Yanes, L. Udvardi, L. Szunyogh, and U. Nowak. [Skyrmions with Attractive Interactions in an Ultrathin Magnetic Film](#). *Physical Review Letters* 117 (2016).
- [130] J. Slonczewski. [Current-driven excitation of magnetic multilayers](#). *Journal of Magnetism and Magnetic Materials* 159, L1–L7 (1996).
- [131] F. Matsukura, Y. Tokura, and H. Ohno. [Control of magnetism by electric fields](#). *Nature Nanotechnology* 10, 209–220 (2015).
- [132] H. Ohno, D. Chiba, F. Matsukura, T. Omiya, E. Abe, T. Dietl, Y. Ohno, and K. Ohtani. [Electric-field control of ferromagnetism](#). *Nature* 408, 944–946 (2000).
- [133] P. Rovillain, R. de Sousa, Y. Gallais, A. Sacuto, M.-A. Méasson, D. Colson, A. Forget, M. Bibes, A. Barthélémy, and M. Cazayous. [Electric-field control of spin waves at room temperature in multiferroic BiFeO<sub>3</sub>](#). *Nature Materials* 9, 975–979 (2010).
- [134] M. Soda, K. Kimura, T. Kimura, M. Matsuura, and K. Hirota. [Electric Control of Spin Helicity in Multiferroic Triangular Lattice Antiferromagnet CuCrO<sub>2</sub> with Proper-Screw Order](#). *Journal of the Physical Society of Japan* 78, 124703 (2009).

- [135] M. Schott, A. Bernard-Mantel, L. Ranno, S. Pizzini, J. Vogel, H. Béa, C. Baraduc, S. Auffret, G. Gaudin, and D. Givord. [The Skyrmion Switch: Turning Magnetic Skyrmion Bubbles on and off with an Electric Field](#). *Nano Letters* 17, 3006–3012 (2017).
- [136] L. Gerhard, T. Yamada, T. Balashov, A. Takács, R. Wesselink, M. Däne, M. Fechner, S. Ostanin, A. Ernst, I. Mertig, and W. Wulfhekel. [Magnetolectric coupling at metal surfaces](#). *Nature Nanotechnology* 5, 792–797 (2010).
- [137] J. Simmons. [Generalized Formula for the Electric Tunnel Effect between Similar Electrodes Separated by a Thin Insulating Film](#). *Journal of Applied Physics* 34, 1793–1803 (1963).
- [138] A. Sonntag, J. Hermenau, A. Schlenhoff, J. Friedlein, S. Krause, and R. Wiesendanger. [Electric-Field-Induced Magnetic Anisotropy in a Nanomagnet Investigated on the Atomic Scale](#). *Physical Review Letters* 112, 017204 (2014).
- [139] C. Girard, C. Joachim, C. Chavy, and P. Sautet. [The electric field under a STM tip apex: implications for adsorbate manipulation](#). *Surface Science* 282, 400–410 (1993).
- [140] I. Ekvall, E. Wahlström, D. Claesson, H. Olin, and E. Olsson. [Preparation and characterization of electrochemically etched W tips for STM](#). *Measurement Science and Technology* 10, 11–18 (1999).
- [141] Q. Dubout, F. Donati, C. Wäckerlin, F. Calleja, M. Etzkorn, A. Lehnert, L. Claude, P. Gambardella, and H. Brune. [Controlling the Spin of Co Atoms on Pt\(111\) by Hydrogen Adsorption](#). *Physical Review Letters* 114, 106807 (2015).
- [142] A. Khajetoorians, M. Valentyuk, M. Steinbrecher, T. Schlenk, A. Shick, J. Kolorenc, A. I. Lichtenstein, T. Wehling, R. Wiesendanger, and J. Wiebe. [Tuning emergent magnetism in a Hund’s impurity](#). *Nature Nanotechnology* 10, 958–964 (2015).
- [143] B. Santos, S. Gallego, A. Mascaraque, K. McCarty, A. Quesada, A. N’Diaye, A. K. Schmid, and J. de la Figuera. [Hydrogen-induced reversible spin-reorientation transition and magnetic stripe domain phase in bilayer Co on Ru\(0001\)](#). *Physical Review B* 85, 134409 (2012).
- [144] D. Iaia, A. Kubetzka, K. von Bergmann, and R. Wiesendanger. [Structural and magnetic properties of Ni/Fe nanostructures on Ir\(111\)](#). *Physical Review B* 93, 134409 (2016).
- [145] G. Chen, J. Zhu, A. Quesada, J. Li, A. N’Diaye, Y. Huo, T. Ma, Y. Chen, H. Kwon, C. Won, Z. Qiu, A. Schmid, and Y. Wu. [Novel Chiral Magnetic Domain Wall Structure in Fe/Ni/Cu\(001\) Films](#). *Physical Review Letters* 110, 177204 (2013).

- [146] F. Meier, K. von Bergmann, P. Ferriani, J. Wiebe, M. Bode, K. Hashimoto, S. Heinze, and R. Wiesendanger. [Spin-dependent electronic and magnetic properties of Co nanostructures on Pt\(111\) studied by spin-resolved scanning tunneling spectroscopy](#). *Physical Review B* 74, 195411 (2006).
- [147] J. Sassmanshausen. Rastertunnelmikroskopie ultradünner Bleischichten auf Fe/Ir(111). Master thesis. Universität Hamburg, 2016.

# List of publications

## Articles

P.-J. Hsu, L. Rózsa, A. Finco, L. Schmidt, K. Palotás, E. Vedmedenko, L. Udvardi, L. Szunyogh, A. Kubetzka, K. von Bergmann, and R. Wiesendanger. [Inducing skyrmions in ultrathin Fe films by hydrogen exposure](#). *Nature Communications* 9, 1571 (2018).

A. Finco, L. Rózsa, P.-J. Hsu, A. Kubetzka, E. Vedmedenko, K. von Bergmann, and R. Wiesendanger. [Temperature-Induced Increase of Spin Spiral Periods](#). *Physical Review Letters* 119, 037202 (2017).

P.-J. Hsu, A. Kubetzka, A. Finco, N. Romming, K. von Bergmann, and R. Wiesendanger. [Electric-field-driven switching of individual magnetic skyrmions](#). *Nature Nanotechnology* 12, 123–126 (2017).

A. Finco, P.-J. Hsu, A. Kubetzka, K. von Bergmann, and R. Wiesendanger. [Tailoring noncollinear magnetism by misfit dislocation lines](#). *Physical Review B* 94, 214402 (2016).

P.-J. Hsu, A. Finco, L. Schmidt, A. Kubetzka, K. von Bergmann, and R. Wiesendanger. [Guiding Spin Spirals by Local Uniaxial Strain Relief](#). *Physical Review Letters* 116, 017201 (2016).

## Invited talks

- A. Finco, P.-J. Hsu, L. Rózsa, A. Kubetzka, E. Vedmedenko, K. von Bergmann, R. Wiesendanger, **Various ways to tune non-collinear magnetism in ultrathin films**, *Intermag, Singapore*, 04.2018.
- A. Finco, P.-J. Hsu, N. Romming, A. Kubetzka, K. von Bergmann, R. Wiesendanger, **Electric field induced switching of magnetic skyrmions and strain relief effects**, *SPIE Optics+Photonics, San Diego, USA*, 08.2017.
- A. Finco, P.-J. Hsu, N. Romming, T. Eelbo, A. Kubetzka, K. von Bergmann, R. Wiesendanger, **Electric field switching of skyrmions and non-collinear magnetism at room temperature investigated by STM techniques**, *SOCSIS, Spetses, Greece*, 07.2016.

## Contributed talks, seminar talks and posters

- A. Finco, P.-J. Hsu, L. Rózsa, A. Kubetzka, E. Vedmedenko, K. von Bergmann, R. Wiesendanger, **Various ways to tune non-collinear magnetism in ultrathin films**, *Seminar talk, Laboratoire Charles Coulomb, Montpellier, France, 03.2018.*
- A. Finco, P.-J. Hsu, A. Kubetzka, K. von Bergmann, R. Wiesendanger, **Structure and magnetism of an hydrogenated Fe monolayer on Ir(111)**, *Contributed talk, DPG Spring Meeting, Berlin, Germany, 03.2018.*
- A. Finco, P.-J. Hsu, L. Rózsa, A. Kubetzka, E. Vedmedenko, K. von Bergmann, R. Wiesendanger, **Various ways to tune non-collinear magnetism in ultrathin films**, *Seminar talk, SPINTEC, Grenoble, France, 02.2018.*
- A. Finco, P.-J. Hsu, L. Rózsa, A. Kubetzka, N. Romming, E. Vedmedenko, K. von Bergmann, R. Wiesendanger, **Modifying non-collinear magnetism with strain, temperature and electric field**, *Poster, Skymag, Paris, France, 05.2017.*
- A. Finco, P.-J. Hsu, A. Kubetzka, K. von Bergmann, R. Wiesendanger, **Tailoring non-collinear magnetism by misfit dislocation lines**, *Contributed talk, DPG Spring Meeting, Dresden, Germany, 03.2017.*
- A. Finco, P.-J. Hsu, T. Eelbo, N. Romming, A. Kubetzka, K. von Bergmann, R. Wiesendanger, **Non-collinear magnetic order at room temperature**, *Contributed talk, DPG Spring Meeting, Regensburg, Germany, 03.2016.*
- A. Finco, P.-J. Hsu, T. Eelbo, L. Schmidt, N. Romming, A. Kubetzka, K. von Bergmann, R. Wiesendanger, **Temperature and field dependent SP-STM investigation of the non-collinear magnetic structures of several layers of Fe on Ir(111)**, *Contributed talk, MMM, San Diego, USA, 01.2016.*
- A. Finco, P.-J. Hsu, L. Schmidt, A. Kubetzka, K. von Bergmann, R. Wiesendanger, **Investigation of the chiral spin structure of the double layer Fe on Ir(111) using SP-STM in a 3D vector magnetic field system**, *Poster, DPG Spring Meeting, Berlin, Germany, 03.2015.*

# Acknowledgements/Remerciements

I finally thank all the people who helped and supported me during these years in Hamburg:

- Prof. Dr. Wiesendanger for offering me the chance to work in his group, to present my results at various conferences all over the world and of course for supervising my thesis;
- Dr. Kirsten von Bergmann und Dr. André Kubetzka for their valuable help and advices as well as the proofreading of this work;
- Prof. Pin-Jui Hsu for our great and very fruitful collaboration on Fe/Ir(111);
- Dr Levente Rózsa for his theoretical support which improved substantially my understanding of the data;
- all the colleagues from lab013 for their daily help and the nice work together;
- also the whole group R, for useful hints and discussions and the friendly atmosphere;
- the technical and administrative teams, the helium team, as well as the mechanical and electronic workshops for their indispensable support;
- tous ceux qui sont venus jusqu'ici nous rendre visite, parfois même plusieurs fois;
- mes parents, pour leur soutien moral et logistique à toute épreuve et leurs nombreuses visites ainsi que mes petites soeurs, Constance (en premier, je n'ai pas oublié), Pauline (merci pour la pénible relecture) et Cécile;
- et Étienne, qui pendant ces quatre ans, grâce aux services de la DB aura parcouru, à raison de deux voyages par mois, environ  $4 \times 25 \times 2 \times 200 = 40\,000$  km soit le tour de la terre (en ICE !), juste pour venir me voir. Merci.



# Eidesstattliche Versicherung

## Declaration on oath

Hiermit versichere ich an Eides statt, die vorliegende Dissertationsschrift selbst verfasst und keine anderen als die angegebenen Hilfsmittel und Quellen benutzt zu haben.

Die eingereichte schriftliche Fassung entspricht der auf dem elektronischen Speichermedium.

Die Dissertation wurde in der vorgelegten oder einer ähnlichen Form nicht schon einmal in einem früheren Promotionsverfahren angenommen oder als ungenügend beurteilt.

Hamburg, den